Mechanistic studies of acid-catalysed hydrocarbon reactions in zeolitic materials

Dissertation for the degree of

Philosophiae Doctor

Marius Westgård Erichsen

Department of Chemistry

Faculty of Mathematics and Natural Sciences

UNIVERSITY OF OSLO

June 2014

Series of dissertations submitted to the
Faculty of Mathematics and Natural Sciences, University of Oslo
No. 1549

ISSN 1501-7710

Cover: Inger Sandved Anfinsen.
Printed in Norway: AIT Oslo AS.

Produced in co-operation with Akademika Publishing.
The thesis is produced by Akademika Publishing merely in connection with the thesis defence. Kindly direct all inquiries regarding the thesis to the copyright holder or the unit which grants the doctorate.

Preface

The work presented in this thesis was carried out between August 2010 and June 2014 as part of a four year PhD scholarship financed jointly by the Department of Chemistry, University of Oslo, and the CRI-centre "Innovative Natural Gas Products and Processes" (inGAP). As part of the scholarship, one semester of undergraduate teaching has been performed, and one semester has been spent working for INEOS ChlorVinyls in Porsgrunn. Prof. Unni Olsbye has acted as main supervisor and Prof. Stian Svelle as co-supervisor during the entire project.

I am grateful to Prof. Unni Olsbye for allowing me to perform this work and to both of my supervisors for all their help along the way. Thanks to Terje Fuglerud and the others at INEOS for receiving me and giving me the chance to see how chemistry is used outside academia. Kristof De Wispelaere and others at the Centre for Molecular modelling, Ghent University, are greatly acknowledged for very fruitful discussions and a good collaboration. Thanks to Einar Uggerud and Osamu Sekiguchi at the mass spectrometry laboratory for all their help. I am furthermore grateful that I was allowed to co-supervise Magnus Mortén during an undergraduate project and Christian Ahoba-Sam towards a master's degree. These experiences as supervisor have been very rewarding for me, and I wish you both the very best for the future.

The entire catalysis group is acknowledged for providing a friendly and stimulating work environment. Special thanks to Bjørn Tore Lønstad Bleken for his willingness to discuss all manner of issues, whether scientific or not, during the years we have shared an office.

Finally, I wish to thank my dear Stine for sticking with me and supporting me despite the long hours I have spent away from home during the last couple of years.

Abbreviations used in this thesis

a. u.	Arbitrary units
$AlPO_4$	Aluminophosphate
BET	Braunauer-Emmet-Teller
CBU	Composite building unit
DFT	Density functional theory
DME	Dimethyl ether
EDS	Energy dispersive x-ray spectroscopy
FID	Flame ionisation detector
FTIR	Fourier transform infrared spectroscopy
GC	Gas Chromatograph
$HeptaMB^+$	Heptamethylbenzenium cation
HexaMB	Hexamethylbenzene
HMMC	1,2,3,3,4,5-hexamethyl-6-methylene-1,4-cyclohexadiene
HTI	Hydrogen transfer index (sum of alkanes / sum of alkenes+alkanes)
IZA	International Zeolite Association
MD	Molecular dynamics
MeAPO	Metal-substituted aluminophosphate
MeAPSO	Metal-substituted silicoaluminophosphate
MeSpaI	N(16)-methylsparteinium iodide
MeSpaOH	N(16)-methylsparteinium hydroxide

MOGD	Mobil olefins to gasoline and distillate
MS	Mass Spectrometer
MTG	Methanol to gasoline
MTH	Methanol to hydrocarbons
MTO	Methanol to olefins
MTP	Methanol to propene
NMR	Nuclear magnetic resonance
PolyMB(s)	Polymethylbenzene(s)
SAPO	Silicoaluminophosphate
SBU	Secondary building unit
SEM	Scanning electron microscope
TGA	Thermogravimetric analysis
TIGAS	Topsøe integrated gasoline synthesis
ToF	Time-of-flight
TPA	Temperature programmed adsorption
TPD	Temperature programmed desorption
WHSV	Weight hourly space velocity
XRD	X-ray diffraction
Å	Ångstrøm (1 Å = 0.1 nm)

Table of contents

List of publications

This thesis is based on the six manuscripts listed and numbered in chronological order below. The full manuscripts are collected in the appendix.

Paper I: *H-SAPO-5 as methanol-to-olefins (MTO) model catalyst: Towards elucidating the effects of acid strength.*
M. Westgård Erichsen, S. Svelle, U. Olsbye*, Journal of Catalysis, 298 (2013) 94.

Paper II: *The influence of catalyst acid strength on the methanol to hydrocarbons (MTH) reaction.*
M. Westgård Erichsen, S. Svelle, U. Olsbye*, Catalysis Today, 215 (2013) 216.

Paper III: *Shape selectivity in zeolite catalysis. The Methanol to Hydrocarbons (MTH) reaction.*
S. Teketel, M. Westgård Erichsen, F. Lønstad Bleken, S. Svelle, K. P. Lillerud, U. Olsbye*, Catalysis: Volume 26, The Royal Society of Chemistry, 2014, pp. 179.

Paper IV: *Syngas to liquids via oxygenates.*
M. Westgård Erichsen, J. S. Martinez-Espin, F. Joensen, S. Teketel, P. d. C. Huertas, K. P. Lillerud, S. Svelle, P. Beato, U. Olsbye*, Submitted as book chapter in "Small-Scale Gas to Liquid Fuel Synthesis", CRC press

Paper V: *How zeolitic acid strength and composition alter the reactivity of alkenes and aromatics towards methanol.*
M. Westgård Erichsen, K. De Wispelaere, K. Hemelsoet, S. Moors T. Deconinck, M. Waroquier, S. Svelle, V. Van Speybroeck, U. Olsbye*, Manuscript in preparation.

Paper VI: *Reactivity of the heptamethylbenzenium cation – a combined mass spectrometric and catalytic investigation*
M. Westgård Erichsen*, M. Mortén, O. Sekiguchi, S. Svelle, E. Uggerud, U. Olsbye, Manuscript in preparation.

* corresponding author

The author's contribution

Paper I: The author participated in planning the work and performed all the experiments. The author was strongly involved in data interpretation and preparation of the manuscript.

Paper II: The author performed all experiments and data analysis. The author was also strongly involved in planning the work, interpretation of the results and in preparation of the manuscript.

Paper III: The author performed all new experiments required for preparation of the manuscript (catalytic tests of H-SSZ-24, H-MOR, H-BEA and H-ZSM-22), and was strongly involved in both planning and writing of the manuscript.

Paper IV: The author was strongly involved in the planning and writing of the manuscript.

Paper V: The author planned and performed all catalytic experiments, and was strongly involved in interpretation of the results. The author also prepared the manuscript together with K. De Wispelaere.

Paper VI: The author planned the work, performed all catalytic tests, and prepared the manuscript together with U. Olsbye. Furthermore, the author co-supervised M. Mortén during a Bachelor degree project on synthesis and catalytic testing of HMMC.

List of conference contributions

Mechanisms of olefin formation in H-SAPO-5 during methanol-to-hydrocarbons (MTH) catalysis.
M. Westgård Erichsen, M. H. Nilsen, K. P. Lillerud, S. Svelle, U. Olsbye
Poster presented at the XIIth Netherlands' Catalysis and Chemistry Conference, March 10th-12th, 2011, Noordwijkerhout, The Netherlands

Conversion of methanol to hydrocarbons over H-SAPO-5: Towards elucidating the effects of acid strength.
M. Westgård Erichsen, S. Svelle, U. Olsbye
Keynote lecture given at SynFuel2012, June 29-30, 2012, Munich, Germany

H-SAPO-5 as model catalyst for methanol conversion: Does a lower acid strength shift the alkene formation mechanism?
M. Westgård Erichsen, S. Svelle, U. Olsbye
Poster presented for poster symposium at the 15th International Catalysis Conference, July 1-6, 2012 Munich, Germany

The influence of catalyst acid strength on reactions relevant to methanol-to- hydrocarbons (MTH) catalysis.
M. Westgård Erichsen, S. Svelle, U. Olsbye
Poster presented for poster symposium at Europacat 2013, September 1-6, 2013, Lyon, France

The influence of catalyst acid strength on reactions relevant for Methanol To Hydrocarbons (MTH) catalysis.
M. Westgård Erichsen, K. De Wispelaere, J. Van der Mynsbrugge, S. Moors, T. Deconinck, S. Svelle, K. Hemelsoet, V. Van Speybroeck, U. Olsbye
Oral presentation at the 16th Nordic Symposium on Catalysis, June 15-17, 2014, Oslo, Norway

Scope

The scope of this PhD project was to study reaction mechanisms and kinetics of acid-catalysed hydrocarbon reactions over zeolitic catalysts, with the effects of catalyst acid strength as the main focus. The first goal was to study in detail the reaction mechanisms of the commercially interesting methanol to hydrocarbons (MTH) reaction over the weakly acidic zeotype H-SAPO-5. Subsequently the structurally identical strongly acidic zeolite H-SSZ-24 should be synthesised, and a detailed comparison of the two catalysts in the MTH reaction performed. The third aim was to study the kinetics of single reactions over these two catalysts.

The large amount of work related to the MTH reaction also led to involvement in studies of other catalysts for the same reaction. For this reason, work and discussions on the MTH reaction constitutes a large portion of this thesis. Two single reaction steps were studied in more detail: methylation and polymethylbenzene de-alkylation. While a full kinetic study of the methylation of benzene and propene over the two catalysts was initiated, it was not completed due to experimental difficulties. Nevertheless, novel results on how acid strength affected methylation of aromatics and alkenes were obtained and are reported here.

The first two chapters of this thesis provide a background for the work performed. First, general aspects of catalysis and zeolite chemistry are discussed, including a section on acidity. Secondly, an overview of the field of MTH chemistry, de-alkylation and methylation reactions and previous work concerning the effect of catalyst acid strength on reactions is given. Chapter three provides details on experimental methods. Chapter four summarises the work performed during this project. The full details of the work performed can be found in the papers collected in the appendix.

1 Catalysis and zeolitic materials

1.1 Catalysis

Catalysis plays an integral part both in most industrial chemical processes and in the chemical reactions of living organisms, and thus impacts strongly on our everyday lives. Stated briefly, a catalyst accelerates a chemical reaction without itself being consumed and without altering the overall thermodynamics of the reaction. This means that catalysis enables reactions to proceed more efficiently and under milder conditions than what would be possible otherwise. An example of how a catalytic reaction differs from a non-catalytic reaction is illustrated by the potential energy diagram in Figure 1.1.

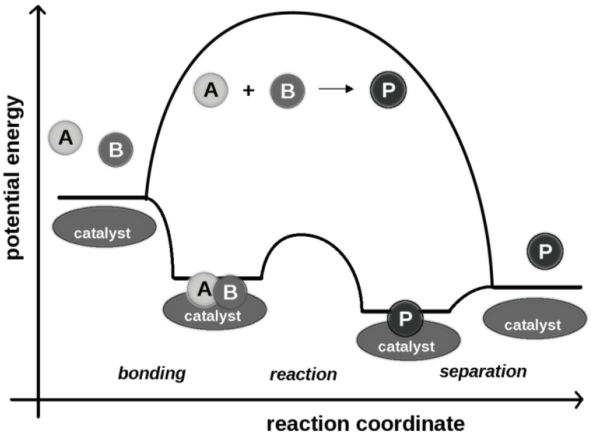

Figure 1.1: Potential energy diagram of a non-catalysed (upper curve) and a catalysed reaction (lower curve). Figure adapted from [1].

From Figure 1.1 it is apparent that the catalyst offers an alternative reaction path that is more complex than the non-catalysed path, but contains significantly lower activation barriers. The added complexity is common for catalysed reactions, as some form of bonding between the catalyst and the reactant (substrate) must occur. This inevitably leads to more reaction steps. In order to accelerate the reaction, the catalyst must stabilise the transition state of the reaction more than it stabilises the reactants [2].

A second important observation from Figure 1.1 is that the overall energy change from reactants to products is identical in the catalysed and un-catalysed reactions. This means that a catalyst will not in any way affect the position of equilibrium for the reaction. Catalysis thus falls solely within the field of kinetics.

The word catalysis was first coined by Jöns Jacob Berzelius in 1836 [3]. However, the phenomenon, although not previously defined, had gained practical importance before this. For instance, Humphry Davy had already observed in 1817 that a pre-heated platinum wire would glow white hot in a mixture of air and alcohol or coal gas until all the flammable material was consumed, and Gottlieb Kirchoff had reported the conversion of starch into sugars by dilute acids in 1814 [4]. Even as far back as the 8th century, the writings of the Arabic [5] (or possibly Persian) alchemist Jabir Ibn Haiyan mention the use of mineral acids for dehydration of alcohol to ether [4]. The first large-scale commercial use of catalysts was made possible by Johan Wolfgang Döbereiner, whose experiments enabled mass production of a lighter based on the incineration of hydrogen over a fine platinum sponge. By 1828, some 20 000 such lighters were in use in England and Germany alone, and it was still in use at the beginning of the First World War [4, 6].

In principle a catalyst can take any form, including atoms, small or large molecules, and solids such as metal or oxide surfaces. It is customary to distinguish between homogeneous catalysis, where the reactants and catalysts are in the same phase, and heterogeneous catalysis, where the catalyst is in a different phase from the reactant. In addition, the field of biocatalysis or enzymatic catalysis is usually treated as a separate discipline. This thesis focuses on heterogeneous catalysis of hydrocarbons in gas phase reacting over solid zeolitic oxide catalysts.

1.2 Zeolitic materials

Zeolites are a class of crystalline aluminosilicates with uniform intracrystalline porosity [7, 8]. They are a subclass of the tectosilicates, meaning that they consist of a three-dimensional network of TO_4 tetrahedra, where T is either Al or Si. These TO_4 units are connected to each other through the oxygen at the vertices, and can assemble into a large variety of microporous (pore dimensions <2 nm [9]) three-dimensional frameworks. Some examples of how TO_4 tetrahedra can assemble to produce structures with different pore geometries are shown in Figure 1.2.

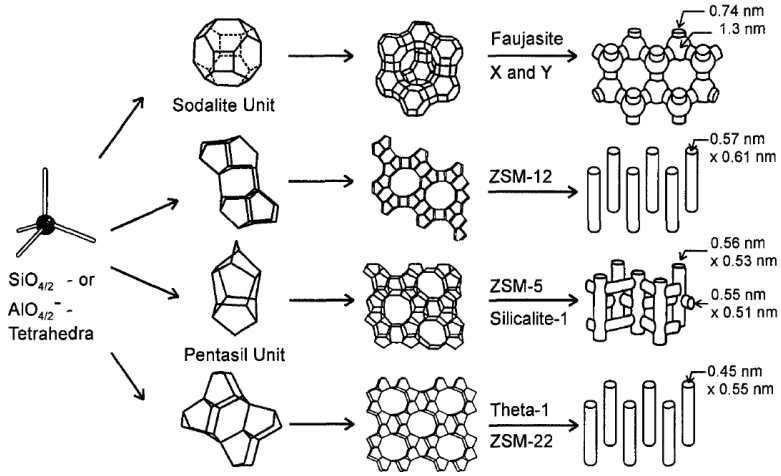

Figure 1.2: Examples of how TO_4 tetrahedra can connect in four different manners in order to form four different zeolite structures. Illustration from [10].

Due to the molecular dimensions of zeolitic pores, small molecules are selectively adsorbed into the porous framework, whilst larger molecules are rejected. This ability is often referred to as molecular sieving [7]. In addition to this, zeolitic pores can contain easily exchangeable cations or well-defined acid sites. This combination of properties makes zeolites highly successful for a number of commercial applications within sorption, ion-exchange and catalysis, and several million tons are used annually [8, 11, 12].

The word zeolite is derived from the Greek words “zeo” (boiling) and “lithos” (stone), and was coined in 1756 by the Swedish geologist Axel Fredrick Cronstedt to describe a newly discovered class of minerals that bubbled and swelled due to loss of water when heated [13]. Later research has identified one of the samples studied by Cronstedt as

a mixture of the isostructural zeolites stellerite and stilbite [14]. Even though zeolites were regarded as rare minerals for centuries after their discovery, the increased availability of X-ray characterisation facilities in the 1950's revealed that these minerals are in fact abundant in nature [8].

Despite the early discovery of zeolites, and their abundance in nature, zeolites did not gain commercial importance before Barrer and Milton [8, 10] managed to synthesise zeolites by low-temperature hydrothermal methods in the 1940s' and 50's. Since then, the importance of zeolites has grown tremendously, not least due to their use as catalysts. Major milestones include the discovery of shape selective catalysis [15-17] and intensive research on acid properties by Rabo and others [11]. The number of different framework structures synthesised has also increased dramatically, with 218 different zeolite structures recognized by the International Zeolite Association (IZA) [18] at the time of writing. All recognized frameworks are identified by a unique three letter code. Not all of these structures are aluminosilicates, as numerous zeolitic materials of other compositions have also been synthesised or discovered [19-23].

The increasingly large variety of zeolite-like materials makes it difficult to find a suitable definition of which materials are actually zeolites, and this topic has been subject to debate [24-29]. This work will follow the recommendation by Dyer [7] and others, and reserve the name zeolites for aluminosilicate materials built into frameworks approved by the IZA. Materials containing other elements will be referred to as zeotypes, and the term zeolitic will be used more loosely to cover both zeolites and zeotype materials.

Zeolitic structures are complex and varied, and it is not necessarily easy to visualise them from their unit cell parameters alone. In order to facilitate easier visualisation and comparisons of framework structures, a number of secondary and composite building units shared between many structures have been recognized. Secondary building units (SBUs) are finite and achiral units that can be used to construct an entire framework. Often, a given framework can be constructed from several different SBUs. Composite building units (CBUs) are larger units which are not necessarily achiral, and some CBUs may be infinitely extended (i.e. chains or layers). They are useful in ascertaining relations between different framework types, but cannot necessarily be used to construct whole frameworks. Some examples of SBUs and CBUs are presented in Figure 1.3.

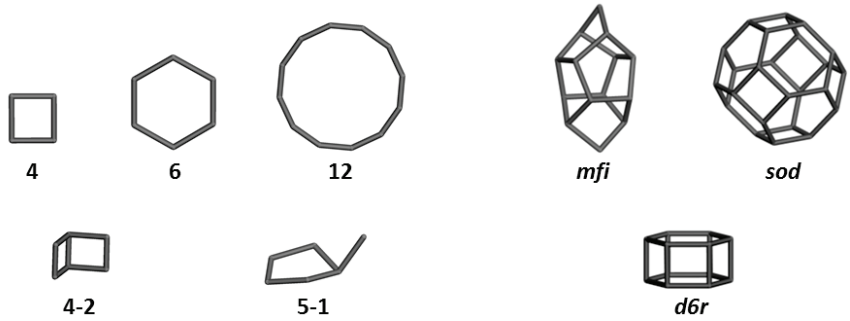

Figure 1.3: Some examples of SBUs (left) and CBUs (right). Bridging O-atoms have been omitted and T-O-T bonds drawn as straight lines for clarity in the drawings.

While SBUs and CBUs are very useful in visualizing the full framework, for many applications a more general way to describe them is by the features of their pore system. The pore system may extend in one, two or three dimensions and may or may not contain inner cavities that are larger than the apertures leading into them. The pore size of a material is typically characterised by the size of the smallest ring in the pore and named after how many T-atoms it contains. The most common pore sizes contain 8, 10 or 12 T-atoms, and materials containing these are often referred to as small-, medium- and large-pore zeotypes. In addition, a number of so-called extra-large-pore materials, containing pores with 14 or more T-atoms, have been discovered [30-33]. The free diameters of circular 8-, 10- and 12-ring pores are roughly 4.1, 5.5 and 7.4 Å respectively [34], but distorted rings may deviate significantly from these diameters. A good example of deviating pore dimensions can be found in the AFI and MTW frameworks. Both structures contain 12-ring one-dimensional pores, but their maximum diameters are 7.3 Å and 6.0 Å respectively [18].

While the structural framework determines the porosity of the materials, chemical properties are dependent on the T-atom composition. If we consider a framework consisting of SiO_4 tetrahedra only, this will be electronically neutral and hydrophobic. As aluminium is trivalent and silicon is tetravalent, substitution of Al for Si leads to a net negative charge in the framework, which must be balanced by a cation residing inside the channel system. Such cations are exchangeable, and thus give rise to the ion-exchange capabilities of zeolites. In addition to increasing the number of ion-exchange sites, increasing the amount of Al relative to Si T-atoms in a zeolite also gradually changes the material from hydrophobic to hydrophilic, with zeolites of low Si/Al ratios being strongly

hydrophilic [12]. Normally, the amount of Al in any zeolite is limited to half the T-atoms, since two Al-containing tetrahedra cannot share an oxygen atom [35]. Materials with elemental composition near the minimum Si/Al ratio of 1 tend to be less thermally stable than their silicon-rich counterparts [12].

Other atoms can replace Si and Al in zeolitic structures, which will alter the properties of the material. For instance, main group elements such as Be, B, Ga and Ge and a number of transition metals have been shown to substitute either Al or Si [22-24, 36, 37]. A class of zeotype materials where half the T-atoms are Al and the other half P, in a strictly alternating fashion, was synthesised by workers at Union Carbide in 1982 [20]. Such a combination of T-atoms leads to a framework with localised charges, but a net charge of zero. The result is a moderately hydrophilic framework that does not possess ion-exchange capabilities. However, ion-exchange capability can be introduced by substitution of aluminium or phosphorous by elements of different valence. While a large number of elements can be incorporated into $AlPO_4$ structures [19], perhaps the most common class of such materials are the silicoaluminophosphate (SAPO) materials first reported in 1984 [21]. In the SAPO materials, Si substitutes for P to produce a net negative charge analogously to substitution of Al for Si in zeolites. In addition to this, other phosphate based zeotypes incorporating Be, Zn or Ga instead of Al have also been reported [32, 38, 39].

1.3 Catalysis by zeolitic materials

One of the largest commercial markets for zeolites is their use as acid catalysts. Their use dates back to the 1950's, when it was discovered that zeolite X was a much more active acid catalyst than the amorphous silica-alumina catalysts used commercially at the time [11, 12]. Today, zeolite catalysts are employed extensively for hydrocarbon conversion reactions in petrochemical industry [40, 41]. As solids, the zeolites offer the advantage of easier separation inherent in heterogeneous catalysis. However, two properties set the zeolites apart from other (amorphous) solid acid catalysts: well-defined catalytic sites and shape selectivity. Of these, the second will be discussed here, while acidity will be discussed in Section 1.4.

Shape selectivity results from the uniform pores present in the zeolite frameworks. The size of the pores determines which reactions can occur inside the materials, based on whether the chemical species involved have sufficient space to reside inside the pore system. Shape selectivity is usually divided into three differing types [42-45]: reactant-, product- and (restricted) transition state shape selectivity. These are schematically illustrated in Figure 1.4.

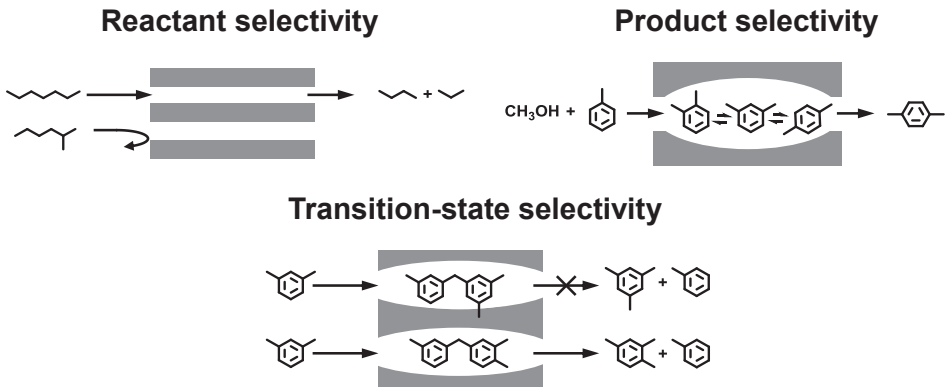

Figure 1.4: The three classes of shape selectivity, adapted from [43].

In reactant selectivity (top left in Figure 1.4) bulky reactants are prevented from diffusing into the pore system, while smaller molecules diffuse more easily into the pores. Larger molecules will thus be unable to reach an active site, and will not react. Product shape selectivity (top right in Figure 1.4) is observed when some of the product molecules are too

large to diffuse out of the pore system. This is often observed in zeolites featuring large internal cavities connected by narrow apertures. Large molecules can be formed in the cavities but are restricted from diffusing out of the structure unless they react further to form less bulky molecules. In (restricted) transition state shape selectivity (bottom of Figure 1.4) neither the product nor the reactant are hindered from diffusing into or out of the zeolite, but the available space cannot accommodate certain transition states. Transition state shape selectivity may also lead to some transition states being stabilised more than others due to a "good fit" with the available space [46].

Since both reactant and product shape selectivity are based on mass transfer limitations, they are affected by the size of the catalyst crystal. On the other hand, this is not the case for transition state selectivity which does not involve hindered diffusion. Studies of catalysts of different crystal size can thus be used to discriminate between product and transition state shape selectivity [47]. Concerning all types of shape selectivity, it is important to keep in mind that it occurs only in the bulk of the zeolitic crystals. In crystals small enough that a large fraction of the active sites are accessible from the external surface, the effects of shape selectivity will be greatly diminished.

1.4 Zeolitic acidity

Well-defined catalytically active acid sites in zeolitic materials are obtained when protons act as charge-compensating cations for a net negatively charged framework. In this case, the framework will contain an acidic OH group at one of the corner positions between two TO_4 of different valence. Figure 1.5 shows the acid site in an aluminosilicate zeolite and a silicoaluminophosphate (SAPO) zeotype material. Note that while the OH group is at a shared corner between a SiO_4 and an AlO_4^- tetrahedra in both materials, the identities of the neighbouring T atoms differs, and thus the chemical environment around the OH group is also different.

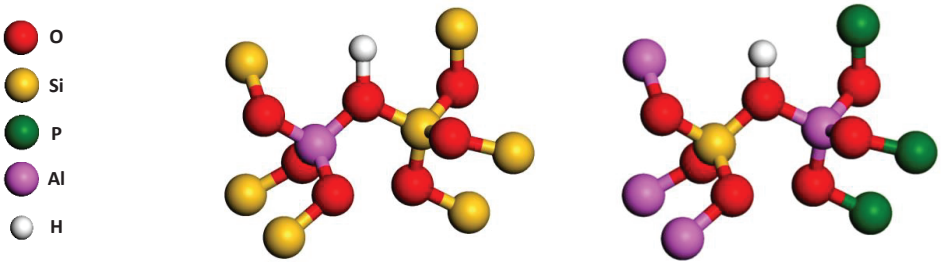

Figure 1.5: A Bridging OH group in a zeolite (left) and a SAPO (right).

In an ideal H-exchanged zeolite these Brønsted acidic (proton donating) OH groups are the only type of acid site present. This means that the acid site density (or number of acid sites) of an ideal zeotype material is equal to the number of substituted framework atoms (with respect to an electronically neutral framework). For zeolites, the molar ratio between silicon and aluminium (Si/Al) or their corresponding oxides (SiO_2/Al_2O_3) is often reported, and this value is inversely proportional to the acid site density of the material. A similar ratio of (Al+P)/Si can be used for SAPO materials.

Some materials also contain Lewis acid (electron accepting) sites. These are usually associated either with defects or the presence of extra-framework aluminium in the channels, but can also be introduced by ion-exchange with polyvalent cations [11]. While Lewis acidity may play a role in some reactions, the catalytic hydrocarbon cracking activity of high silica zeolites has been shown to depend linearly on the number of Brønsted sites [48-50], and it is therefore generally accepted that these are the most important catalytic sites in aluminosilicate zeolites.

The topic of acidity in solids is complex and even the term itself is fraught with ambiguity [51]. Firstly, the terms acidity and acid strength are sometimes used to describe both the acid strength (related to the ease of removing the proton) and acid site density of a material. While both properties are important in catalysis, such an imprecise expression may easily lead to confusion. This thesis will use the term acid site density to describe the number of acid sites, while reserving the term acid strength to describe the ease of breaking the acid site O-H bond.

Secondly, zeolite acid strength has proven very difficult both to define and determine. Until a few decades ago, zeolites were treated as superacids, a view which shaped many of the early proposals for reaction mechanisms in zeolite catalysis [51]. However, this view was largely abandoned over time as several works failed to observe carbocations in zeolites that were persistent in liquid superacids or on metal halide powders at low temperature [52-56]. On the other hand, the deprotonation energy of zeolite frameworks have been calculated to be below 1200 kJ/mol [57], which is lower than the gas phase acidity of H_2SO_4 [58]. Thus, comparing zeolite acidity with solution phase acids is not straight-forward, and doing so may be more confusing than helpful [59]. Indeed, predicting the catalytic activity of zeolitic materials for any given reaction is still a challenge. This is partly due to the fact that the catalytic activity is not determined by the deprotonation energy of the framework alone, but also by a "solvation" effect dependent on the zeolite framework [60]. The situation is summarized elegantly by the following quote from James Haw [54]:

"Zeolites are not superacids; they are smart and subtle acids that find shortcuts past high-energy intermediates and the even higher energy transition states that must lead to them".

In many zeolites, individual acid sites have been shown to possess nearly identical acid strength [61, 62]. An exception to this homogeneity of acid sites occurs when the acid sites are not isolated from each other, as acid sites in close proximity to each other will have a lower acid strength than isolated sites. This effect usually becomes prominent when the Si/Al ratio is below 10 [63-65].

The acid strength of silicoaluminophosphate (SAPO) zeotype materials have not been studied in as great detail as for zeolites. It is usually assumed that isolated acid sites in SAPOs are less acidic than those in zeolites. This has been verified in the CHA structure

by several studies [66-68]. However, SAPO materials present some additional complications due to the possibility of SiO_4 clustering together in "silicon islands". Such clustering of SiO_4 tetrahedra means that the number of acidic OH groups may be lower than one per Si atom [69-71]. In addition, the strength of the acid site increases with the number of SiO_4 neighbours (up to 3), meaning that a range of different acid strengths is possible [72]. SAPO structures may even contain large siliceous or aluminosilicate domains [73], with the latter containing acid sites similar to those found in zeolites.

1.4.1 Measuring zeolitic acidity

While an exhaustive review of all techniques employed to characterise acidity is beyond the scope of this work, a short overview of some common methods for characterisation both of acid site density and acid strength is given below.

The most obvious way to measure the acid site density of a given zeotype material would be to determine the elemental composition of the material. However, direct correlations between elemental ratios and acid site density should not be automatically assumed. Where elemental ratios are determined by elemental analysis, there is no discrimination between framework and extra-framework elements. Various defects in the crystal structure may also lead to differences between elemental ratios and the number of acid sites, or may result in acid sites that are inaccessible to reactant molecules. Together, these considerations mean that direct measurements of the acid site density rather than the elemental composition are desirable. Such measurements will often yield the number of acid sites in mmol per gram of catalyst. A useful rule of thumb is that 0.41 mmol/g corresponds to a perfect zeolite framework with a Si/Al ratio of 40.

One of the most common methods for measurements both of acid strength and acid site density is temperature programmed desorption (TPD) of ammonia. Unfortunately, this method suffers from several disadvantages that complicate the interpretation of results. For samples such as H-ZSM-5 (MFI structure, see Section 1.5.2) [74] a desorption peak at low temperature, attributed to weakly bound NH_3, and a high-temperature peak attributed to NH_3 bound to the Brønsted acid sites are usually observed. In principle, the amount of NH_3 desorbing in the high temperature region should correspond to the number of acid sites in the sample. However, NH_3 can also interact strongly both with Lewis acids and with materials not commonly classified as acidic, such as calcium oxide [75]. Thus, the amount

of ammonia desorbed at high temperature does not necessarily equal the number of Brønsted acid sites in a zeolite containing defects, non-framework alumina or other impurities. Furthermore some samples, such as H-SAPO-5 [76], give rise to only one broad desorption peak. This makes quantification of Brønsted sites even more difficult. While NH_3 TPD can provide useful information on some samples, conclusions based on this technique should only be drawn with great care. It has been shown that transport limitations can have a strong influence on the desorption temperature [77], meaning that pore size may be equally important as acid strength for the desorption temperature.

Several other methods for determination of acid site density have been reported, although few are used as regularly as NH_3 TPD. One alternative is the use of Fourier Transform Infrared (FTIR) spectroscopy to monitor adsorption of a strong base, such as pyridine [78, 79]. In principle, such techniques allow quantification of the number of acid sites through integration of bands caused by the protonated base, while at the same time monitoring which OH groups are interacting with the base. Unfortunately, molar extinction coefficients for adsorbed species are hard to determine accurately, and the literature values vary greatly [80]. Combined Thermogravimetry and FTIR [81] provides an elegant solution to this problem, but requires highly specialized apparatus. Another option involves titration of OH groups by H/D exchange [82]. While this enables determination of the total number of O-H groups present, it should not be assumed that all O-H groups confer catalytic activity to the zeolite.

Another promising method for quantification of acid sites across different zeolite structures and compositions is TPD of reactive probe molecules such as alkylamines [59, 60, 77]. With the exception of methylamine all alkylammonium ions, formed by protonation of alkylamines on the acid sites, react in a narrow temperature range to form ammonia and the corresponding alkene. The reaction temperature is mainly dependent on the amine used, and not the composition of the lattice [60]. By measuring the amount of desorbed alkenes, the method selectively quantifies Brønsted acid sites of sufficient strength to protonate and to retain the ions up the characteristic reaction temperature (usually between ~250 and 450 °C depending on substitution at the α-carbon). The method has been shown to produce consistent results both in vacuum and under flow conditions [83]. Alkylamines of different sizes may even be used to probe the concentration of acid sites in each of the components of a cracking catalyst containing both H-ZSM-5 and H-Y

(FAU structure: 3D 12-rings and large cavities) in addition to amorphous silica-alumina [84].

While the deprotonation energy provides arguably the only rigorous measure of acid strength, this value cannot be easily measured. It can be calculated using theoretical measurements, but reliable values are not yet available for the majority of zeolitic materials. Use of microcalorimetry to obtain the heats of adsorption for basic probe molecules, such as ammonia and pyridine, have provided valuable insights. However, it must be combined with other methods in order to verify the nature of the adsorption sites. It should also be noted that even when adsorption occurs with proton transfer at the acid site, the measured value is not a measure of the proton affinity of the site [60]. The heat of adsorption also includes the interaction energy of the formed ion pair, and this quantity is dependent on both the framework structure and composition and on the adsorbed base. For this reason, the heat of adsorption is not a rigorous measure of intrinsic acidity of the acid site.

A common method to measure acidity differences utilises FTIR spectroscopy to investigate the perturbation of the O-H bands during adsorption of a weak base [85]. For example, adsorption of carbon monoxide at -196 °C results in moderate red-shift of the hydroxyl stretching frequency. A longer red-shift indicates stronger acidity. However, indications of spectral interference with the shifted absorption band and a large spread in reported values for similar zeolites mean that small differences in the shifts should be interpreted with caution [86].

1.5 Zeolitic structures relevant to this thesis

The most important catalysts employed in this work were the isostructural aluminosilicate H-SSZ-24 and the silicoaluminophosphate H-SAPO-5. The AFI framework topology, common to both catalysts, is therefore described in detail below. In addition, a number of different zeolites were compared in Papers III and IV and their structures are described in less detail. For more information on these structures, the reader is referred to the IZA webpage [18] or the atlas of zeolite framework types [28].

1.5.1 The AFI framework

The first report of a material with the AFI framework topology dates back to 1982 when Wilson et al. [20], working at the Union Carbide labs, presented the first aluminophosphate zeotypes. The novel structure of this material, called AlPO-5, was determined soon after [87]. When silicoaluminophosphate (SAPO) materials were reported in 1984, an analogous structure named SAPO-5 was reported [21]. Thereafter, numerous metals have been incorporated into $AlPO_4$-5 and SAPO-5 lattices, creating MeAPO and MeAPSO materials respectively [19]. An isostructural zeolite called SSZ-24 has also been synthesised, initially only in pure siliceous form by van Nordstrand et al. [88], but later with boron and aluminium incorporated [89, 90]. Curiously, the AFI structure may have been the first structure for which a silica zeotype was discovered after its aluminophosphate analogue [88].

The AFI framework is composed of columns of twisted four- and six- rings, together forming one-dimensional twelve ring channels running parallel to the c-axis. These channels are nearly circular, and measure 7.3 Å in diameter. The framework can be constructed from either of the secondary building units 4, 6 or 12. Alternatively, it can be visualised as comprising any of the CBUs *bog, afi* or the *nsc* (narsarsukite) chain [18]. Figure 1.6 shows both the composite building units and a detailed view of the AFI framework.

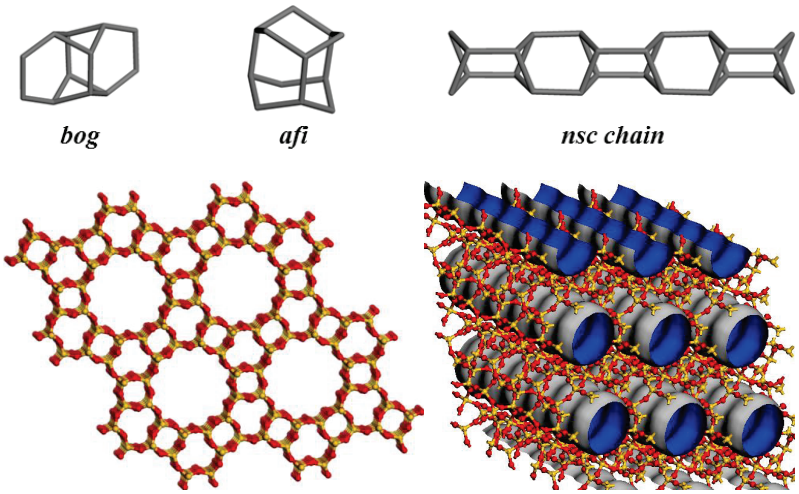

Figure 1.6: The AFI topology seen along the c-axis (bottom left) and a slightly tilted view highlighting the 12-ring tubular pores (bottom right). The channels have been drawn with blue insides and grey outsides. The CBUs present in the AFI structure are displayed in the top row, with the framework oxygens omitted for clarity.

The rather simple framework of the AFI structure makes it well suited as a model material for both experimental and theoretical investigations of zeolite- and zeotype-catalysed reactions. In addition, the framework is one of few where both silicoaluminophosphate and high-silica aluminosilicate variants are known. The aluminosilicate H-SSZ-24 contains stronger acid sites than the silicoaluminophosphate H-SAPO-5 due to their different elemental composition (see Section 1.4). A comparison of these two catalysts thus enables investigation of the effects of catalyst acid strength on reactions in otherwise identical materials.

1.5.2 Other relevant frameworks

A number of other zeolitic frameworks are also relevant to the work in this thesis. Particularly in Papers III and IV, a large number of structures are discussed. The structures CHA, MFI and *BEA are discussed frequently also throughout the remainder of the work. These three structures are displayed in Figure 1.7. The CHA framework, shared by the silicoaluminophosphate SAPO-34 and the aluminosilicate SSZ-13, consists of large cavities connected in three-dimensions by 8-ring apertures of 3.8 × 3.8 Å. The MFI framework, most known as the structure of ZSM-5, contains a pore system of interconnecting straight and sinusoidal 10-ring channels with dimensions 5.1 × 5.5 Å and 5.3 × 5.6 Å respectively. The *BEA structure of zeolite Beta is a disordered zeolitic structure (a star prior to the 3-letter code signifies a disordered structure) with a 3-dimensional pore system made from two orthogonal and intersecting 12-ring channels with dimensions 7.3 × 7.1 Å and 5.6 × 5.6 Å respectively.

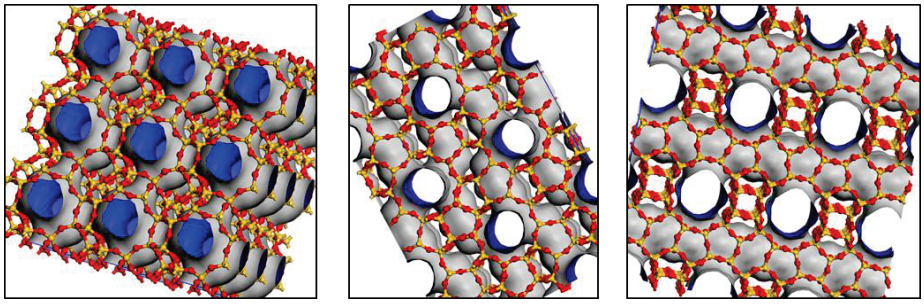

Figure 1.7: The CHA (left), MFI, (middle) and *BEA (right) frameworks. The pore system has been drawn with blue insides and grey outsides.

Three one-dimensional 10-ring frameworks: TON (ZSM-22), MTT (ZSM-23) and *MRE (ZSM-48) are shown in Figure 1.8. The TON and MTT framework have very similar pore dimensions (5.7 × 4.6 Å and 5.2 × 4.5 Å respectively), but with slightly different pore shape. The *MRE structure is disordered, but contains nearly circular channels 5.6×5.3 Å in diameter [91].

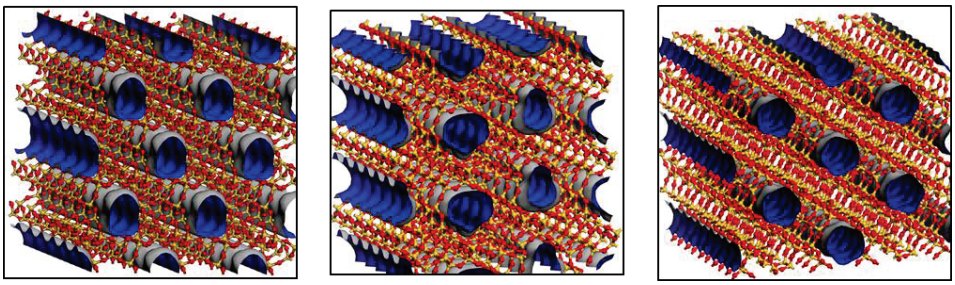

Figure 1.8: The TON (left), MTT, (middle) and *MRE (right) frameworks. The pore system has been drawn with blue insides and grey outsides.

The MEL (ZSM-11), IMF (IM-5) and TUN (TUN-9) all contain 3-dimensional 10-ring pore systems of similar dimensions to the MFI structure (Figure 1.9). The MEL framework is crystallographically closely related to the MFI framework, but a difference in the pentasil chain stacking leads to two perpendicular and intersecting systems of identical (5.3 × 5.4 Å) straight channels. The IMF framework consists of two interconnected 10-ring channel systems with channel diameters of 5.5 × 5.6 Å and 5.3 × 5.4 Å forming small cavities at the intersections. The pore system has only limited 3-dimensionality since only a few layers are connected and a "wall" of dense material separates them from other layers in the [010] direction. The TUN framework is a complex structure of two differently sized channel systems with channel dimensions 6.0 × 5.2 Å and 5.4 × 5.5 Å, respectively. Large cavities are present at the channel intersections, where one of the 10-rings is expanded to a 12-ring.

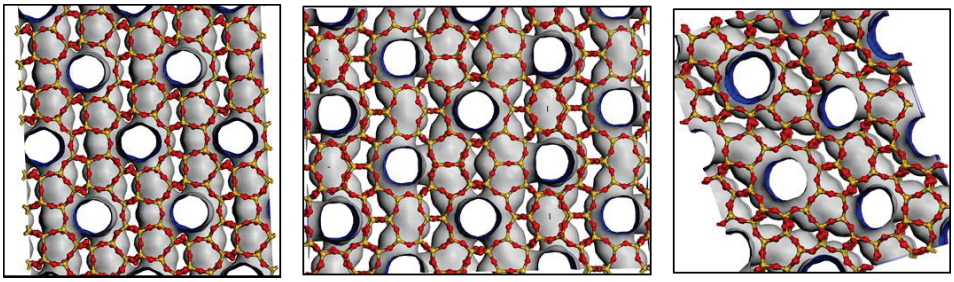

Figure 1.9: The MEL (left), IMF, (middle) and TUN (right) frameworks. The pore system has been drawn with blue insides and grey outsides.

Figure 1.10 displays the MOR, MWW and EUO frameworks. The MOR framework possessed by the zeolite Mordenite consists of 1-dimensional 12-ring channels with channel dimensions of 7.0 × 6.5 Å. While a system of 8-ring channels connects the 12-ring channels, these are limited by very narrow apertures of 5.7 × 2.6 Å. In practice, as few molecules can diffuse through these 8-rings, the channel structure is best described as a one-dimensional 12-ring channel with side pockets. Both the MWW (MCM-22) and EUO (EU-1) frameworks contain a system of 10-ring channels measuring 5.5 × 4.0 Å and 5.1 × 4.1 Å for MWW and 5.4 × 4.1 Å for the one-dimensional channels of EUO. However, the defining feature of these two frameworks and the zeolites is their large 12-ring side pockets or cavities.

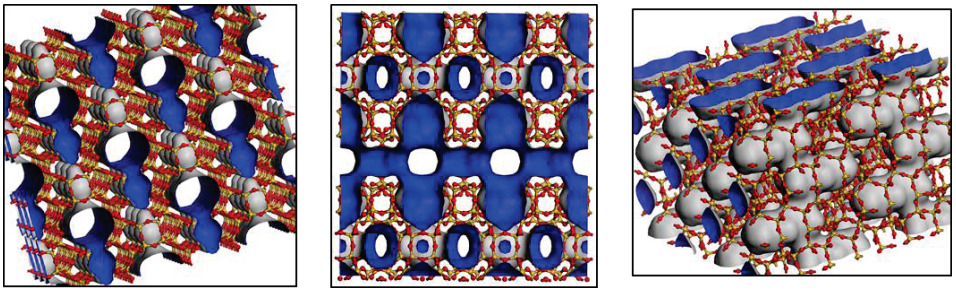

Figure 1.10: The MOR (left), MWW, (middle) and EUO (right) frameworks. The pore system has been drawn with blue insides and grey outsides.

2 Reactions relevant to this work

2.1 Conversion of methanol to hydrocarbons (MTH)

2.1.1 Introduction and commercial status

The conversion of methanol to hydrocarbons (MTH) over a zeolite catalyst was first reported by researchers at Mobil in the 1970's [92, 93]. When feeding *i*-butane and methanol over zeolite H-ZSM-5, they discovered that a mixture of alkanes and aromatics similar to high octane gasoline was produced even though *i*-butane was not consumed. Due to the Arab oil embargo and subsequent oil crisis, alternative carbon sources were already being sought [94, 95]. As methanol can be produced from any gasifiable carbon-based feedstock (via syngas: a mixture of H_2 and CO), this discovery sparked an extensive research effort and considerable commercial interest.

The stoichiometry of the acid-catalysed methanol to hydrocarbons reaction can be represented by the general reaction equation:

$$CH_3OH \xrightarrow{H^+} \text{"}CH_2\text{"} + H_20$$

where "CH_2" represents a wide range of both aliphatic and aromatic hydrocarbons. The exact product distribution can be altered through variations in process conditions or the use of shape-selective zeolite catalysts. The general reaction path consists of an initial equilibration of methanol to dimethyl ether (DME) and water, before this mixture reacts further to form alkenes. These alkenes then react further to form paraffins, aromatics and larger olefins, as shown in Scheme 2.1.

The reaction is strongly exothermic, and this makes control and removal of reaction heat a major factor in process design. The amount of heat released during the reaction depends on the exact product distribution [96], but the dehydration of methanol to DME accounts for a significant fraction of the total reaction heat. For this reason, some processes use a mixture of methanol and DME as feed for the MTH reactor.

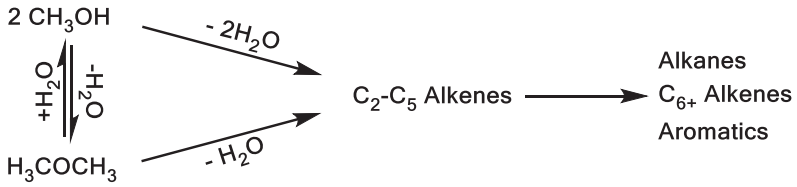

Scheme 2.1: General scheme of the methanol to hydrocarbons reaction. Adapted from [96].

Several processes based on the reaction have been developed, and the first commercial natural gas to gasoline plant utilising Mobil's methanol-to-gasoline (MTG) process was opened in New Zealand in 1985 [97]. Haldor Topsøe also developed an alternative gasoline technology called the Topsøe integrated gasoline synthesis (TIGAS) [98]. This process combines methanol and gasoline synthesis from synthesis gas in a single loop, leading to a higher conversion of the syn-gas feed. A fluid bed process developed by Mobil could further produce either gasoline or light alkenes over H-ZSM-5 by varying the process conditions [99]. Olefin production can also be coupled with a second step to produce gasoline and distillate fuels, as in the Mobil olefins to gasoline and distillate process (MOGD) [100].

Shortly after the construction of the MTG plant in New Zealand oil prices plummeted. For this reason, the gasoline plant shut down in the mid-nineties. Nevertheless, methanol conversion to hydrocarbons has remained an important research topic both in academia and industry. Now that oil prices have risen again, the reaction is also being commercialised again. Perhaps most notably, commercialisation on a large scale in China for production of olefins from coal is in progress. So far, plants based on three different technologies have been constructed: The Lurgi methanol to propylene (MTP) process [101], the UOP/Norsk Hydro (now UOP/INEOS) methanol to olefins (MTO) process [102] and the Dalian methanol to olefins (DMTO) process. Of these, Lurgi's process utilises H-ZSM-5 in a parallel fixed-bed setup with feed injection between beds and product recycle to maximise propene yields, while the latter two processes utilise the narrow-pore zeotype catalyst H-SAPO-34 in fluidised bed reactors to produce a mixture of ethene and propene.

2.1.2 Reaction mechanisms

Ever since the discovery of the methanol to hydrocarbons (MTH) reaction, the reaction mechanisms have been studied and debated. The reaction was first reviewed by Chang in 1983 [96], and again several times in the following decades [95, 103, 104]. Recently, three separate reviews appeared within the space of one year [105-107]; more than 35 years after the initial publication on the reaction.

The early MTH mechanistic research was devoted to direct formation of carbon-carbon bonds from C_1 units (methanol or dimethyl ether), and several mechanisms were proposed [96, 104]. However, the proposed mechanisms lack experimental evidence [105] and already in 1979 Chen and Reagan proposed that the MTH reaction was autocatalytic [108]. 20 years later, Song et al. performed the MTH reaction using extremely purified reagents and reported a dramatic decrease in the initial rate of methanol conversion [109]. It was suggested from the observation that the rate at which the direct $C_1 - C_1$ coupling operates is irrelevant compared to the rate at which trace impurities of C_{2+} compounds initiate the reaction. This conclusion has been further verified by both theoretical [110, 111] and experimental [112] studies. For this reason, direct $C_1 - C_1$ coupling mechanisms will not be discussed further.

At present, the MTH reaction is believed to proceed through an indirect mechanism, wherein hydrocarbon species act as reaction centres for product formation [105, 113-115]. The hydrocarbon reaction centres may be alkenes [116, 117], aromatic species [118-123], or a combination of both [118]. The following sections will describe, in a roughly chronological order, some of the efforts leading towards the current mechanistic understanding of the reaction.

Auto-catalysis and indirect mechanisms

After the suggestion by Chen and Reagan [108] that the reaction was autocatalytic, several indirect mechanisms were proposed during the early 1980's. Dessau and co-workers [116, 117], from the Mobil research laboratories, proposed that the reaction over H-ZSM-5 was driven by a continuous cycle of alkene methylation and cracking, as illustrated in Scheme 2.2.

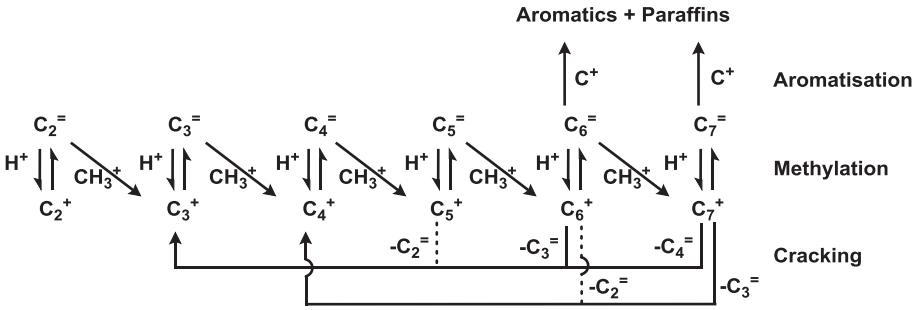

Scheme 2.2: The methylation/cracking mechanism proposed by Dessau. Adapted from [117]

According to this mechanism, the initial alkenes are formed from reactions involving carbon-carbon bond formation, but once alkenes are present the reaction leading to their formation is irrelevant, in accordance with Chen and Reagan's autocatalytic reaction scheme [108]. Dessau's MTH reaction mechanism considers ethene as a product obtained from secondary re-equilibration of primary alkenes and not as a primary product obtained from methanol. In addition, aromatic species formed during the MTH reaction are presented as end products (or coke precursors) resulting from hydrogen transfer reactions, with no contribution to effluent product formation.

At approximately the same time Langner [124] reported that the addition of small amounts of higher alcohols, and especially cyclohexanol, to the methanol feed dramatically reduced the induction period over NaH-Y zeolite. While this result agreed with Dessau's proposal, Langner suggested a reaction mechanism where methylated cyclic intermediates could undergo a "paring reaction" to produce light alkenes. This "paring reaction" was first proposed by Sullivan et al. [125] to explain the formation of alkanes (especially *i*-butane) from hexamethylbenzene (HexaMB), and involves ring-contraction and -expansion steps connected to the de-alkylation. Work by Mole and co-workers [126, 127] in 1983 led to a similar conclusion when they added 1 wt% of toluene or p-xylene to the methanol feed and observed a dramatic increase in methanol conversion. However, based on co-reactions with isotopically labelled aromatics over H-ZSM-5, they suggested a mechanism of alkene formation where polymethylbenzenium ions are deprotonated to form exo-methylenecyclohexadiene species. The exocyclic double bond of these compounds may be methylated, and the resulting alkyl side chain successively eliminated. These two mechanisms will be discussed in more detail in Section 2.2.

The "hydrocarbon pool"

In the mid-1990's, Dahl and Kolboe carried out isotopic labeling experiments by co-feeding alkene precursors (ethanol, propanol) and ^{13}C-methanol over a H-SAPO-34 (CHA) catalyst. Analysis of the effluent showed that most of the products were formed exclusively from methanol under the applied reaction conditions [113-115]. Hence, a parallel indirect mechanism, the "hydrocarbon pool" was proposed. While their proposal shared many similarities with previous works, this schematic concept had a greater immediate influence than the works of the previous decade [103]. The original hydrocarbon pool model, as shown in Scheme 2.3, assumed that methanol was continuously added to a pool of adsorbed hydrocarbons, which successively eliminated light alkenes.

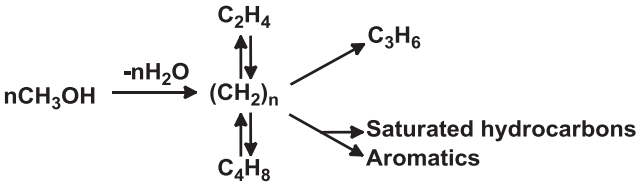

Scheme 2.3: The hydrocarbon pool mechanism proposed by Dahl and Kolboe. Adapted from [115].

The initial hydrocarbon pool was given an overall stoichiometry $(CH_2)_n$, and the chemical structure was not specified [113-115]. Thus, the concept of the hydrocarbon pool could cover all intermediates in the proposed indirect mechanisms from the previous decade. However, studies performed the following decade focused mainly on aromatic or cyclic intermediates. The group of Haw et al. [128-131] used MAS NMR spectroscopy to identify a number of benzenium and cyclopentadienyl cations present inside the catalyst under working conditions, while Mikkelsen et al. [120] found support for the hydrocarbon pool in large-pore zeolites from co-reactions between methanol and aromatics. The groups of Haw and Kolboe simultaneously concluded that polymethylbenzenes (PolyMBs) were the main hydrocarbon pool species in H-SAPO-34 (CHA) [121, 123, 132]. Additional evidence for the hydrocarbon pool mechanism in H-ZSM-5, H-SAPO-34 (CHA) and H-SAPO-18 (AEI) was also provided by Hunger et al. [133-135]. Later studies of the MTH reaction in zeolite H-Beta (*BEA) cemented the importance of PolyMB intermediates in this catalyst [136, 137].

The dual cycle concept

After a period focusing mainly on aromatic intermediates in the MTH reaction, steady-state isotope transient studies over H-ZSM-5 revealed that aromatics did not act as intermediates for all alkenes formed [118, 119]. This finding gave rise to the dual cycle concept, which states that the hydrocarbon pool proceeds through two partly separated cyclic reaction mechanisms, as shown in Scheme 2.4. One of these cycles (the alkene cycle) involves methylation and cracking of alkenes in a similar manner to what was previously proposed by Dessau [116, 117]. A main difference from the proposal by Dessau is that ethene formation from the alkene cycle is assumed to be neglible. The other cycle (the arene cycle) involves continuous methylation of aromatic molecules, and their subsequent de-alkylation. The mechanism for de-alkylation has not yet been fully elucidated, but will be discussed in more detail in Section 2.2.

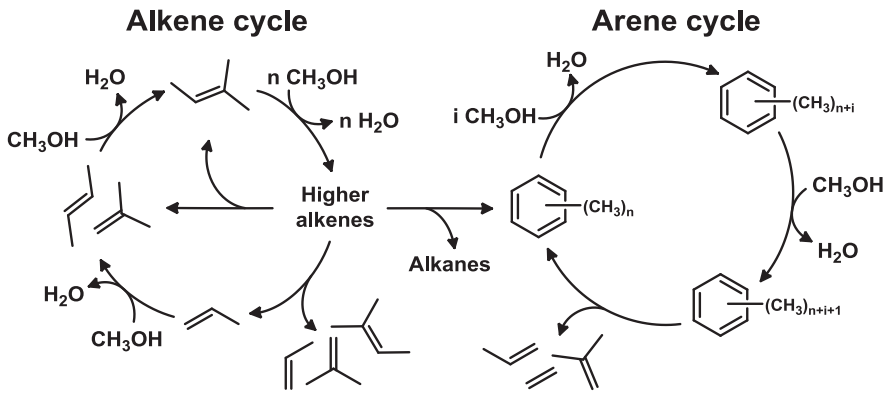

Scheme 2.4: General scheme of the dual-cycle mechanism. Both the relative propagation of each cycle and the exact structure of the intermediates depend on the catalyst employed and the reaction conditions. This in turn means that all products shown here are not necessarily observed in all systems.

The dual cycle proposal initiated a series of similar studies over different catalysts with the aim of relating catalyst structure to product selectivity. Several studies have shown that pore size is an important parameter determining which of the two cycles is favoured. In general, it has been found that the arene cycle is more favoured in large-pore than in medium pore catalysts [122, 138-141]. However, it has also been suggested that

large-pore zeolites favour the alkene cycle at high pressure and low temperatures [142, 143].

Furthermore, the dual cycle concept raised an interesting fundamental question of whether it was possible to run one cycle independently of the other [118, 119]. As both cycles are active in the large pore zeolite H-Beta (although the arene cycle is favoured) [122], attention turned to whether a catalyst with smaller pores than H-ZSM-5 would suppress formation of aromatics and force the alkene cycle to operate on its own. In a rare example of rational catalyst design, this question was answered by studies of the unidimensional narrow 10-ring zeolite H-ZSM-22 (TON). This catalyst was indeed found to strongly favour the alkene cycle, while suppressing the formation of aromatic products [144, 145]. The resultant product spectrum was rich in C_{3+} alkenes, with a high fraction of branched and di-branched C_{5+} products and very low amounts of aromatics.

2.2 De-alkylation of polymethylbenzenes

The structure and reactivity of (poly)methylbenzenes and their corresponding arenium ions are of relevance to several important areas in chemistry. Not least due to their role as reaction intermediates in electrophilic aromatic substitutions [2], (alkyl)arenium ions have been studied extensively both in gas phase [146] and in superacids [147, 148]. In zeolites, polymethylbenzenium ions have been observed during reactions between methanol and aromatics at 300 °C [131]. It has also been shown by Bjørgen et al. [149, 150] that PolyMBs with four or more methyl groups form persistent cations at room temperature in zeolite H-Beta.

In the methanol to hydrocarbons reaction, polymethylbenzenium ions are central intermediates of the arene cycle. However, the mechanism by which these de-alkylate to form alkenes is still debated. The two mechanistic proposals most often invoked, the paring reaction and the side-chain (or exocyclic) methylation mechanism, are illustrated in Scheme 2.5. As shown, both reactions involve methylation of HexaMB to form a heptamethylbenzenium cation (heptaMB$^+$) as the first step. This ion has previously been shown to be the terminal product of the friedel-craft methylation of benzene [151]. However, it is hypothesised that aromatics with fewer methyl groups could also form polymethylbenzenium cations and undergo similar reactions.

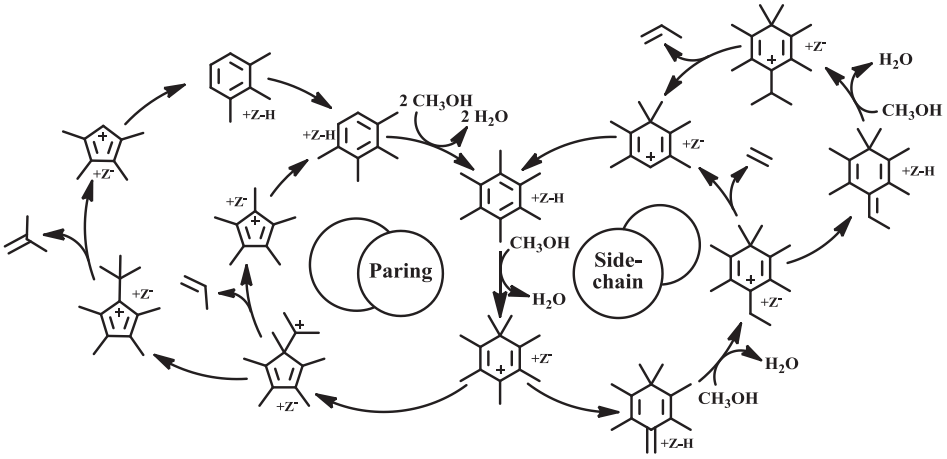

Scheme 2.5: The paring and side chain reaction pathways for de-alkylation of aromatics.

The paring reaction was first proposed by Sullivan et al. [125] to account for the high yield of *i*-butane during hydrocracking of HexaMB. It involves the rearrangement of $HeptaMB^+$ to a five-membered ring with an alkyl substituent. This smaller ring can then either split off propene directly, or reorganise further to eliminate *i*-butene before deprotonation and expansion back to a six-ring. The side-chain methylation pathway was first proposed by Mole and co-workers [126, 127], and later refined by Haw et al. [103, 137], and involves deprotonation of $HeptaMB^+$ to form 1,2,3,3,4,5-hexamethyl-6-methylene-1,4-cyclohexadiene (HMMC). The exocyclic double bond present in HMMC can subsequently be methylated to form an ethyl side-chain, which may be eliminated as ethene. Alternatively, another deprotonation and methylation reaction may lead to an *i*-propyl side-chain and subsequent elimination of propene.

A notable difference between the paring and side-chain methylation mechanisms is that the paring reaction involves the use of a ring carbon to grow an alkyl chain, while in the side-chain methylation reaction the aromatic ring is not broken during the reaction. This difference was exploited by Bjørgen et al. [136] and Sassi et al. [137], who performed extensive isotopic labelling and co-feed studies aimed at elucidating the reaction mechanisms of de-alkylation over zeolite H-Beta. Sassi et al. [137] worked at high temperatures (350-450 °C) and concluded that side-chain methylation was the most important pathway to alkenes, in part because 5 equivalents of methanol to one of toluene was more reactive than HexaMB reacted alone or together with water. Also, they found that the produced ethene and propene contained an excess of carbon atoms from methanol compared to what would be expected from the paring reaction. On the other hand, Bjørgen et al. [136] found that the majority of the propene and *i*-butane (the latter formed directly from *i*-butene by hydride transfer) formed at temperatures below 300 °C contained exactly one ring-carbon, as expected from the paring mechanism. Further, no indication of side-chain methylation was found when methanol was introduced into a catalyst known to contain active PolyMBs.

Unimolecular de-alkylation from polymethylbenzenium ions has also been demonstrated experimentally in gas phase using mass spectrometry [152, 153]. These reveal that with a higher number of methyl groups, the chance of alkene loss relative to methyl, methane or H_2 increases. It was also found that average size of the alkenes eliminated increased with a higher number of methyl groups, which corresponds well with findings in zeolite catalysed reactions [122, 139].

Whether side-chain methylation becomes more important at higher temperatures is an open question: Isotopic labelling experiments performed under typical MTH conditions are very difficult to analyse, due to the possibility for both independent reactions leading to ring/methyl carbon exchange without de-alkylation [136, 137] and parallel alkene formation via the alkene cycle.

The two de-alkylation mechanisms have also been investigated theoretically. Using cluster calculations, Arstad et al. [154] concluded that side-chain methylation was a viable pathway in the MTH reaction. Later, McCann et al. [155] reported a full paring cycle to produce *i*-butene in a large cluster model of H-ZSM-5. Using similar methods, Lesthaeghe et al. [156] found that an ethyl side-chain could grow from o-xylene via deprotonation and methylation. However, the barrier for ethene elimination was high. Later work by Kolboe [157-159] revealed that elimination of an alkyl chain can occur with much lower barriers through a π-complex between the benzene ring and the alkyl fragment. This observation led De Wispelaere et al. [160] to propose a complete low-barrier side-chain methylation mechanism in H-SAPO-34.

Arstad et al. [161-163] have also illuminated many aspects of de-alkylation and ring scrambling of polymethylbenzenium ions in their extensive gas phase calculations. In addition to the classical paring mechanism, their work also includes an alternative unimolecular mechanism involving expansion of the PolyMB to a tropylium-type cation. This mechanism shares many features with the paring mechanism, including ring scrambling to incorporate ring carbons into the eliminated alkenes. For this reason both unimolecular reaction mechanisms are referred to as paring-type reactions in this work in order to distinguish them from the multimolecular side-chain mechanism.

Due to the high basicity of the $HeptaMB^+$ cation, it is a pertinent question whether appreciable amounts are deprotonated and available for side-chain methylation under reaction conditions. The work by Bjørgen et al. [136] suggests that this is not the case at low temperature, while the theoretical deprotonation steps suggested by De Wispelaere et al. ([160], supporting information) display very high reverse (protonation) rates. If deprotonation is a rate-limiting step in side-chain methylation, it is possible that a lower catalyst acid strength will favour this reaction.

2.3 Zeolite-catalysed methylation reactions

Methylation plays an important role in many zeolite-catalysed reactions. For example, in the MTH reaction, methylation of alkenes and aromatics constitute key reaction steps in the alkene and arene cycles respectively (see Scheme 2.4). However, while acid catalysed methylation is a seemingly simple reaction, the reaction mechanism is still not fully understood. A review of zeolite-catalysed methylation reactions was recently published [164]. Two distinctively different mechanisms are usually considered for methylation of alkenes and aromatics: A stepwise and a concerted mechanism. These two mechanisms are illustrated for the methylation of benzene in Scheme 2.6.

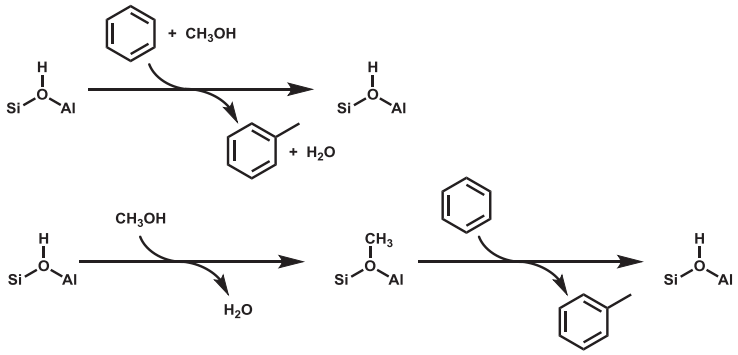

Scheme 2.6: The concerted (top) and stepwise (bottom) mechanisms for methylation of benzene to form toluene. Adapted from [165].

In the concerted mechanism, an adsorbed methanol molecule interacts directly with the species that is being methylated. Then, in a single step, the methyl group is transferred and the OH group and acidic proton are eliminated as water. A protonated methylation product is then formed, which can reorient and transfer the proton back to the zeolite to form a neutral product and regenerate the acid site. On the other hand, the stepwise mechanism involves dehydration of methanol to a surface-bound methoxy group with the acid site as the first step. The methoxy group then interacts with the molecule being methylated in a second step to form the protonated methylation product, which is successively deprotonated to form the neutral product and regenerate the acid site.

While methanol is depicted as the reactant in Scheme 2.6, methanol is easily dehydrated to DME over zeolitic catalysts, which complicates the situation slightly.

However, several studies indicate that DME can undergo analogous reactions to those in Scheme 2.6 [166-168] but eliminating methanol instead of water. A second complication is that some substituted benzenes and branched alkenes have a higher proton affinity than methanol (see e.g. [169]) and would thus be expected to be protonated and reside mainly on the acid site. A mechanism involving proton transfer from an initially protonated methylbenzene to methanol before a reaction resembling the concerted reaction in Scheme 2.6 has been found to be viable as well [165].

From experimental studies at 350 °C over H-ZSM-5 [170], ethene methylation has been found to be zero order with respect to methanol, and first order with respect to the alkene. The same was observed for propene and *t-2*-butene [171], although some deviations were observed at high alkene pressures for the latter two. Similar studies using a large excess of DME as methylating agent at low temperatures reproduced this result over several zeolites [172, 173]. In line with the expected trend for carbocation stability, higher apparent methylation rates and lower apparent barriers with increasing alkene size and substitution were found. This trend has also been reproduced by theoretical calculations of alkene methylations via the concerted pathway [174, 175].

Similarly, experimental and theoretical studies of the methylation of benzene have found that the rate of methylation increases from benzene to toluene in H-ZSM-5 [176], but that the methylation of the more bulky xylenes is hindered by the framework. However, in zeolites H-Beta and H-Mordenite, the methylation rate increases still further as the number of methyl groups increases [177]. Calculations using a small cluster to represent the zeolite support this, showing that methylation will easily proceed all the way to form HeptaMB$^+$ [178]. The methylation of benzene has also been reported to be first order with respect to the aromatics and zero order with respect to methanol in both H-ZSM-5 and H-Beta [179].

With respect to reaction mechanism, the insights are still inconclusive [164]. While methoxy groups have been observed in zeolites in several spectroscopic studies [164], they were not observed in a recent FTIR investigation of benzene methylation at 350 °C [180]. Despite the latter result, it is possible that the coverage of methoxy groups may be too low to observe during reaction conditions. Furthermore, theoretical studies comparing both reactions including entropic effects indicate that the stepwise mechanism becomes increasingly favoured at higher temperatures [168, 181].

2.4 Effects of catalyst acid strength

Few literature reports specifically pertaining to the effects of acid strength exist, but this section nevertheless attempts to give an overview of the field. One early report by Tielen et al. [37] observed that a higher acid strength led to more cracking relative to isomerisation during bifunctional *n*-decane conversion, and attributed this to longer life-times of carbocation intermediates on the stronger acid sites. Later, Bourdillon et al. [182] compared various reactions over zeolite H-Y while blocking sites of differing acid strengths with pyridine, and found that while isomerisation of 3,3-dimethyl-1-butene was facile over weak acid sites, *n*-hexane transformations required much stronger acid sites.

For the conversion of methanol to hydrocarbons, Yuen et al. [183] compared catalysts of varying acid strength with CHA and AFI frameworks. They concluded that while borosilicate catalysts were not strong enough acids to convert methanol to hydrocarbons, both zeolites and the less acidic SAPO catalysts were. They reported that the stronger acidic CHA catalyst (H-SSZ-13) produced more alkanes than the weaker acid H-SAPO-34, and also deactivated faster due to coke formation. For the AFI catalysts, they reported similar product distributions for all the three increasingly strong acids H-SAPO-5, H-SSZ-24 and MgAPO-5 at full methanol conversion, but did not provide details. More recently, Bleken et al. [184] performed a detailed comparison of H-SAPO-34 and H-SSZ-13 with similar crystal size and identical acid site density in the MTH reaction. They found that H-SSZ-13 was more active and deactivated faster at optimal conditions than the less acidic H-SAPO-34, but that the methanol conversion capacity (i.e. the cumulative methanol conversion before full deactivation) was higher in H-SSZ-13 at temperatures below 375 °C. Furthermore, they observed that less basic methylbenzenes (with fewer methyl groups) could decompose in the stronger acid H-SSZ-13 during flushing experiments. Unfortunately, detailed mechanistic insights proved difficult to obtain due to the severe restrictions on diffusion in the CHA structure leading to a high degree of product shape selectivity [140].

Homogeneously catalysed conversion of methanol to hydrocarbons over ZnI_2 and InI_3 at low temperature was studied by Bercaw and Hazari et al. [185, 186]. Under these conditions, alkene methylation up to C_7 is strongly favoured, leading to high yields of triptane (2,2,3-trimethylbutane). They found that the stronger acid InI_3 was more active than ZnI_2, but also that hydride transfer reactions were favoured in the stronger acid. This

in turn led to higher amounts of aromatics and alkanes. They also reported a much higher ability to activate alkanes for InI_3 than ZnI_2 [187]. Later, similar results for a heterogeneous system were reported by the group of Iglesia [188, 189] for comparisons of zeolites and amorphous SiO_2-Al_2O_3 with the strongly acidic $H_3PW_{12}O_{40}$ during dimethyl ether conversion to triptane.

Research on Keggin polyoxometalate clusters with different central atoms (and thus different acid strength) in addition to zeolite H-Beta has provided more detailed information on the effects of acid strength. Work by Macht et al. [190] and Carr et al. [191] has revealed that while the activation energies of hexane isomerisation, butanol dehydration reactions and dimethyl ether formation depend linearly on the calculated deprotonation energy (DPE) of the acid catalyst, the slope is always less than unity and differs for the three reactions. They concluded that the higher activation energy caused by increases in DPE are partly compensated by better stabilisation of the transition state ion pairs as DPE increases. Furthermore, they suggested that the ion-pair stabilisation depended on the degree of charge localisation in the transition state. Transition states with more localised charge are better stabilised by the densely charged conjugate bases of weak acids, and are thus less sensitive to acid strength. For example, the diffuse cyclopropyl cation formed in the transition state for hexene isomerisation leads to a higher dependence on DPE than what was observed for 2-butanol dehydration, which proceeds through a transition state with a higher charge density [190].

Recent calculations by Wang and Brogaard et al. [192] has further demonstrated that in addition to the inverse dependence on DPE, the ion-pair stabilisation energy is also affected by the chemical composition of the surrounding framework. Thus, reactivity does not always linearly depend on DPE alone, even in isostructural frameworks.

3 Experimental methods

3.1 Synthesis of Zeolitic catalysts

3.1.1 H-SAPO-5

H-SAPO-5 was synthesised hydrothermally from water, triethylamine (TEA, 99.5 %, Fluka), orthophosphoric acid (85 %, Merck), Cab-O-Sil M5 (Riedel-de Haën) and Catapal B (Vista). Typically, 82.80 g distilled water and 24.76 g orthophosphoric acid were mixed before addition of 14.67 g Catapal B. Thereafter, 0.64 g Cab-O-Sil M5 and 42 g TEA were added, and the mixture was shaken vigorously until a homogeneous mixture was obtained. This mixture, with the composition $50H_2O$: $1Al_2O_3$: $1P_2O_5$: $0.1SiO_2$: 3.9TEA, was then distributed into two 50 ml Teflon liners that were subsequently inserted into stainless steel autoclaves. The autoclaves were mounted onto a rotor rack inside a heating cabinet preheated to 200 °C. While a motor continuously tumbled the autoclaves, the mixture crystallised over the course of 4 hours at 200 °C.

After crystallisation, the autoclaves were removed from the oven and quenched in a bucket of ice-water. The products were then washed with distilled water and recovered by centrifugation (20 minutes at 3000 rpm). Washing and centrifugation was repeated four times, and afterwards the sample was dried overnight at 60 °C. Removal of the structure directing agent (TEA) was performed by calcination in static air at 600 °C for 2 h, leaving the sample on H-form.

From several reproductions of the synthesis, it was found that the exact crystallisation time was critical in order to avoid impurities of the CHA structure. The addition of seeds from a previous synthesis also increased the purity of the AFI phase formed. For more details on the synthesis of H-SAPO-5, see [193].

3.1.2 H-SSZ-24

The synthesis of H-SSZ-24 was based on work by Kubota and Maekawa et al. [194, 195]. It utilises an aluminium-containing Beta zeolite as the source of aluminium, and N(16)-methylsparteinium hydroxide (MeSpaOH) as the structure-directing agent. The synthesis procedures for both of these are described after the synthesis procedure for H-SSZ-24.

For crystallisation of H-SSZ-24, a mixture with composition $50H_2O$: $1SiO_2$: $0.005Al_2O_3$: $0.075Na_2O$: 0.15MeSpaOH was prepared from water, NaOH, MeSpaOH, Cab-O-Sil M5 (Riedel-de-Haën) and H-Beta zeolite. Typically, 5.89 g distilled water, 2.27 g of a 0.66 mmol/g aqueous solution of MeSpaOH and 0.24 g aqueous NaOH (6.3 mmol/g) were mixed directly in a 13 ml Teflon liner and stirred for 10 minutes. Subsequently, 0.18 g H-Beta and 0.43 g Cab-O-Sil were added and the mixture stirred for 4 hours. These amounts assumes an H-Beta sample with Si/Al = 30 (confirmed by energy dispersive x-ray spectroscopy: EDS), and must be adjusted for other H-Beta Si/Al ratios. The mixture was then crystallised for 25 hours at 175 °C before thermal quenching of the autoclaves in ice-water. Washing of the product with distilled water and subsequent recovery by centrifugation (30 minutes at 3000 rpm) was repeated four times. The sample was then dried overnight at 60 °C.

Removal of the structure directing agent (MeSpaOH) was performed by calcination in a tubular oven with a continuous flow of 25 % O_2 in N_2. The sample was heated to 550 °C over the course of 10 hours, and subsequently held at 550 °C for 10 hours. The resulting Na-SSZ-24 was ion-exchanged to yield H-SSZ-24 by mixing with an excess (30 g solution / 1 g zeolite) of 1M NH_4NO_3 solution and keeping the suspension at 80 °C for 3 hours. The powder was then recovered by centrifugation (30 minutes at 3000rpm) and the ion exchange repeated twice more. After the third ion-exchange, the sample was washed with distilled water, recovered by centrifugation and dried overnight at 60 °C. The same calcination procedure as above was then repeated to bring the sample from NH_4 to H-form.

While the syntheses of the samples used for this thesis were made from homemade H-Beta, it was found that the varying quality of this Beta zeolite led to poor reproducibility of the H-SSZ-24 synthesis. Later syntheses utilising a commercial Beta sample (Zeolyst CP814C* ion-exchanged to H-form by the method described above) proved equally or

more successful. The amounts of H-Beta and Cab-O-Sil were adjusted to account for the higher concentration of Al in this sample (Si/Al = 19).

Synthesis of the H-Beta zeolite

The H-Beta synthesis was based on the recipe by Cardoso et al. [196], but no Ti was added. First, 12.2 g Cab-O-Sil M5 (Riedel-de-Haën), 46.35g tetraethylammonium hydroxide (TEAOH, 40 %, Aldrich) and 6.7 g distilled water were mixed in a large beaker and stirred until all the Cab-O-Sil was dissolved and a homogeneous mixture obtained. Typically, this took 30 minutes. While this mixture was stirred, a separate mixture of 0.47 g $Al(NO_3)_3 \times 9H_2O$ (95 %, BDH) dissolved in 30.7 g distilled water was prepared. The latter mixture was then added to the first and the resulting mixture was stirred for 15 minutes before transfer to a 150 ml Teflon liner and subsequent enclosure in a stainless steel autoclave. The mixture was then crystallised at 140 °C for 96 hours, after which the autoclave was removed from the oven and cooled in a bucket of ice-water. The product was washed with distilled water and centrifuged (45 minutes at 3000 rpm) four times before drying overnight at 60 °C. Removal of the structure directing agent (TEAOH) was performed by calcination in static air. The sample was heated to 550 °C over the course of 10 hours, and this temperature was maintained for another 10 hours.

Synthesis of the structure-directing agent

The synthesis of the structure directing agent (MeSpaOH) was based on procedures previously described by Lobo et al. [90] and Kubota et al. [197], but with slight modifications. An overview of the synthesis is given in Scheme 3.1.

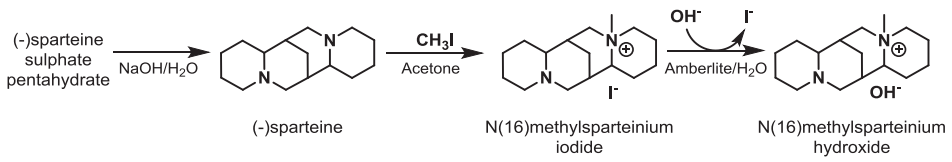

Scheme 3.1: The reaction steps involved in the synthesis of N(16)-methylsparteinium hydroxide from (-)sparteine sulphate pentahydrate.

Pure (-)sparteine was obtained from (-)sparteine sulphate pentahydrate (ABCR) by stirring 25 g (59 mmol) of the latter vigorously for 20 minutes at room temperature in an aqueous NaOH solution (10 % w/w, 60 ml). The product was then extracted with CH_2Cl_2 (3 x 50 ml) and dried with K_2CO_3. The K_2CO_3 was then removed by filtration and the solvent by evaporation under vacuum. Typically, yields above 90 % of (-)sparteine were obtained in this step.

The recovered (-)sparteine was dissolved in acetone (100 ml). CH_3I (7.5 ml, 120 mmol ~2 eq.) was then added dropwise through a septum and the mixture subsequently stirred in darkness (the extracted sparteine decomposes in light) for 45 hours. When the reaction was finished, diethylether (50 ml) was added before the crystals were filtered and washed with a 50/50 (200 ml) mixture of Acetone and diethyl ether.

Purification of the the N(16)-methylsparteinium iodide (MeSpaI) was performed by dissolving the crystals in 100ml boiling 2-propanol and recrystallized. The recrystallized product was then filtered and washed with ice-cooled 2-propanol (100 ml). Yields around 60 % were typically obtained in this step. ^{13}C NMR was used to confirm the purity of the MeSpaI (see [197]). If *i*-propanol was observed in the NMR spectrum, this was removed by dissolving the crystals in water and evaporation under vacuum.

The MeSpaI was ion-exchanged by Amberlite IRN78 ion exhange resin (Supelco) to obtain MeSpaOH. 240 g (300 mmol OH^- exchange capacity) of Amberlite in 300 ml distilled water were used to exchange 27.5 g MeSpaI (3 equivalents OH^- to I^-). The slurry was stirred for 48 hours before filtering off the ion exchange resin. Some of the water was then evaporated to obtain an aqueous solution of 0.66 mmol/g MeSpaOH. The concentration was determined by titration with 0.01M HCl using bromothymol blue as indicator.

3.2 Synthesis of Hexamethylmethylenecyclohexadiene

The synthesis of 1,2,3,3,4,5-hexamethyl-6-methylene-1,4-cyclohexadiene (HMMC) was based on work by Doering et al. [151] and Bjørgen et al. [198], but used benzene and methyl iodide as the starting reagents. The synthesis was performed by Magnus Mortén, Department of Chemistry, University of Oslo.

A 50 ml round-bottom flask equipped with a magnetic stir bar and condenser fitted with $CaCl_2$ drying tubes was used for the reaction. First, freshly ground $AlCl_3$ (1.86 g, 13.9 mmol, 2.1 eq.) was placed in the flask before benzene (0.53 g, 0.60 ml, 6.7 mmol, 1.0 eq.) was added and the mixture was heated to reflux. Thereafter CH_3I (31.9 g, 14.0 ml, 225 mmol, 34 eq.) was added drop-wise and the reaction mixture refluxed for 20 hours. After reaction, the mixture was cooled on an ice bath. Purification was then performed by a series of extractions and washing in acidic and basic media, taking advantage of the high basicity of HMMC:

After cooling, the reaction mixture was added drop-wise, while stirring, to a flask containing pentane (20 ml) and water (5 ml) at 0 °C. NaOH (50 % w/w) was then added until pH = 14. After phase separation, the aqueous phase was extracted with pentane (3 x 10 ml). The combined organic phases were cooled to 0 °C and HCl (12 M) was added drop-wise until pH = 0. After phase separation, the organic phase was extracted with HCl (12 M, 3 x 10 ml). The combined aqueous phases were cooled to 0 °C before addition of NaOH (50 % w/w) drop-wise until pH = 14. The solution was then extracted with diethyl ether (4 x 10 ml), and the combined organic phases washed with brine (10 ml) and dried with $MgSO_4$. The solvent was removed under vacuum, affording the product as yellow crystals (1.00 g, 5.70 mmol, 85 % yield).

For the synthesis of selectively labelled HMMC, $^{13}C_6$ benzene (Cambridge Isotope Laboratories, 99 %) was methylated with $^{12}CH_3I$ to yield a product with labelled ring carbons and unlabelled methyl groups.

3.2.1 Characterization

The purity of the synthesised HMMC was confirmed by GC-FID/MS on an Agilent 7890/5975C GC/MS with a J&W HP-5MS column (60 m × 0.25 mm × 0.25 µm) and with ^1H and ^{13}C NMR on a Bruker Avance DPX300 or DPX400 instrument.

3.3 Catalyst characterization

3.3.1 Powder XRD

Powder X-ray diffraction was performed on the catalysts to analyse phase purity of the synthesised materials. Samples were prepared by mixing the powder with ethanol or water before dispersing it on a glass plate sample holder and allowing the liquid to evaporate. Diffractograms were collected between $2\theta = 3\text{-}60°$.

Two different instruments were employed: a Bruker D8 Discover and a Siemens D-500. Both instruments had Bragg-Brentano geometry and Cu Kα radiation was used ($\lambda = 1.5406$ Å).

3.3.2 Scanning electron microscopy

Scanning electron microscopy (SEM) was performed to determine particle sizes and morphologies of synthesised samples. The instrument used was a FEI Quanta 200 FEG-ESEM equipped with both an Everhart-Thornley secondary electron detector and a detector for backscattered electrons. In addition, it provided the possibility of performing EDS. Microscopy was usually performed at working distances of around 10 mm with acceleration voltages between 5-10 kV. High vacuum conditions were employed for all samples studied.

3.3.3 FTIR

FTIR measurements were performed in transmission mode on a Bruker Vertex 80 instrument with an MCT detector. A quartz sample cell with KBr windows was employed. The samples were either deposited on a silicon wafer or pressed into a self-supporting disc and were pre-treated under vacuum by heating to 120 °C for 1 hour, 300 °C for 1 hour and 450 °C for 1 hour.

For CO adsorption measurements, CO was allowed into the sample cell before the samples were cooled to 77 K with liquid nitrogen. The CO was then gradually pumped out of the cell while spectra were recorded at regular intervals.

3.3.4 N_2 adsorption

N_2 adsorption isotherms were measured at -196 °C, using a BEL BELSORP-mini II instrument. The samples were outgassed in vacuum first for 1 hour at 80 °C and subsequently at 300 °C for an additional 3 hours. Specific surface area was calculated using the BET equation based on p/p_0 data in the range 0.01 - 0.15.

3.3.5 NH_3 TPA

Temperature programmed adsorption of NH_3 was performed in a TGA setup, using a Mettler Toledo TGA / SDTA851e. Samples were heated to 500 °C in a flow of N_2 at a rate of 10 °C min^{-1} and held there for 15 minutes before switching to a flow of 2 % NH_3 in N_2. After a further 40 minutes, the temperature was decreased to 400 °C (10 °C min^{-1}). This temperature was again held for 40 minutes before decreasing to 300 °C, which was held for another 40 minutes before decreasing to 200 °C. The weight gain after each temperature decrease was logged and used for calculating the amount of adsorbed NH_3 per gram catalyst.

3.3.6 TPD of *n*-propylamine

Temperature programmed desorption of *n*-propylamine was performed in a manner similar to that described by Gorte et al. [59, 77, 83]. 20 mg catalyst placed in an 11 mm glass reactor and was pretreated in a flow of oxygen at 550 °C, before cooling to 150 ºC. A stream of nitrogen (80 ml/min) bubbled through *n*-propylamine at room temperature was then fed over the catalyst for 20 minutes in order to adsorb *n*-propylamine at 150 °C. After this, the catalyst was left at 150 °C for 4 hours in a stream of 80 ml/min nitrogen to desorb excess *n*-propylamine. The temperature was then ramped at 20 °C/min up to 550 °C, and the amount of propene desorbed was quantified using an on-line Pfeiffer Omnistar quadrupole mass spectrometer.

3.4 Catalytic testing

3.4.1 Test-rig setup

Catalytic testing experiments were performed in U-shaped glass or quartz reactors with inner diameters of either 5 or 8 mm, with a 3 mm wide thermocouple well (glass or quartz) inserted into the middle of the catalyst bed in order to monitor the reaction temperature. The catalyst particles were pressed, gently crushed and sieved to particle sizes between 0.25 - 0.42 mm. The reactor was made so that the catalyst bed would always sit in the isothermal zone of the oven during testing. In some experiments, quartz was used to dilute the catalysts (in order to avoid bypass when small amounts of sample were used). The quartz was sieved to 0.25 - 0.42 mm particle size and calcined overnight at 800 °C.

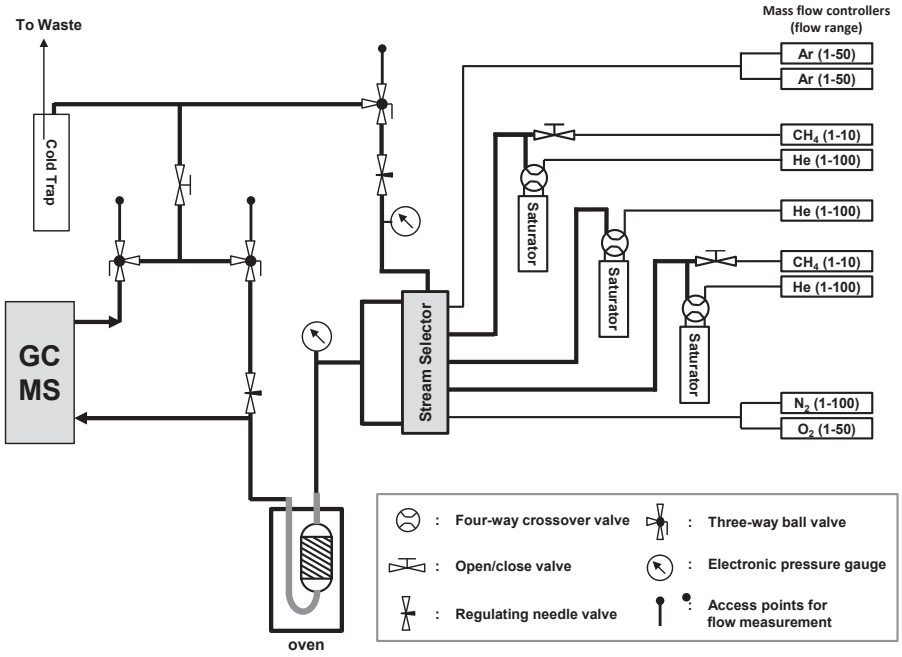

Figure 3.1: Schematic drawing of the setup employed for catalytic testing in this work. Note that all tubing drawn in bold was heated and insulated.

Schematics of the setup constructed for catalytic testing is shown in Figure 3.1. The setup contained 9 mass flow controllers for various gases, and these were joined together

to form five separate gas lines. Each of these lines was controlled by a stream selector and could be independently directed either to the reactor or to a separate waste line. The stream selector consisted of 5 Swagelock TT2B3 modules (with a low internal dead volume) and each module was operated pneumatically by a solenoid valve. All tubing and valves were 316 stainless steel with dimensions of 1/8" or 1/16". The tubing between the saturators and the reactor (including the stream selector) could be heated to ~150 °C, while all tubing after the reactor was heated to >200 °C.

The system was controlled via a LabView interface programmed by Terje Grønås at the Department of Chemistry, University of Oslo.

3.4.2 Saturators

Two types of saturators for feeding liquid reagents were employed during this work. During the early parts of the work (Papers I and II), liquid reactants were fed by bubbling helium through a simple glass saturator immersed in water. However, as a stable water temperature could not be maintained for long periods of time, a more sophisticated system was constructed for the remaining work. The new saturators were based on a two-stage design previously employed by C. Sprung [199].

The setup consists of a glass container, between 10 ml and 1 litre depending on reactant used, with a Vigreux column inside a water jacket attached to the top. The glass container was heated by a silicone-oil bath, while the temperature in the Vigreux column was kept at a constant (lower) temperature by a circulating thermostated water bath. Helium was introduced through a glass frit and bubbled through the container of boiling liquid before continuing upwards and condensing in the Vigreux column. The partial pressure of the reactant was thus determined by the temperature in the column (which was checked by a thermocouple inserted at the top of the column). To ensure efficient heat transfer, the Vigreux column was filled with small pieces of glass capillaries.

This setup could deliver stable vapour pressures over a range of temperatures and flows as long as the liquid remains boiling in the main container. If the liquid was not boiling, a variable flow and delayed response to flow changes was observed. This effect was especially severe for the large 1 litre saturator employed for methanol, while it was less of a problem for small saturators (smaller than ~50 ml).

3.4.3 GC/MS setup

For the majority of the tests performed, the reactor effluent was analysed by an on-line GC-FID/MS analysis (Agilent 7890/5975C GC/MS) using two Restek Rtx-DHA-150 columns (150 m, 0.25 mm i.d., stationary phase thickness 1 μm). The two columns were attached to the same inlet, but to different detectors (flame ionisation detector and MS detector respectively). A small restrictor was added between the column and MS detector in order to ensure similar flow through both columns. Hydrogen (purity 6.0) was used as carrier gas.

For the transient experiments performed in Paper I the gas phase effluent was sampled from the reactor outlet using a syringe, and analysed by injection into a HP6890/5973 GC/MS with a GS GasPro column (30 m, 0.32 mm i.d.) using helium (purity 5.0) carrier gas.

3.4.4 Analysis of compounds retained in the catalyst

Analysis of hydrocarbons retained in the catalyst after reaction was done by a fast transfer of the catalyst powder from the reactor to a glass vial at room temperature, thus quenching the reaction. The catalyst sample was then dissolved in an aqueous solution of 15 % HF (1 ml HF solution to 50 mg catalyst) and the hydrocarbons extracted with 0.5-1 ml CH_2Cl_2 (Merck, 99.9 %).

The organic phase was then analysed on an Agilent 6890/5973 GC/MS with an Agilent J&W HP-5MS column (60 m × 0.25 mm × 0.25 μm).

3.4.5 Analysis of isotopic distributions

Determination of the isotopic distribution in products was done by performing a linear regression analysis on the ion fragments found by mass spectrometry. The method employed was based on previous work by P.O. Rønning [200]. In all the analyses, it was assumed that kinetic isotope effects on MS fragmentations were negligible. Furthermore, the method only analyses molecular ions and fragments with intact carbon skeletons.

As ^{13}C makes up 1.11 % all naturally occurring carbon atoms, it is necessary to correct for this amount in order to obtain a pure ^{12}C mass spectrum. For an ion of mass m/z consisting of N carbon atoms, the probability of containing n ^{13}C atoms is given by:

$$P_n = \left[\frac{N!}{n!\,(N-n)!}\right] * 0.0111^n * 0.9889^{N-n}$$

The bracketed part of the equation above represents the number of permutations possible for n ^{13}C atoms in an ion of N carbon atoms. The single ion peak area corrected for naturally occurring ^{13}C is thus given by:

$$A_{corr}(i) = A_{obs}(i) - \frac{\sum_{n=1}^{N} A_{corr}(i-n) * P_n}{0.9889^N}$$

Where $A_{corr}(i)$ is the corrected ion peak area, $A_{obs}(i)$ the observed ion peak area and $A_{corr}(i - n)$ is the Corrected peak area of ions with mass i-n. When the corrected peak areas are known, the distribution of fragment ions in a pure ^{12}C spectrum is obtainable.

The isotopic composition of a compound can then be found by integration of single ion peaks from MS data. Each single ion peak will contain contributions from ions of the same mass number but different number of hydrogen atoms and/or ^{13}C atoms. Based on this knowledge, a general formula for the observed area as a linear combination of the fractions of ^{13}C atoms in the ions can be constructed:

$$A_{obs}(i) = A_{sum} D_{12C}(i) X_{12C} + \sum_{n=1}^{N} A_{sum} D_{12C}(i-n) X(n)$$

In the equation above, A_{sum} is the sum of ion peak areas while $D_{12C}(i)$ the fraction of ions with mass number i in a purely ^{12}C spectrum of the compound. X(n) and X_{12C} are the fractions of ions containing n ^{13}C atoms and containing only ^{12}C atoms, respectively.

For every mass number there will be a linear equation, and a set of these can be solved by linear regression analysis to give the fractions of ions containing n ^{13}C atoms.

3.5 Mass spectrometry

For the gas phase reactions of HeptaMB$^+$, a three sector mass spectrometer with QHT (quadrupole/hexapole/time-of-flight) geometry (QToF 2, Micromass/Waters, Manchester, UK) was used. The pathlength of the hexapole collision cell was 16 cm, and the ToF analyser was of the reflectron type.

The injection and generation of HeptaMB$^+$ was done from a 0.0002 M solution of HMMC in methanol and 1 % CF_3COOH, which was ionised by an electrospray ion source working at atmospheric pressure. Upon entering the high-vacuum region of the instrument, the ions were focused into a quadrupole mass filter set to transmit only the molecular ion of HeptaMB$^+$. These ions were then accelerated or decelerated to a variable energy E_{lab} of 2-42 eV, corresponding to $E_{C.M.}$ 0.36 - 7.53 eV or 0.37 - 7.37 eV for ions 177 and 183 respectively, before entering a collision cell where they collided with Argon at low pressure ($1*10^{-4}$ mbar). After leaving the collision cell, the ions were accelerated by a few eV and transferred into the high-vacuum time-of-flight region. Here, the ion beam was extracted and accelerated to 9.1 keV orthogonally to the optical axis by a high voltage pulse.

4 Synopsis of results

The aim of this work was to investigate mechanisms and kinetics of selected acid-catalysed hydrocarbon reactions in zeolitic catalysts. Emphasis was set on the effects of acid strength on the kinetics and preferred pathways of the selected reactions. Two isostructural catalysts with different acid strength, H-SSZ-24 and H-SAPO-5, were synthesised and characterised, and were central to the work performed.

A detailed study of general MTH reaction mechanisms and alkene formation from PolyMBs over the moderately acidic H-SAPO-5 formed the basis of Paper I. Comparisons of H-SAPO-5 with the stronger acid H-SSZ-24, revealing significant differences between the two catalysts during MTH catalysis, resulted in Paper II.

A natural extension to the work on acid strength effects was the study of single reaction steps. Kinetic studies of methylation reactions proved challenging due to very fast secondary and competing reactions, in addition to fast catalyst deactivation. However, it was observed that the reactivity of propene and benzene towards methanol is altered by changing the acid strength (Paper V). In addition, a desire to understand the detailed mechanism of unimolecular PolyMB de-alkylation (a key step in the MTH reaction) led to a combined gas phase and catalytic study of the heptamethylbenzenium cation. This study is reported in Paper VI.

The large amount of work performed on the MTH reaction also led to involvement in the preparation of two perspective articles. Paper III compares a large number of zeolite catalysts with differing pore size for the MTH reaction, while Paper IV concerns a possible industrial process based on the use of medium-pore one-dimensional zeolites to produce branched alkenes in the gasoline range.

The following section presents a brief synopsis of the results obtained during this work. Rather than presenting the papers in a chronological order, the results are presented in the most natural order to create a coherent overview. For this reason, the synopsis is divided into three distinct subtopics. For more details on the experiments and a detailed discussion, the reader is referred to the papers attached as an appendix to this thesis.

4.1 Shape selectivity in the MTH reaction

As a lead-up to the detailed work on methanol conversion performed over H-SAPO-5 and H-SSZ-24, a discussion on the general features of the methanol to hydrocarbons (MTH) reaction is in order. Paper III presents a perspective on how shape selectivity affects the MTH reaction. The paper gives a general overview of zeolites, shape selectivity and the current state of the art within MTH research before providing an analysis of the product selectivity over nine different zeolite catalysts. Large portions of the reported data have been previously published [184, 201, 202], but some new experiments were performed in order to compare the structures at the same temperature and methanol partial pressure over a large conversion range.

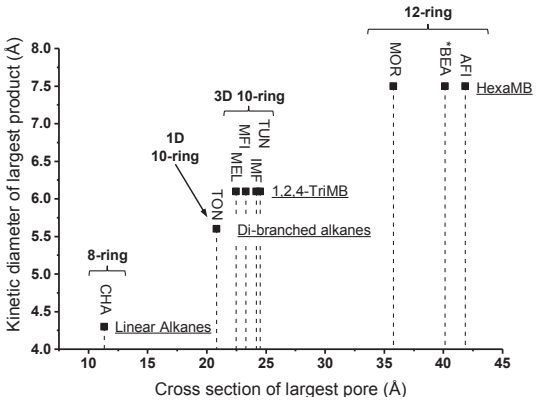

Figure 4.1: Cross section of the largest pore versus the kinetic diameter of largest product. Cross sections are calculated assuming a perfectly elliptical pore whose axes are the largest and smallest diameters listed in the IZA structure database [18]. This is not entirely correct for all materials, but provides a good indication of pore size. The kinetic diameters were found in refs. [203-206].

Figure 4.1 displays a plot of the nine zeolite catalysts investigated, and relates the maximum pore diameter to the largest products observed in appreciable amounts (defined as >4 % yield) during the MTH reaction. A direct correlation between these two parameters was observed, which demonstrates that product shape selectivity leads to a distinct cut-off in the effluent product distribution. The 8-rings of the CHA structure (H-SSZ-13) limits the products to linear alkenes, while the 10-ring structures allow either branched alkenes or small methylbenzenes, depending on the exact channel diameters. Zeolites with 12-ring channels allow formation of HexaMB, which is also the largest major

product observed during homogenous catalysis of the same reaction [185]. Thus, it appears that 12-ring channels provide little or no product shape-selectivity for the MTH reaction.

While Figure 4.1 shows the largest major product formed, there are some fine details not covered by the figure. For instance, contrary to *BEA and AFI (H-SSZ-24), MOR favours pentamethylbenzene over the larger HexaMB due to its smaller channel size [207]. Structures containing large cavities or side-pockets also tend to produce some products larger than expected based on their pore size, as has been reported for TUN [201], and has been found to be even more prominent over EUO [202] and MWW [203, 208]. The latter two possess large (12-ring) side-pockets that, if exposed to the external surface, will decrease the effect of shape selectivity during the MTH reaction.

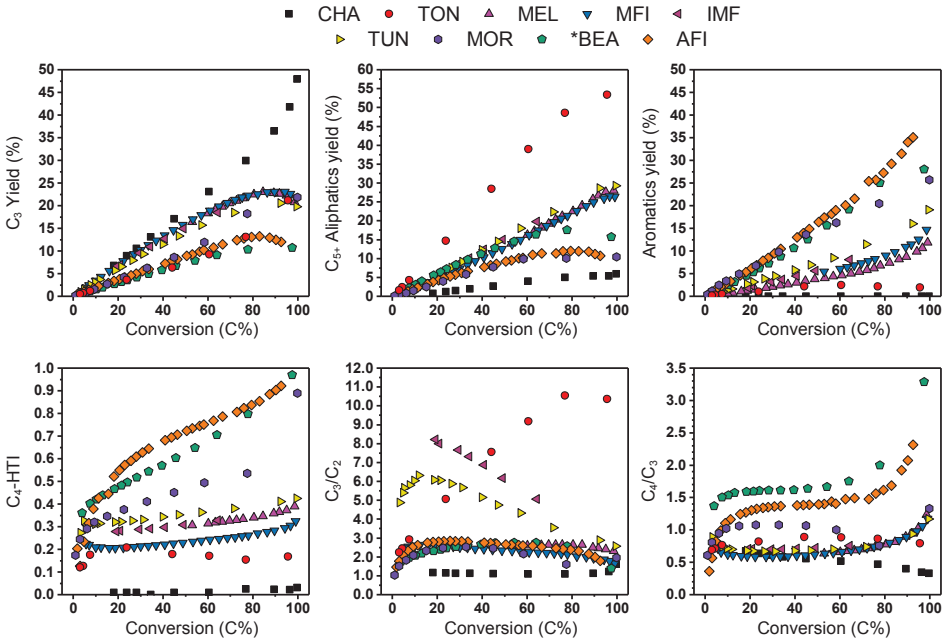

Figure 4.2: Product yields for C_3, C_{5+} aliphatics and aromatics as a function of overall methanol conversion (top) and key product ratios versus methanol conversion (bottom). The C_4-HTI (Hydrogen Transfer Index) is a measure of aromatics formation, and is defined as the ratio [alkane/(alkene + alkane)] for the C_4 product fraction. All datasets were obtained during deactivation at 350 °C and P_{MeOH} = 130 mbar.

Figure 4.2 displays the yields of key product ranges and ratios assumed indicative of transition-state shape selectivity versus methanol (and DME) conversion for all the compared samples. The data for each sample were mainly collected during catalyst

deactivation in a single test, assuming non-selective deactivation (i.e. that the product selectivity is independent of deactivation) during the MTH reaction. Non-selective deactivation was originally proposed by Janssens [209] and has been verified for a number of zeolite catalysts [201, 202, 210, 211]. A possible exception to this general rule is the CHA structure, where product shape selectivity due to growth of hydrocarbon residues has been proposed to explain the increasing yield of ethene with time on stream (see ref. [140] and refs therein). However, this conclusion has been disputed by other researchers [212].

As shown in the upper plots in Figure 4.2, the product yield versus conversion curves are generally linear in the 0–80 % conversion range, and then change rapidly at high conversion. This change in selectivity can be attributed to exhaustion of methanol, leading to a higher degree of alkene interconversions. In general, Figure 4.2 reveals similar trends for structures with similar pore size. The majority of these observations can be rationalised in terms of the hydrocarbon pool mechanism (see Scheme 2.4) and the transition-state selectivity imposed by the structure. However, product shape selectivity dominates over the 8-ring CHA structure and only linear light alkenes are observed.

The yield of aromatics (and thus the C_4-HTI) follows the pore size, suggesting that intermolecular hydride transfer reactions are among the most space-demanding reactions. Furthermore, the presence of large aromatics leads to the arene cycle being favoured, and in turn to a low C_{5+} aliphatics yield (the arene cycle produces mainly C_2-C_4 alkenes). With smaller pores, fewer and smaller aromatics are formed. Thus, the alkene cycle will be more favoured, leading to increased C_{3+} yields. The particularly high C_3/C_2 ratio observed over the two 10-ring materials with the largest intersection volumes (TUN and IMF) may result from a combination of a high preference for the alkene cycle combined with the large methylbenzenes (that predominantly eliminate C_3-C_4 alkenes) present in the pores [201]. Narrow one-dimensional 10-ring pores (TON) severely restrict intermolecular hydride transfers and formation of aromatics and thus strongly favours the alkene cycle, giving low ethene and high C_{5+} aliphatics yields. The very high yields of the latter products may further suggest that either alkene cracking reactions or methylation to form the easily cracked branched C_7 and C_8 alkenes are sterically restricted in this material. Due to the carbocation intermediates involved in the reactions, a large increase in cracking rates with increasing alkene size and branching is expected [143, 213].

The unique selectivity of one-dimensional 10-rings is further of interest as a means to produce clean-burning gasoline with a low content of aromatics. This led Teketel et al.

[202] to investigate the product selectivity of one-dimensional 10-ring pores structures. This study concluded that both H-EU-1 (EUO) and H-ZSM-48 (*MRE) produced significant amounts of aromatics due to side pockets and larger pore size respectively. However, H-ZSM-22 (TON) and H-ZSM-23 (MTT) gave very similar product distributions with a high selectivity to C_{5+} aliphatics.

Paper IV describes a potential industrial process for production of clean-burning gasoline from synthesis gas. The overall scheme of the process (Figure 4.3) resembles the Haldor Topsøe TIGAS process [98] in that the syngas is first converted into DME and CO_2 at a moderate pressure before being fed to the gasoline synthesis unit. ~95 % syngas conversion could be obtained at 50 bar pressure with a modest recycle, and product separation is achieved efficiently at 5 °C. Due to the high solubility of CO_2 in DME, CO_2 functions as an inert diluent to maintain control of the reaction temperature in the gasoline synthesis reactor.

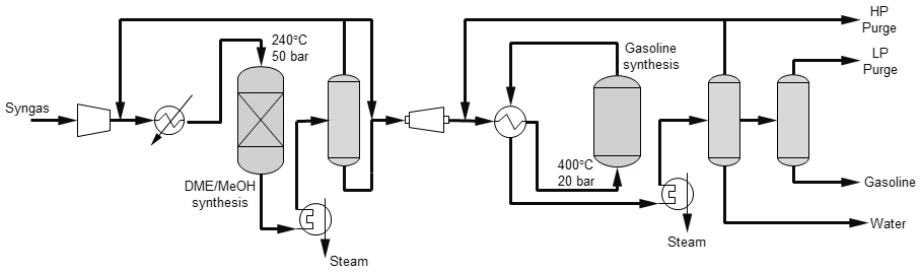

Figure 4.3: Process flow scheme of the integrated synthesis of gasoline from syngas via oxygenates.

A high selectivity towards gasoline range products could be obtained over both H-ZSM-22 and H-ZSM-23, although selectivity drops at near 100 % conversion. It was also found that the product selectivity was not altered at higher pressure (Figure 4.4). However, high pressure led to a more rapid deactivation of the catalyst, similarly to what has been observed previously for H-ITQ-13 [211]. This may be caused by an increased selectivity to aromatic products trapped inside the catalyst, although this has not been investigated further.

Furthermore, it was found that a recycle of the light products may lead to a significant increase in C_{5+} aliphatics selectivity. As shown in Figure 4.5, addition of small amounts of *i*-propanol (which is rapidly dehydrated to propene) did not change the effluent composition from the reactor. Furthermore, the addition of alcohols led to an increased

catalyst lifetime before deactivation. A full study of simulated recycle by addition of alcohols will be published elsewhere by Teketel et al. [214].

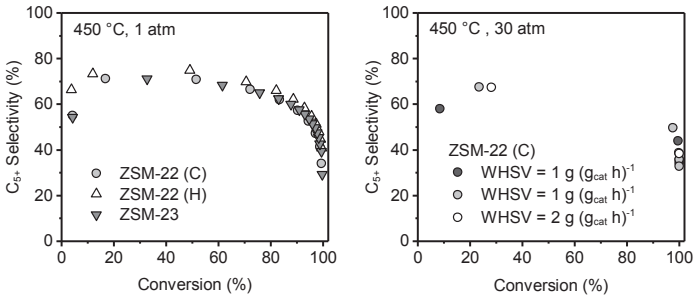

Figure 4.4: C_{5+} selectivity as a function of methanol conversion over two samples of H-ZSM-22 and over H-ZSM-23 at atmospheric pressure (left panel, WHSV = 2 $gg_{cat}^{-1}h^{-1}$, 450 °C) and at 30 atm (right panel, WHSV = 1 and 2 $gg_{cat}^{-1}h^{-1}$) over H-ZSM-22 (C). The mole fraction of methanol in the 1 and 30 atm experiments was 13 and 5.6 % respectively. The data at high pressure were collected from three experiments: one at WHSV = 2 $gg_{cat}^{-1}h^{-1}$, with the first analysis after 10 minutes on stream; and two experiments at WHSV = 1 $gg_{cat}^{-1}h^{-1}$, where the first analysis was performed after either 10 or 50 minutes on stream.

In summary, this means that selectivity higher than 75 % to gasoline range alkenes can be achieved if conversion can be kept at less than 100 %, and a recycle of light alkenes is employed. The use of a fluidized bed reactor would be beneficial as it provides excellent control of the reaction temperature and allows stable operation at less than 100 % conversion. However, the fast deactivation and low activity of both H-ZSM-22 and H-ZSM-23, when compared to other commercial zeolite catalysts such as H-ZSM-5 [215] is a challenge for successful commercialisation.

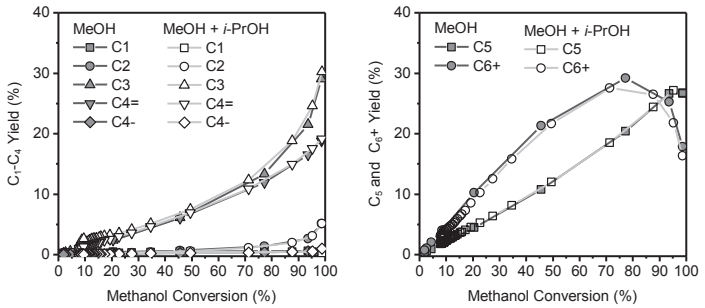

Figure 4.5: Product yields during conversion of methanol (closed symbols) and a 102.8/2.2 methanol/i-propanol mixture (open symbols) over H-ZSM-22 at 400 °C. Adapted from [214].

4.2 Effects of catalyst acid strength

As seen from the results presented in Section 4.1, the pore size of zeolitic catalysts affects the reaction mechanisms and product selectivity of the MTH reaction. In this section the effects of changing the composition of the catalyst, and thereby the strength of the individual acid sites, will be discussed. The two catalysts utilised for this investigation were the large-pore zeolite H-SSZ-24 and the isostructural weaker acid H-SAPO-5 (both AFI). The acid strength of the two samples was compared by FTIR spectroscopy of CO adsorption at -196 °C. The FTIR spectra shown in Figure 4.6 contain many features that have previously been observed and explained [216-220], and these will not be discussed in detail here. Overall, the key difference between the H-SAPO-5 and H-SSZ-24 was the significant difference in magnitude of the shift in OH stretching frequency for the Si-OH-Al groups when they interact with CO. The largest shift observed in H-SAPO-5 is $\Delta\tilde{\nu}$(OH) = -265 cm^{-1} while the shift in H-SSZ-24 is $\Delta\tilde{\nu}$(OH) = -317 cm^{-1}, meaning that the acid sites of H-SSZ-24 are significantly stronger than those of H-SAPO-5. These values correspond fairly well with the differences found by Bordiga et al. [67] between the isostructural zeotypes H-SAPO-34 and H-SSZ-13 (both CHA).

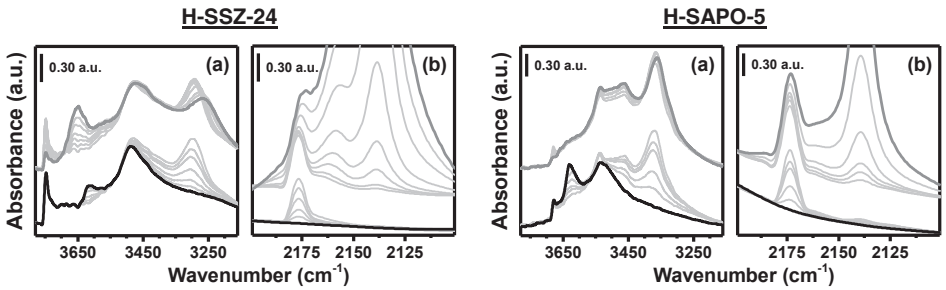

Figure 4.6: FT-IR spectra of increasing dosages of CO on H-SSZ-24 (left two panels) and H-SAPO-5 (right two panels) at −196 °C. Panels labelled (a) show the OH stretching region, while those labelled (b) show the CO stretching region. The black bold curves correspond to the activated samples, while the grey bold curves correspond to the spectra of highest CO loading. In the activated samples, the Brønsted acidic OH groups give rise to a band at 3612 cm^{-1} in H-SSZ-24 and 3630 cm^{-1} in H-SAPO-5.

Since H-SAPO-5 is a large pore zeotype, the arene cycle was expected to play an important part in product formation. However, the investigation of this catalyst (Paper I) indicated that the alkene cycle was significantly more important than in previously studied large-pore catalysts. During MTH reaction over H-SAPO-5, C_3-C_5 alkenes were observed

as the dominant products, while the yields of aromatics and ethene were low. Furthermore, steady-state methanol isotope transient experiments (Figure 4.7a) revealed a more rapid incorporation of ^{13}C in alkene products than in the retained PolyMBs. This method has previously been employed to gauge the relative importance of the alkene and arene cycle, since an active intermediate will incorporate the labelled component more rapidly than, or equally fast as, the product molecules. When comparing the results in H-SAPO-5 to previously reported similar experiments over the catalysts H-Beta [138], H-ZSM-5 [138] and H-ZSM-22 [144], it became clear that while the PolyMBs were not inactive as in H-ZSM-22, they were much less important intermediates than in H-Beta.

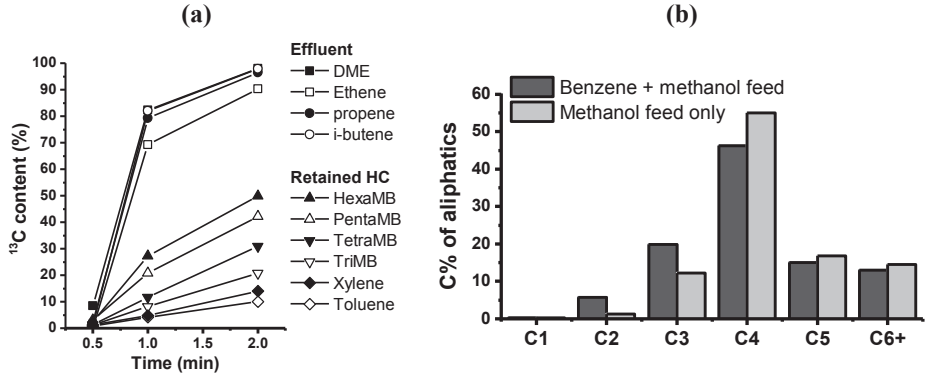

Figure 4.7: **(a)** Evolution of ^{13}C in effluent and retained aromatics after switching from ^{12}C to ^{13}C methanol after 18 min on stream at 450 °C and WHSV 0.93 h^{-1}. **(b)** A comparison of the distribution within the aliphatic products range during co-reaction of benzene and methanol and for pure methanol feed.

Further evidence that the arene cycle was not as important as the alkene cycle in H-SAPO-5 was obtained during co-reactions of benzene and methanol. When 3 equivalents of benzene were added to the methanol feed, the relative selectivity towards C_2 and C_3 hydrocarbons increased significantly at the expense of C_{4+} selectivity (Figure 4.7b). In addition, isotopic labelling suggested that formation of *i*-butene and *i*-pentene from aromatic intermediates was negligible.

While the investigation of H-SAPO-5 reported in Paper I revealed a preference for a different reaction pathway compared to previously studied large-pore catalysts, the difference could not be unambiguously attributed to the lower acid strength. For this reason, a detailed comparison with the isostructural H-SSZ-24 was carried out, and the results were published in Paper II. In addition to its higher activity, it was found that the

product selectivity of H-SSZ-24 during methanol conversion to hydrocarbons differed from H-SAPO-5. As observed from Figure 4.8, much higher yields of aromatics were observed over H-SSZ-24 than over H-SAPO-5. H-SSZ-24 also produced more ethene and propene relative to C_{4+} aliphatics when compared to H-SAPO-5. Although ethene is not a major product in either catalyst, the difference was significant. Further differences were observed in the C_4/C_3 and C_3/C_2 ratios, which were relatively independent of conversion in H-SSZ-24, but varied considerably in H-SAPO-5. This observation may suggest that C_2-C_4 alkenes are formed mainly from a common precursor in H-SSZ-24, but not in H-SAPO-5.

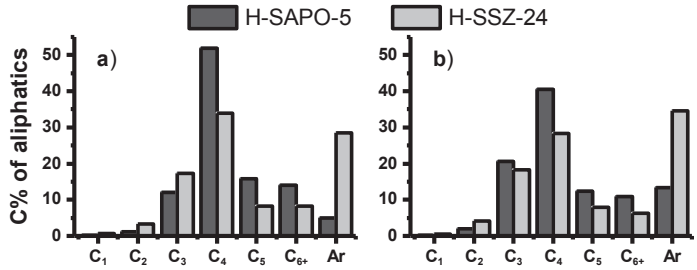

Figure 4.8: Product selectivities for H-SAPO-5 (dark grey) and H-SSZ-24 (light grey) at 350 °C at 20 % (a) and 60 % (b) conversion. The data were obtained during deactivation of H-SSZ-24 at WHSV = 1.24 h^{-1} and of H-SAPO-5 at WHSV = 0.62 h^{-1} (a) and 0.31 (b).

Together, these observations are consistent with a more active arene cycle in H-SSZ-24 compared to H-SAPO-5, as the arene cycle is expected to produce mainly C_2-C_4 alkenes, while the alkene cycle produces larger alkenes. However, a less active arene cycle may have been caused simply by the lower amount of PolyMBs formed in H-SAPO-5. Since computational studies suggest that cyclisation reactions are facile [221], hydride transfers are likely rate-determining steps in the formation of aromatics. As discussed in Section 2.4, a link between acid strength and hydride transfers has been proposed previously [183, 186]. Alternatively, key reaction steps of the alkene and arene cycles could display different sensitivity to acid strength. In an attempt to distinguish between these possibilities, co-reactions between ^{12}C-benzene and ^{13}C labelled methanol (molar ratio 1:3) were performed as part of Paper II. As the concentration of PolyMB molecules was greatly enhanced inside the catalysts compared to ordinary MTH experiments under these conditions, PolyMB reactivity could be investigated more directly.

It was difficult to obtain similar conversion over the two catalysts, as H-SSZ-24 was still significantly more active than H-SAPO-5 at 1/8 of the contact time. While a direct comparison was not achieved, some clear trends were nevertheless observed. In line with the observations from conversion of methanol alone, H-SAPO-5 was much more selective towards C_4 than H-SSZ-24. Furthermore, the isotopic distribution of the alkene products after 2 minutes on stream (displayed in Figure 4.9) differed for the two catalysts. At 250 °C, one ^{12}C atom originating from benzene was incorporated in ethene and propene over H-SAPO-5. However, the abundant *i*-butene formed over H-SAPO-5 contained a significantly larger fraction of ^{13}C atoms than the lighter compounds, and the all-^{13}C isotopologue was dominant. On the other hand, the majority of all three alkenes contained one ^{12}C atom over H-SSZ-24 at the same temperature. At higher temperature, the isotopic distribution became less clear, but while all alkenes were composed mostly of ^{13}C from methanol over H-SAPO-5, a significant fraction of alkenes containing one ^{12}C atom was still observed over H-SSZ-24.

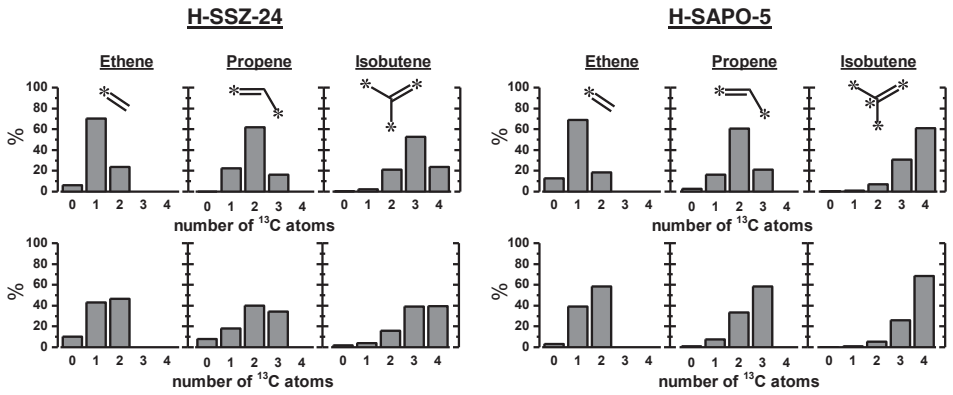

Figure 4.9: Observed distribution of ^{13}C atoms after 2 minutes co-reaction of methanol and benzene (molar ratio 3:1) over H-SSZ-24 (left) and H-SAPO-5 (right). Each figure shows the distribution in ethene (left), propene (middle) and *i*-butene (right) at 250 °C (top) and 300 °C (bottom). The molecules above the graphs are drawn with stars signifying labelled carbon atoms representative of the most abundant isotopologues found at 250 °C.

Assuming a similar mechanism for PolyMB de-alkylation in both materials (which is likely due to the similar ethene and propene isotopologues observed), these results imply that the most abundant alkene in H-SAPO-5 (*i*-butene) was not formed from aromatic intermediates. The high abundance of ^{13}C in *i*-butene can be satisfactorily explained by a cycle of successive alkene methylation and cracking (i.e. the alkene cycle). In such a cycle,

the abundance of ^{13}C would increase with each cycle if the starting molecule was e.g. $^{12}C^{13}C_2$-propene, as only ^{13}C methanol is consumed. The nearly complete scrambling and low incorporation of ^{12}C observed combined with an even higher yield of C_{4+} aliphatics over H-SAPO-5 at 300 °C thus suggests that the alkene cycle dominates over this catalyst. Considering the large excess of aromatics present in the system, the rate constants for key steps of the alkene cycle must be much higher than those of the arene cycle over H-SAPO-5. On the other hand, the results suggest that C_2-C_4 alkene formation at 250 °C over H-SSZ-24 mainly proceeds through aromatic intermediates (i.e. the arene cycle), and that this same mechanism contributes strongly even at 300 °C. A further discussion on the implication of the observed labelling patterns on the de-alkylation mechanism will be given in Section 4.3.

The results discussed so far strongly suggest that key reaction steps of the alkene and arene cycles are affected differently by a change in acid strength. Macht et al. [190] has previously proposed that the main reason why *n*-hexane isomerisation is more sensitive to a change in acid strength than butanol dehydration is the more localised charge in the transition state of the latter reaction compared to the former. It is plausible that the positive charges of transition states involving arenes are more diffuse than those involving alkenes, which could mean that the reactions of the arene cycle are more sensitive to acid strength than those of the alkene cycle.

However, a deeper understanding of this issue requires investigation and comparison of isolated reaction steps in the two cycles. Methylation reactions are important in both the alkene and arene cycles, and a comparison of alkene and arene methylation rates over the two catalysts could provide insight into why a difference in acid strength apparently causes a shift of the favoured reaction mechanism in the MTH reaction. Such a study was performed in Paper V.

Co-reactions of benzene and methanol were again performed, but contrary to the reactions in Paper II molar ratios near 1 and an excess of benzene were employed. The conversion was also kept much lower (generally ~ 0.2 % benzene conversion at 250 °C). The net formation rate of toluene, other aromatics (mainly PolyMBs) and aliphatics as a function of varying the molar ratio of methanol to benzene is displayed in Figure 4.10. While toluene was the main product over both catalysts at low methanol partial pressures, significant differences were observed between the two catalysts as the molar ratio of methanol to benzene was increased.

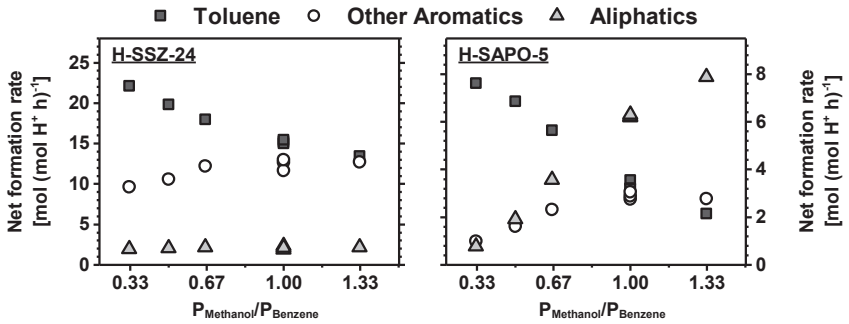

Figure 4.10: Net rates of formation of the main product groups during co-reactions of benzene and methanol as a function of the methanol to benzene molar feed ratio at 250 °C over H-SSZ-24 (left) and H-SAPO-5 (right). $P_{Benzene}$ = 60 mbar. Benzene feed rate = 13×10^3 mol (mol H^+)$^{-1}$ h^{-1} over H-SSZ-24 and 2.9×10^3 mol (mol H^+)$^{-1}$ h^{-1} over H-SAPO-5. Total WHSV = 140-191 h^{-1} (H-SSZ-24) or 17.5-24 h^{-1} (H-SAPO-5). The data have been corrected for deactivation.

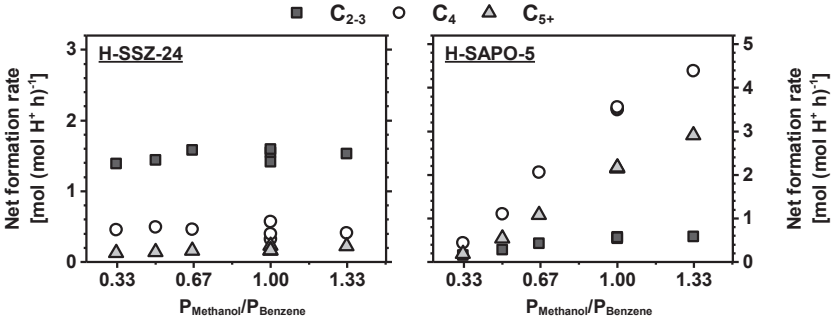

Figure 4.11: Net rates of formation for aliphatic products during co-reactions of benzene and methanol as a function of the methanol to benzene molar feed ratio at 250 °C over H-SSZ-24 (left) and H-SAPO-5 (right). $P_{Benzene}$ = 60 mbar. Benzene feed rate = 13×10^3 mol (mol H^+)$^{-1}$ h^{-1} over H-SSZ-24 and 2.9×10^3 mol (mol H^+)$^{-1}$ h^{-1} over H-SAPO-5. Total WHSV = 140-191 h^{-1} (H-SSZ-24) or 17.5-24 h^{-1} (H-SAPO-5). The data have been corrected for deactivation.

As seen from Figure 4.10, an increase in methanol partial pressure led to an increase in the net rate of formation of other aromatics and a similar decrease in the net formation rate of toluene over H-SSZ-24. This is consistent with an increasing rate of methylation for each methyl group present on the aromatic ring [176-178]. Interestingly, the ratio between rates of formation for other aromatics and aliphatics remains roughly constant throughout the investigated range, which is in agreement with formation of aliphatics mainly resulting from de-alkylation of aromatics. Unlike over H-SSZ-24, the rate of aliphatic formation over H-SAPO-5 increased rapidly with increasing methanol

pressure. At a 1:1 molar feed ratio of benzene and methanol, aliphatic products account for about 50 % of the total molar amount of products formed. Contrary to H-SSZ-24, the formation rates of aliphatics and other aromatics did not appear correlated over H-SAPO-5.

Figure 4.11 shows a breakdown of the different aliphatic products produced, grouped by their carbon number. A clear difference in the size of the aliphatics produced over the two catalysts was observed: The aliphatics formed over H-SSZ-24 were mainly C_2-C_3, while most of the aliphatics formed over H-SAPO-5 contained four or more carbons. This product distribution is again in line with the observations of Paper II, and contributes to an increasingly clear picture of H-SAPO-5 favouring the alkene cycle at all investigated conditions. Scheme 4.1 displays the likely reactions occurring during these experiments, with the reactions to the left expected to be strongly favoured due to the conditions employed. When benzene was present in excess, the expected product toluene dominated. However, as the relative amount of methanol was increased, an increased rate of successive methylations to form PolyMBs was observed. Some of these aromatics further de-alkylated to form light alkenes. This accounts for the aliphatics observed in H-SSZ-24 and thus for all observed products over this catalyst. On the other hand, aliphatics are methylated at the expense of the aromatics in H-SAPO-5, and a cycle of alkene methylation and cracking dominates the reaction. This leads to a significant decrease in benzene conversion and an increasing yield of C_{4+} aliphatics with increasing methanol partial pressure over H-SAPO-5.

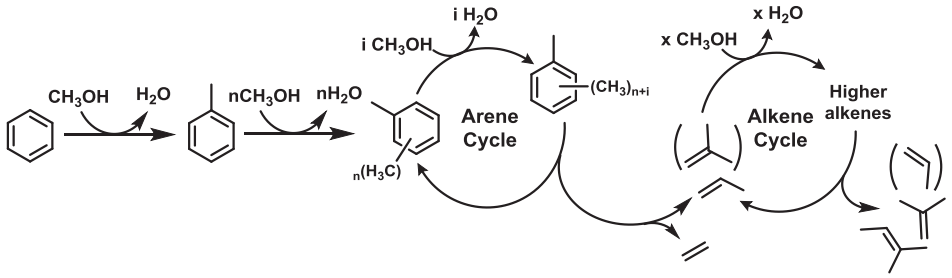

Scheme 4.1: Possible reaction mechanisms during methanol/benzene co-reactions. Benzene is first methylated to form toluene, which can then be methylated to form PolyMBs. These PolyMBs can then de-alkylate as part of the arene cycle to give lower alkenes. The alkenes may react further in an alkene cycle, where they are methylated to higher alkenes, and crack to form mainly branched C_4 and C_5 alkenes. It is assumed that ethene leaves the catalyst without further reaction due to its low methylation rate [170-172].

In order to obtain a more fundamental understanding of the differences observed during co-reactions of benzene and methanol, a direct comparison of the rate of propene and benzene methylation was performed. Methylation of the two hydrocarbons was conducted alternately, and several times each, to obtain the best possible comparison between the two rates and minimise the influence of deactivation. Due to difficulties in obtaining sufficient selectivity to the first methylation product of propene methylation at low temperatures, all experiments were performed at 400 °C and 350 °C, and with a 1:1 molar ratio of methanol to alkene/benzene. These conditions provided an adequate selectivity for both reactions at high feed rates, and the net formation rates of the first methylation product (*n*-butene or toluene) are displayed in Figure 4.12a. While the net rate of benzene methylation was observed to be 2-3 times faster than propene methylation over H-SSZ-24, this difference was not observed over H-SAPO-5. Instead, the net rates of propene and benzene methylation were fairly similar over H-SAPO-5. Considering that the rate of methylation increases more going from propene to *i*-butene (due to increased branching) [173], than from benzene to toluene [177], it can be expected that methylation of *i*-butene and *i*-pentene is significantly faster than methylation of benzene and PolyMBs over H-SAPO-5. Together, these factors can explain the high C_{4+} aliphatics yield previously observed during co-reactions of benzene and methanol (Figure 4.10 and Figure 4.11)

The methylation experiments were accompanied by complementary theoretical studies of adsorption behaviour and reactivity for methanol and the hydrocarbons in both materials. The theoretical studies were performed by a combination of DFT-based static and molecular dynamics (MD) simulations. Each technique enlightens an aspect of the co-adsorption of methanol and benzene or propene, enabling detailed molecular level insight. Static calculations are well suited for adsorption studies in zeolitic materials [222], while molecular dynamics studies reveal the dynamical character of adsorption complexes at the reaction temperature [223]. Significant differences were found for the two materials. In H-SSZ-24, a high probability for the formation of a reactive adsorption complex of methanol (resembling the transition state during methylation) coupled with a high degree of protonation predicted a high reactivity for benzene methylation. On the other hand, a lower probability for formation of a reactive methanol/propene adsorption complex and a lower degree of protonation in this complex implied a significantly lower methylation rate of propene in the same structure. The theoretical studies further predicted a lower reactivity

for H-SAPO-5 than H-SSZ-24 for both reactions, and a smaller difference between the reactivity of propene and benzene in H-SAPO-5 than in H-SSZ-24. Indeed, a slightly higher rate of propene than benzene methylation in H-SAPO-5 was predicted by theory. Figure 4.12b shows the predicted chance of forming a pre-reactive complex versus the degree of protonation.

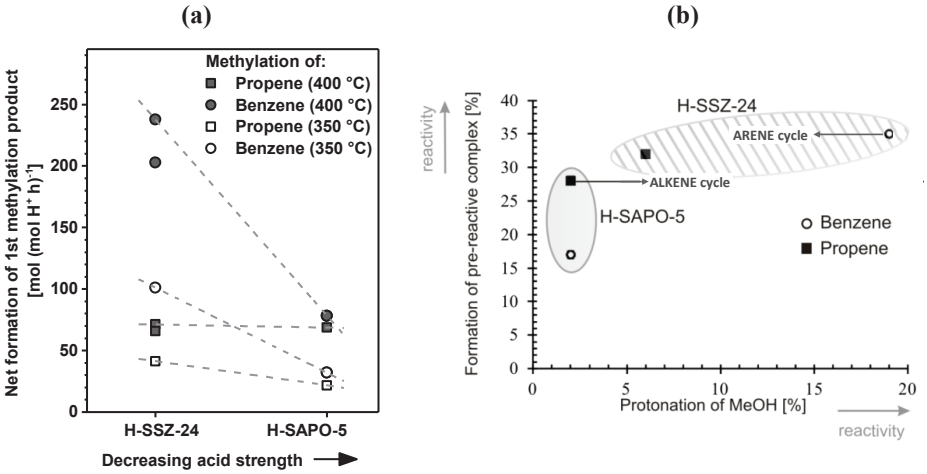

Figure 4.12: (a) Rates of formation for *n*-butenes (circles) and toluene (squares) during co-reactions of methanol and propene or benzene, respectively, at 400 °C and 350 °C over H-SSZ-24 and H-SAPO-5. Note that the rates are given per gram catalyst, and that H-SSZ-24 has nearly twice the number of acid sites as H-SAPO-5. **(b)** Degree of protonation of methanol versus the probability for the formation of a pre-reactive complex from MD simulations at 350 ºC for benzene and propene in H-SSZ-24 (shaded area) and H-SAPO-5 (filled area).

In summary, the work described in this section shows that a decrease in acid strength decreases the rate of reactions involving aromatics to a larger extent than those involving alkenes. The experimentally observed difference could be partly explained by theoretical calculations. However, whether cracking reactions/de-alkylation rates are also affected differently is unknown. In addition, a lower acid strength decreases the rate of hydride transfers relative to other reactions (in line with previous observations [183, 189]) which leads to lower yields of aromatic products in the weaker acid H-SAPO-5 than in the stronger H-SSZ-24.

4.3 Polymethylbenzene de-alkylation

As described in Section 2.2, whether PolyMB de-alkylation proceeds by side-chain methylation or by the paring reaction has long been debated. A key difference between the paring and side-chain mechanisms is that the former systematically incorporates a ring carbon into the eliminated alkene. A simplified scheme of these two reaction pathways is presented in Scheme 4.2, showing the positions of the carbon atoms originally present as methyl groups. While this was not initially remarked on, the isotopic distributions observed during co-reaction of benzene and methanol (Figure 4.9) therefore allow discrimination between the side-chain and paring mechanisms. For the experiments reported in Paper I and II, the methyl groups consisted predominantly of ^{13}C originating from methanol. While Scheme 4.2 depicts HeptaMB$^+$ as the main intermediate, similar mechanisms are assumed to exist for polymethylbenzenium cations with fewer methyl groups, and the labelling patterns are also expected to be similar if the elimination products are ethene or *i*-butene instead of propene (i.e. one unlabelled carbon should be observed in both alkenes if the paring mechanism dominates).

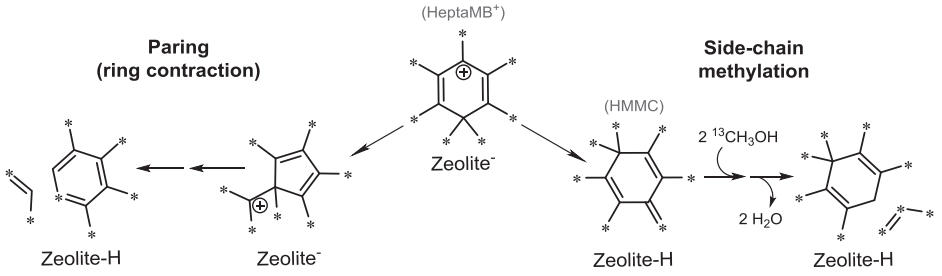

Scheme 4.2: Expected labelling patterns when propene is eliminated from a selectively labelled heptaMB$^+$ via paring or exocyclic mechanisms. Stars are used in order to keep track of the carbons originally present as methyl groups. The paring pathway involves systematic scrambling of labelled carbons into the benzene ring, while the exocyclic methylation does not.

As observed from Figure 4.9, the labelling patterns of all three alkenes at 250 °C over H-SSZ-24 fit with a paring-type mechanism, as they all contain one ^{12}C atom. On the other hand, over H-SAPO-5 ethene and propene contained one ^{12}C atom, while *i*-butene contained mainly ^{13}C atoms. Thus, the labelling patterns of ethene and propene were consistent with a paring reaction, while *i*-butene was not. The isotopic distribution of *i*-butene could indicate that de-alkylation proceeds by side-chain methylation but, as inferred

from Scheme 4.2, this would require 3 sequential deprotonation and methylation steps. It is not likely that such a sequence of steps would lead selectively to *i*-butene formation, while giving insignificant amounts of ethene and propene. Furthermore, the labelling patterns of *i*-butene and higher alkenes can be better explained by formation from the alkene cycle (see Section 4.2).

In summary, it appears likely that a paring reaction is responsible for all PolyMB de-alkylation in both H-SSZ-24 and H-SAPO-5 at the reaction conditions investigated. This implies that even though a decrease in acid strength decreases the relative rate of PolyMB de-alkylation relative to alkene methylation and cracking, the mechanism of the former reaction is not affected. Previous studies of benzene/methanol co-reactions in H-Beta [136] at similar conditions have also indicated that the paring mechanism dominates. A recent report by Ilias and Bhan [224], published after the work performed in Paper I and II, reached the same conclusion for H-ZSM-5 at 250 - 450 °C.

While formation of ethene containing one ring-carbon (from benzene) was reported in Paper I and II, it should be noted that ethene elimination is not usually associated with the paring reaction. If the starting molecule is HeptaMB$^+$ as shown in Scheme 4.2, there is no obvious pathway for ethene elimination available. However, Arstad et al. [161-163] has suggested that expansion of the aromatic ring to a tropylium-type ion followed by contraction may yield an ethyl chain. Alternatively, it is possible that ethene elimination only occurs from PolyMBs with six or fewer methyl groups, as this allows methyl shifts from the propyl chain to the cyclopentadienyl ring prior to elimination.

In order to further investigate the mechanism of unimolecular de-alkylation, the conjugate base of HeptaMB$^+$ (HMMC) was synthesised, both unlabelled and with ^{13}C ring-carbons (but ^{12}C methyl groups). The reactivity of this key intermediate was studied both in gas phase and over H-SSZ-24 in Paper VI. While such studies have been performed previously [153, 198], this is the first time isotopic labelling has been employed. It is also the first time HMMC has been studied over a zeolite at less than full conversion. While reaction studies over a zeolite can be complicated due to secondary and competing reactions, gas phase reactions performed in vacuum allows the study of unimolecular reactions without any interference. Although reaction energies in gas phase and inside a zeolite will differ, the reaction pathways available to HeptaMB$^+$ are likely similar. A comparison of gas phase unimolecular reactivity and experiments over a zeolite thus provides a unique opportunity to investigate reaction mechanisms.

When HMMC was protonated to form HeptaMB$^+$, and then collisionally activated with argon at 1×10^{-4} mbar, the dominant reaction was elimination of a methyl radical. Similarly to this, the dominant product of HMMC (which is expected to be protonated rapidly on the acid sites due to its high basicity [151]) reaction over H-SSZ-24 was HexaMB. While no methyl fragments can be observed in the zeolite, a plausible explanation is that methoxy groups are formed, replacing the protons on the Brønsted acidic sites of the zeolite. Due to the aromaticity of the product HexaMB, this reaction is assumed to be energetically favourable. Figure 4.13 gives an overview of the observed fragmentations in vacuum, while Figure 4.14 shows the conversion and yields after 2 minutes of HMMC reaction over H-SSZ-24.

In addition to the loss of methyl groups, C_2-C_5 alkenes were observed over the H-SSZ-24 catalyst (and some C_6, but only at high temperature). Similarly, fragments corresponding to loss of C_2-C_5 alkenes were also observed in gas phase. At the highest energies, ethane loss (exclusively from methyl carbons) was prominent in gas phase, but this was not observed in the catalytic experiments. Isotopic labelling (see Figure 4.13) revealed that eliminated ethene and propene contained one ^{13}C atom (ring carbon). On the other hand, butene could be eliminated with either one or two ring-carbons, and pentene with two ring-carbons. As seen from the bar graphs at the far right of Figure 4.13 and Figure 4.14, the relative amounts of the main alkene isotopologues formed were similar in gas phase and during catalytic reaction over H-SSZ-24.

The catalytic experiments (Figure 4.14) revealed similar isotopic distributions for propene, butene and *i*-pentenes (few *n*-pentenes were observed). Interestingly, *i*-butene contained predominantly one ^{13}C atom while *n*-butenes contained two, possibly indicating different formation mechanisms. Contrary to the gas-phase experiments, both ethene and propene contained mainly ^{12}C at low temperatures. This may be caused by side-chain methylation by the methoxy groups produced during HexaMB formation as this mechanism involves only ^{12}C atoms originating in methyl groups. Due to the high yield of HexaMB, the majority of the acid sites are likely covered by methoxy groups after the first turnover of HMMC. As the effluent analysis is performed after 3-4 turnovers, methylation rather than protonation should have been significant. The only position available for methylation on HMMC is the exocyclic double bond, leading to an ethylhexamethylcyclohexadienyl cation, which is the first intermediate of the side-chain methylation pathway (recall Scheme 2.5 or Scheme 4.2).

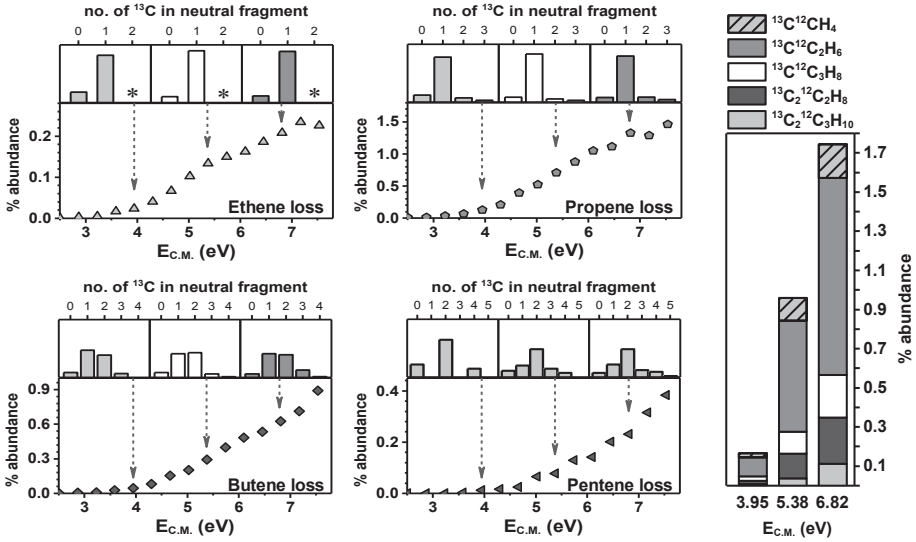

Figure 4.13: Abundance (% of total ion current) of fragments related to loss of ethene (top left), propene (top right), butene (bottom left) and pentene (bottom right) after collisional activation of HeptaMB^{+}. The bar graphs above each plot show the relative distribution of ^{13}C carbons (originating from the aromatic ring) in the eliminated alkenes. The bar graph to the far right displays the relative amounts of the major isotopologue(s) of the alkenes eliminated at the same collision energies.

* Ethene containing two ^{13}C could not be detected due the overlapping mass of unlabelled ethane.

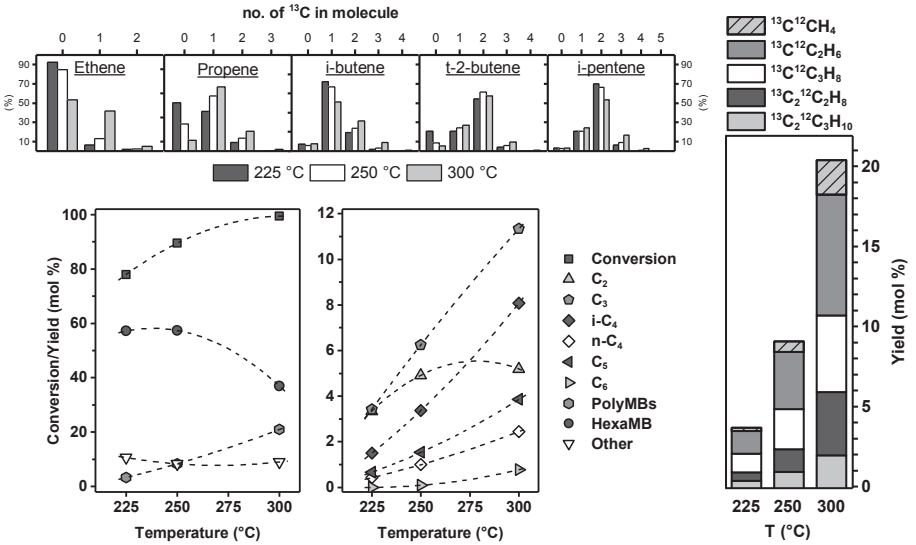

Figure 4.14: Conversion and product yields (bottom left, two panels) after 2 minutes of HMMC reaction over H-SSZ-24 as a function of reaction temperature. The "other" fraction contains mainly unidentified HMMC isomers and other aromatics. The top bar graphs display the number of ^{13}C atoms in the C_2-C_5 alkenes at the same conditions. The graph on the far right displays the relative amounts of the isotopologues associated with unimolecular de-alkylation at the three different temperatures.

As HMMC can only be formed by the thermodynamically unfavourable deprotonation of HeptaMB$^+$ during normal MTH conditions, the current conditions (containing both gas-phase HMMC and a methylation reagent) should strongly favour side-chain methylation. However, even at low temperature, products associated with side-chain methylation accounts for less than half the total alkenes formed, and at higher temperature (where conversion was also higher) they are much less prominent. The low fraction of all ^{12}C alkenes observed strongly suggests that the side-chain methylation reaction is slow compared to unimolecular de-alkylation. This conclusion was not altered by co-reactions of methanol with HMMC, as side-chain products still accounted for less than half of the total amount of alkenes formed.

Thus, it seems clear that unimolecular de-alkylation mechanisms are more important than side-chain methylation at temperatures below 300 °C, and no indications that side-chain becomes more favoured at higher temperature has been found. However, the mechanism of the unimolecular de-alkylation is uncertain. A proposed mechanism must be able to account for production of both ethene and the two products containing two ring-carbons (*n*-butenes and *i*-pentenes) that are not associated with the classical paring mechanism (Scheme 2.5). After a survey of the available literature on ring-expansions and contractions, it was concluded that no completely satisfactory mechanism has been proposed so far. In particular no mechanism has suggested that accounts for *n*-butene and *i*-pentene elimination, as neither of these products have previously been associated with the paring or side-chain reactions.

For this reason, a mechanism based on the classical paring mechanism combined with related cations previously observed in superacidic solutions [225, 226] was suggested. As shown in Scheme 4.3, it is suggested that HeptaMB$^+$ can contract in either of two ways: Either resembling the paring mechanism, as proposed by Arstad et al. [162] to form the heptamethylbicyclo[3.1.0]hexenyl cation (c1) or to the heptamethylbicyclo[2.2.0]hexenyl cation (c2). A contraction similar to the latter (i.e. from a six-ring to two joined four-rings) has been previously shown to occur in pyrones during ultraviolet radiation in ether [227]. Cation c2 is also related to c1 through a heptamethylbicyclo[2.1.1]hexenyl cation (c3) [225, 226]. It is further proposed that cation c1 may eliminate propene or *i*-butene (the latter after a methyl shift); c2 may eliminate *i*-pentene or *n*-butene containing two ring-carbons; and c3 may eliminate ethene or propene. However, the mechanism for de-alkylation and re-expansion to a PolyMB is uncertain as previous calculations on the

paring mechanism all find a high barrier to re-expansion from the cyclopentadienyl cation [155, 162, 228]. In addition, this cation is already significantly less stable than other intermediates during the reaction. For the proposed reaction pathway to be viable, another mechanism for de-alkylation and re-expansion must be found. Possibly, expansion could occur before de-alkylation, or both could occur simultaneously in a concerted step. It is suggested that computational methods are employed to study the cations c1-c3 and to search for facile de-alkylation and re-expansion mechanisms. Better understanding of these mechanisms is a prerequisite for predictive modelling of the arene cycle during the MTH reaction.

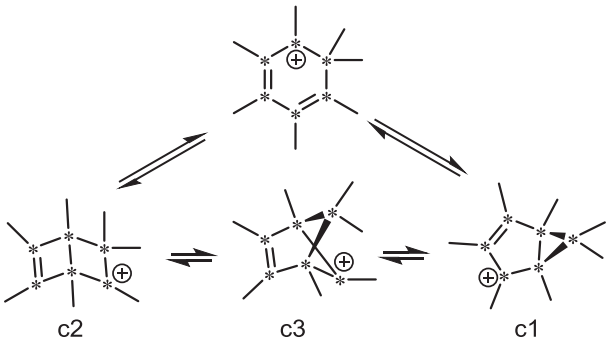

Scheme 4.3: Illustration of two ions formed from contraction of HeptaMB$^+$, and a possible intermediate for interconversion between them. Stars signify the ^{13}C atom labels employed in Paper VI. These ions are suggested as intermediates for unimolecular de-alkylation of C_2-C_5 alkenes.

4.4 Main conclusions

- The size of the largest products formed in the MTH reaction over zeolitic catalysts is mainly determined by the largest pore size of the catalyst, but large cavities exposed to the external surface may lead to discrepancies. Product distributions can generally be rationalised from the dual-cycle mechanism.

- A process producing branched alkenes in the gasoline range from syngas via DME/methanol is viable, although the fast deactivation and low activity of the H-ZSM-22 (TON) and H-ZSM-23 (MTT) catalysts may be problematic.

- The moderately acidic H-SAPO-5 produces significantly less aromatics during MTH catalysis at 350-450 °C than the stronger acid H-SSZ-24.

- Reactions of methanol to hydrocarbons over the moderately acidic H-SAPO-5 catalysts acid proceeds mainly through the alkene cycle at 350-450 °C. This in turn leads to higher yields of C_{3+} alkenes over H-SAPO-5 than over H-SSZ-24 and other large-pore catalysts possessing a higher acid strength.

- Methylation of benzene is significantly more favoured than methylation of propene over H-SSZ-24 between 250 and 400 °C, while the rates of propene and benzene methylation are similar over H-SAPO-5. This can be explained by the probabilities of forming reactive co-adsorption complexes of methanol with benzene or propene in the catalysts found from DFT molecular dynamics and static calculations.

- At 200-300°C, alkene formation from PolyMBs occurs mainly by unimolecular de-alkylation reactions, and not by side-chain methylation, regardless of acid strength.

- Unimolecular de-alkylation of the heptamethylbenzenium ion can result in C_2-C_5 alkenes. The reaction leads to systematic incorporation of 1 carbon atom originating from the aromatic ring into ethene, propene and *i*-butene, while 2 carbon atoms are incorporated into *n*-butenes and *i*-pentene.

4.5 Suggestions for further work

- While it was found that methylation of propene and benzene were affected differently by a change in acid strength, a full kinetic investigation of both activation energies and reaction orders may provide even more fundamental insight. Especially if combined with a complimentary theoretical study.

- Spectroscopic *operando* studies may enable further elucidation of whether methylation reactions follow the stepwise or concerted mechanism, and whether the pathway is affected by acid strength.

- Expanding the study of acid strength to other members of the AFI framework. H-[Fe]SSZ-24 and H-MgAPO-5 are especially interesting, as the former is predicted to be equally reactive to H-SAPO-5 despite the different composition, while the latter has the strongest acid sites of any zeotype composition [192].

- Further computational investigations of unimolecular de-alkylation are necessary to fully elucidate the reaction mechanism.

- Investigate the effect of acid strength on single reaction steps other than methylation. Cracking of alkenes and alkyl-aromatics are both relevant to the MTH reaction, and may display different sensitivity to changes in acid strength. Other interesting reactions include hydride transfers and cyclisation reactions.

- Many of the commonly employed methods to investigate acid strength densities suffer from large drawbacks. Thus, better methods or refinement of existing methods for quantification of acid strength would be preferable.

References

[1] I. Chorkendorff, J.W. Niemantsverdriet, Concepts of Modern Catalysis and Kinetics, 2nd ed., Wiley-VCH Verlag GmbH & Co. KGaA, Weinheim, 2007.

[2] E.V. Anslyn, D.A. Dougherty, Modern Physical Organic Chemistry, University Science Books, Sausalito, California, 2006.

[3] J.J. Berzelius, Edinburgh New Philos. J., 21 (1836) 223.

[4] J.M. Thomas, Angew. Chem. Int. Ed., 33 (1994) 913.

[5] E.J. Holmyard, Makers of chemistry, Clarendon Press, Oxford, 1931.

[6] P.M.D. Collins, Platinum Met. Rev., 30 (1986) 141.

[7] A. Dyer, An Introduction To Zeolite Molecular Sieves, 1st ed., John Wiley & sons, Chichester, 1988.

[8] A.F. Masters, T. Maschmeyer, Microporous Mesoporous Mater., 142 (2011) 423.

[9] D.H. Everett, Pure Appl. Chem., 31 (1972) 577.

[10] J. Weitkamp, Solid State Ionics, 131 (2000) 175.

[11] J.A. Rabo, M.W. Schoonover, Appl. Catal. A, 222 (2001) 261.

[12] E.M. Flanigen, Pure Appl. Chem., 52 (1980) 2191.

[13] A.F. Cronstedt, Kongl. Svenska Vetenskaps Academiens Handlingar, 17 (1756) 120.

[14] C. Colella, A.F. Gualtieri, Microporous Mesoporous Mater., 105 (2007) 213.

[15] P.B. Weisz, V.J. Frilette, J. Phys. Chem., 64 (1960) 382.

[16] V.J. Frilette, P.B. Weisz, R.L. Golden, J. Catal., 1 (1962) 301.

[17] P.B. Weisz, V.J. Frilette, R.W. Maatman, E.B. Mower, J. Catal., 1 (1962) 307.

[18] C. Baerlocher, L.B. McCusker, Database of Zeolite Structures, http://www.iza-structure.org/databases/ (Accessed 25.05.2014).

[19] E.M. Flanigen, B.M. Lok, R.L. Patton, S.T. Wilson, Pure Appl. Chem., 58 (1986) 1351.

[20] S.T. Wilson, B.M. Lok, C.A. Messina, T.R. Cannan, E.M. Flanigen, J. Am. Chem. Soc., 104 (1982) 1146.

[21] B.M. Lok, C.A. Messina, R.L. Patton, R.T. Gajek, T.R. Cannan, E.M. Flanigen, J. Am. Chem. Soc., 106 (1984) 6092.

[22] N.A. Kutz, ACS Symp. Ser., 368 (1988) 532.

[23] W.M. Meier, Pure Appl. Chem., 58 (1986) 1323.

[24] J.V. Smith, Zeolites, 4 (1984) 309.

[25] F. Liebau, Zeolites, 3 (1983) 191.

[26] L.V.C. Rees, Nature, 296 (1982) 491.

[27] F. Liebau, H. Gies, R.P. Gunawardane, B. Marler, Zeolites, 6 (1986) 373.

[28] C. Baerlocher, L.B. McCusker, D.H. Olson, Atlas of Zeolite Framework Types, 6th ed., Elsevier, Amsterdam, 2007.

[29] D.S. Coombs, A. Alberti, T. Armbruster, G. Artioli, C. Colella, E. Galli, J.D. Grice, F. Liebau, J.A. Mandarino, H. Minato, E.H. Nickel, E. Passaglia, D.R. Peacor, S.

Quartieri, R. Rinaldi, M. Ross, R.A. Sheppard, E. Tillmanns, G. Vezzalini, Eur. J. Mineral., 10 (1998) 1037.
[30] M.E. Davis, Nature, 417 (2002) 813.
[31] J.X. Jiang, J.H. Yu, A. Corma, Angew. Chem. Int. Ed., 49 (2010) 3120.
[32] M. Estermann, L.B. Mccusker, C. Baerlocher, A. Merrouche, H. Kessler, Nature, 352 (1991) 320.
[33] M.E. Davis, C. Saldarriaga, C. Montes, J. Garces, C. Crowder, Zeolites, 8 (1988) 362.
[34] L.B. McCusker, C. Baerlocher, in: J. Čejka, H. van Bekkum, A. Corma, F. Schüth (Eds.) Introduction to Zeolite Science and Practice, Elsevier, Amsterdam, 2007, pp. 13.
[35] W. Loewenstein, Am. Mineral., 39 (1954) 92.
[36] A. Corma, J. Catal., 216 (2003) 298.
[37] M. Tielen, M. Geelen, P.A. Jacobs, Proc. Int. Symp. Zeolite Catal., Siofok, Hungary (1985) 1.
[38] T.E. Gier, G.D. Stucky, Nature, 349 (1991) 508.
[39] G. Harvey, W.M. Meier, Stud. Surf. Sci. Catal., 49 (1989) 411.
[40] G. Busca, Chem. Rev., 107 (2007) 5366.
[41] A. Corma, Chem. Rev., 95 (1995) 559.
[42] P.B. Weisz, Pure Appl. Chem., 52 (1980) 2091.
[43] S.M. Csicsery, Pure Appl. Chem., 58 (1986) 841.
[44] B. Smit, T.L.M. Maesen, Nature, 451 (2008) 671.
[45] T.F. Degnan, J. Catal., 216 (2003) 32.
[46] D. Lesthaeghe, B. De Sterck, V. Van Speybroeck, G.B. Marin, M. Waroquier, Angew. Chem. Int. Ed., 46 (2007) 1311.
[47] W.O. Haag, R.M. Lago, P.B. Weisz, Faraday Discuss., 72 (1981) 317.
[48] W.O. Haag, R.M. Lago, P.B. Weisz, Nature, 309 (1984) 589.
[49] D.H. Olson, W.O. Haag, R.M. Lago, J. Catal., 61 (1980) 390.
[50] W.O. Haag, Stud. Surf. Sci. Catal., 84 (1994) 1375.
[51] J.F. Haw, Phys. Chem. Chem. Phys., 4 (2002) 5431.
[52] M.T. Aronson, R.J. Gorte, W.E. Farneth, D. White, J. Am. Chem. Soc., 111 (1989) 840.
[53] J.F. Haw, B.R. Richardson, I.S. Oshiro, N.D. Lazo, J.A. Speed, J. Am. Chem. Soc., 111 (1989) 2052.
[54] J.F. Haw, J.B. Nicholas, T. Xu, L.W. Beck, D.B. Ferguson, Acc. Chem. Res., 29 (1996) 259.
[55] J.B. Nicholas, J.F. Haw, L.W. Beck, T.R. Krawietz, D.B. Ferguson, J. Am. Chem. Soc., 117 (1995) 12350.
[56] T. Xu, P.D. Torres, L.W. Beck, J.F. Haw, J. Am. Chem. Soc., 117 (1995) 8027.
[57] M. Brandle, J. Sauer, J. Am. Chem. Soc., 120 (1998) 1556.
[58] I.A. Koppel, R.W. Taft, F. Anvia, S.Z. Zhu, L.Q. Hu, K.S. Sung, D.D. Desmarteau, L.M. Yagupolskii, Y.L. Yagupolskii, N.V. Ignatev, N.V. Kondratenko, A.Y. Volkonskii, V.M. Vlasov, R. Notario, P.C. Maria, J. Am. Chem. Soc., 116 (1994) 3047.

[59] R.J. Gorte, Catal. Lett., 62 (1999) 1.
[60] W.E. Farneth, R.J. Gorte, Chem. Rev., 95 (1995) 615.
[61] D.J. Parrillo, C. Lee, R.J. Gorte, Appl. Catal. A, 110 (1994) 67.
[62] D.J. Parrillo, R.J. Gorte, J. Phys. Chem., 97 (1993) 8786.
[63] D. Barthomeuf, Mater. Chem. Phys., 17 (1987) 49.
[64] L.A. Pine, P.J. Maher, W.A. Wachter, J. Catal., 85 (1984) 466.
[65] D. Freude, M. Hunger, H. Pfeifer, W. Schwieger, Chem. Phys. Lett., 128 (1986) 62.
[66] J. Sauer, K.P. Schroder, V. Termath, Collect. Czech. Chem. Commun., 63 (1998) 1394.
[67] S. Bordiga, L. Regli, D. Cocina, C. Lamberti, M. Bjørgen, K.P. Lillerud, J. Phys. Chem. B, 109 (2005) 2779.
[68] R. Shah, J. D. Gale, M. C. Payne, Chem. Commun., (1997) 131.
[69] J. Chen, P.A. Wright, J.M. Thomas, S. Natarajan, L. Marchese, S.M. Bradley, G. Sankar, C.R.A. Catlow, P.L. Gai-Boyes, J. Phys. Chem., 98 (1994) 10216.
[70] D.M. Marcus, W. Song, L.L. Ng, J.F. Haw, Langmuir, 18 (2002) 8386.
[71] M. Zokaie, U. Olsbye, K.P. Lillerud, O. Swang, J. Phys. Chem. C, 116 (2012) 7255.
[72] D. Barthomeuf, in: J. Fraissard, L. Petrakis (Eds.) Acidity and Basicity of Solids: Theory, Assessment and Utility, Kluwer Academic Publ, Dordrecht, 1994, pp. 375.
[73] J.A. Martens, P.J. Grobet, P.A. Jacobs, J. Catal., 126 (1990) 299.
[74] L. Rodriguez-Gonzalez, F. Hermes, M. Bertmer, E. Rodriguez-Castellon, A. Jimenez-Lopez, U. Simon, Appl. Catal. A, 328 (2007) 174.
[75] M.V. Juskelis, J.P. Slanga, T.G. Roberie, A.W. Peters, J. Catal., 138 (1992) 391.
[76] A.I. Biaglow, A.T. Adamo, G.T. Kokotailo, R.J. Gorte, J. Catal., 131 (1991) 252.
[77] R.J. Gorte, Catal. Today, 28 (1996) 405.
[78] J.A. Lercher, A. Jentys, in: J. Čejka, H. van Bekkum, A. Corma, F. Schüth (Eds.) Introduction to Zeolite Science and Practice, Elsevier, Amsterdam, 2007, pp. 435.
[79] C.A. Emeis, J. Catal., 141 (1993) 347.
[80] E. Selli, L. Forni, Microporous Mesoporous Mater., 31 (1999) 129.
[81] F. Thibault-Starzyk, B. Gil, S. Aiello, T. Chevreau, J.-P. Gilson, Microporous Mesoporous Mater., 67 (2004) 107.
[82] B. Louis, S. Walspurger, J. Sommer, Catal. Lett., 93 (2004) 81.
[83] O. Kresnawahjuesa, R.J. Gorte, D. de Oliveira, L.Y. Lau, Catal. Lett., 82 (2002) 155.
[84] C. Pereira, R.J. Gorte, Appl. Catal. A, 90 (1992) 145.
[85] A. Zecchina, G. Spoto, S. Bordiga, Phys. Chem. Chem. Phys., 7 (2005) 1627.
[86] K. Chakarova, K. Hadjiivanov, J. Phys. Chem. C, 115 (2011) 4806.
[87] J.M. Bennett, J.P. Cohen, E.M. Flanigen, J.J. Pluth, J.V. Smith, ACS Symp. Ser., 218 (1983) 109.
[88] R.A. Van Nordstrand, D.S. Santilli, S.I. Zones, ACS Symp. Ser., 368 (1988) 236.
[89] S.I. Zones, L.T. Yuen, Y. Nakagawa, R.A. Van Nordstrand, S.D. Toto, Proc. 9th Int. Zeolite Conf., (1993) 163.
[90] R.F. Lobo, M.E. Davis, Microporous Mater., 3 (1994) 61.

[91] J.L. Schlenker, W.J. Rohrbaugh, P. Chu, E.W. Valyocsik, G.T. Kokotailo, Zeolites, 5 (1985) 355.
[92] C.D. Chang, A.J. Silvestri, J. Catal., 47 (1977) 249.
[93] S.L. Meisel, J.P. Mccullough, C.H. Lechthaler, P.B. Weisz, Chem. Tech., 6 (1976) 86.
[94] F.J. Keil, Microporous Mesoporous Mater., 29 (1999) 49.
[95] S. Kvisle, T. Fuglerud, S. Kolboe, U. Olsbye, K.P. Lillerud, B.V. Vora, in: Handbook of Heterogeneous Catalysis, Wiley-VCH Verlag GmbH & Co. KGaA, 2008.
[96] C.D. Chang, Catal. Rev. Sci. Eng., 25 (1983) 1.
[97] C.D. Chang, Catal. Today, 13 (1992) 103.
[98] J. Topp-Jørgensen, Stud. Surf. Sci. Catal., 36 (1988) 293.
[99] H.R. Grimmer, N. Thiagarajan, E. Nitschke, Stud. Surf. Sci. Catal., 36 (1988) 273.
[100] A.A. Avidan, Stud. Surf. Sci. Catal., 36 (1988) 307.
[101] H. Koempel, W. Liebner, Stud. Surf. Sci. Catal., 167 (2007) 261.
[102] B.V. Vora, T.L. Marker, P.T. Barger, H.R. Nilsen, S. Kvisle, T. Fuglerud, Stud. Surf. Sci. Catal., 107 (1997) 87.
[103] J.F. Haw, W.G. Song, D.M. Marcus, J.B. Nicholas, Acc. Chem. Res., 36 (2003) 317.
[104] M. Stöcker, Microporous Mesoporous Mater., 29 (1999) 3.
[105] U. Olsbye, S. Svelle, M. Bjørgen, P. Beato, T.V.W. Janssens, F. Joensen, S. Bordiga, K.P. Lillerud, Angew. Chem. Int. Ed., 51 (2012) 5810.
[106] K. Hemelsoet, J. Van der Mynsbrugge, K. De Wispelaere, M. Waroquier, V. Van Speybroeck, ChemPhysChem, 14 (2013) 1526.
[107] S. Ilias, A. Bhan, ACS Catal., 3 (2013) 18.
[108] N.Y. Chen, W.J. Reagan, J. Catal., 59 (1979) 123.
[109] W.G. Song, D.M. Marcus, H. Fu, J.O. Ehresmann, J.F. Haw, J. Am. Chem. Soc., 124 (2002) 3844.
[110] D. Lesthaeghe, V. Van Speybroeck, G.B. Marin, M. Waroquier, Angew. Chem. Int. Ed., 45 (2006) 1714.
[111] D. Lesthaeghe, V. Van Speybroeck, G.B. Marin, M. Waroquier, Ind. Eng. Chem. Res., 46 (2007) 8832.
[112] D.M. Marcus, K.A. McLachlan, M.A. Wildman, J.O. Ehresmann, P.W. Kletnieks, J.F. Haw, Angew. Chem. Int. Ed., 45 (2006) 3133.
[113] I.M. Dahl, S. Kolboe, J. Catal., 161 (1996) 304.
[114] I.M. Dahl, S. Kolboe, Catal. Lett., 20 (1993) 329.
[115] I.M. Dahl, S. Kolboe, J. Catal., 149 (1994) 458.
[116] R.M. Dessau, R.B. Lapierre, J. Catal., 78 (1982) 136.
[117] R.M. Dessau, J. Catal., 99 (1986) 111.
[118] M. Bjørgen, S. Svelle, F. Joensen, J. Nerlov, S. Kolboe, F. Bonino, L. Palumbo, S. Bordiga, U. Olsbye, J. Catal., 249 (2007) 195.
[119] S. Svelle, F. Joensen, J. Nerlov, U. Olsbye, K.-P. Lillerud, S. Kolboe, M. Bjørgen, J. Am. Chem. Soc., 128 (2006) 14770.

[120] Ø. Mikkelsen, P.O. Rønning, S. Kolboe, Microporous Mesoporous Mater., 40 (2000) 95.
[121] B. Arstad, S. Kolboe, J. Am. Chem. Soc., 123 (2001) 8137.
[122] S. Svelle, U. Olsbye, F. Joensen, M. Bjørgen, J. Phys. Chem. C, 111 (2007) 17981.
[123] B. Arstad, S. Kolboe, Catal. Lett., 71 (2001) 209.
[124] B.E. Langner, Appl. Catal., 2 (1982) 289.
[125] R.F. Sullivan, C.J. Egan, G.E. Langlois, R.P. Sieg, J. Am. Chem. Soc., 83 (1961) 1156.
[126] T. Mole, G. Bett, D. Seddon, J. Catal., 84 (1983) 435.
[127] T. Mole, J.A. Whiteside, D. Seddon, J. Catal., 82 (1983) 261.
[128] P.W. Goguen, T. Xu, D.H. Barich, T.W. Skloss, W. Song, Z. Wang, J.B. Nicholas, J.F. Haw, J. Am. Chem. Soc., 120 (1998) 2650.
[129] J.F. Haw, P.W. Goguen, T. Xu, T.W. Skloss, W. Song, Z. Wang, Angew. Chem. Int. Ed., 37 (1998) 948.
[130] J.F. Haw, J.B. Nicholas, W. Song, F. Deng, Z. Wang, T. Xu, C.S. Heneghan, J. Am. Chem. Soc., 122 (2000) 4763.
[131] T. Xu, D.H. Barich, P.W. Goguen, W. Song, Z. Wang, J.B. Nicholas, J.F. Haw, J. Am. Chem. Soc., 120 (1998) 4025.
[132] W.G. Song, J.F. Haw, J.B. Nicholas, C.S. Heneghan, J. Am. Chem. Soc., 122 (2000) 10726.
[133] M. Hunger, M. Seiler, A. Buchholz, Catal. Lett., 74 (2001) 61.
[134] M. Seiler, U. Schenk, M. Hunger, Catal. Lett., 62 (1999) 139.
[135] M. Seiler, W. Wang, A. Buchholz, M. Hunger, Catal. Lett., 88 (2003) 187.
[136] M. Bjørgen, U. Olsbye, D. Petersen, S. Kolboe, J. Catal., 221 (2004) 1.
[137] A. Sassi, M.A. Wildman, H.J. Ahn, P. Prasad, J.B. Nicholas, J.F. Haw, J. Phys. Chem. B, 106 (2002) 2294.
[138] M. Bjørgen, F. Joensen, K.-P. Lillerud, U. Olsbye, S. Svelle, Catal. Today, 142 (2009) 90.
[139] W. Song, H. Fu, J.F. Haw, J. Am. Chem. Soc., 123 (2001) 4749.
[140] B.P.C. Hereijgers, F. Bleken, M.H. Nilsen, S. Svelle, K.P. Lillerud, M. Bjørgen, B.M. Weckhuysen, U. Olsbye, J. Catal., 264 (2009) 77.
[141] M. Bjørgen, S. Akyalcin, U. Olsbye, S. Benard, S. Kolboe, S. Svelle, J. Catal., 275 (2010) 170.
[142] J.H. Ahn, B. Temel, E. Iglesia, Angew. Chem. Int. Ed., 48 (2009) 3814.
[143] D.A. Simonetti, J.H. Ahn, E. Iglesia, J. Catal., 277 (2011) 173.
[144] S. Teketel, U. Olsbye, K.P. Lillerud, P. Beato, S. Svelle, Microporous Mesoporous Mater., 136 (2010) 33.
[145] S. Teketel, S. Svelle, K.P. Lillerud, U. Olsbye, ChemCatChem, 1 (2009) 78.
[146] D. Kuck, Mass Spectrom. Rev., 9 (1990) 583.
[147] D. Farcasiu, Acc. Chem. Res., 15 (1982) 46.
[148] G.A. Olah, R.H. Schlosberg, R.D. Porter, Y.K. Mo, D.P. Kelly, G.D. Mateescu, J. Am. Chem. Soc., 94 (1972) 2034.

[149] M. Bjørgen, F. Bonino, S. Kolboe, K.-P. Lillerud, A. Zecchina, S. Bordiga, J. Am. Chem. Soc., 125 (2003) 15863.
[150] M. Bjørgen, F. Bonino, B. Arstad, S. Kolboe, K.-P. Lillerud, A. Zecchina, S. Bordiga, ChemPhysChem, 6 (2005) 232.
[151] W.V. Doering, M. Saunders, H.G. Boyton, H.W. Earhart, E.F. Wadley, W.R. Edwards, G. Laber, Tetrahedron, 4 (1958) 178.
[152] O. Sekiguchi, V. Meyer, M.C. Letzel, D. Kuck, E. Uggerud, Eur. J. Mass Spectrom., 15 (2009) 167.
[153] S. Svelle, M. Bjørgen, S. Kolboe, D. Kuck, M. Letzel, U. Olsbye, O. Sekiguchi, E. Uggerud, Catal. Lett., 109 (2006) 25.
[154] B. Arstad, J.B. Nicholas, J.F. Haw, J. Am. Chem. Soc., 126 (2004) 2991.
[155] D.M. McCann, D. Lesthaeghe, P.W. Kletnieks, D.R. Guenther, M.J. Hayman, V. Van Speybroeck, M. Waroquier, J.F. Haw, Angew. Chem. Int. Ed., 47 (2008) 5179.
[156] D. Lesthaeghe, A. Horre, M. Waroquier, G.B. Marin, V. Van Speybroeck, Chem. Eur. J., 15 (2009) 10803.
[157] S. Kolboe, J. Phys. Chem. A, 116 (2012) 3710.
[158] S. Kolboe, S. Svelle, B. Arstad, J. Phys. Chem. A, 113 (2009) 917.
[159] S. Kolboe, J. Phys. Chem. A, 115 (2011) 3106.
[160] K. De Wispelaere, K. Hemelsoet, M. Waroquier, V. Van Speybroeck, J. Catal., 305 (2013) 76.
[161] B. Arstad, S. Kolboe, O. Swang, J. Phys. Org. Chem., 17 (2004) 1023.
[162] B. Arstad, S. Kolboe, O. Swang, J. Phys. Chem. A, 109 (2005) 8914.
[163] B. Arstad, S. Kolboe, O. Swang, J. Phys. Org. Chem., 19 (2006) 81.
[164] S. Svelle, M. Visur, U. Olsbye, S. Saepurahman, M. Bjørgen, Top. Catal., 54 (2011) 897.
[165] S. Svelle, M. Bjørgen, J. Phys. Chem. A, 114 (2010) 12548.
[166] S. Svelle, S. Kolboe, O. Swang, U. Olsbye, J. Phys. Chem. B, 109 (2005) 12874.
[167] I.I. Ivanova, A. Corma, J. Phys. Chem. B, 101 (1997) 547.
[168] R.Y. Brogaard, R. Henry, Y. Schuurman, A.J. Medford, P.G. Moses, P. Beato, S. Svelle, J.K. Nørskov, U. Olsbye, J. Catal., 314 (2014) 159.
[169] P.J. Linstrom, W.G. Mallard (Eds.) NIST Chemistry WebBook, NIST Standard Reference Database Number 69, National Institute of Standards and Technology, Gaithersburg MD, 20899, http://webbook.nist.gov (Accessed 23/05/2014).
[170] S. Svelle, P.O. Rønning, S. Kolboe, J. Catal., 224 (2004) 115.
[171] S. Svelle, P.O. Rønning, U. Olsbye, S. Kolboe, J. Catal., 234 (2005) 385.
[172] I.M. Hill, S.A. Hashimi, A. Bhan, J. Catal., 291 (2012) 155.
[173] I.M. Hill, Y.S. Ng, A. Bhan, ACS Catal., 2 (2012) 1742.
[174] S. Svelle, C. Tuma, X. Rozanska, T. Kerber, J. Sauer, J. Am. Chem. Soc., 131 (2009) 816.
[175] V. Van Speybroeck, J. Van der Mynsbrugge, M. Vandichel, K. Hemelsoet, D. Lesthaeghe, A. Ghysels, G.B. Marin, M. Waroquier, J. Am. Chem. Soc., 133 (2010) 888.
[176] I. Hill, A. Malek, A. Bhan, ACS Catal., 3 (2013) 1992.

[177] J.H. Ahn, R. Kolvenbach, S.S. Al-Khattaf, A. Jentys, J.A. Lercher, ACS Catal., 3 (2013) 817.
[178] B. Arstad, S. Kolboe, O. Swang, J. Phys. Chem. B, 106 (2002) 12722.
[179] J. Van der Mynsbrugge, M. Visur, U. Olsbye, P. Beato, M. Bjørgen, V. Van Speybroeck, S. Svelle, J. Catal., 292 (2012) 201.
[180] S. Saepurahman, M. Visur, U. Olsbye, M. Bjørgen, S. Svelle, Top. Catal., 54 (2011) 1293.
[181] A.M. Vos, K.H.L. Nulens, F. De Proft, R.A. Schoonheydt, P. Geerlings, J. Phys. Chem. B, 106 (2002) 2026.
[182] G. Bourdillon, C. Gueguen, M. Guisnet, Appl. Catal., 61 (1990) 123.
[183] L.-T. Yuen, S.I. Zones, T.V. Harris, E.J. Gallegos, A. Auroux, Microporous Mater., 2 (1994) 105.
[184] F. Bleken, M. Bjørgen, L. Palumbo, S. Bordiga, S. Svelle, K.P. Lillerud, U. Olsbye, Top. Catal., 52 (2009) 218.
[185] J.E. Bercaw, P.L. Diaconescu, R.H. Grubbs, N. Hazari, R.D. Kay, J.A. Labinger, P. Mehrkhodavandi, G.E. Morris, G.J. Sunley, P. Vagner, Inorg. Chem., 46 (2007) 11371.
[186] N. Hazari, J.A. Labinger, V.J. Scott, J. Catal., 263 (2009) 266.
[187] J.E. Bercaw, N. Hazari, J.A. Labinger, V.J. Scott, G.J. Sunley, J. Am. Chem. Soc., 130 (2008) 11988.
[188] D.A. Simonetti, R.T. Carr, E. Iglesia, J. Catal., 285 (2012) 19.
[189] N. Hazari, E. Iglesia, J.A. Labinger, D.A. Simonetti, Acc. Chem. Res., 45 (2012) 653.
[190] J. Macht, R.T. Carr, E. Iglesia, J. Am. Chem. Soc., 131 (2009) 6554.
[191] R.T. Carr, M. Neurock, E. Iglesia, J. Catal., 278 (2011) 78.
[192] C.-M. Wang, R.Y. Brogaard, B.M. Weckhuysen, J.K. Nørskov, F. Studt, J. Phys. Chem. Lett., 5 (2014) 1516.
[193] M. Westgård Erichsen, Master Thesis, Dept. of Chemistry, University of Oslo, 2010.
[194] Y. Kubota, H. Maekawa, S. Miyata, T. Tatsumi, Y. Sugi, Microporous Mesoporous Mater., 101 (2007) 115.
[195] H. Maekawa, Y. Kubota, Y. Sugi, Chem. Lett., 33 (2004) 1126.
[196] D. Cardoso, in: H. Robson (Ed.) Verified Syntheses of Zeolitic Materials, Elsevier, 2001, pp. 118.
[197] Y. Kubota, S. Tawada, K. Nakagawa, C. Naitoh, N. Sugimoto, Y. Fukushima, T. Hanaoka, Y. Imada, Y. Sugi, Microporous Mesoporous Mater., 37 (2000) 291.
[198] M. Bjørgen, U. Olsbye, S. Svelle, S. Kolboe, Catal. Lett., 93 (2004) 37.
[199] C. Sprung, PhD Thesis, Dept. of Chemistry, University of Oslo, 2012.
[200] P.O. Rønning, Dr. Scient Thesis, Dept. of Chemistry, University of Oslo, 1998.
[201] F. Bleken, W. Skistad, K. Barbera, M. Kustova, S. Bordiga, P. Beato, K.P. Lillerud, S. Svelle, U. Olsbye, Phys. Chem. Chem. Phys., 13 (2011) 2539.
[202] S. Teketel, W. Skistad, S. Benard, U. Olsbye, K.P. Lillerud, P. Beato, S. Svelle, ACS Catal., 2 (2012) 26.

[203] R. Ravishankar, D. Bhattacharya, N.E. Jacob, S. Sivasanker, Microporous Mater., 4 (1995) 83.
[204] M.W. Anderson, J. Klinowski, J. Am. Chem. Soc., 112 (1990) 10.
[205] D. Breck, Zeolite molecular Sieves, John Wiley and Sons, New York, 1979.
[206] M.L. Maloncy, L. Gora, J.C. Jansen, T. Maschmeyer, Ars Separatoria Acta, 2 (2003) 18.
[207] O. Mikkelsen, S. Kolboe, Microporous Mesoporous Mater., 29 (1999) 173.
[208] S.L. Lawton, M.E. Leonowicz, R.D. Partridge, P. Chu, M.K. Rubin, Microporous Mesoporous Mater., 23 (1998) 109.
[209] T.V.W. Janssens, J. Catal., 264 (2009) 130.
[210] F.L. Bleken, T.V.W. Janssens, S. Svelle, U. Olsbye, Microporous Mesoporous Mater., 164 (2012) 190.
[211] W. Skistad, S. Teketel, F.L. Bleken, P. Beato, S. Bordiga, M.H. Nilsen, U. Olsbye, S. Svelle, K.P. Lillerud, Top. Catal., 57 (2013) 143.
[212] Z. Li, J. Martinez-Triguero, P. Concepcion, J. Yu, A. Corma, Phys. Chem. Chem. Phys., 15 (2013) 14670.
[213] J.S. Buchanan, J.G. Santiesteban, W.O. Haag, J. Catal., 158 (1996) 279.
[214] S. Teketel, U. Olsbye, P. Beato, K.P. Lillerud, S. Svelle, Manuscript in preparation.
[215] T.V.W. Janssens, S. Svelle, U. Olsbye, J. Catal., 308 (2013) 122.
[216] J. Martinez-Triguero, M.J. Diaz-Cabañas, M.A. Camblor, V. Fornés, T.L.M. Maesen, A. Corma, J. Catal., 182 (1999) 463.
[217] B. Zibrowius, E. Loffler, M. Hunger, Zeolites, 12 (1992) 167.
[218] F. Schuth, D. Demuth, B. Zibrowius, J. Kornatowski, G. Finger, J. Am. Chem. Soc., 116 (1994) 1090.
[219] S.G. Hedge, P. Ratnasamy, L.M. Kustov, V.B. Kazansky, Zeolites, 8 (1988) 137.
[220] J. Chen, P.A. Wright, S. Natarajan, J.M. Thomas, Stud. Surf. Sci. Catal., 84 (1994) 1731.
[221] M. Vandichel, D. Lesthaeghe, J. Van der Mynsbrugge, M. Waroquier, V. Van Speybroeck, J. Catal., 271 (2010) 67.
[222] J. Van der Mynsbrugge, K. Hemelsoet, M. Vandichel, M. Waroquier, V. Van Speybroeck, J. Phys. Chem. C, 116 (2012) 5499.
[223] S.L.C. Moors, K. De Wispelaere, J. Van der Mynsbrugge, M. Waroquier, V. Van Speybroeck, ACS Catal., 3 (2013) 2556.
[224] S. Ilias, A. Bhan, J. Catal., 311 (2014) 6.
[225] L.A. Paquette, G.R. Krow, J.M. Bollinger, G.A. Olah, J. Am. Chem. Soc., 90 (1968) 7147.
[226] R.F. Childs, D.L. Mulholland, J. Am. Chem. Soc., 105 (1983) 96.
[227] E.J. Corey, J. Streith, J. Am. Chem. Soc., 86 (1964) 950.
[228] C.-M. Wang, Y.-D. Wang, H.-X. Liu, Z.-K. Xie, Z.-P. Liu, Microporous Mesoporous Mater., 158 (2012) 264.

Appendix (Papers I-VI)

“H-SAPO-5 as methanol-to-olefins (MTO) model catalyst: Towards elucidating the effects of acid strength”

M. Westgård Erichsen, S. Svelle, U. Olsbye*

Journal of Catalysis, 298 (2013) 94.

I

“The influence of catalyst acid strength on the methanol to hydrocarbons (MTH) reaction”

M. Westgård Erichsen, S. Svelle, U. Olsbye*

Catalysis Today, 215 (2013) 216.

II

“Shape selectivity in zeolite catalysis. The Methanol to Hydrocarbons (MTH) reaction”

S. Teketel, M. Westgård Erichsen, F. Lønstad Bleken, S. Svelle, K. P. Lillerud, U. Olsbye*

Catalysis: Volume 26, The Royal Society of Chemistry, 2014, pp. 179

III

Shape selectivity in zeolite catalysis. The Methanol to Hydrocarbons (MTH) reaction

Shewangizaw Teketel, Marius Westgård Erichsen, Francesca Lønstad Bleken, Stian Svelle, Karl Petter Lillerud and Unni Olsbye*

DOI: 10.1039/9781782620037-00179

Zeolites are crystalline aluminosilicates with pores of molecular dimensions. They are extensively used as catalysts in the chemical industry. Recently, zeolite catalysts have found a new application in the methanol to hydrocarbons (MTH) reaction, which is currently of growing industrial significance, especially for the production of polymer-grade alkenes. In this chapter, the general characteristics of zeolites are summarized, with emphasis on a selection of zeolite structures which are of interest as MTH catalysts. Subsequently, industrial and fundamental aspects of the MTH reaction are reviewed, with emphasis on mechanistic insight. Finally, the selected zeolite structures are compared as catalysts for the MTH reaction, and the influence of product and transition state shape selectivity is discussed.

1 Zeolites

1.1 Material properties

Zeolites are crystalline aluminosilicates with a three-dimensional framework that consists of nanometer-sized channels and cavities, giving a high porosity and a large surface area to the material.[1] The three-dimensional framework of zeolites is constructed from corner-shared tetrahedra (T-atoms) of silicon and aluminum, bridged with oxygen atoms. The dimensions of zeolite channels, channel intersections and/or cavities are typically less than 1 nm. The International Union of Pure and Applied Chemistry (IUPAC) classifies porous materials as mirocoporous, mesoporous and macroporous based on sizes < 2 nm, 2–50 nm and > 50 nm respectively,[2] therefore zeolites are referred to as microporous materials. Figure 1 illustrates examples of selected zeolite structures along with their pore systems. The zeolite pore size is mainly determined by the number of T-atoms defining the entrance (ring-size) to the interior of the crystal, for example in Fig. 1 the pore size of TON (10-ring) is smaller than that of ZSM-12 (12-ring). Accordingly, zeolites are classified as having small, medium, large, and extra-large pore structures for pore windows delimited by 8, 10, 12, and more than 12 T-atoms, respectively.[3] The pores in zeolites can be one-dimensional (Fig. 1, MTW (ZSM-12) and TON (ZSM-22)), two-dimensional (for example MWW (MCM-22)[4]), or three-dimensional (Fig. 1, MFI (ZSM-5) and FAU (Faujasite)). The pore sizes of zeolites are within the range of the

inGAP Centre for Research-based Innovation, Department of Chemistry, University of Oslo, Sem Sælands vei 27, 0315 Oslo, Norway. E-mail: unni.olsbye@kjemi.uio.no

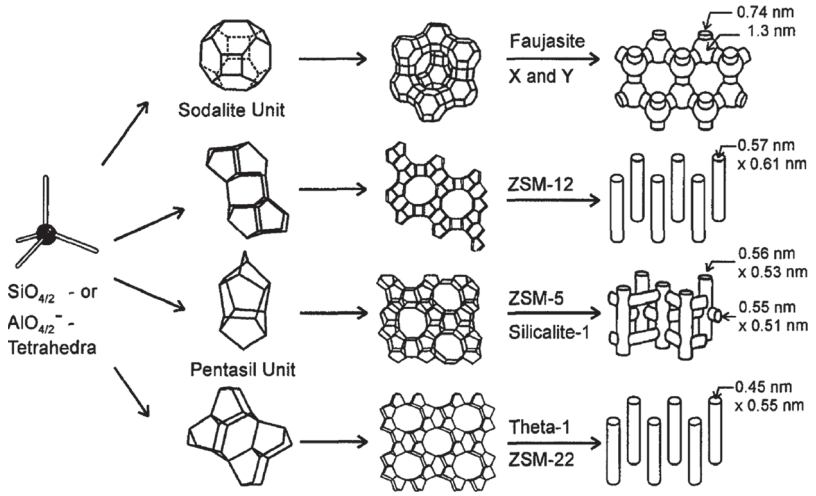

Fig. 1 Structures of zeolites (from top to bottom: faujasite or zeolite X, Y; zeolite ZSM-12; zeolite ZSM-5 or silicalite-1; zeolite TON) and their micropore system. Adapted from Ref. 6.

molecular diameters of many organic compounds, and only molecules with similar or smaller free diameters than the zeolite pores can have access to the interior of the zeolite crystals. Due to such ability to sort molecules based on sizes, zeolites are often described as molecular sieves.[5]

The first naturally occurring zeolite was recognized in 1756 by a Swedish mineralogist, Cronstedt.[5] He named it ''zeolite'' from the Greek words ''zeo'' (boiling) and ''lithos'' (stone) because the new material released large amounts of steam and water upon heating. Currently there are nearly 200 zeolites maintained in the database of the International Zeolite Association (IZA).[4] All zeolite structures are given a three capital letters code, following the rule set by an IUPAC Commission on Zeolite Nomenclature.[7,8] About one fifth of the zeolites in the IZA database are naturally occurring, and the rest are synthetic zeolites made in laboratories. Furthermore, computer prediction of hypothetical zeolites shows several million possible structures, of which 450000 are potentially stable when their calculated lattice energies are compared with those of known zeolite structures.[3] Hypothetical zeolite structures are also maintained in an online database.[9,10]

The synthesis of zeolites is usually carried out under hydrothermal conditions, from sources of silicon, aluminum dissolved in aqueous solution of alkali hydroxide and a structure directing agent (SDA), illustrated in Fig. 2. Zeolites are metastable and the final synthesis product is determined by factors such as the nature and concentration of reactants, and synthesis conditions (temperature, crystallization time, and pH). The hydrothermal synthesis of zeolites is often carried out in an autoclave at elevated temperature and autogenous pressure. Crystallization from solution generally occurs *via* the sequential steps of nucleation of the phase(s), dictated by the composition of the solution, followed by growth of the nuclei to larger sizes by incorporation of solute

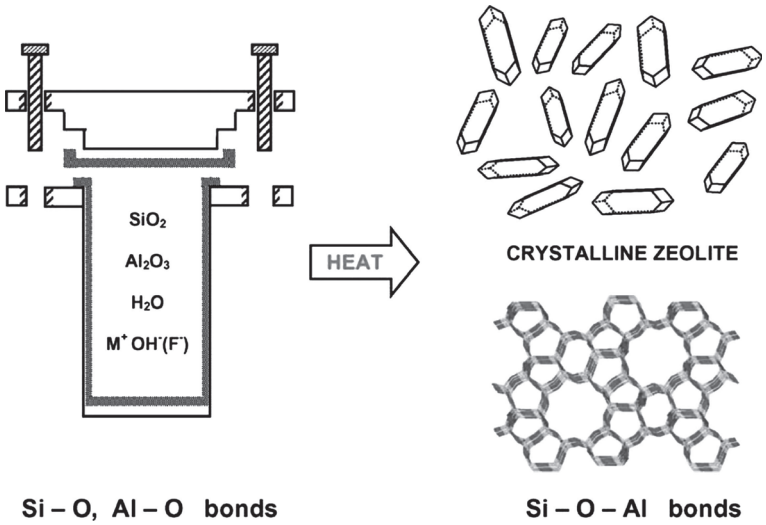

Fig. 2 Illustration of hydrothermal zeolite synthesis. Adapted from Ref. 17.

from the solution.[11] The final crystal size is a function of the ratio between rate of nucleation and rate of growth of the nuclei.[12] The zeolite crystallization process is dependent upon a number of parameters such as: ageing of the synthesis gel,[13] solubility of silicon,[14] crystallization temperature,[15] and addition of seed crystals.[16]

Crystal sizes play important roles in the application of zeolites as catalysts. For example, catalyst effectiveness is larger for smaller crystals, but filtration and recovery of very small crystals can be a practical challenge. On the other hand, deactivation can be more severe, and regeneration of used catalyst can be more difficult for larger crystals.[12]

Zeolites have widespread applications such as catalysts in oil refineries, adsorbents for gas separation, and in ion exchange.[18–21] However considering market values, the catalytic application of zeolites is the most important.[22] The possibility of generating functionality within the zeolite pores by introducing heteroatoms into the framework and/or extra framework make them attractive for a wide range of applications. Such functionality may have acid, base, redox or bifunctional properties, and act as an active site to catalyze numerous reactions.[23]

The name zeolite is restricted to frameworks constructed from silicon and aluminum as central atoms (T-atoms). There are other zeotype materials with structures similar to zeolites, but different types of T-atoms. Examples of such zeotype materials are: SAPO (in which the T-atoms are Si, Al, and P), $AlPO_4$ (in which the T-atoms are Al, and P), MeAPO (in which the T-atoms are metal cations (Me), Al, and P), and MeSAPO (in which the T-atoms are metal cations, Si, Al, and P).

Zeolites and zeotype materials can be distinguished from denser materials of similar type based on their framework density (FD), the number of T-atoms per 1000 $Å^3$. For zeolites and zeotype materials, values in the range of 12.1 T-atoms up to around 20.6 T-atoms per 1000 $Å^3$ are observed, while dense materials have at least 20 T-atoms per 1000 $Å^3$.[7]

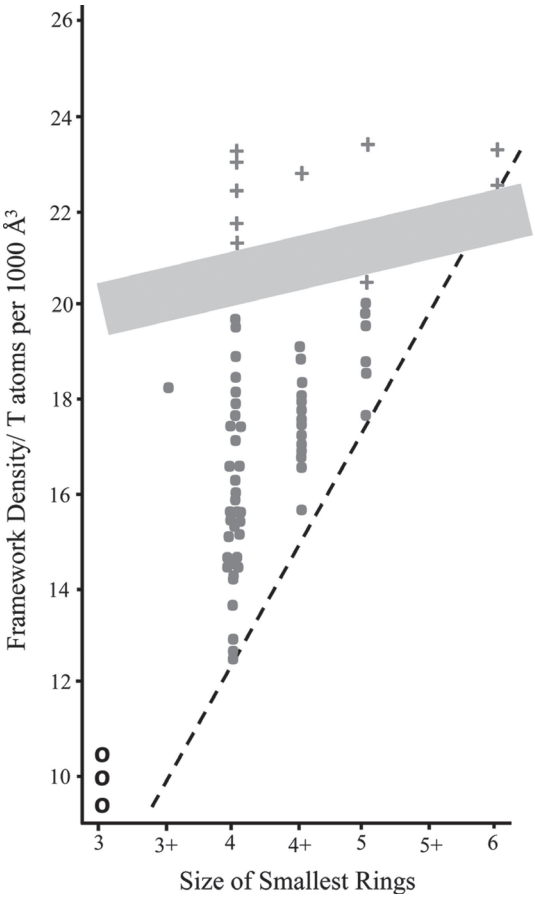

Fig. 3 Distribution of framework density (FD) versus size of smallest ring in the framework. Framework types: a) + dense framework; ● zeolite; **o** hypothetical. Adapted from Ref. 3, similar figures can be found in Refs. 7, 24.

Figure 3 displays a distribution of framework density versus size of the smallest ring in the framework. The range of the observed FD values depends on the type and relative number of the smallest rings in the tetrahedral networks, and the frameworks of the lowest density are those with a maximum number of 3-rings.[24,25] A gap in FD values is observed between zeolites and denser frameworks.

1.2 Zeolites as acid catalysts

The first use of zeolites as acid catalysts goes back to 1959 when zeolite Y was used as an isomerization catalyst by Union Carbide. In 1962, incorporation of relatively small amounts of zeolite X as a promoter greatly improved the performance of silica/alumina- or silica/clay-based catalysts for petroleum cracking (*i.e.* the production of petrol from crude oil).[5] The application of acid zeolites within refineries has been responsible for the huge amount of money and time that has been invested in zeolite research. To this day, zeolites remain inevitable in hydrocarbon conversion reactions in oil refineries as shape selective catalysts.[23,26] One

third of all gasoline utilized today is produced *via* zeolite-based catalytic cracking of vacuum gas oil and similar heavy feedstocks.[27,28]

The *acidity* of zeolites and zeotypes is a perhaps surprisingly complex issue. Acidity may refer to the type of acid site, the density and distribution of these sites, as well as the acid strength of each individual acid site. Moreover, it should be realized that these properties are interdependent. It is well beyond the scope of this chapter to treat these issues in detail. However, a brief account will be given.

A zeolite framework constructed from silicon and oxygen atoms only is neutral, but replacing a tetravalent Si atom with a trivalent Al atom creates a negative charge on the framework, which must be neutralised by an ion-exchangable cation such as K^+, Na^+, NH_4^+ *etc.* that resides inside zeolites pores. If these cations are ion exchanged with protons, strong Brønsted acidic sites are formed within the zeolite framework, as illustrated in Fig. 4.[29] In silicoaluminophosphates (SAPOs) the substitution of framework P(V) by Si(IV) will give rise to a corresponding Brønsted acid site.

Protonated zeolites were previously considered as superacids, but later studies have shown that the sites are weaker than 100% sulfuric acid, which is the measure of superacidity.[30] The precise acid strength of the Brønsted sites depends on (at least) the nature of the substitutional defect, the material topology, and the framework composition. It is known that for zeolites other trivalent cations from elements such as Ga, B, and Fe may be incorporated in the framework, and this typically gives rise to lower acidic strength,[31] or no strong acidity at all.[32] Generally, SAPOs show a lower Brønsted acid strength than the corresponding zeolites.[33–35] Among the aluminosilicate zeolites, topological effects have been investigated, showing that H-ZSM-5 (MFI), H-mordenite (MOR), and H-beta (BEA) display similar acid strength, whereas a significantly lower acid strength was found for H-Y (FAU).[36]

The density of acid sites may, as a first approximation, be assumed to be directly related to framework composition, *i.e.* to the number or density of (*e.g.*) Al substitutions for aluminosilicates. In a key publication, Haag and Chen showed that the cracking activity was linearly dependent of the Al content.[37] Nevertheless, it has been speculated that the density of acid sites may influence the acid strength of individual acid sites, through some form of cooperative action.[38–40] Obviously, given a sufficiently high density of acid sites, the idea of an isolated Brønsted site becomes irrelevant, and the effect

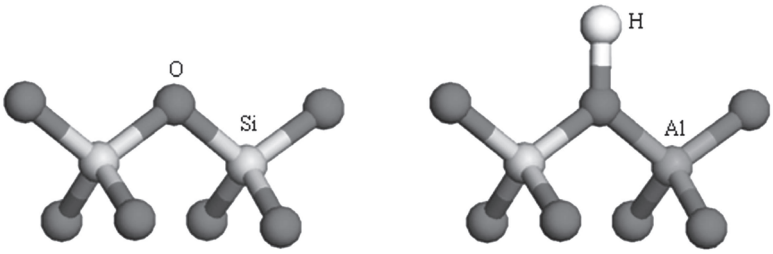

Fig. 4 Illustration of Brønsted acid site in zeolite.

appears only for very high Al contents.[41] Very clearly, the density of acid sites will in many cases affect reaction selectivity.

It is also well known that zeolites may possess Lewis sites within the micropores, which will inevitably affect the catalytic properties of the zeolite. Such active sites are believed to be associated with extra-framework Al species. The exact structure of these extra-framework Al species remains elusive, but many proposals exist.[42] Reasonably, Lewis acid sites are more prominent in high Al materials or zeolites subjected to steam and/or thermal treatments.

A wide variety of techniques exist for the characterization of zeolite and zeotype acidity. Again, a detailed treatise is beyond the present scope, and the interested reader is referred to several more specialized reviews.[41,43,44] Temperature programmed desorption of basic probe molecules, *e.g.* ammonia, is a common and experimentally straightforward technique, which provides a quantitative measure of acid site density. Information regarding acid site strength or type is often attempted, inferred from the temperature of the desorption maximum. However, it is the opinion of the authors that such considerations provide limited information, in particular when comparing widely different catalyst samples, due to complications arising from differences in diffusivities. Such experiments are also sensitive to the exact experimental protocol (heating rates, *etc.*). Catalytic test reactions, such as cracking of hexane, may constitute an indirect measure of the accessible acidity. This is of course information of great practical value. However, the interpretation of measurements of catalyst performance in what might seemingly be a simple reaction is easily complicated by the complex nature of the hydrocarbon chemistry involved.[41] Spectroscopic methods, in particular FTIR in combination with probe molecules interacting with the zeolite/zeotype surface sites, can provide both quantitative and qualitative information. FTIR with pyridine allows quantification of the density of both Brønsted and Lewis acid sites in a relatively straightforward experiment.[44] Assessment of acid site strength is best measured using more weakly interacting probes, where complete proton transfer does not occur. Molecular probes like CO and H_2 are preferred for probing surface sites.[36,43]

In summary, we reiterate that zeolite or zeotype acidity is an issue with many facets. A thorough discussion of the topic requires distinction between acid site strength, density, and type. Site accessibility constitutes another complicating factor. As always, a complete description can be obtained only by the combination of several complementary characterization techniques, some of which are outlined above.

Shape selectivity: One of the most important applications of zeolites is shape selective catalysis. The concept of shape selectivity in zeolite catalysis was introduced in the 1950s: the chemical transformation of molecules depends on the space available inside the zeolite pores.[1]

Shape selectivity in zeolites is described on the basis of mass transport limitations or transition state control of reactions.

- *Reactant shape selectivity* (Fig. 5a) is encountered when bulkier molecules in a reactant mixture are prevented from reaching the active

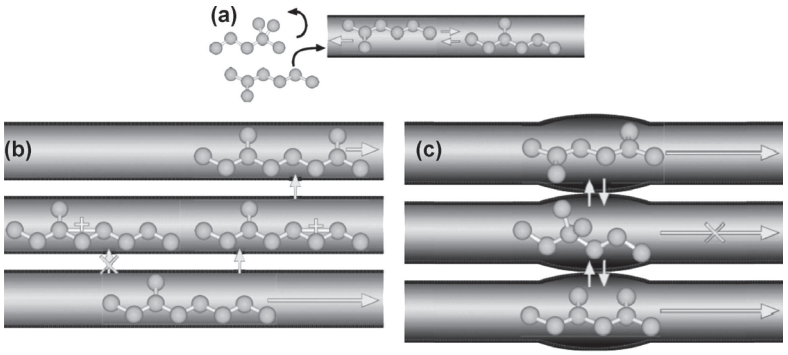

Fig. 5 Illustration of zeolite shape selectivity a) reactant selectivity, b) restricted transition state selectivity and c) product selectivity. Adopted from Ref. 1.

sites within the zeolite crystal.[45] Only molecules that are small enough to enter the pore openings of the zeolite can be converted at the active sites.

- *Restricted transition state selectivity* (Fig. 5b) is encountered in chemical reactions that involve transition states which are too bulky to be accommodated inside the zeolite pores.[46] In this case, products are formed only from reactions with intermediates small enough to fit inside the pores of the zeolite. In restricted transition state selectivity, neither reactants nor potential products are hindered from diffusing in or out of the zeolite crystal.[46]
- *Product shape selectivity* (Fig. 5c) is encountered when certain product molecules are too big to diffuse intact out of the zeolite pores.[45] Some zeolite structures have cavities which allow formation of both small and bulky products. However, the apertures are small, and the bulky product molecules must undergo further reactions to smaller molecules in order to leave the zeolite crystal.

In general, both reactant and product shape selectivities occur due to mass transfer limitations. In reactant shape selectivity all molecules that diffuse to and from the active sites sufficiently fast will be converted, while in product shape selectivity molecules with high mass transport limitations remain in the adsorbed phase and continue to react for a longer period of time than species less affected by mass transfer limitations. Therefore, both reactant and product shape selectivities are affected by crystal sizes, whereas restricted transition state selectivity, which is not caused by mass transfer limitations, does not depend on crystal size.[46]

In brief, shape selective catalysis may contribute to limiting byproduct formation and thus can make processes more environmentally friendly and more cost-effective.[46]

1.3 Catalysts described in this work

In this Section, shape selectivity will be illustrated by a selection of small (8-ring), medium (10-ring) and large (12-ring) pore zeolites. Table 1 presents a list of those materials with a description of their pore systems.

The pore systems of the zeolites are further illustrated in Figs. 6–9. In these figures the framework is removed and only the channel structure

Table 1 List and descriptions of zeolite structures discussed in this chapter.

Material	Dimensionaliaty	Largest channel dimension (Å)[4]	Cross section of channel (Å)²**	Channel size
CHA (SSZ-13)	3D	3.8 × 3.8	11.3	8-ring
EUO (EU-1)	1D	5.4 × 4.1	17.7	10-ring
MWW (MCM-22)	2D	5.5 × 4.0	17.7	10-ring
MTT (ZSM-23)	1D	5.2 × 4.5	18.4	10-ring
TON (ZSM-22)	1D	5.7 × 4.6	20.8	10-ring
MEL (ZSM-11)	3D	5.4 × 5.3	22.4	10-ring
MFI (ZSM-5)	3D	5.6 × 5.3	23.3	10-ring
IMF (IM-5)	3D	5.6 × 5.5	24.1	10-ring
TUN (TNU-9)	3D	6.0 × 5.2	24.5	10-ring
MOR (Mordenite)	1D	7.0 × 6.5	35.7	12-ring
*BEA (Beta)	3D	7.7 × 6.6	40.1	12-ring
AFI (SSZ-24)	1D	7.3 × 7.3	41.8	12-ring

*Disordered structures
**Cross-section calculated from the two perpendicular diameters of the largest channel, assuming it to be perfectly elliptical.

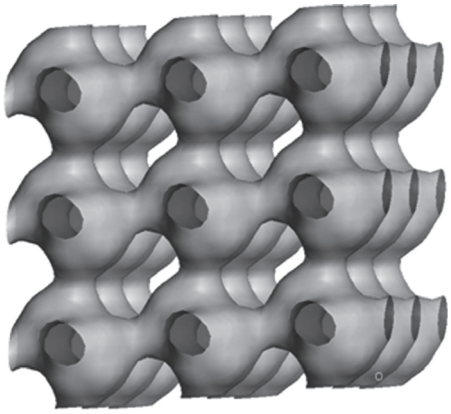

Fig. 6 Illustration of the pore system in CHA zeolite.

shown. The blue (dark) color represents the accessible space inside the pores, while the grey (light) color represents the outer limits of the pores. The channel (pore) sizes described in this section are based on atomic coordinates of the *Type material* and an oxygen radius of 1.35 Å, as described by Meier *et al.*[7] The crystallographic free diameters of the channels (interatomic distance vectors) are presented in Ångstrom (10^{-10} meter) units.

Figure 6 displays the pore system of the CHA structure. It consists of large cavities with 7.3 Å × 12 Å dimensions that are connected by 8-ring windows of 3.8 × 3.8 Å dimensions.[4]

Figure 7 displays displays pore system of the one-dimensional 10 ring zeolites, TON, MTT and EU-1, and two-dimensional zeolite MWW. The 10-ring channels of TON are elliptical and slightly zigzag in shape, and have dimensions 5.7 × 4.6 Å.[4,7] MTT has tear-drop shaped 10-ring channels

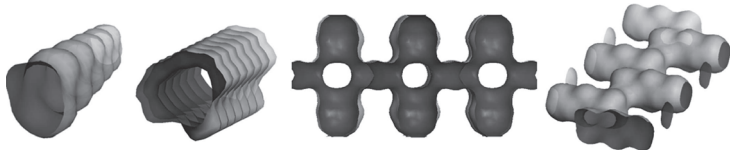

Fig. 7 Illustration of the pore system in a) TON b) MTT c) MWW and d) EUO zeolites.

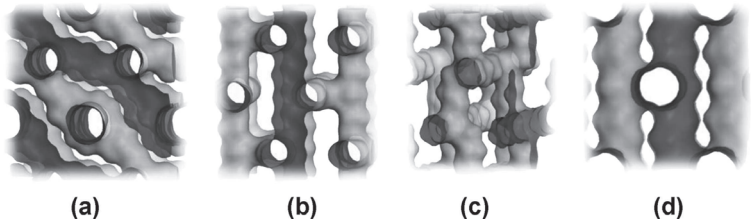

Fig. 8 Illustration of the pore systems in a) TUN, b) IMF, c) MFI and d) MEL zeolites.

measuring 5.2×4.5 Å.[4] MTT and EUO zeolites have 10-ring channels slightly narrower than the pores in TON. However unlike TON, these zeolites contain very large 12-ring pore extensions (12-ring side pockets).[4]

Figure 8 displays the pore systems of three-dimensional 10-ring zeolites TUN, IMF, MFI and MEL. TUN consists of two differently sized channel systems with channel dimensions 6.0×5.2 Å and 5.4×5.5 Å, respectively. The smaller channels have full 2D connectivity and the bigger channels provide connections between these 2-dimensional sheets, thus forming a 3D channel system. The TUN topology consists of large intersections where one of the 10-rings is expanded to a 12-ring. IMF is a 10-ring zeolite consisting of two interconnected 2D channel systems, thus providing limited 3D connectivity. The larger 2D channel system has channel diameters 5.5×5.6 Å and 5.3×5.4 Å, and the smaller one has channel diameters 4.8×5.4 Å and 5.1×5.3 Å. These two channel systems are connected by a channel with diameter 5.3×5.9 Å. A side pocket in one of the channels leads to an extended channel intersection volume. Slabs of three 2D channel systems are separated by a dense framework, thus forming limited 3-dimensionality. MFI has a pore system made from interconnecting straight and sinusoidal 10-ring channels. The straight and sinusoidal channels have dimensions 5.1×5.5 Å and 5.3×5.6 Å respectively. MEL has channels with diameter 5.3×5.4 Å in two directions, and 3-dimensionality is created at the interface between two perpendicular, slightly shifted straight channels.

Figure 9 displays the pore systems of 12-ring zeolites, AFI, MOR and BEA. AFI has a cylindrical straight one-dimensional pore system. MOR is a one-dimensional 12-ring zeolite. The material has 8-ring pores limited by apertures of 5.7×2.6 Å between the 12-ring channels. In practice, these 8-rings are not accessible to diffusion species, and the channel structure is best described as a one-dimensional 12-ring channel with side pockets. BEA is a disordered three-dimensional large pore zeolite consisting of 12-ring pores of dimensions 7.3×7.1 Å and 5.6×5.6 Å.[4]

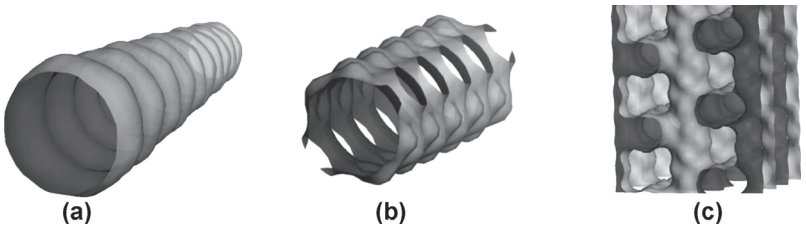

Fig. 9 Illustration of the pore systems in a) AFI, b) MOR and c) BEA zeolites.

Table 2 Density and strength of acid sites in zeolite catalysts reported in this contribution.

Topology (Material)	Dimensionality/ ring size	Si/Al ratio	$\Delta\nu$(OH) (cm^{-1}) upon CO adsorption	Reference
CHA (SSZ-13)	3D/8 ring	12	314	47
TON (ZSM-22)	1D/10 ring	~30	320	48
MEL (ZSM-11)	3D/10 ring	~20	328	49
IMF (IM-5)	3D/10 ring	~20	328	49
MFI (ZSM-5)	3D/10 ring	~20	328	49
TUN (TNU-9)	3D/10 ring	~20	328	49
MOR (Mordenite)	1D/12 ring	22	332[a]	50
BEA (Beta)	3D/12 ring	19	319[b]	36
AFI (SSZ-24)	1D/12 ring	35	316	51

[a]Data from literature, using a material with Si/Al = 18.
[b]Data from literature, using a material with Si/Al = 12.5.

1.3.1 Acid properties. In this work, the O-H stretch frequency of selected materials was monitored by FTIR before and after adsorption of a small, weakly basic probe, CO. The measured change in the O-H stretch frequency upon CO adsorption at −196 °C was used as a measure of the acid strength and is reported in Table 2.

2 The Methanol to Hydrocarbons (MTH) reaction

The global demand for energy and petrochemical products is increasing and it is forecasted that crude oil reservoirs will soon be insufficient to meet the increasing demand. This situation calls for both alternative and supplementary carbon sources to supply the planet with fuels and chemicals in the future. Alternative carbon sources such as coal, natural gas, petrochemical residue, agricultural wastes, municipal garbage and wood *etc.* are believed to be successors of the depleting crude oil in the future.[46] Even CO_2 is considered to be a future carbon source.[52,53] Methanol is a highly relevant chemical intermediate in this respect, because it may be produced from practically any of the carbon sources mentioned above. The conversion of methanol to hydrocarbons (MTH) constitutes the final step in one conversion route of such alternative sources to value added products.

2.1 Historical development

The catalytic conversion of methanol to hydrocarbons (MTH) was fortuitously discovered by Mobil in the 1970s.[54] Researchers at Mobil

were aiming to discover new ways of making high octane gasoline from methanol and isobutane over ZSM-5.[55,56] They imagined that methanol would be added to isobutane to form highly branched higher alkanes. Instead, a wide range of hydrocarbons were formed from methanol even when the isobutane feed was cut. Shortly after the discovery, bench-scale and pilot-scale demonstration plants were constructed. Since then the MTH chemistry has been studied for decades over several zeolite and zeotype materials. Depending on the catalyst topology and process conditions used, a wide range of products can be obtained from the MTH reaction.[57] Commercial or near-commercial processes such as methanol to olefins (MTO); methanol to gasoline (MTG); and methanol to propene (MTP) have been developed.[58]

- *The methanol to gasoline (MTG) process* is catalyzed using the medium pore zeolite, ZSM-5, with MFI topology. In this process methanol is converted to mainly gasoline range hydrocarbons (C_5+). The first MTG plant was built and commercialized in New Zealand by Mobil in 1985, with a production of 14500 barrels per day (about 30% of the country's need) of gasoline. Later as oil prices decreased the MTG section of the unit was shut down, and only the methanol production part from natural gas remained in operation.[59–61]
- *The methanol to olefins (MTO) process* is catalyzed using a small-pore zeotype material, SAPO-34, with CHA topology. In this process methanol is converted to light alkenes, mainly ethene and propene. The narrow pores of the material restrict diffusion of large hydrocarbons.[62] The Advanced MTO process combines the UOP/Hydro MTO process with Total's olefins cracking process.[47]
- *The methanol to propene (MTP) process* is catalyzed using ZSM-5 (MFI) catalyst. In this case, methanol is converted to propene with some by-product gasoline and LPG-type fuels. The selectivity of the process is optimized towards propene by high temperature and low pressure employed during the reaction, as well as recycling of the heavier hydrocarbons. The process was developed by Lurgi.[63]

In a later development of Mobil's MTG technology, light alkenes produced during gasoline production are further converted to higher hydrocarbons through another ZSM-5- (MFI-) based process: Mobil's olefin-to-gasoline and distillate process (MOGD). In the MOGD reaction, ZSM-5 (MFI) oligomerises light alkenes into higher-molecular-weight alkenes that fall into the gasoline, distillate and lubricant range.[58,64]

Table 3 presents an overview of the industrial-scale process developments and new licensing agreements for the MTH reaction.

As seen from Table 3, there has been an increased interest in the commercialization of the MTH process during the last five years. This illustrates the vital importance of the process at the current time as well as in the near future.

2.2 Reaction mechanism

Since the discovery of the MTH reaction by Mobil, researchers have been working on reaction mechanism investigations. The early MTH

Table 3 An overview of MTH process development.

Year	Developed by	Process	Statues
1981–1984	Mobil	MTG	Demonstrated on a 4 b/d plant in Paulsboro, NJ, USA.[65]
1981–1984	Mobil	MTG	Demonstrated on a 100 b/d plant in Wesseling, Germany.[66]
1985	Mobil	MTG	Commercialized in New Zealand (14500 b/d).[59]
1980s	Haldor Topsøe	TIGAS[b]	A demonstration plant developed based on ZSM-5 (1 t/d).[67]
2009	Shanxi Coal Institute	MTG	A demonstration plant brought on stream in Shanxi, province, China (100 kt/y).[47]
2009	UOP/INEOS and Total OCP[a]	MTO	A semi-commercial demonstration unit built in Feluy, Belgium (10 t/d).[68]
2010	CAC Chemnitz	STF	Currently in a demonstration phase syngas-to-fuel unit, developed in Germany.[69]
2010	Haldor Topsøe	TIGAS	Currently being demonstrated in Des Plaines, USA, where a wood gasifier is running.[70]
2010	Dalian Institute for Chemical Physics	DMTO[c]	A plant based on SAPO-34 started in Baotou, China (600 kt/y).[47]
2010	Lurgi	MTP	First plant started in China (500 kt/y propene and 185 kt/y gasoline).[47]
2011	UOP	Advanced MTO	Construction of a plant in Nanjing, China announced (295 kt/y).[47]
2012	ExxonMobil	MTG	Announced a licensing agreement with Sundrop Fuels Inc. (3,500 b/d).[71]
2012	UOP	Advanced MTO	Announced a licensing agreement with China's Jiutai Energy (Zhungeer) Co. Ltd. (600 kt/y).[72]
2012	UOP	Advanced MTO	Announced a licencing agreement with Shandong Yangmei Hengtong Chemicals Co. Ltd. (295 kt/y)[73]
2013	UOP	Advanced MTO	Announced a licensing agreement with Jiangsu Sailboat Co. Ltd. (833 kt/y)[73]

[a]Olefin cracking process.
[b]Topsøe integrated gasoline synthesis process.
[c]Dalian methanol to olefins.

mechanistic works were devoted to direct formation of carbon-carbon bonds from C_1 units (methanol or dimethyl ether), and several mechanisms were proposed.[47] However, high energy barriers are involved in the direct coupling of C_1 units, and the proposed mechanisms lack experimental evidence.[47] Already in 1979, Chen and Reagan suggested that the MTH reaction was autocatalytic.[74] 20 years later, Song *et al.* performed the MTH reaction using extremely purified reagents and reported a dramatic decrease in the initial rate of methanol conversion.[75] It was suggested from the observation that the rate at which the direct C_1–C_1 coupling operates is irrelevant compared to the rate at which trace impurities of C_{2+} compounds initiate the reaction. Recent theoretical work also illuminate the main bottlenecks of C_1-C_1 coupling reactions, and support the conclusion that this route is not viable.[76] At present, the

MTH reaction is believed to proceed through an indirect mechanism, wherein hydrocarbon species act as reaction centers for product formation.[47,77–79] The hydrocarbons that act as reaction centers may be alkenes,[80,81] aromatic species,[82–87] or both alkenes and aromatics simultaneously.[82] In the following section, the efforts leading to the current mechanistic understanding of the MTH reaction are presented in a roughly chronological order. Isotopic labeling experiments have been instrumental in several breakthrough contributions, and the first section is therefore dedicated to a brief introduction to such studies.

2.2.1 Isotopic labeling studies. Two types of isotopic labeling studies are commonly used. The first is co-feed studies, in which $^{13}CH_3OH$ is co-fed with unlabeled hydrocarbons and the products of reaction are studied with respect to ^{13}C content and distribution. Products which are formed by simple methylation reactions will contain the same number of ^{13}C as the number of carbons introduced in the product by sequential methylation, whereas products which are formed by a more complex mechanism, or by several parallel mechanisms, will contain a statistical distribution of ^{13}C atoms.

The other type of isotopic labeling studies is steady-state isotope transient experiments, in which the feed is switched from unlabeled to labeled reactant after a predetermined time on stream, and the ^{13}C contents of reactant and products are followed as a function of time after switching the feed (Fig. 10). Such experiments are commonly used in catalysis research to distinguish between reaction intermediates and spectator molecules. In general, an active intermediate will incorporate the labelled component more rapidly than, or equally fast as, the product molecules. On the other hand, a spectator molecule will incorporate the labelled component more slowly than the products.

2.2.2 Alkene based mechanism. To the best of our knowledge, Dessau and coworkers from Mobil were the first to use $^{13}CH_3OH/^{12}C$-alkene and -arene co-feed studies to elucidate mechanistic details about the MTH reaction. Based on such co-feed studies over H-ZSM-5 (MFI) zeolite, they proposed that the reaction proceeds by an alkene methylation/cracking mechanism, illustrated in Scheme 1.[80,81]

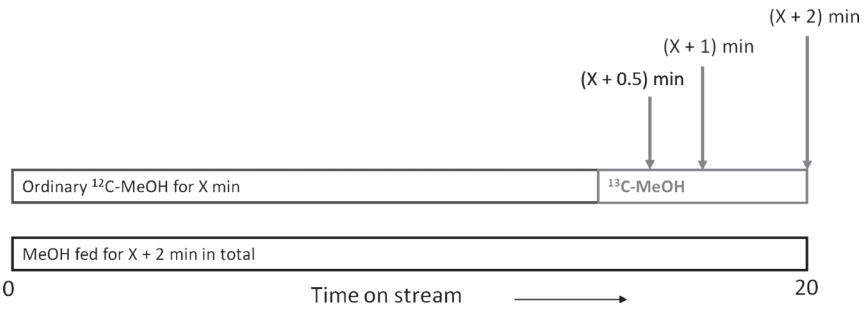

Fig. 10 Illustration of steady-state isotopic transient experiments with switching from ^{12}C methanol to ^{13}C methanol after a predefined time on stream, X.

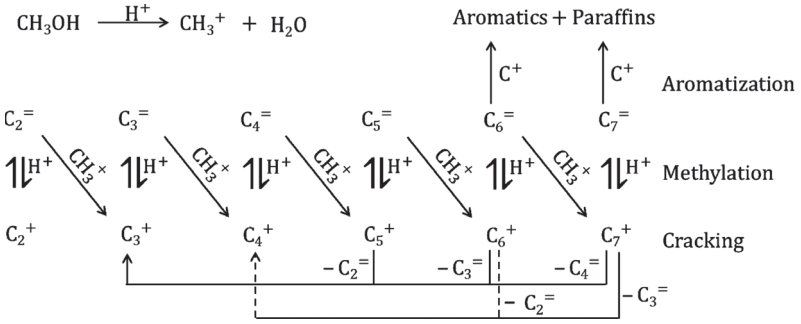

Scheme 1 Methylation/cracking mechanism proposed by Dessau. Adapted from Refs. 80, 81.

According to this mechanism, the initial alkenes are formed from reactions involving carbon-carbon bond formation, but once alkenes are formed, the reaction leading to their formation is irrelevant, in accordance with Chen and Reagan's autocatalytic reaction scheme.[74] In a similar proposal in 1986, Dessau stated that: ''Asking where the first olefin molecule comes from is analogous to asking where the first peroxide comes from in an autooxidation reaction''.[81] The statement further illustrates that the first alkenes are important only during the initiation phase of the reaction, which is responsible for producing little of the total product observed. The first alkene could also come from impurities in the zeolite, reactant methanol or carrier gas. As little as a single alkene molecule was speculated to be sufficient to trigger the MTH reaction. Dessau's MTH reaction mechanism considers ethene as a product obtained from secondary re-equilibration of primary alkenes and not as a primary product obtained from methanol. In addition, aromatic species formed during the MTH reaction are presented as end products (or coke precursors) resulting from hydrogen transfer reactions, with no contribution to effluent product formation.

Langner[88] later reported that the addition of small amounts of higher alcohols to the methanol feed dramatically reduced the induction period over NaH-Y (FAU) zeolite. While this result agreed with Dessau's proposal, Langner found that cyclohexanol had the greatest effect and thus suggested a reaction mechanism where cyclic intermediates were of great importance. His proposed reaction scheme involved higher methylated cyclic intermediates, which could enter into the ''paring reaction'' to produce light alkenes. This paring reaction was first proposed by Sullivan *et al.*[89] to explain the formation of alkenes (especially isobutene) from hexamethylbenzene, and proceeds through ring-contractions and expansions (See Section 2.2.5). Work by Mole and co-workers[90,91] in 1983 led to a similar conclusion when they found that the addition 1 wt% of toluene or p-xylene to the methanol feed led to a dramatic increase in methanol conversion. However, based on co-reactions with isotopically labelled aromatics over H-ZSM-5 (MFI), they suggested a mechanism of alkene formation where polymethylbenzenium ions were deprotonated to form exo-methylenecyclohexadiene species. The exocyclic double bonds of these species could then be methylated to form an alkyl side chain, which could subsequently be eliminated (See Section 2.2.5).

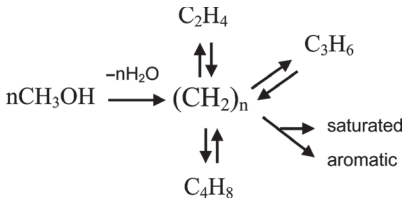

Scheme 2 The hydrocarbon pool mechanism as proposed by Dahl and Kolboe for CHA (SAPO-34). Adapted from Refs. 77–79.

2.2.3 The "hydrocarbon pool". In the mid-1990's, Dahl and Kolboe proposed the "hydrocarbon pool mechanism" for the MTH reaction.[77,79] They carried out isotopic labeling experiments by co-feeding alkene precursors (ethanol, propanol) and ^{13}C-methanol over a SAPO-34 (CHA) catalyst. Analysis of the effluent showed that most of the products were formed exclusively from methanol under the applied reaction conditions.[77–79] Hence, a parallel indirect mechanism, the ''hydrocarbon pool'', was proposed. While their proposal shared many similarities with previous works, this schematic concept had a greater immediate influence than the works of the previous decade.[92] The original hydrocarbon pool model, as shown in Scheme 2, assumed that methanol was continuously added to a pool of adsorbed hydrocarbons, which successively eliminated light alkenes.

The initial hydrocarbon pool was given an overall stoichiometry $(CH_2)_n$, and the chemical structure was not specified.[77–79] Thus, the concept of the hydrocarbon pool could cover both the alkene intermediates proposed by Dessau,[80,81] the aromatic intermediates proposed by Mole *et al.*,[90,91] and other types of intermediates. However, studies of the hydrocarbon pool in the following decade focused mainly on aromatic or cyclic intermediates. The group of Haw *et al.*[93–96] used MAS-NMR spectroscopy to identify a number of benzenium and cyclopentadienyl cations present inside the catalyst under working conditions, while Mikkelsen *et al.*[83] found support for the hydrocarbon pool in large-pore zeolites from co-reactions of aromatics and methanol. The groups of Haw and Kolboe simultaneously concluded that polymethylbenzenes were the main hydrocarbon pool species in H-SAPO-34 (CHA).[84,85,97] Additional evidence for the hydrocarbon pool mechanism in H-ZSM-5 (MFI), H-SAPO-34 (CHA) and H-SAPO-18 (AEI) was also provided by Hunger *et al.*[98–100] Later studies of the MTH reaction with zeolite H-Beta (BEA) cemented the importance of polymethylbenzene intermediates in this catalyst.[101,102]

2.2.4 The dual cycle concept. After the long period focusing on aromatic intermediates in the MTH reaction, steady-state isotope transient studies (as described in Section 2.2.1) over the medium-pore H-ZSM-5 (MFI) catalyst revealed that not all alkenes were formed from aromatics. While ethene and the lower polymethylbenzenes (toluene to tetramethyl benzene) displayed similar contents of ^{13}C, the higher alkenes (C_{3+}) displayed a higher reactivity for the incoming ^{13}C methanol than the

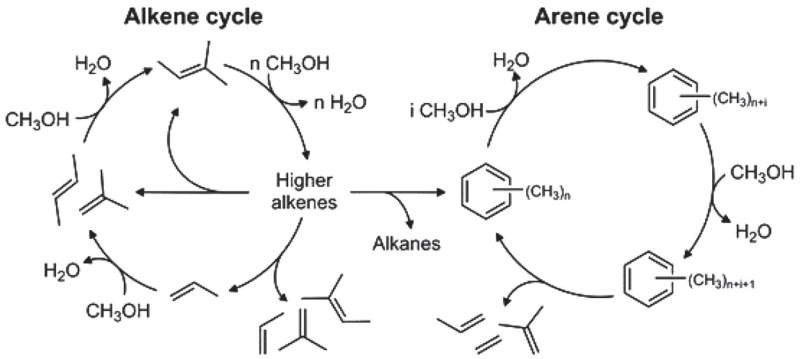

Scheme 3 Suggested dual cycle concept for methanol conversion over ZSM-5. The relative importance of each cycle as well as the exact structure of intermediates depends on the catalyst employed and the process conditions. Thus, not all products shown here are observed in all systems. Reproduced from Ref. 51.

polymethylbenzenes, suggesting formation from a mechanism not involving polymethylbenzenes.[82,103] This finding gave rise to the dual cycle concept, which states that the hydrocarbon pool proceeds through two partly separated cyclic reaction mechanisms, as shown in Scheme 3. One of these cycles (the arene cycle) involves aromatic intermediates, while the other (the alkene cycle) involves methylation and cracking of alkenes in a similar manner to what was previously proposed by Dessau.[80,81] A main difference from the proposal by Dessau (in addition to confirming the importance of the arene cycle even in H-ZSM-5 (MFI)) is that ethene formation from the alkene cycle was assumed to be neglible.

The dual-cycle proposal initiated a series of similar studies over different catalysts with the aim of relating catalyst structure to product selectivity. Comparisons of H-ZSM-5 (MFI) and H-Beta (BEA) led Svelle and Bjørgen *et al.*[87,104] to conclude that the alkene cycle played a much more significant role in H-ZSM-5 (MFI) than in the more spacious channels of H-Beta (BEA). The active intermediates of the arene cycle were also found to differ for the two catalysts: While the largest polymethylbenzenes were most active in H-Beta (BEA), the lower homologues were more active in H-ZSM-5 (MFI). This difference in turn leads to a change in product selectivity, as the larger polymethylbenzenes produce more isobutene and propene relative to ethene. A similar correlation between the size of polymethylbenzenes and the yield of ethene in H-SAPO-34 (CHA) had previously been suggested by Song *et al.*[105] Further work on H-SAPO-34 (CHA) also revealed that the large cavities of this catalyst favour the arene cycle, with higher polymethylbenzenes being the most active species.[106] Recently, methanol/benzene co-reactions over two other large-pore zeolites H-MOR (MOR) and H-MCM-22 (MWW)[107] showed that these structures behave similarly to H-Beta.

An important implication of the dual cycle concept is that it might be possible to separate the two cycles by sterically suppressing the formation of large aromatics.[86] This hypothesis was tested by studying the narrow-pore 10-ring zeolite H-ZSM-22 (TON), which was indeed found to strongly favour the alkene cycle, while suppressing the formation of aromatic

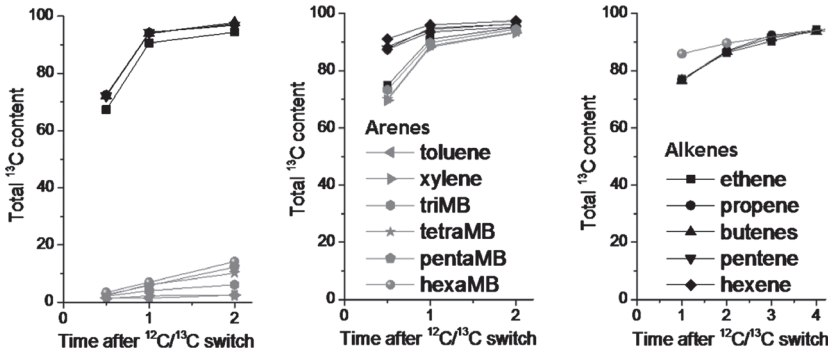

Fig. 11 Incorporation of ^{13}C in MTH products in the reactor effluent or retained in the catalyst versus time after the ^{12}C-/^{13}C-methanol switch. Left: TON (data from,[48] 18 minutes ^{12}C methanol reaction followed by switching to ^{13}C at 400 °C and WHSV = 2 $gg^{-1}h^{-1}$), middle: MFI (data from,[86] 18 minutes ^{12}C methanol reaction followed by switching to ^{13}C at 350 °C and WHSV = 7 $gg^{-1}h^{-1}$), right: CHA zeotype (data from,[106] 3 minutes ^{12}C methanol reaction followed by switching to ^{13}C at 350 °C and WHSV = 6.2 $gg^{-1}h^{-1}$).

products.[48,108] A selection of steady-state isotopic transient analysis experiments used for the deduction of mechanistic details versus structure is shown in Fig. 11.

The contributions cited above strongly suggest that zeolite structures which contain pores large enough to accommodate larger polymethylbenzenes favour the arene cycle. However, other parameters may counter-balance the effect of pore size: Iglesia and co-workers have shown that the alkene cycle dominates in dimethyl ether (DME) conversion over several large-pore zeolites at low temperatures and high reactant partial pressures.[109–111] This observation is in line with a recent contribution by Schulz, who suggested that dealkylation of polymethylbenzenes in zeolites is thermodynamically restricted at temperatures below 350 °C.[112] The strength of the catalyst's Brønsted acid sites also appears to affect the relative preference for the two reaction cycles, as evidenced over the two isostructural large-pore catalysts H-SSZ-24 and H-SAPO-5 (both AFI, but different composition).[51] The moderate acid strength of H-SAPO-5 appeared to favour propagation of the alkene cycle relative to the arene cycle.

2.2.5 Alkene formation in the arene cycle. It is now generally accepted that the arene cycle proceeds by methylation of polymethylbenzenes followed by dealkylation (Scheme 3). However, the dealkylation mechanism has been debated for many years, and two main mechanistic proposals have been put forth: the paring reaction and the side-chain (or exocyclic) methylation mechanism. The two mechanisms are schematically presented in Scheme 4. As shown, both reactions involve methylation of hexamethylbenzene to form a heptamethylbenzenium cation (heptaMB$^+$) as the first step. However, it is hypothesised that aromatics with fewer methyl groups could also form polymethylbenzenium cations and undergo similar reactions.

The paring reaction was first proposed by Sullivan *et al.*[89] to account for the high yield of isobutane during hydrocracking of

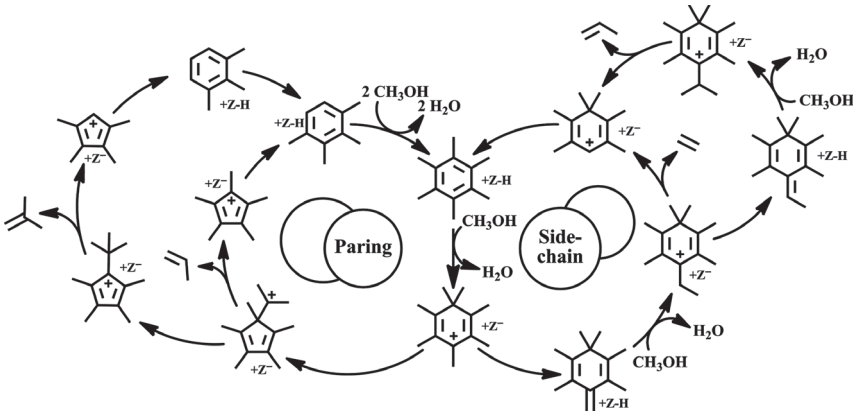

Scheme 4 The paring and side chain reaction pathways for de-alkylation of polymethylbenzenes.

hexamethylbenzene. It involves the rearrangement of HeptaMB$^+$ to a five-membered ring with an alkyl substituent. This smaller ring can then either split off propene directly or reorganise further to eliminate isobutene before deprotonation and expansion back to a six-ring. The side-chain methylation pathway was first proposed by Mole and co-workers,[90,91] and later refined by Haw *et al.*,[92,102] and involves deprotonation of HeptaMB$^+$ to form 1,2,3,3,4,5-hexamethyl-6-methylene-1,4-cyclohexadiene (HMMC). The exocyclic double bond can subsequently be methylated to form an ethyl side-chain, which may be eliminated as ethene. Alternatively, another deprotonation and methylation reaction may lead to an isopropyl side-chain.

A notable difference between the paring and side-chain methylation mechanisms is that the paring reaction involves the use of a ring carbon to grow an alkyl chain, while in the side-chain methylation reaction the aromatic ring is not broken during the reaction. This difference was exploited by Bjørgen *et al.*[101] and Sassi *et al.*,[102] who performed extensive isotopic labeling and co-feed studies aimed at elucidating the reaction mechanisms of de-alkylation over zeolite H-Beta (BEA). Sassi *et al.*[102] worked at high temperatures (350–450 °C) and concluded that side-chain methylation was the most important pathway to alkenes, in part due to their finding that 5 equivalents of methanol to one of toluene was more reactive than hexamethylbenzene reacted alone or together with water. Also, they found that the ethene and propene formed contained an excess of carbons from methanol, compared to what would be expected from the paring reaction. On the other hand, Bjørgen *et al.*[101] found that the majority of propene and isobutane (which they inferred was formed from isobutene by simple hydride transfer) formed at temperatures below 300 °C contained exactly one ring-carbon, as expected from a paring mechanism. Further, no indication of side-chain methylation was found when reacting methanol over a catalyst known to contain active polymethylbenzenes.

Recently, Westgård Erichsen *et al.*[51,113] performed isotopic labeling studies over zeolite H-SSZ-24 (AFI) and the isostructural SAPO material

H-SAPO-5 (AFI) at low temperatures, and concluded that a paring-type reaction dominated alkene formation from aromatic intermediates over both materials. The systematic incorporation of one carbon from the aromatic ring, as observed in these studies, provides strong evidence that a ring expansion or contraction step is involved in de-alkylation of polymethylbenzenes at low temperature. Whether side-chain methylation becomes more important at higher temperatures is an open question: isotopic labeling experiments performed under typical MTH conditions are very difficult to analyse, due to the possibility of independent reactions leading to ring/methyl carbon exchange without de-alkylation[101,102] combined with parallel alkene formation *via* the alkene cycle.

The two dealkylation mechanisms have also been investigated theoretically, but studies directly comparing the two mechanisms in the same catalyst are still missing. McCann *et al.*[114] and Lesthaeghe *et al.*[115] investigated the paring reaction and side-chain methylation respectively over H-ZSM-5 (MFI), but considered different end-products. While McCann's paring cycle showed no major bottlenecks to produce alkenes, Lesthaeghe found that an ethyl chain could grow from o-xylene, but with barriers higher than 200 kJ/mol for ethene elimination. Later work by Kolboe[116–118] revealed that elimination of an alkyl chain can occur with much lower barriers through a π-complex between the benzene ring and the alkyl fragment. This observation led de Wispelaere[119] to suggest a complete low-barrier side-chain methylation mechanism, where all barriers are below 100 kJ/mol.

A pertinent question regarding the side-chain methylation mechanism is whether appreciable amounts of $HeptaMB^+$ are ever deprotonated and available for side-chain methylation under reaction conditions. The work by Bjørgen *et al.*[101] suggests that this is not the case at low temperature, while the deprotonation steps suggested by de Wispelaere *et al.*,[119] (supporting information) display very high reverse (protonation) rates.

Regarding the paring reaction, the observation of similar isotopic labeling patterns (one ring carbon incorporated) for ethene, propene and isobutene challenges the classical paring pathway, since this reaction is normally not associated with ethene. The lack of an obvious pathway to ethene from $HeptaMB^+$ through a paring reaction leads to two possibilities: Either ethene is formed from lower polymethylbenzenes, or chain growth must proceed *via* another mechanism than hitherto proposed, that can also account for the systematic carbon scrambling. One possibility is expansion to a tropylium-type cation and subsequent contraction before de-alkylation. This type of mechanism has been subjected to studies of gas phase kinetics by Arstad *et al.*[120] (theory) and Sekiguchi *et al.*[121] (experiment). High barriers were found in both studies.

2.3 Recent research trends

2.3.1 Experimental studies. Due to the complexity of the MTH reaction, several recent research efforts have focused on the kinetics of elementary reaction steps. For a detailed description of the state of the art, we refer to a recent review by Ilias and Bhan, who focused on six

individual reaction steps in the MTH reaction, namely methylation of alkenes and arenes, hydrogen transfer, cyclization, alkene cracking, and aromatic dealkylation.[122] In this contribution, we will give a brief outline of some recent contributions to the field. As will be seen, kinetic information for some of the reactions has been extracted without the complications associated with secondary reactions, while in other cases relative kinetic information was obtained using (*e.g.*) isotopic labelling experiments.

Alkene and arene methylation reactions in MTH have been investigated by co-reaction of a methylating agent (methanol or DME) and alkene or aromatics under conditions that suppress secondary reactions, *i.e.*, relatively low temperatures and short contact times. There are two proposed mechanisms by which methylation reactions occur. The stepwise mechanism, in which surface methoxide groups are formed from methanol/DME and subsequently methylate the alkene/aromatic molecule; and the co-adsorption mechanism, in which methanol/DME and the alkene/aromatic molecule form a co-adsorbed complex over the acid site. There are experimental indications for the existence of both proposed mechanisms over MFI zeolite.[123,124]

Svelle *et al.*[125,126] investigated the kinetics of C_2-C_4 alkene methylation over MFI zeolite and Hill *et al.*[127] extended the work to other zeolites (MFI, BEA, FER, and MOR) using methanol and DME methylating agents, respectively. Both authors reported that the alkene methylation rate has a first-order dependence on the alkene pressure and a zero-order dependence on the methylating agent. In addition, the alkene methylation rate increases and the activation barrier decreases systematically with increasing alkene size. Apparent activation energies in the range 94–109 kJ/mol were reported. Comparison of the four zeolites by Hill *et al.*[127] showed similar activation barriers for C_3 and C_4 methylation. However, higher methylation rates and pre-exponential factors were observed over MFI and BEA compared to MOR and FER, and indicate that alkene methylation reactions are topology dependent.

Similar to alkene methylation, aromatics methylation reactions play a crucial role in the MTH reaction. Recently, Hill *et al.*[128] investigated methylation of aromatic molecules over MFI and observed first order dependence on the aromatic molecule and a zero-order dependence on the methylating agent for benzene and toluene. Energy barriers for the aromatic methylations were found to be in the range 52–62 kJ/mol and methylation of benzene and toluene proceeded with similar rates and activation energies as propene and n-butene respectively. The energy barriers reported by Hill *et al.* are comparable with toluene methylation energy barriers of 50–80 kJ/mol found in previous literature.[129–131] In a recent study, Van der Mynsbrugge *et al.* reported that the benzene methylation reaction occured at a considerably faster rate over MFI than over BEA.[132] The difference was allocated to an optimum confinement effect of the reacting species in MFI.

Dealkylation of polymethylated benzene molecules was described in Section 2.2.

Cyclisation and aromatisation of alkenes constitute another family of reactions in the MTH reaction scheme. Two reactions are involved,

cyclization of alkenes followed by dehydrogenation to aromatics or dehydrogenation of the alkenes to form dienes and trienes, followed by cyclization. There is no experimental evidence nor kinetic data revealing whether cyclization occurs prior to dehydrogenation or vice versa. In both cases, dehydrogenation occurs *via* intermolecular hydrogen transfer reactions in which alkenes or cycloalkanes donate hydrogen to another hydrocarbon. Hazari *et al.*[133] investigated the relative rates of hydrogen transfer versus methylation reactions over indium iodide and zinc iodide catalysts. The reaction involved co-conversion of cyclohexadiene (hydrogen donor) and C_7 alkenes with different degrees of substitution around the double bond. The authors quantified hydrogen transfer and methylation rates from the amount of C_7 alkane or C_8 hydrocarbon formed, respectively. It was observed that the relative rate of methylation and hydrogen transfer varied systematically with the degree of alkene substitution. The highest ratio of methylation to hydrogen transfer reaction was observed for the alkenes with high substitution, and the addition of hydrogen donors like cyclohexadiene affected the relative rates of the reaction compared to reactions involving only the alkenes. In a related work, Simonetti *et al.*[110,134] attempted to quantify the relative rates of methylation and hydrogen transfer reactions over BEA zeolite in a reaction involving ^{13}C labeled DME and C_4–C_7 alkenes. The authors observed that the hydrogen transfer reaction was favored for hydrocarbons that form stable carbocation transition state complexes. Some authors have studied the intermolecular hydride transfer reaction alone. Mullen and Janik studied hydride transfer between various combinations of hydride donor and acceptor molecules over protonated MOR and FER zeolite by DFT modelling, and reported that the reaction barrier in MOR decreased starting from the reactants forming *prim*, then *via sec* to *tert* carbocation intermediates.[135] They further concluded that shared hydrided carbonium ions represented the transition state of reaction. While no steric repulsion was observed in MOR, the smaller pores of the FER zeolite led to steric repulsion of the larger *t*-butyl species. Very recently, Borghese *et al.* published an *in situ* MAS-NMR study of hydride transfer between isobutane molecules over USY zeolite.[136] H-D labeling experiments showed that the hydride transfer occurred on the methine position of the molecule, with an activation energy of *ca.* 55 kJ/mol. The authors concluded that the hydride transfer reaction is a bimolecular reaction.

Finally, *cracking of large hydrocarbons to smaller fractions* is known to occur over zeolites under MTH reaction conditions. For alkenes possessing carbon atoms at the β-position from the double bond, cracking will proceed *via* an alkoxide intermediate (protonated alkene) followed by a β-scission reaction to form a small alkene and a small alkoxide. Hence, the rate of the β-scission reaction is crucial. Simonetti *et al.*[110] quantified the β-scission reaction rate for C_5-C_8 alkenes during co-conversion of ^{13}C-DME and the alkenes over BEA zeolite and observed comparable rates for β-scission and skeletal isomerization reactions, while in most cases methylation reactions of the alkenes were significantly faster (>40 times) than the β-scission reaction. Buchanan *et al.*[137] investigated the relative rates of cracking of C_5-C_8 alkenes over MFI and reported a significant

increase in cracking rates with increasing alkene size. Furthermore, cracking rates of liner and highly branched C_8 alkenes were shown to be greatly affected by diffusion limitations over MFI. From this perspective, the relative rates of cracking, methylation *etc.* mentioned in this contribution are likely to depend on zeolite topology, and this parameter is so far scarcely studied.

Overall, the individual reactions in MTH follow the expected carbocationic chemistry in that the rates and activation barriers of alkene methylation, cracking, hydrogen transfer and cyclization reactions depend on the stability of carbocationic transition states formed during the reaction, meaning that longer chains and branching generally result in higher reaction rates.[110] Considering heavier hydrocarbons with a high degree of substitution and aromatics, diffusion limitations come into play and deviations from the general carbocationic chemistry are observed.

2.3.2 Theoretical studies. Obtaining kinetic data for individual catalytic cycles by experiment is a challenging task due to the plethora of reactions taking place simultaneously inside the zeolite. Theoretical studies coordinated to experiments may provide improved mechanistic insight. One advantage with computational studies is that different aspects of the system can be isolated and their influence on individual reactions may be studied independently. Large efforts in the international community in developing cost efficient and reliable methodologies have now reached a point where the theoretical toolbox can provide ''near-chemical accuracy''.[138,139] However, the approach is not without hurdles.

The MTH system is a complex hybrid consisting of a crystalline periodic inorganic structure and of organic reactions which do not occur in a periodic manner within the zeolite cavities. This is a complicated combination since accurate description of the periodic inorganic framework coupled with organic (non-periodic) reactions is challenging. A brief description of the methodologies to meet these challenges follows. For a comprehensive review of the state-of-the-art we refer to Hemelsoet *et al.*[140]

The first attempts at modeling reactions relevant for MTH, reported in the late 1990s and early 2000s, were limited to small clusters with 3 to 5 T-atoms in the gas phase representing the zeolite.[84,85,120,141–149] Such small clusters are sufficient to model an isolated Brønsted acid site and were therefore a good starting point, but they are not sufficient to model the topological constraints imposed on the organic reaction by the internal pore system of the zeolite. With increased computational resources and further development of software it has become possible to increase the size of the studied system in terms of number of lattice atoms.[140] There are two viable methodologies: 1) Extend the cluster representing the zeolite in order to model larger parts of the crystals or 2) perform periodic calculations by simulating an infinitely extended repetition of zeolite unit cells. In the first case the periodic structure of the zeolite is not considered while in the latter both the zeolite and the organic reactions are modeled with periodicity. Periodic calculations are well suited to accurately model the crystalline zeolite material but particular care must be taken to minimize unphysical interactions between the organic

components in neighboring unit cells. It is therefore necessary to ensure that the unit cells are large enough, and the use of (computationally expensive) super cells may be required. In contrast, extended clusters represent only a small fragment of the zeolite, and while the (unwanted) periodic description of the organic reaction is avoided, the zeolite fragment must be carefully treated in order to avoid unphysical properties. Particularly, the clusters must be correctly terminated so that the materials do not collapse during geometry optimizations. This is achieved by terminating all external dangling bonds of the fragment with H, which are then anchored in space.

In addition, computational models are historically developed for either organic reactions or inorganic (solid) materials. In the MTH reaction, both chemical environments are present, and it is therefore crucial to choose a methodology which describes both parts of the system correctly.[150]

State-of-the-art methodologies can in general be described with an ''onion''-analogy: The parts of the large cluster that are farther from the reaction center are modeled with a less computationally expensive method, while the atoms taking part in the breaking and making of bonds and the surrounding closest atoms are modeled by much more accurate, but also demanding methods.[140] Thus the reaction center is modeled by highly sophisticated quantum mechanical (QM) methods while the outer layer of the onion is treated with molecular mechanics (MM) or cheaper QM methods, denoted QM/MM and QM/QM methods respectively.

Density Functional Theory (DFT) is widely used for both extended cluster and periodic studies since it offers reliable data at low computational cost.[140] Previously, a significant drawback of DFT was its inability to model dispersion forces, but satisfactory solutions to this problem have been developed, notably the Grimme correction.[151] For the organic MTH reactions Van del Waals interactions give significant contributions to, for instance, adsorption energies, and it is therefore crucial that these be implemented to obtain chemically reliable data.[138,139]

The classic Brønsted acid site has been studied by various groups with results in agreement with experimental observations.[140] Simple methylation reactions have been studied successfully. The initial theoretical studies performed as gas phase simulations with very small clusters representing the zeolite provide useful information on reactivity of possible hydrocarbon pool intermediates. However it is necessary to take the zeolite environment into account in the investigation of large, bulky hydrocarbon pool species and coke precursors, due to possible interaction with the inorganic framework and steric limitations.[140]

Svelle *et al.* obtained theoretical data in very good agreement with experimental data on the methylation of alkenes in H-ZSM-5 (MFI). Full catalytic cycles for both the paring[114] and side-chain[119] mechanisms have been found by computational studies, although in different host materials. The first complete catalytic route reported involves isobutene formation through a paring type mechanism in H-ZSM-5 (MFI).[114] A low barrier path for the side-chain mechanism has so far only been identified

in H-SAPO-34 (CHA), as other reported side-chain cycles have at least one barrier above 200 kJ/mol.[115,144,152] Also, a proposed route for the alkene-based reactions in the dual-cycle reaction scheme has been investigated.[153] Energy barriers for chain growth by methylation were 60–80 kJ/mol, similar to the methylation of HMB in H-SSZ-13 (CHA) and of lower methylbenzenes. Energy barriers for cracking were found to be between 70 and 120 kJ/mol and generally higher for the formation of ethene compared to propene. This is in agreement with propene, but not ethene, being a favored product in the alkene based cycle.

So far, there are few reports comparing zeolites with differing topology for the modeled reactions. Lesthaeghe *et al.* showed that activation barriers for gem-methylation of aromatic hydrocarbons were strongly dependent on the reaction environment within the catalyst.[154] It was found that the CHA framework offers favorable electrostatic surroundings for the methylation of HMB by methanol, compared to MFI and BEA, resulting in the following order of reactivity: CHA > MFI > BEA. Similar studies for all possible reaction steps in the various proposed cycles are necessary in the investigation of topology effects on the MTH-reaction.

Calculations of rate coefficients have been accomplished recently, and this opens up possibilities for further detailed reaction analysis directly linked to experimental results.[140] We anticipate publication of such comparisons in the near future, as both chemical accuracy and plausible full reaction cycles are now available.

3 Shape selectivity in the MTH reaction

3.1 General

Product selectivity in the MTH reaction results from a combination of kinetic and thermodynamic driving forces. Thermodynamically, the conversion of methanol to hydrocarbons and water, as well as the conversion of alkenes to aromatics and alkanes, are favored under all relevant conditions. Within the typical temperature range of the MTH reaction (350–550 °C), increasing temperatures favor short alkenes over long-chain alkenes,[155] and dealkylation of alkylbenzenes is typically favored at temperatures above 350 °C (depending on pressure and length of the molecules).[112]

Kinetically, the rate of each elementary reaction is determined both by operational parameters such as pressure and temperature, and by material parameters such as Brønsted acid strength, acid site density, pore and cavity size and shape, crystal size and defect type and concentration (see Section 3.2).

In this contribution, our ambition is to illustrate how zeolite topology influences product selectivity in the MTH reaction, and to relate those observations to the current knowledge about the MTH reaction mechanism. For this purpose, a selection of zeolite samples has been tested as MTH catalysts using a quasi-single-parameter variation approach. This means that the operational parameters (temperature, methanol pressure, reactor type) were equal in each experiment. Furthermore, the zeolite

samples had similar Si/Al ratio, Brønsted acid strength (they were all Si-Al-O zeolites) and crystal size, but varying topology.

Since it is only possible to prepare samples with similar, but not identical, material parameters, a summary of previous studies about the influence of Si/Al ratio, acid strength and crystal size is given in Section 3.2. The experimental set-up for the catalytic tests is described in Section 3.3, and test data are described and discussed in Section 3.4.

3.2 Influence of material parameters other than topology

In the literature, the effect of Si/Al ratio and crystal size has mainly been studied for H-ZSM-5 (MFI). In general, the literature studies conclude that a higher Si/Al ratio (which corresponds to a lower density of acid sites) leads to higher selectivity towards C_2-C_4 alkenes and lower selectivities toward aromatic products, in accordance with a predominantly sequential reaction scheme. In such a scheme, alkenes are formed first and sequentially converted into aromatic and alkane products, as originally suggested by Chang and Silvestri.[55] Chang *et al.* studied the MTH reaction over MFI with two Si/Al ratios, *i.e.*, 70 and 3340, while intermediate Brønsted acid site densities were obtained by partial $H^+ - Na^+$ cationic exchange. At 370 °C and full conversion, the C_2-C_4 alkene selectivity was 30% and 46% for Si/Al = 70 and 3340, respectively. Lower Si/Al ratios led to higher ethene selectivities and lower propene selectivities.[156] Prinz and Riekert tested MFI catalysts with varying Si/Al ratios (34–660) or crystal sizes (0.5–8 μm) for the MTH reaction at 290–360 °C in a batch reactor, and reported that increasing Si/Al ratios led to increasing light alkene selectivities and propene-to-ethene ratios. A similar effect was reported for decreasing crystal sizes (0.5 versus $2 \times 2 \times 6$ micron crystals); however, it is worth noting that for conversions in excess of 80% the selectivity differences due to crystal size vanished.[157] Recently, Liu *et al.* tested MFI samples with Si/Al ratios ranging from 12–360 at 460 °C, and observed a gradual increase in propene selectivity from 16% to 52%, respectively, at full methanol conversion. Concurrently, the propene to ethene ratio increased from 2.0 to 6.5.[158] We recently studied the MTH reaction over three MFI catalysts with different Si/Al ratios (12, 50 and 140, respectively) under the conditions reported in Figs. 12–16, and observed that the C_3 selectivity decreased, while the HTI (hydrogen transfer index, see Section 3.4.2) and aromatics selectivity increased, with a decrease in Si/Al ratio (*i.e.* an increase in acid site density), throughout the conversion range tested (50–100% conversion). This behaviour is in line with the cited literature reports.[156–158] For ethene the picture was more complex: The samples with the highest density of acid sites gave an intermediate selectivity to ethene, compared to the two samples of medium (highest ethene selectivity) and low (lowest ethene selectivity) acid site density. These observations suggest that correlating ethene selectivity with material parameters is not a straightforward task and should be performed with care.

Very recently, Westgård Erichsen *et al.*[51] elucidated the effect of acid strength in MTH catalysts by comparing two isostructural materials,

H-SAPO-5 and H-SSZ-24, for the title reaction at 350–450 °C. Both materials have an AFI structure (Fig. 9), which allows both aliphatic and aromatic products to diffuse out, and is therefore more suited for such studies than the more common CHA structure (Fig. 6). The strongly acidic H-SSZ-24 was found to be more selective towards aromatic products and C_2–C_3 hydrocarbons as compared to the moderately acidic H-SAPO-5, which produced more non-aromatic C_{4+} hydrocarbons. Co-reactions of $^{13}CH_3OH$ and benzene at 250–300 °C, with low conversion of both reactants further suggested that a lower acid strength promotes an alkene-mediated MTH reaction mechanism.[51]

3.3 Experimental

Catalytic tests were carried out using samples with the following topologies: CHA (H-SSZ-13), TON (H-ZSM-22), MEL (H-ZSM-11), MFI (H-ZSM-5), IMF (H-IM-5), TUN (H-TNU-9), MOR (H-mordenite), BEA (H-beta), and AFI (H-SSZ-24). The Si/Al ratio of the samples as well as their O-H frequency shifts when subjected to CO adsorption at −196 °C are shown in Table 2. As observed from Table 2, all samples had similar acid strength (frequency shift). Most of them had Si/Al ratios around 20, with CHA (Si/Al = 12), TON (Si/Al = 30) and AFI (Si/Al = 35) as the exceptions.

All catalytic tests were performed at 350 °C using fixed bed reactors with 3–8 mm inside diameter. The powder catalysts were pressed, gently crushed and sieved to obtain particles in the range 0.25–0.42 mm. From 40–100 mg of the sieved fraction was tested under methanol flow at WHSV (weight hourly space velocity) between 1 and 9 $gg^{-1}\,h^{-1}$, and with P(MeOH) = 13 kPa. The product stream was analyzed with an Agilent 6890 A gas chromatograph (GC) with FID detector and automatic sampling (Supelco SPB-5 capillary column; 60 m, 0.530 mm id, stationary phase thickness 3 mm) or with an Agilent 7890 GC with FID on a Restek Rtx®-DHA-150 column (150 m, 0.25 mm i.d., stationary phase thickness 1 μm).

In order to compare product selectivities of the materials, catalytic test data are presented as product yield versus methanol conversion plots in Section 3.4 below. With few exceptions, each graph in Section 3.4 represents data obtained during catalyst deactivation in a single test, thus assuming non-selective deactivation of each catalyst. This procedure has been justified by previous studies of a number of zeolite catalysts, including MEL, IMF, TUN,[49] MFI,[159] TON, MTT, EUO,[160] AFI,[113] ITH,[161] all of which showed that the product selectivity is independent of deactivation during the MTH reaction. The CHA structure represents an exception: an increase of the ethene to propene ratio was observed with time on stream in previous studies (see ref. 106 and refs therein), and was ascribed to increasing diffusion hindrance, as the adsorbed hydrocarbon residues inside the cavities gradually grew bigger.

3.4 Shape selectivity

A typical gas chromatogram showing the effluent composition of the MTH reaction over wide-pore BEA zeolite is shown in Fig. 12. Products range from C_2 alkanes and alkenes to C_{12} aromatic products, and over a hundred individual product peaks may be distinguished.

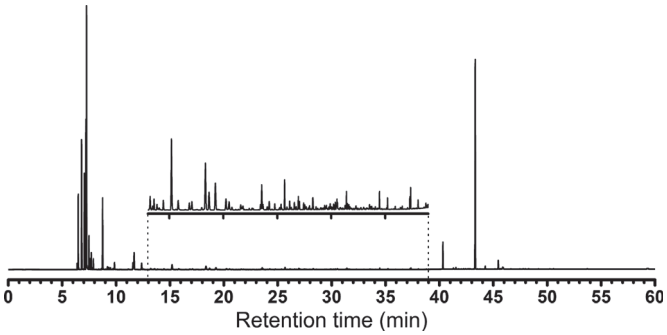

Fig. 12 A typical gas chromatogram of the reactor effluent from the MTH reaction over BEA zeolite at 78% conversion.

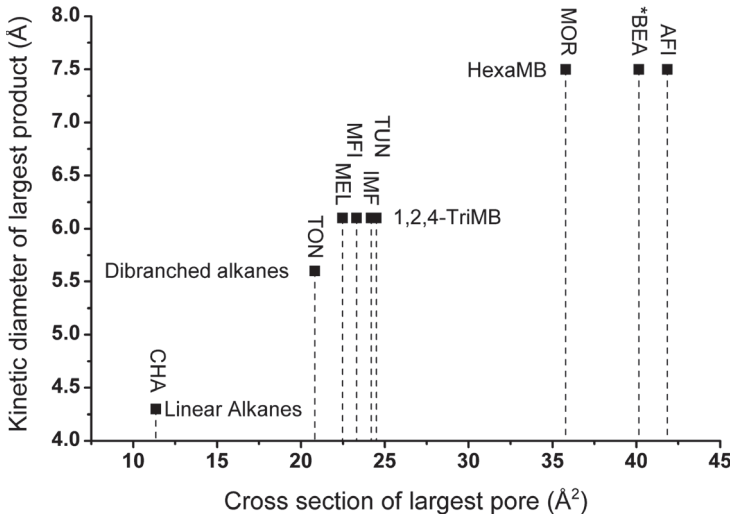

Fig. 13 Cross section of the largest pore *vs.* kinetic diameter of largest product. Cross sections are calculated assuming a perfectly elliptical pore whose axes are the largest and smallest diameters. This is not entirely correct for all materials. The kinetic diameters were found in refs. 163–166.

Figure 12 nicely illustrates the complexity of the MTH product mixture and the need for selectivity-enhancing catalysts. In the following, only main products and product groups will be considered.

3.4.1 Product shape selectivity. The channel dimensions of a number of zeolite catalysts were described in Table 3. Figure 13 shows a plot of the kinetic diameter of the largest product formed in appreciable amounts (>4% yield, thereby omitting products likely to be formed on the outer zeolite surface) in the MTH reaction over each of those materials versus the cross-sectional area of their largest channel. A general, direct correlation between these two parameters is observed, which demonstrates that proper selection of channel diameter gives a distinct cut-off in the effluent product distribution. As may be seen, products diffusing out of 8-ring channels are limited to linear alkenes, while the

use of 10-ring channel zeolites limit the effluent products to either branched alkenes or aromatic products (up to 1,2,4 trimethyl or 1,2,4,5 tetramethylbenzene), depending on the exact channel diameter. The smaller 10 rings such as TON and MTT (ZSM-23,[160]; not included in Fig. 13 because test results were available only at 400 °C) give branched alkenes/alkanes as the largest effluent products, while the larger 10-rings of MFI, MEL, TUN and IMF yield methylbenzenes in the effluent. Zeolites with 12-ring channels allow production of the heaviest methylated benzene, hexamethylbenzene. As this is also the largest observed major product during homogenous catalysis of the same reaction,[162] it appears that 12-ring channels provide little or no product shape-selectivity for the MTH reaction.

While Fig. 13 shows the general rule of how channel dimensions limit the product size, cavities and side-pockets on the main channels may complicate the picture. Of the structures discussed here, TUN, IMF and MOR contain cavities that provide significantly more space than main channels. In the effluents from these structures, it is possible to find heavier products than would be expected based on channel size. Examples include a relatively high yield of HexaMB from TUN[49] at 20% conversion (above 1% yield) and a tendency for MOR to form more large 2-ring aromatics than BEA and AFI at lower conversion.

Even more extreme examples can be found for EUO (EU-1)[160] and MWW (MCM-22) structures[163] which both have smaller 10-ring channels than the TON structure. However, both of these catalysts have large pore extensions (side-pockets) in their main channels, which are delimited by 12-rings.[160,167] Literature studies of the MTH reaction over these catalysts report product distributions that are unexpected from medium pore (10-ring) zeolites, that is, high yields of aromatic products.[160,163] A plausible explanation for the unexpected product distributions over EUO[112,160] and MWW[163] zeolites might be the involvement of the 12-ring side pockets on the outer surface of the crystal during the MTH reaction.

3.4.2 Transition state or intermediate shape selectivity. Transition state or intermediate shape selectivity is tightly integrated with mechanistic understanding, which was presented in Section 2.2. Product distribution versus methanol (and DME) conversion data are shown in Figs. 14–16. The following criteria were used for selection of parameters to be plotted:

- Product ranges of special interest (*e.g.* C_3 alkenes for polypropene production and C_{5+} hydrocarbons for gasoline production),
- Indicators of aromatics formation (*i.e.*, hydrogen transfer index, HTI, which is defined as the [alkane/(alkene + alkane)] ratio for a C_n species), and
- Ratios between individual components which might potentially be altered by intermediate shape selectivity, based on previous mechanistic studies (*i.e.* C_4/C_3 and C_3/C_2 ratio) (Section 2.2).

Concentrating first on the C_3 products (Fig. 14 left), the C_3 selectivity is highest for the 8-ring CHA structure, followed by the 3D 10-ring

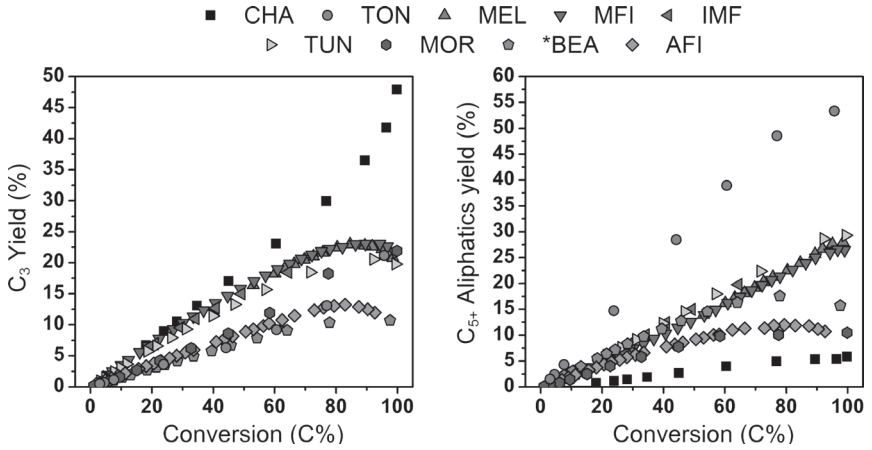

Fig. 14 C_3 (left panel) and C_{5+} aliphatic (right panel) yield as a function of conversion over the various MTH catalysts at 350 °C and P(methanol) = 13 kPa.

topologies (MFI, MEL, TNU, IMF), which form an ensemble of similar C_3 selectivities, and subsequently the 12-ring topologies (BEA, MOR, AFI), which form another ensemble with lower C_3 selectivities. Interestingly, the 1D 10-ring topology, TON, gives similar C_3 product selectivity as the 12-ring materials. The product yield versus conversion curves are generally linear in the 0–80% conversion range, and then change slope in the upwards or downwards direction. The slope change mainly corresponds to an increased net conversion of light alkenes to aromatic molecules and alkanes (See Fig. 16) with the exhaustion of methanol. This observation is in agreement with C_2-C_4 methylation studies performed over MFI, which showed that alkene interconversion reactions were suppressed in the presence of methanol, possibly due to competitive adsorption at the Brønsted acidic sites (See Section 2.3).[125] As mentioned in Section 3.2, CHA is the only structure among those presented here for which a change in selectivity has been observed with increasing deactivation. As such, the upwards slope of the C_3 yield versus methanol conversion curve for CHA is in agreement with a higher diffusion resistance for a coked catalyst, thereby favoring propene (over ethene) production only at high conversion. No straightforward explanation has so far been found for the upwards curvature observed for TON and MOR at high conversions. TON has previously been tested at different residence times, leading to the conclusion that its product selectivity is independent of deactivation.[160]

Turning to the C_{5+} aliphatics product group (Fig. 15 right), 1D 10-ring TON zeolite gives dramatically higher C_{5+} aliphatics selectivity than any of the other catalysts in the entire methanol conversion range. In fact, when summing the yields of C_{5+} aliphatics and aromatics (Fig. 16 right), then the TON zeolite gives the highest overall C_{5+} hydrocarbons yield of all tested catalysts. The 3D 10-ring zeolites form an ensemble of intermediate selectivities to C_{5+} aliphatics, while the 12-ring zeolites give scattered C_{5+} aliphatics selectivities, although at the lower range of the

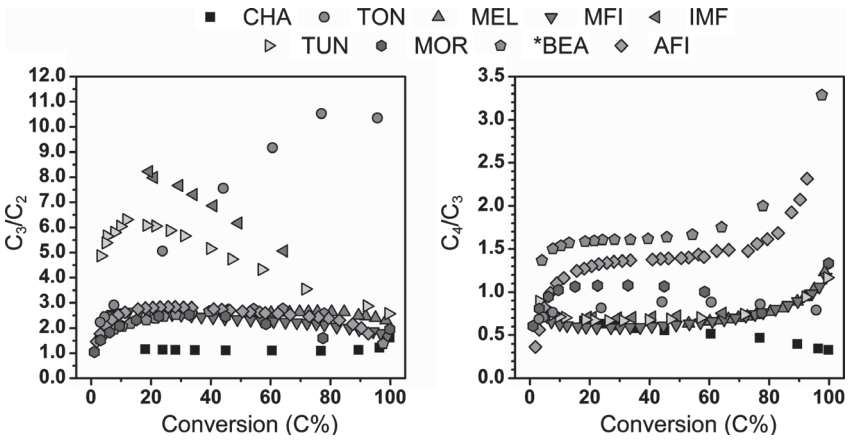

Fig. 15 C_3/C_2 (left panel) and C_4/C_3 yield ratios (right panel) as a function of conversion over the various MTH catalysts at 350 °C and P(methanol) = 13 kPa.

3D 10-ring structures. As expected from its small pore size, 8-ring CHA gives the lowest C_{5+} aliphatics selectivity.

C_3/C_2 and C_4/C_3 ratios versus methanol conversion are shown in Fig. 15. The C_3/C_2 ratio is rather constant at 10–95% methanol conversion for most materials. 8-ring CHA gives the lowest C_3/C_2 ratio of around 1, followed by a ratio of about 1.5–2.5 for most 3D 10-ring and all 12-ring materials. Again, TON is an exception to the general picture, with a C_3/C_2 ratio around 10 at high conversion, decreasing towards 2 at low conversion. Two 3D 10-ring materials, IMF and TUN, also show peculiar behavior, with an increase in C_3/C_2 ratio with methanol conversion to a maximum of 6 and 8, respectively, at 20 % conversion, followed by a decrease towards 2 at high methanol conversion. Again, no straightforward explanation has been found for the particularly low ethene selectivities observed over these two materials. However, close inspection of the aromatic product spectrum for these two materials (see ref. 49) revealed that the selectivity to the heavier methylbenzenes (penta- and hexa-methylbenzene) was at a maximum at the same conversion level as the maximum in C_3/C_2 ratios for these two structures (vide infra). According to mechanistic studies, heavier polymethylbenzenes favour propene and butene, and not ethene, formation (Section 2.2). The plot of C_4/C_3 ratios (Fig. 15 right) shows that the highest C_4/C_3 ratios are obtained over the 12-ring materials. The C_4/C_3 ratio generally shows an upwards curvature at methanol conversions above 80%, again reflecting the changing reaction environment when methanol is depleted. The exceptions to this observations are TON and CHA, which give a slight decrease in C_4/C_3 ratio with increasing conversion. At conversions lower than 10%, the C_4/C_3 ratio decreases dramatically for the 12-ring materials, while it increases slightly for the 3D 10-ring materials.

Turning finally to the aromatic products, which are represented by the hydrogen transfer index, HTI, here plotted for the C_4 product group (Fig. 16 left) and by the yield versus conversion curves for the aromatics fraction (Fig. 16 right), clear differences are again observed for

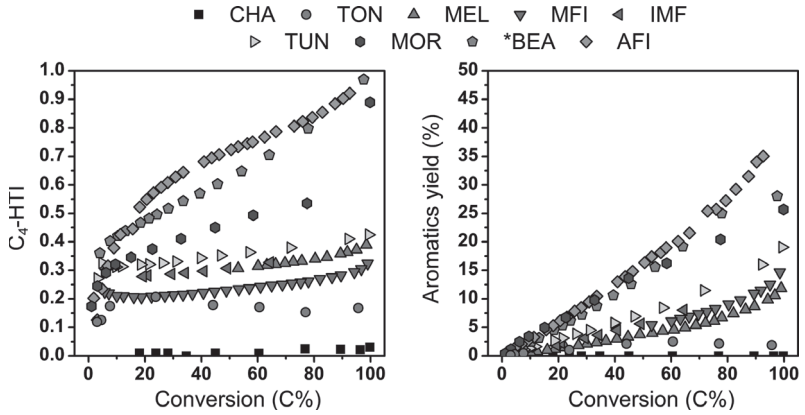

Fig. 16 C_4-HTI (left panel) and aromatics yield (right panel) as a function of conversion over the various MTH catalysts at 350 °C and P(methanol) = 13 kPa.

the 8- versus 10- and 12-ring topologies. The 12-ring topologies have higher C_4 HTIs than the 3D 10-ring materials, which again give higher C_4 HTIs than the 1D 10-ring material, and especially the 8-ring CHA. However, the value for CHA is not representative of aromatics formation because only linear products can escape the crystals. Among the 12-ring topologies, a difference is observed between the materials with larger pore size (BEA, AFI) and MOR, which has smaller pore size (see Fig. 12) and gives a lower C_4 HTI. For the two materials with largest pore size, dimensionality does not seem to influence aromatics formation, since the C_4 HTI of 1D AFI is slightly higher than that of 3D BEA. Among the 3D 10-ring materials, MFI, with its small intersection volume, gives the lowest C_4 HTI. The slope of the C_4 HTI versus conversion curve is highest for the 12-ring materials. There is in general a good correlation between C_4 HTI and the aromatics selectivity for all materials, which decreases in the order: 12-ring > 3D 10-ring > 1D 10-ring > 8-ring materials (Fig. 16 right).

Turning next to a discussion of the product selectivities observed in Figs. 14–16 versus catalyst structure, a main concern about a possible influence of parameters other than topology relates to the TON sample, which has a Si/Al ratio higher than the other samples, as well as a distinct selectivity pattern. This sample has previously been compared to other samples with 1D 10-ring topology, including ZSM-23 with MTT structure (Fig. 7).[160] MTT has a slightly smaller pore diameter (5.2×4.5 Å) than TON. The comparison was performed at 400–450 °C, with WHSV = 2 h^{-1}. The MTT sample had a Si/Al ratio of 26, *i.e.*, close to the majority of samples in Table 3. It was found that the TON and MTT structures yielded very similar product distributions throughout the conversion range tested (5–100% conversion).[160] Based on this comparison, we find it reasonable to ascribe the distinctive selectivity pattern of the TON structure, shown in Figs. 14–16, to its topology.

Turning our attention to the data in Figs. 14–16, the materials can be classified into four main groups based on their selectivity patterns: The 12-ring, the 3D 10-ring, the 1D 10-ring and the 8-ring structures. As stated

above, MTH product selectivity in 8-ring CHA has previously been reported to be determined mainly by product shape selectivity,[106] hence its selectivity pattern will not be further discussed here.

An internal comparison of the three 12-ring structures (BEA, AFI, MOR) show that their C_4 HTIs and aromatics selectivities follow their pore size, in the order: AFI > BEA > MOR. Furthermore, their C_4/C_3 ratios differ significantly and decrease in the order: BEA > AFI > MOR. The C_4/C_3 ratio differences are probably related to the aromatics selectivities, since iso-C_4 (the main C_4 isomer) is more readily hydrogenated than propene. The relative C_3 and C_{5+} aliphatics selectivities of these materials are similar and generally mirror each other, and their C_3/C_2 ratios are also similar. It is interesting to note that the aromatics selectivity is higher in 1D AFI than in 3D BEA. This observation suggests that there is sufficient space for bimolecular hydride transfer reactions (See Section 2.3) in both of these structures, so that the extra space related to channel intersections is no longer needed. In 1D MOR, with a slightly smaller pore size (see Fig. 13), however, intermolecular hydride transfer reactions seem to be slightly more restricted.

Proceeding to a comparison between 12-ring structures and 3D 10-ring structures, several differences are observed. First, the aromatics selectivities and hence, the C_4 HTIs, are significantly lower for the 3D 10-ring structures than for the 12-ring structures. This observation suggests a further hindrance of intermolecular hydride transfer reactions in 3D 10-ring structures. Typically, among the 3D 10-ring materials, the highest aromatics selectivity and C_4 HTI are observed for TUN, which has the largest intersection volume among them. As a second observation, the C_3 selectivities, the C_2 selectivities (as indicated by the similar C_3/C_2 ratios of the two material groups) and the C_{5+} aliphatics selectivities are significantly higher for the 3D 10-ring materials than for the 12-ring materials, whereas the C_4 selectivities are slightly lower. The observed differences in C_4 selectivity may stem from the higher fraction of saturated C_4 products from the 12-ring materials, since those products are inert toward further reaction (see Sch. 4). The higher C_2 and C_3 selectivities generally observed in the 3D 10-ring materials compared to the 12-ring materials might relate to the dominance of light methylbenzenes in 3D 10-ring materials compared to the large fraction of the heaviest methylbenzene, hexamethylbenzene, in 12-ring materials. As referred to in Section 2.2, previous mechanistic studies have suggested that the lower methylbenzenes favor formation of ethene and propene, whereas the highest methylbenzenes favor formation of propene and butene in the arene cycle (Sch. 4). Furthermore, the alkene cycle has been suggested to favor C_{3+} alkene formation (See Section 2.2). The data reported in Figs. 14–16 are in general agreement with those studies. It is furthermore interesting to observe that the two 3D 10-ring structures with the largest intersection volumes, TUN and IMF, yielded higher C_3/C_2 ratios and hence lower C_2 selectivities than the other 3D 10-ring materials. Thorough inspection of the aromatics fraction obtained over these materials showed that both materials yielded hexamethylbenzene, which showed a contact time behavior typical of a reaction intermediate[49] Hence, the aromatic cycle

might produce mainly propene and butene in these two materials. At the same time, their aromatics content was lower than in the 12-ring materials, which probably means the alkene cycle, with its preference for C_{3+} alkene formation, was more abundant in these materials than in the 12-ring materials, together contributing to their particularly low C_2 selectivity.

Proceeding last to a comparison between the 3D 10-ring materials and 1D 10-ring TON, they gave similar C_3 selectivities. The C_4 selectivity of TON was slightly higher, and the C_2 selectivity much lower, than for the 3D 10-ring materials. TON furthermore gave significantly lower C_4 HTI and aromatics selectivity and a much higher C_{5+} aliphatics selectivity than the 3D 10-ring materials. This last observation shows that the absence of intersection volumes and cavities in the TON structure heavily restricts its ability to form aromatic molecules by intermolecular hydride transfer reactions. The high C_{5+} aliphatics selectivity (which is higher than the combined C_{5+} aliphatics and aromatics selectivities of any other material reported here) further suggests that alkene cracking reactions are sterically restricted in this material. The low C_2 selectivity is further in line with mechanistic studies, which indicated that the alkene cycle dominates in the MTH reaction over TON (See Section 2.2), and with the low selectivity towards ethene in alkene cracking reactions reported in literature.[168]

4 Summary and outlook

Fundamental insight into the MTH reaction has now reached a level where there is general agreement between the currently accepted dual cycle mechanism, which results from decades of mechanistic studies and is reviewed in Section 2 of this contribution and the main trends in shape selectivity observed in the quasi-single parameter study of zeolite structures, reported in Section 3 of this contribution.

Shortly summarised, the product selectivities observed over the 8-ring CHA structure are restricted by product shape selectivity, while the product selectivities observed over 10- and 12-ring zeolites are further restricted by transition-state or intermediate shape selectivity. In particular, it is observed that zeolites with large pores and cavities favor products formed from the arene cycle, with either light or heavy methylbenzenes as main hydrocarbon pool species. Not unexpectedly, these results further suggest that the more space-demanding reaction is the intermolecular hydride transfer reaction, which determines the relative fraction of aromatic versus alkene products, and, hence, influences the relative occurrence of the alkene versus the arene cycle. Within the alkene cycle, cracking reactions appear as the more space-demanding reactions, while methylation reactions are less space-demanding. Moving from large to medium pore zeolites, the product spectrum may thereby be altered from an aromatics- and alkanes-dominated product mixture, *via* a balanced mixture of aliphatic and aromatic products in the C_2–C_{10} range, and finally to a C_{5+}-dominated alkenes product mixture, controlled by transition state or intermediate shape selectivity.

Among open questions, ethene selectivity versus zeolite structure is not straightforwardly explained and deserves further attention. The same applies for the unconventional C_3 yield versus methanol conversion behaviour of TON and MOR zeolites.

Furthermore, systematic studies of parameters other than topology, such as acid strength, acid site density and defect type and concentration, as well as combinations thereof, are presently scarce and therefore heartily welcome.

From a longer perspective, experimental difficulties related to the preparation and detailed characterisation of zeolite/zeotype materials, as well as the complexity of the MTH reaction, point to a predictive modeling approach. As briefly reflected upon in Section 2.3, computational methods have now reached a level of ''near-chemical'' accuracy, and should be further developed. Kinetic studies of individual reaction steps, using a single parameter variation approach, are required for benchmarking of the computational methods. A field which is still in its infancy, but will be increasingly important for establishing truly predictive models for zeolite-catalysed reactions in the future, is multi-scale modeling, taking into account intrinsic reaction rates as well as mass and heat transfer limitations.

References

1 B. Smit and T. L. M. Maesen, *Nature*, 2008, **451**, 671.
2 L. B. McCusker, F. Liebau and G. Engelhardt, *Pure Appl. Chem.*, 2001, **73**, 381.
3 J. X. Jiang, J. H. Yu and A. Corma, *Angew. Chem., Int. Ed.*, 2010, **49**, 3120.
4 C. Baerlocher and L. B. Mccusker, Database of Zeolite Structures: http://www.iza-structure.org/databases/, Accessed 11/04/2013.
5 A. Dyer, An introduction to zeolite molecular sieves, John Wiley and Sons Inc., Chichester, 1988.
6 J. Weitkamp, *Solid State Ionics*, 2000, **131**, 175.
7 W. M. Meier, D. H. Olson and C. Baerlocher, *Atlas of Zeolite Structure Types*, Elsevier, Amsterdam, 5th edn, 2007.
8 R. M. Barrer, *Pure Appl. Chem.*, 1979, **51**, 1091.
9 M. D. Foster and M. M. J. Treacy, http://www.hypotheticalzeolites.net/, Accessed 14/04/2013.
10 Y. Li, J. H. Yu and R. R. Xu, http://mezeopor.jlu.edu.cn/. Accessed 14/04/2013
11 H. Robsen and K. P. Lillerud, *Verified Synthesis of Zeolitic Materials*, Elsevier, Amsterdam, 2nd edn, 2001.
12 F. Di Renzo, *Catal. Today*, 1998, **41**, 37.
13 P. M. Slangen, J. C. Jansen and H. van Bekkum, *Microporous Mater.*, 1997, **9**, 259.
14 K. E. Hamilton, E. N. Coker, A. Sacco, A. G. Dixon and R. W. Thompson, *Zeolites*, 1993, **13**, 645.
15 N. N. Feoktistova and S. P. Zhdanov, *Zeolites*, 1989, **9**, 136.
16 H. Kacirek and H. Lechert, *J. Phys. Chem.*, 1975, **79**, 1589.
17 C. S. Cundy and P. A. Cox, *Microporous Mesoporous Mater.*, 2005, **82**, 1.
18 M. W. Ackley, S. U. Rege and H. Saxena, *Microporous Mesoporous Mater.*, 2003, **61**, 25.

19 R. E. Morris, *Angew. Chem., Int. Ed.*, 2008, **47**, 442.
20 A. Corma, L. T. Nemeth, M. Renz and S. Valencia, *Nature*, 2001, **412**, 423.
21 M. E. Davis, *Nature*, 2002, **417**, 813.
22 J. A. Rabo and M. W. Schoonover, *Appl. Catal., A*, 2001, **222**, 261.
23 A. Corma, *J. Catal.*, 2003, **216**, 298.
24 G. O. Brunner and W. M. Meier, *Nature*, 1989, **337**, 146.
25 A. Corma, M. J. Diaz-Cabanas, J. Jiang, M. Afeworki, D. L. Dorset, S. L. Soled and K. G. Strohmaier, *Proc. Natl. Acad. Sci. U. S. A.*, 2010, **107**, 13997.
26 G. Busca, *Chem. Rev.*, 2007, **107**, 5366.
27 J. A. Moulijn, M. Makkee and A. V. Diepen, *Chemical Process Technology*, Jon Wiley and Sons, New York, 2001.
28 T. F. Degnan, *J. Catal.*, 2003, **216**, 32.
29 A. Corma, *Chem. Rev.*, 1995, **95**, 559.
30 J. F. Haw, *Phys. Chem. Chem. Phys.*, 2002, **4**, 5431.
31 S. Svelle, M. Bjørgen, Selective catalysts for petrochemical industry – shape selectivity in microporous materials, in *Selective Nanocatalysts and Nanoscience: Concepts for Hetereogeneous and Homogeneous Catalysis*, ed. A. Zecchina, S. Bordiga, E. Groppo, Wiley-VCH, 1st edn, 2011.
32 L. Regli, S. Bordiga, C. Lamberti, K. P. Lillerud, S. I. Zones and A. Zecchina, *J. Phys. Chem. C*, 2007, **111**, 2992.
33 J. D. Gale, R. Shah, M. C. Payne, I. Stich and K. Terakura, *Catal. Today*, 1999, **50**, 525.
34 S. Bordiga, L. Regli, D. Cocina, C. Lamberti, M. Bjørgen and K. P. Lillerud, *J. Phys. Chem. B*, 2005, **109**, 2779.
35 S. Bordiga, L. Regli, C. Lamberti, A. Zecchina, M. Bjørgen and K. P. Lillerud, *J. Phys. Chem. B*, 2005, **109**, 7724.
36 C. Paze, S. Bordiga, C. Lamberti, M. Salvalaggio, A. Zecchina and G. Bellussi, *J. Phys. Chem. B*, 1997, **101**, 4740.
37 W. O. Haag and N. Y. Chen, in *Catalyst Design: Progress and Perspectives*, Hegedus, L. L. Ed., New York, 1987.
38 S. Li, A. Zheng, Y. Sul, H. Zhang, L. Chen, J. Yang, C. Ye and F. Deng, *J. Am. Chem. Soc.*, 2007, **129**, 11161.
39 C. J. A. Mota, D. L. Bhering and N. Rosenbach, *Angew. Chem. Int. Ed.*, 2004, **43**, 3050.
40 E. Brunner, H. Ernst, D. Freude, T. Fröhlich, M. Hunger and H. Pfeifer, *J. Catal.*, 1991, **127**, 34.
41 W. E. Farneth and R. J. Gorte, *Chem. Rev.*, 1995, **95**, 615.
42 M. S. Holm, S. Svelle, F. Joensen, P. Beato, C. H. Christensen, S. Bordiga and M. Bjorgen, *Appl. Catal., A*, 2009, **356**, 23.
43 H. Knözinger and S. Huber, *J. Chem. Soc., Faraday Trans.*, 1998, **94**, 2047.
44 J. A. Lercher and A. Jentys, *Stud. Surf. Sci. Catal.*, 2007, **168**, 435.
45 P. B. Weisz, *Pure Appl. Chem.*, 1980, **52**, 2091.
46 S. M. Csicsery, *Pure Appl. Chem.*, 1986, **58**, 841.
47 U. Olsbye, S. Svelle, M. Bjørgen, P. Beato, T. V. W. Janssens, F. Joensen, S. Bordiga and K. P. Lillerud, *Angew. Chem., Int. Ed.*, 2012, **51**, 5810.
48 S. Teketel, U. Olsbye, K. P. Lillerud, P. Beato and S. Svelle, *Microporous Mesoporous Mater.*, 2010, **136**, 33.
49 F. Bleken, W. Skistad, K. Barbera, M. Kustova, S. Bordiga, P. Beato, K. P. Lillerud, S. Svelle and U. Olsbye, *Phys. Chem. Chem. Phys.*, 2011, **13**, 2539.
50 N. S. Nesterenko, F. Thibault-Starzyk, V. Montouillout, V. V. Yuschenko, C. Fernandez, J. P. Gilson, F. Fajula and I. I. Ivanova, *Microporous Mesoporous Mater.*, 2004, **71**, 157.
51 M. Westgård Erichsen, S. Svelle and U. Olsbye, *Catal. Today*, 2013, **215**, 216.

52 J. Kim, C. A. Henao, T. A. Johnson, D. E. Dedrick, J. E. Miller, E. B. Stechel and C. T. Maravelias, *Energy Environ. Sci.*, 2011, **4**, 3122.
53 G. A. Olah, A. Goeppert and G. K. S. Prakash, *J. Org. Chem.*, 2009, **74**, 487.
54 C. D. Chang, *Catal. Rev.-Sci. Eng.*, 1983, **25**, 1.
55 C. D. Chang and A. J. Silvestri, *J. Catal.*, 1977, **47**, 249.
56 S. L. Meisel, J. P. Mccullough, C. H. Lechthaler and P. B. Weisz, *ChemTech*, 1976, **6**, 86.
57 H. Ertl, F. Knözinger, F. Schüth and J. Weitkamp, *Handbook of Heterogeneous Catalysis*, 2nd edn., Wiley-VCM, Weinheim, 2008.
58 M. Stöcker, *Microporous Mesoporous Mater.*, 1999, **29**, 3.
59 J. Cobb, New Zealand Synfuel: The Story of the World's First Natural Gas to Gasoline Plant, Cobb/Horwood Publications, Auckland, New Zealand, 1995.
60 F. J. Keil, *Microporous Mesoporous Mater.*, 1999, **29**, 49.
61 C. D. Chang, *Catal. Today*, 1992, **13**, 103.
62 J. Q. Chen, A. Bozzano, B. Glover, T. Fuglerud and S. Kvisle, *Catal. Today*, 2005, **106**, 103.
63 H. Koempel and W. Liebner, *Stud. Surf. Sci. Catal.*, 2007, **167**, 261.
64 M. Stöcker, *Microporous Mesoporous Mater.*, 2005, **82**, 257.
65 S. Yurchak, *Stud. Surf. Sci. Catal.*, 1988, **36**, 251.
66 S. A. Tabak and S. Yurchak, *Catal. Today*, 1990, **6**, 307.
67 J. Topp-Jørgensen, *Stud. Surf. Sci. Catal.*, 1988, **36**, 293.
68 http://www.uop.com/honeywells-uop-total-petrochemicals-successfully-demonstrate-technology-produce-plastics-feedstocks-oil/, Accessed 29/05/2013.
69 http://www.process-worldwide.com/engineering_construction/plant_design/basic_detail_engineering/articles/393431/, Accessed 29/05/2013.
70 http://www.topsoe.com/about_us/green_commitment/tigas.aspx, Accessed 29/05/2013.
71 http://www.exxonmobil.com/Apps/RefiningTechnologies/default.aspx, Accessed 14/04/2013.
72 http://www.uop.com/honeywells-uop-methanoltoolefins-technology-selected-convert-coal-highvalue-petrochemicals-china/, Accessed 14/04/2013.
73 http://www.uop.com/honeywells-uop-wins-fourth-license-breakthrough-technology-convert-methanol-coal-plastics/, Accessed 28/05/2013.
74 N. Y. Chen and W. J. Reagan, *J. Catal.*, 1979, **59**, 123.
75 W. G. Song, D. M. Marcus, H. Fu, J. O. Ehresmann and J. F. Haw, *J. Am. Chem. Soc.*, 2002, **124**, 3844.
76 D. Lesthaeghe, V. Van Speybroeck, G. B. Marin and M. Waroquier, *Angew. Chem. Int. Ed.*, 2006, **45**, 1714.
77 I. M. Dahl and S. Kolboe, *J. Catal.*, 1996, **161**, 304.
78 I. M. Dahl and S. Kolboe, *Catal. Lett.*, 1993, **20**, 329.
79 I. M. Dahl and S. Kolboe, *J. Catal.*, 1994, **149**, 458.
80 R. M. Dessau and R. B. Lapierre, *J. Catal.*, 1982, **78**, 136.
81 R. M. Dessau, *J. Catal.*, 1986, **99**, 111.
82 M. Bjørgen, S. Svelle, F. Joensen, J. Nerlov, S. Kolboe, F. Bonino, L. Palumbo, S. Bordiga and U. Olsbye, *J. Catal.*, 2007, **249**, 195.
83 Ø. Mikkelsen, P. O. Rønning and S. Kolboe, *Microporous Mesoporous Mater.*, 2000, **40**, 95.
84 B. Arstad and S. Kolboe, *J. Am. Chem. Soc.*, 2001, **123**, 8137.
85 B. Arstad and S. Kolboe, *Catal. Lett.*, 2001, **71**, 209.
86 S. Svelle, F. Joensen, J. Nerlov, U. Olsbye, K. P. Lillerud, S. Kolboe and M. Bjørgen, *J. Am. Chem. Soc.*, 2006, **128**, 14770.

87 S. Svelle, U. Olsbye, F. Joensen and M. Bjørgen, *J. Phys. Chem. C*, 2007, **111**, 17981.
88 B. E. Langner, *Appl. Catal.*, 1982, **2**, 289.
89 R. F. Sullivan, R. P. Sieg, G. E. Langlois and C. J. Egan, *J. Am. Chem. Soc.*, 1961, **83**, 1156.
90 T. Mole, G. Bett and D. Seddon, *J. Catal.*, 1983, **84**, 435.
91 T. Mole, J. A. Whiteside and D. Seddon, *J. Catal.*, 1983, **82**, 261.
92 J. F. Haw, W. G. Song, D. M. Marcus and J. B. Nicholas, *Acc. Chem. Res.*, 2003, **36**, 317.
93 P. W. Goguen, T. Xu, D. H. Barich, T. W. Skloss, W. Song, Z. Wang, J. B. Nicholas and J. F. Haw, *J. Am. Chem. Soc.*, 1998, **120**, 2650.
94 J. F. Haw, P. W. Goguen, T. Xu, T. W. Skloss, W. Song and Z. Wang, *Angew. Chem. Int. Ed.*, 1998, **37**, 948.
95 J. F. Haw, J. B. Nicholas, W. Song, F. Deng, Z. Wang, T. Xu and C. S. Heneghan, *J. Am. Chem. Soc.*, 2000, **122**, 4763.
96 T. Xu, D. H. Barich, P. W. Goguen, W. Song, Z. Wang, J. B. Nicholas and J. F. Haw, *J. Am. Chem. Soc.*, 1998, **120**, 4025.
97 W. G. Song, J. F. Haw, J. B. Nicholas and C. S. Heneghan, *J. Am. Chem. Soc.*, 2000, **122**, 10726.
98 M. Hunger, M. Seiler and A. Buchholz, *Catal. Lett.*, 2001, **74**, 61.
99 M. Seiler, U. Schenk and M. Hunger, *Catal. Lett.*, 1999, **62**, 139.
100 M. Seiler, W. Wang, A. Buchholz and M. Hunger, *Catal. Lett.*, 2003 **88**, 187.
101 M. Bjørgen, U. Olsbye, D. Petersen and S. Kolboe, *J. Catal.*, 2004, **221**, 1.
102 A. Sassi, M. A. Wildman, H. J. Ahn, P. Prasad, J. B. Nicholas and J. F. Haw, *J. Phys. Chem. B*, 2002, **106**, 2294.
103 M. Bjørgen, S. Svelle, F. Joensen, J. Nerlov, U. Olsbye, K. P. Lillerud and S. Kolboe, *J. Am. Chem. Soc.*, 2006, **128**, 14770.
104 M. Bjørgen, F. Joensen, K. P. Lillerud, U. Olsbye and S. Svelle, *Catal. Today*, 2009, **142**, 90.
105 W. Song, H. Fu and J. F. Haw, *J. Am. Chem. Soc.*, 2001, **123**, 4749.
106 B. P. C. Hereijgers, F. Bleken, M. H. Nilsen, S. Svelle, K. P. Lillerud, M. Bjørgen, B. M. Weckhuysen and U. Olsbye, *J. Catal.*, 2009, **264**, 77.
107 M. Bjørgen, S. Akyalcin, U. Olsbye, S. Benard, S. Kolboe and S. Svelle, *J. Catal.*, 2010, **275**, 170.
108 S. Teketel, S. Svelle, K. P. Lillerud and U. Olsbye, *ChemCatChem*, 2009, **1**, 78.
109 J. H. Ahn, B. Temel and E. Iglesia, *Angew. Chem., Int. Ed.*, 2009, **48**, 3814.
110 D. A. Simonetti, J. H. Ahn and E. Iglesia, *J. Catal.*, 2011, **277**, 173.
111 D. A. Simonetti, R. T. Carr and E. Iglesia, *J. Catal*, 2012, **285**, 19.
112 H. Schulz, *Catal. Today*, 2010, **154**, 183.
113 M. Westgård Erichsen, S. Svelle and U. Olsbye, *J. Catal.*, 2013, **298**, 94.
114 D. M. McCann, D. Lesthaeghe, P. W. Kletnieks, D. R. Guenther, M. J. Hayman, V. Van Speybroeck, M. Waroquier and J. F. Haw, *Angew. Chem., Int. Ed.*, 2008, **47**, 5179.
115 D. Lesthaeghe, A. Horre, M. Waroquier, G. B. Marin and V. Van Speybroeck, *Chem. Eur. J.*, 2009, **15**, 10803.
116 S. Kolboe, *J. Phys. Chem. A*, 2012, **116**, 3710.
117 S. Kolboe, S. Svelle and B. Arstad, *J. Phys. Chem. A*, 2009, **113**, 1869.
118 S. Kolboe, *J. Phys. Chem. A*, 2011, **115**, 3106.
119 K. De Wispelaere, K. Hemelsoet, M. Waroquier and V. Van Speybroeck, *J. Catal.*, 2013, **305**, 76.
120 B. Arstad, S. Kolboe and O. Swang, *J. Phys. Chem. A*, 2005, **109**, 8914.

121 O. Sekiguchi, V. Meyer, M. C. Letzel, D. Kuck and E. Uggerud, *Eur. J. Mass Spectrom.*, 2009, **15**, 167.
122 S. Ilias and A. Bhan, *ACS Catal.*, 2013, **3**, 18.
123 G. Mirth and J. A. Lercher, *J. Phys. Chem.*, 1991, **95**, 3736.
124 S. Saepurahman, M. Visur, U. Olsbye, M. Bjørgen and S. Svelle, *Top. Catal.*, 2011, **54**, 1293–1301.
125 S. Svelle, P. O. Rønning, U. Olsbye and S. Kolboe, *J. Catal.*, 2005, **234**, 385.
126 S. Svelle, P. O. Rønning and S. Kolboe, *J. Catal.*, 2004, **224**, 115.
127 I. M. Hill, S. A. Hashimi and A. Bhan, *J. Catal.*, 2012, **285**, 115.
128 I. Hill, A. Malek and A. Bhan, *ACS Catal.*, 2013, **3**, 1992.
129 R. Mantha, S. Bhatia and M. S. Rao, *Ind. Eng. Chem. Res.*, 1991, **30**, 281.
130 S. Rabiu and S. Al-Khattaf, *Ind. Eng. Chem. Res.*, 2008, **47**, 39.
131 H. Vinek, M. Derewinski, G. Mirth and J. A. Lercher, *Appl. Catal.*, 1991, **68**, 277.
132 J. Van der Mynsbrugge, M. Visur, U. Olsbye, P. Beato, M. Bjørgen, V. Van Speybroeck and S. Svelle, *J. Catal.*, 2012, **292**, 201.
133 N. Hazari, J. A. Labinger and V. J. Scott, *J. Catal.*, 2009, **263**, 266.
134 D. A. Simonetti, J. H. Ahn and E. Iglesia, *ChemCatChem*, 2011, **3**, 704.
135 G. M. Mullen and M. J. Janik, *ACS Catal.*, 2011, **1**, 105.
136 S. Borghese, M. Haouas, J. Sommer and F. Taulelle, *J. Catal.*, 2013, **305**, 130.
137 J. S. Buchanan, J. G. Santiesteban and W. O. Haag, *J. Catal.*, 1996, **158**, 279.
138 S. Svelle, C. Tuma, X. Rozanska, T. Kerber and J. Sauer, *J. Am. Chem. Soc.*, 2009, **131**, 816.
139 V. Van Speybroeck, J. Van der Mynsbrugge, M. Vandichel, K. Hemelsoet, D. Lesthaeghe, A. Ghysels, G. B. Marin and M. Waroquier, *J. Am. Chem. Soc.*, 2011, **133**, 888.
140 K. Hemelsoet, J. Van der Mynsbrugge, K. De Wispelaere, M. Waroquier and V. Van Speybroeck, *ChemPhysChem*, 2013, **14**, 1526.
141 B. Arstad, S. Kolboe and O. Swang, *J. Phys. Chem. B*, 2002, **106**, 12722.
142 B. Arstad, S. Kolboe and O. Swang, *J. Phys. Org. Chem.*, 2004, **17**, 1023.
143 B. Arstad, S. Kolboe and O. Swang, *J. Phys. Org. Chem.*, 2006, **19**, 81.
144 B. Arstad, J. B. Nicholas and J. F. Haw, *J. Am. Chem. Soc.*, 2004, **126**, 2991.
145 S. Svelle, B. Arstad, S. Kolboe and O. Swang, *J. Phys. Chem. B*, 2003, **107**, 9281.
146 S. R. Blaszkowski, M. A. C. Nascimento and R. A. vanSanten, *J. Phys. Chem.*, 1996, **100**, 3463.
147 S. R. Blaszkowski and R. A. Vansanten, *J. Phys. Chem.*, 1995, **99**, 11728.
148 S. R. Blaszkowski and R. A. vanSanten, *J. Phys. Chem. B*, 1997, **101**, 2292.
149 S. R. Blaszkowski and R. A. vanSanten, *Top. Catal.*, 1997, **4**, 145.
150 F. Bleken, S. Svelle, K. P. Lillerud, U. Olsbye, B. Arstad and O. Swang, *J. Phys. Chem. A*, 2010, **114**, 7391.
151 S. Grimme, *J. Comput. Chem.*, 2004, **25**, 1463.
152 C. M. Wang, Y. D. Wang, Z. K. Xie and Z. P. Liu, *J. Phys. Chem. C*, 2009, **113**, 4584.
153 D. Lesthaeghe, J. Van der Mynsbrugge, M. Vandichel, M. Waroquier and V. Van Speybroeck, *ChemCatChem*, 2011, **3**, 208.
154 D. Lesthaeghe, B. De Sterck, V. Van Speybroeck, G. B. Marin and M. Waroquier, *Angew. Chem., Int. Ed.*, 2007, **46**, 1311.
155 *NIST Standard Reference Database 85 NIST/TRC Table Database WinTable Version 1.5*.

156 C. D. Chang, C. T. W. Chu and R. F. Socha, *J. Catal.*, 1984, **86**, 289.
157 D. Prinz and L. Riekert, *Appl. Catal.*, 1988, **37**, 139.
158 J. Liu, C. X. Zhang, Z. H. Shen, W. M. Hua, Y. Tang, W. Shen, Y. H. Yue and H. L. Xu, *Catal. Commun.*, 2009, **10**, 1506.
159 F. L. Bleken, T. V. W. Janssens, S. Svelle and U. Olsbye, *Microporous Mesoporous Mater.*, 2012, **164**, 190.
160 S. Teketel, W. Skistad, S. Benard, U. Olsbye, K. P. Lillerud, P. Beato and S. Svelle, *ACS Catal.*, 2012, **2**, 26.
161 W. Skistad, S. Teketel, F. L. Bleken, P. Beato, S. Bordiga, M. H. Nilsen, U. Olsbye, S. Svelle and K. P. Lillerud, *Top Catal.*, 2014, DOI: 10.1007/s11244-013-0170-7.
162 J. E. Bercaw, P. L. Diaconescu, R. H. Grubbs, N. Hazari, R. D. Kay, J. A. Labinger, P. Mehrkhodavandi, G. E. Morris, G. J. Sunley and P. Vagner, *Inorg. Chem.*, 2007, **46**, 11371.
163 R. Ravishankar, D. Bhattacharya, N. E. Jacob and S. Sivasanker, *Microporous Mater.*, 1995, **4**, 83.
164 M. W. Anderson and J. Klinowski, *J. Am. Chem. Soc.*, 1990, **112**, 10.
165 D. Breck, *Zeolite Molecular Sieves*, John Wiley and Sons, New York, 1979.
166 M. L. Maloncy, L. Gora, J. C. Jansen and T. Maschmeyer, *Ars Separatoria Acta*, 2003, **2**, 18.
167 S. Lawton, M. E. Leonowicz, R. Partridge, P. Chu and M. K. Rubin, *Microporous Mesoporous Mater.*, 1998, **23**, 109.
168 Y. V. Kissin, *Catal. Rev.-Sci. Eng.*, 2001, **43**, 85.

“Syngas to liquids via oxygenates”

M. Westgård Erichsen, J. S. Martinez-Espin, F. Joensen, S. Teketel,
P. d. C. Huertas, K. P. Lillerud, S. Svelle, P. Beato, U. Olsbye*

Chapter in “Small-Scale Gas to Liquid Fuel Synthesis”, CRC press (submitted)

IV

“How zeolitic acid strength and composition alter the reactivity of alkenes and aromatics towards methanol”

M. Westgård Erichsen, K. De Wispelaere, K. Hemelsoet, S. Moors T. Deconinck, M. Waroquier S. Svelle, V. Van Speybroeck*, U. Olsbye*

Preliminary Manuscript

V

How zeolitic acid strength and composition alter the reactivity of alkenes and aromatics towards methanol

Marius Westgård Erichsen[†], *Kristof De Wispelaere*[‡], *Karen Hemelsoet*[‡], *Samuel L. C. Moors*[‡], *Thomas Deconinck*[‡], *Michel Waroquier*[‡], *Stian Svelle*[†], *Veronique Van Speybroeck*[‡*], *Unni Olsbye*[†*]

[†] inGAP Centre of Research Based Innovation, Department of Chemistry, University of Oslo, N-0315 Oslo, Norway

[‡] Center for Molecular Modeling (CMM), Ghent University, Technologiepark 903, B-9052 Zwijnaarde, Belgium

* *Corresponding authors*

Abstract:

This work encompasses a combined experimental and theoretical assessment of how zeolitic acid strength affects acid catalysed methylation reactions. Overall, higher reaction rates were observed over the material with higher acid strength. Co-reactions of methanol with benzene at 250 °C in the isostructural AFI materials H-SSZ-24 and H-SAPO-5 revealed large differences in selectivity. While the strongly acidic H-SSZ-24 mainly produced toluene and polymethylbenzenes, high yields of C_{4+} aliphatics were observed over H-SAPO-5. These results strongly suggest that alkene methylation is preferred over H-SAPO-5 even at low conversion during methanol/benzene co-reactions. Furthermore, a comparison of benzene and propene methylation at 350-400 °C revealed a significantly faster rate of benzene than propene methylation in H-SSZ-24, whereas the rates of benzene and propene methylation were similar in H-SAPO-5. The observed difference in reactivity of the two hydrocarbons in both catalysts could be understood after defining two reactivity indices during molecular dynamics simulations of the co-adsorbed complexes. It was found that benzene and methanol are more likely to form a reactive co-adsorbed complex in H-SSZ-24 compared to propene and methanol, while the opposite was observed for H-SAPO-5. The probability to form protonated methanol was higher in the more acidic material and was found to depend on the characteristics of the co-adsorbed hydrocarbon. The combination of these two dynamical properties predicted the experimentally observed reactivities very well. This work thus, for the first time, connects a molecular dynamics study of adsorption behaviour with experimentally observed reactivities.

Highlights:

- Alkene and aromatic methylations are both faster in the strong acidic H-SSZ-24 than in the weaker H-SAPO-5.
- H-SAPO-5 favours reactions involving alkenes even during methanol/benzene co-reactions.
- Benzene methylation is significantly faster than propene methylation in H-SSZ-24, while the two reactions proceed with similar rates in H-SAPO-5.
- A dynamical assessment of the co-adsorption complexes of methanol and benzene or propene in both catalysts correlates well with the experimentally observed reactivities.
- A high probability for both methanol protonation and formation of a pre-reactive complex with benzene was found for H-SSZ-24.

Keywords: Methylation reactions; acid strength; ab initio molecular dynamics; co-adsorption; methanol to olefins; methanol to hydrocarbons

1. Introduction

Acid catalysis is of importance in numerous chemical reactions, not least in the petrochemical industry where acidic zeolite catalysts are used in several major processes [1]. It is generally accepted that the most important acid sites for catalysis over zeolitic materials are Brønsted acidic (proton donating) sites [2]. Fundamental understanding of the effect of Brønsted acid strength on reactions is therefore a topic of major interest. Yet, few examples exist of systematic studies aimed at understanding how a change in acid strength influences reactions [3].

During the last decades, conversion of methanol-to-hydrocarbons (MTH) has received significant attention due to its attractiveness in processes where natural gas, coal or biomass is converted to fuels and chemicals. By tuning the catalyst and reaction conditions, a wide variety of hydrocarbons can be produced [4]. The MTH reaction is catalysed by Brønsted-acidic zeolitic catalysts. It proceeds through a complex network of reactions, referred to as the hydrocarbon pool mechanism [4-8]. The hydrocarbon pool mechanism was initially proposed by Dahl and Kolboe [9-11] and has been the subject of numerous other studies [4, 5, 7]. The hydrocarbon pool mechanism mainly consists of two interrelated reaction cycles in which polymethylbenzenes (polyMBs) and alkenes are sequentially methylated and cracked or de-alkylated to form light alkenes (see Scheme 1.1). These two cycles are often simply referred to as the arene and alkene cycles, respectively. The relative importance of each cycle is determined mainly by three factors: (1) catalyst topology, (2) reaction conditions and (3) acid strength. Both cycles operate simultaneously in the medium pore catalyst H-ZSM-5 [12, 13], but the arene cycle can be suppressed in the narrow channels of H-ZSM-22 [14, 15]. At similar conditions, methanol conversion over large-pore zeolites proceeds mainly via the arene cycle [16-19]. However, the reaction conditions are of great importance, as the alkene

cycle can be promoted in large-pore zeolites when low temperatures and high pressures are employed [20, 21]. Finally, some of the present authors recently demonstrated that the relative importance of the arene and alkene cycle is influenced by the zeolitic acid strength [22, 23].

Considering the complexity of the MTH reaction, studies of individual reactions are valuable tools to enhance the fundamental insight into factors that influence zeolite-catalysed reactions. In this work, the influence of zeolitic acid strength on the methylation of arenes and alkenes was studied in the isostructural, but compositionally different, materials H-SSZ-24 and H-SAPO-5 (AFI structure). H-SSZ-24 is an aluminosilicate zeolite, while H-SAPO-5 is a silicoaluminophosphate. This difference in composition leads to a difference in Brønsted acid strength [23-26]. The main emphasis of this work was on the reaction between methanol and benzene. A schematic overview of reactions which are expected to occur during this co-reaction is shown in Scheme 1.1. While methanol/benzene co-reactions have been performed previously over the same catalysts [22, 23], the focus of the current study was on methylation rather than formation of light alkenes. Thus, the current work was performed at low reactant conversion (mainly below 1 %) and at methanol/benzene molar ratios near or below 1. These conditions were expected to strongly favour the reactions to the left in Scheme 1.1. Furthermore, isotopic labelling was employed to distinguish primary from secondary products.

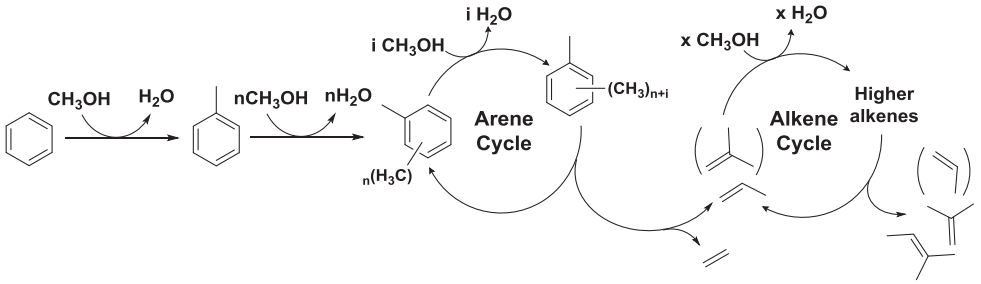

Scheme 1.1: Main reactions occurring during co-reactions between benzene and methanol according to the generally accepted dual cycle mechanism [4, 22]. Benzene is first methylated to form toluene, which may be further methylated to form polymethylbenzenes. These polymethylbenzenes may de-alkylate as part of the arene cycle to yield lower alkenes. The alkenes may react further in an alkene cycle, where they are methylated to higher alkenes, and crack to form mainly branched C_4 and C_5 alkenes. It is assumed that ethene leaves the catalyst without further reaction due to its low methylation rate [27-29].

Additional experiments were performed to directly compare rates of benzene and propene methylation over the two catalysts. The experiments were complemented with a theoretical study on the dynamical adsorption behaviour and reactivity of methanol and the hydrocarbons in both materials. Density Functional Theory (DFT)-based molecular dynamics simulations were found to predict and illuminate the fundamental causes of the experimentally observed differences in reactivity. Recently, some of the present authors performed a molecular dynamics study on the methylation of benzene in H-ZSM-5 and discovered that prior to reaction various protonated methanol clusters can be formed. These methanol clusters seemed to have a lower reactivity towards benzene methylation as compared to single methanol molecules [30]. In this work, dynamical adsorption behaviour is for the first time linked with experimentally observed reactivities.

2. Materials and Methods

2.1. Catalytic tests

The synthesis of H-SSZ-24 and H-SAPO-5 has been described previously [23]. Both samples were characterized by powder XRD, SEM, N_2 adsorption, and CO-adsorption monitored by FT-IR. More details on catalyst characterization are available in the supporting information (S1). Both samples were highly crystalline and exhibited similar BET surface areas. Acid site densities were determined to be 0.11 mmol/g (Si/Al ~ 150) and 0.068 mmol/g (Al+P/Si ~ 240) respectively from TPD of n-propylamine performed in a manner similar to that described by Gorte et al. [31-33]. After pre-treatment in a flow of oxygen at 550 °C, the catalyst was cooled to 150 ºC. 80 ml/min (all flows are at SATP) of N_2 bubbled through a saturator containing n-propylamine at room temperature was then fed over the catalyst for 20 minutes. Subsequently, the catalyst was left at 150 °C in a stream of 80 ml/min N_2 for 4 hours to desorb excess n-propylamine. The temperature was then ramped at 20 °C/min up to 550 °C, and the amount of propene desorbed was quantified using an on-line Pfeiffer Omnistar quadrupole mass spectrometer.

Catalytic tests were performed at atmospheric pressure in fixed bed glass reactors with catalyst powder pressed and sieved to 250-420 μm. Two otherwise identical reactors with inner diameters (i.d.) of 8 mm or 5 mm were employed. Reaction temperature was monitored by a thermocouple protected by a3 mm wide glass sleeve inserted into the middle of the catalyst bed. ^{12}C-methanol (VWR, 99.8 %), ^{13}C-methanol (Cambridge Isotope Laboratories, 99 %), ^{12}C-benzene (Sigma-Aldrich Chromasolv, 99.9 %) and ^{12}C-propene (99.5 %, AGA) were employed as reactants. Liquid reactants were fed over the catalyst by passing a stream of helium through a flask of boiling reactant. The oversaturated helium stream was then passed

upwards through a water-cooled vigreux condenser kept at constant temperature (typically 30°C for methanol and 35°C for benzene) by a circulating thermostat water bath. A range of partial pressures and space velocities could be obtained by adjusting the flow of either of the reactants or a third gas line of pure helium.

Co-reactions between 60 mbar of ^{12}C benzene and a variable partial pressure of ^{12}C or ^{13}C methanol at 250 °C and 350 °C were performed over both catalysts at conditions chosen to obtain low conversion of either reactant. For H-SAPO-5, 40 mg of catalyst in an 8 mm i.d. reactor and a constant total flow of 54.5 ml/min was used, leading to WHSV = 22 $g_{feed}\, g_{catalyst}^{-1}\, h^{-1}$ at partial pressures of 60 mbar for each reactant. For H-SSZ-24, 10 mg catalyst in a 5 mm i.d. reactor was used with a constant total flow of 109 ml/min for a WHSV = 174 $g_{feed}\, g_{catalyst}^{-1}\, h^{-1}$ at 60 mbar partial pressure of each reactant. Two series of experiments (one at each temperature) were performed for each catalyst, where the catalyst was first activated in a flow of oxygen at 550 °C for 1 hour before cooling to reaction temperature and the introduction of reactants. Analyses were performed after 10 minutes time on stream, assuming steady state activity. Between each run, the catalyst was regenerated in oxygen at 550 °C for 1 hour. A slight decrease in catalyst activity was observed between each run. The effects of deactivation on our conclusions were minimized by varying partial pressures in a random order and by periodically returning to a set of reference conditions. This procedure allowed us to report data corrected for deactivation. The correction assumed a constant rate of reaction per acid site irrespective of deactivation.

The rates of benzene and propene methylation were compared at 350 °C and 400 °C. In these experiments, 2.5 mg H-SSZ-24 or 10 mg H-SAPO-5 diluted in 50 mg of quartz (250-420μm) was used in a 5 mm reactor. 60 mbar of methanol was co-reacted with 60 mbar of either benzene or propene, giving WHSV = 762 h^{-1} or 512 h^{-1} respectively over H-SSZ-24 (total flow was 120 ml/min) or 95 h^{-1} or 68 h^{-1} respectively over H-SAPO-5 (total flow was

60 ml/min). The effluent was analysed after 10 minutes of reaction. For the comparison, benzene and propene methylation experiments were performed alternately. Between each run, the catalyst was regenerated for 90 minutes in O_2 at 550 °C.

Both the situation where 2.5 mg catalyst diluted in 50 mg quartz, and when 10 mg catalysed was used alone were checked for bypass by confirming that full conversion of 2-propanol to propene at 200 °C could be achieved in both cases.

Effluent from the reactor was analysed quantitatively by online GC/MS analysis (Agilent 7890 with flame ionisation detector and 5975C MS detector) using two Restek Rtx-DHA-150 columns (150 m, 0.25 mm i.d., stationary phase thickness 1 μm) attached to the same inlet but different detectors. Hydrogen (purity 6.0) was used as carrier gas.

2.2. Computational details

Ab initio calculations in a fully periodic AFI catalyst model were carried out with the CP2K simulation package [34], using a DFT level of theory with a combination of Gaussian and plane wave basis sets (GPW)[35, 36]. The revPBE functional was chosen for its improved catalytic energies compared with the commonly used PBE functional for solid-state calculations [37]. The DZVP-GTH basis set and pseudopotentials were used [38], and the Grimme DFT-D3 approach was applied to account for the attractive van der Waals interactions [39]. The AFI 1x1x2 super cell consists of 145 atoms (Figure S4.1) and contains one Brønsted acid site, which corresponds to Si/Al and (Al+P)/Si ratios of 47 for SSZ-24 and SAPO-5, respectively. Note that this ratio corresponds to a higher acid site density compared

to the samples employed for experiments (150 and 240 respectively). However, the acid site density was still low enough to assume that neighbouring acid sites do not affect each other during reactions. In particular, the shortest distance between two acid sites in the same channel was approximately 17 Å and between two acid sites in adjacent channels 14 Å, indicating that we indeed simulated isolated acid sites. It has previously been found that the rate (per acid site) of propene oligomerisation over H-MFI was affected by the Si/Al ratio for values between 12 and 40, but that a further increase from Si/Al 40 to 140 did not affect the rate [40]. Moreover, mimicking a lower acid site density would require the use of larger super cells, which would increase the computational demands extensively.

Ab initio molecular dynamics (MD) simulations were performed to assess the adsorption behaviour of the guest molecules at realistic reaction temperatures (350 ºC). After an equilibration run of 5 ps, a production run of 50 ps was performed in the NPT ensemble at 1 bar and 350 ºC in which the zeolitic framework is fully flexible. The temperature was controlled via a chain of 5 Nosé-Hoover thermostats. The time-averaged cell parameters were obtained from the NPT MD simulations with the appropriate guest molecules adsorbed in the framework and are summarized in the Supporting Information (section S4). An integration time step of 0.5 fs was applied. A selection of snapshots from the MD simulations was used as input for static geometry optimizations on some relevant adsorption complexes. To calculate the probability that a pre-reactive complex for methylation is formed during an MD simulation of methanol and a co-adsorbed hydrocarbon, the difference between the shortest methanol oxygen – benzene carbon distance and the shortest methanol carbon - benzene carbon distance was traced (SI, Figure S4.2). A sampled state where this difference was higher than 0.5 Å was considered to resemble a pre-reactive complex, as the methyl group pointed towards the benzene ring. The cut-off value of 0.5 Å is chosen arbitrarily, but repetitions of the analysis with other positive cut-off values yielded the same trends. From the

MD runs, the probability to protonate methanol was computed based on a distance criterion; methanol was considered to be protonated if the distance between the Brønsted acid proton and the methanol oxygen was below 1.2 Å. Free energy differences between protonated and neutral methanol were computed from the relative populations of both stable states during an entire MD run, using the following equation [41]:

$$\Delta G_{A,B} = -RT\ ln\frac{P(A)}{P(B)} \qquad (1)$$

Where P(A) and P(B) are the relative populations or probabilities for stable states A and B.

Geometry optimizations were performed based on MD snapshots to calculate (co-) adsorption energies based on the purely electronic energy values, including dispersion corrections. Additionally, transition states were localized using the dimer method implemented in CP2K. A normal mode analysis was performed to confirm that the optimized transition states were true first order saddle points. To determine the pre-reactive complex and products, a quasi-irc approach was applied. A detailed review on various theoretical procedures applied to study zeolite-catalysed reactions can be found in reference [42].

3. Results and discussion

3.1. Co-reactions between benzene and methanol

Figure 3.1 shows the net formation rates of toluene, other aromatic products and aliphatic products over H-SSZ-24 and H-SAPO-5 when 60 mbar of benzene and a variable pressure of methanol were fed over the catalysts at 250 °C. The total rate of hydrocarbon formation was more than twice as high over the stronger acid H-SSZ-24 compared to the weaker acid catalyst H-SAPO-5. At a 1:3 ratio of methanol to benzene (P_{MeOH} = 20 mbar), toluene was the main product in both catalysts. Substantial by-product formation (mainly other aromatics) was observed in H-SSZ-24, while fewer by-products were observed over H-SAPO-5 (see supporting information, S2.1, for detailed selectivity). The other aromatics were mainly polymethylbenzenes (polyMBs) but a significant amount of diphenylmethane was also produced, especially over H-SSZ-24. Isotopic distributions of the aromatic products were found to be consistent with (successive) methylation of ^{12}C benzene by ^{13}C methanol (S2.2). Aliphatic products were produced in too low amounts to enable isotopic analysis.

In addition to the hydrocarbon products displayed in Figure 3.1, significant amounts of dimethyl ether (DME) were formed, in particular over H-SAPO-5 (S2.3). Literature reports conclude that DME and methanol behave similarly as methylating agents, although with slightly higher methylation activity for DME [43-45]. Therefore, no attention will be given to the observed DME/methanol ratios in the following discussion.

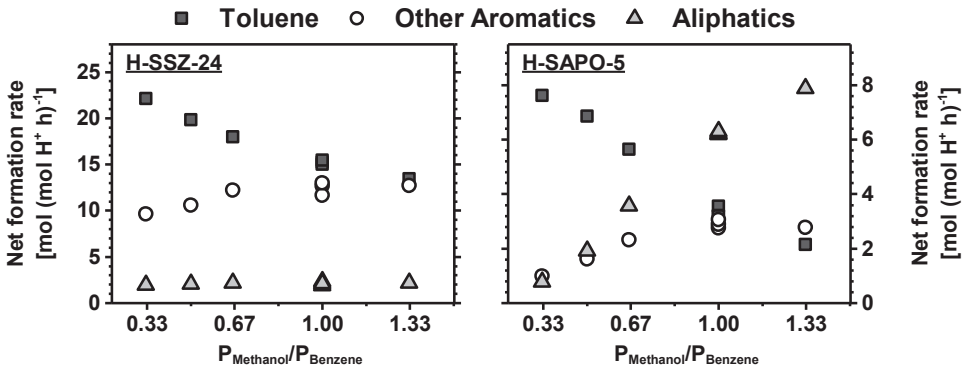

Figure 3.1: Net rates of formation of the main product groups during co-reactions of benzene and methanol as a function of the methanol to benzene molar feed ratio at 250 °C over H-SSZ-24 (left) and H-SAPO-5 (right). $P_{Benzene}$ = 60 mbar. Benzene feed rate = 13×10^3 mol (mol $H^+)^{-1}$ h^{-1} over H-SSZ-24 and 2.9×10^3 mol (mol $H^+)^{-1}$ h^{-1} over H-SAPO-5. Total WHSV = 140-191 h^{-1} (H-SSZ-24) or 17.5-24 h^{-1} (H-SAPO-5). The data have been corrected for deactivation.

Returning to the hydrocarbon product distributions, we concentrate first on H-SSZ-24 (Figure 3.1, left). With increasing methanol partial pressure, the net formation rate of other aromatics slowly increased, while the net toluene formation rate decreased more significantly over H-SSZ-24. A slight decrease in benzene conversion (from 0.21 to 0.18%) with increasing methanol pressure was also observed. The decrease was accompanied by an increased conversion of toluene formed from benzene methylation, to form either polyMBs or diphenylmethane. Rapid methylation of toluene to polyMBs is consistent with an increasing methylation rate per methyl group present on the aromatic ring [46-49]. The fraction of aliphatic products increased slightly (from 1.9 - 2.2 mol [mol H^+ $h]^{-1}$) with increasing methanol partial pressure, but remained small compared to aromatics over H-SSZ-24. Interestingly, the ratio between rates of formation for other aromatics and aliphatics remained roughly constant within the investigated range. This observation strongly suggests that aliphatic products were mainly formed by de-alkylation of aromatics (See Scheme 1.1). This conclusion is consistent with previous co-reactions performed at higher conversion and with an excess of methanol [23].

Figure 3.1 (right) shows that over H-SAPO-5, similarly to what was observed over H-SSZ-24, an increase in methanol partial pressure led to a decrease in the net rate of toluene formation due to over-methylation to other aromatics. Unlike what was observed over H-SSZ-24, the rate of aliphatic formation increased rapidly with increasing methanol pressure over H-SAPO-5. At a 1:1 molar feed ratio of benzene and methanol, aliphatic products accounted for about 50 % of the total molar amount of products formed. Furthermore, the formation rates of aliphatics and other aromatics were not correlated, in contrast to what was found over H-SSZ-24 (Figure 3.1, left). The increased net rate of aliphatics formation was accompanied by a significant decrease in benzene conversion. While 0.27 % of the benzene feed was converted at the lowest molar feed ratio (methanol/benzene = 0.33), benzene conversion was only 0.16 % at the highest molar feed ratio (1.33).

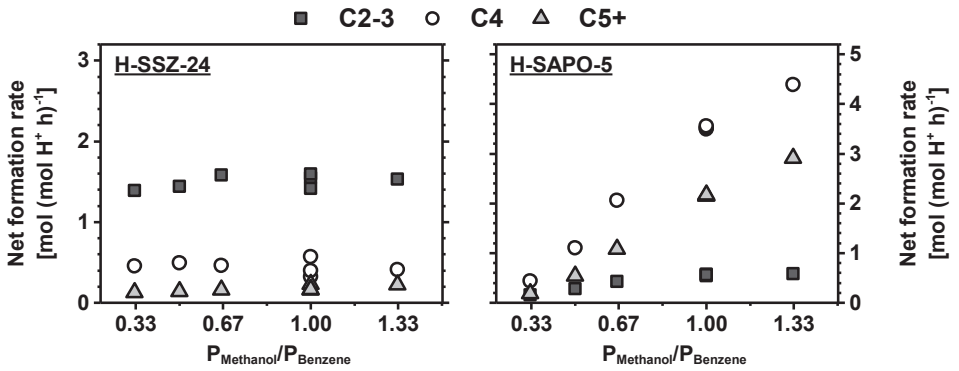

Figure 3.2: Net rates of formation for aliphatic products during co-reactions of benzene and methanol as a function of the methanol to benzene molar feed ratio at 250 °C over H-SSZ-24 (left) and H-SAPO-5 (right). $P_{Benzene}$ = 60 mbar. Benzene feed rate = 13×10^3 mol (mol H^+)$^{-1}$ h^{-1} over H-SSZ-24 and 2.9×10^3 mol (mol H^+)$^{-1}$ h^{-1} over H-SAPO-5. Total WHSV = 140-191 h^{-1} (H-SSZ-24) or 17.5-24 h^{-1} (H-SAPO-5). The data have been corrected for deactivation.

Figure 3.2 displays a breakdown of the different aliphatic products produced, grouped by their carbon number over the two catalysts. A clear difference in the size of the aliphatics was observed over the two materials. While the aliphatics formed over H-SSZ-24 were mainly C_2-C_3, as well as a smaller fraction of C_4, most of the aliphatics formed over H-SAPO-

5 contained four or more carbon atoms. This size difference closely mirrors what was previously observed during co-reactions of ^{13}C-methanol and ^{12}C-benzene at higher conversion and excess methanol [23]. In that work, a distinct isotopic labelling pattern of the aliphatic fraction was observed, leading to the conclusion that polyMB de-alkylation could account for the majority of C_2-C_4 alkene formation over H-SSZ-24. On the other hand, the main aliphatics fraction over H-SAPO-5, C_{4+} alkenes, was predominantly formed via the alkene cycle. It is noteworthy that the aliphatic product distribution in Figure 3.2 matches the expected distribution from polyMB de-alkylation over H-SSZ-24, while the majority of the aliphatics formed in H-SAPO-5 correspond to the expected products of the alkene cycle.

The observations made so far may be understood by linking them to the reaction cycles shown in Scheme 1.1. The data reported in Figures 3.1 and 3.2 show that alkene methylation is strongly favoured over benzene methylation in H-SAPO-5, as the concentration of benzene in the effluent is 2-3 orders of magnitude higher than the concentration of aliphatics. This result is in stark contrast to the situation observed in the stronger acidic catalyst H-SSZ-24, where methylation of aromatics dominates.

Similar experiments were performed at 350 °C, and these are included in the supporting information (Section S3). While the difference between the two samples was not as dramatic at 350 °C as at 250 °C, significantly higher amounts of C_{4+} aliphatics were observed over H-SAPO-5 than over H-SSZ-24 also at the higher temperature. An increased relative importance of benzene methylation in H-SAPO-5 with increasing temperature suggests a higher activation energy for benzene methylation than for methylation of the relevant alkenes. However, this was not investigated further.

3.2. Experimental and theoretical comparison of benzene and propene methylation

3.2.1 Experiment

To obtain a more fundamental understanding of the difference in product selectivity between the catalysts studied here, additional experiments were carried out to compare the rate of alkene methylation to that of benzene methylation. In this case, propene was used as the model compound for the alkene hydrocarbon-pool species. The methylation experiments (^{13}C-methanol plus ^{12}C-propene or ^{12}C-benzene) were conducted alternately in order to obtain the best possible comparison between rates of benzene and propene methylation without the influence of significant deactivation or individual variations of activity between catalyst batches. For an even more detailed understanding of the reactivity of benzene and propene in both materials, a molecular dynamics study was performed to link the dynamical behaviour of co-adsorbed complexes with the observed reactivity towards methylation (*vide infra*).

Due to difficulties in obtaining sufficient selectivity to the first product of propene methylation at low temperatures and conditions similar to those used for benzene methylation, the experiments were performed at 400 °C and 350 °C, and with even higher feed rates than employed in Section 3.1. At 400 °C and a 1:1 molar feed ratio of methanol and benzene, toluene selectivities of approximately 50 mol % and 35 mol % were obtained over H-SSZ-24 and H-SAPO-5 respectively. The dominant by-products in both catalysts were polyMBs. At similar conditions during propene methylation, the selectivity to n-butenes was 29 mol% and 43 mol% in H-SSZ-24 and H-SAPO-5 respectively. The by-products of propene methylation were more varied than during benzene methylation, with branched C_4s and C_6 alkenes as the largest groups. An overview of the experiments, including conversion and selectivities are given in S3.1. The isotopic distributions suggested that C_6 alkenes were mainly formed from dimerization of propene, while branched C_4, aromatic and other aliphatic (C_{2-5}) compounds resulted from a combination of C_4 methylation and cracking (S3.2).

Net formation rates for the first methylation product from each co-feed experiment are shown in Figure 3.3. The net rate of toluene formation from benzene methylation was found to be three times higher than that of n-butene formation from propene methylation over H-SSZ-24 at 400 °C. MS analysis confirmed that the first methylation products in all experiments contained one ^{13}C atom originating from methanol (S3.2). Furthermore, the total conversion of all reactant was nearly twice as high during benzene co-feeding as during propene co-feeding (Figure S3.1). This means that the difference could not be ascribed simply to a selectivity difference. Remarkably, this difference was not observed over H-SAPO-5. Instead, the net rate of propene methylation was only slightly lower than the net rate of benzene methylation over H-SAPO-5. The same was observed for the total conversion of reactants to any product (Figure S3.1).

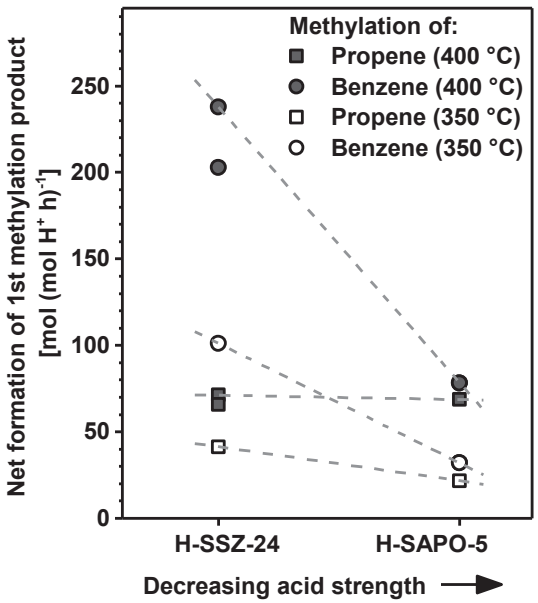

Figure 3.3: Rates of formation for n-butenes (squares) and toluene (circles) during co-reactions of methanol and propene or benzene, respectively, at 400 °C and 350 °C over H-SSZ-24 and H-SAPO-5. All reactant partial pressures were 60 mbar. The data for H-SAPO-5 has been corrected for deactivation, but raw data is reported for H-SSZ-24 as no clear deactivation trend was observed. Thus, there are 2 different data points each for propene and benzene methylation over H-SSZ-24 at 400 °C. Feed rates of propene/benzene/methanol = 6.9×10^3 mmol g_{cat}^{-1} h^{-1} (H-SSZ-24) and 0.87×10^3 mmol g_{cat}^{-1} h^{-1} (H-SAPO-5).

Experiments performed at 350 °C displayed the same trend as at 400 °C. Figure 3.3 clearly shows similar net rates of benzene and propene methylation over H-SAPO-5, but a significantly higher net rate of benzene methylation than propene methylation over H-SSZ-24. However, a lower selectivity to n-butenes than at 400 °C during propene/methanol co-reactions was observed over both materials at 350 °C (22 mol % over H-SSZ-24 and 33 mol% over H-SAPO-5). The main reason for the low selectivity to n-butenes at 350 °C over H-SSZ-24 was an increased rate of propene dimerization compared to at 400 °C. An inverse correlation between temperature and dimerization rate has previously been reported by Svelle et al. [28] over H-ZSM-5. Dimerization was also observed over H-SAPO-5, but the net rate was smaller relative to methylation in comparison with H-SSZ-24, and was lower at 350 °C than 400 °C. The selectivity to toluene at 350 °C was higher than at 400 °C over H-SAPO-5, but slightly lower over H-SSZ-24 (around 45 mol% in both materials) during benzene/methanol co-reactions.

The observed decrease in the methylation rate of both reactants over the weaker acid H-SAPO-5 was expected. However, the large difference in the relative rates of benzene and propene methylation between H-SSZ-24 and H-SAPO-5 is surprising. To the best of our knowledge, the only other report on relative differences in rates based on acid strength was recently performed by Macht et al [50]. They observed that for the two reactions of hexane isomerisation and butanol dehydration, the latter reaction was less sensitive to a decrease in acid strength when utilising Keggin-type polyoxometalate clusters and zeolite H-Beta as catalysts. They proposed that the reason for this difference was that the more localised charge of the butanol dehydration transition state (TS) was better stabilised by a low acid strength than the slightly more delocalised charge of the hexane isomerisation TS. In what follows, a detailed analysis of the adsorption complexes found in both materials is given, based on theoretical calculations.

3.2.2 Molecular modelling

To get a thorough understanding of the experimentally observed difference in reactivity of benzene and propene towards methylation in both AFI materials, MD simulations of co-adsorbed methanol-benzene and methanol-propene complexes were performed. Thereby, two reactivity indices were defined: the probability of forming co-adsorbed complexes exhibiting a proper orientation for methylation and the probability of forming a protonated methanol molecule. For this analysis, MD techniques are required to sample all possible orientations appropriately. During the MD simulations at 350 ºC, the zeolitic framework simulation cell was loaded with 1 methanol and 1 benzene or propene molecule, and a 50 ps simulation was run. It was observed that methanol, rather than benzene or propene, covered the acid site throughout nearly the entire simulation in both materials. This is due to a relatively strong hydrogen bond between methanol and the Brønsted acid site. During the first couple of picoseconds of each simulation, methanol repelled the hydrocarbon from the acid site, as depicted for methanol and benzene in H-SAPO-5 in Figure 3.4. Methanol was considered to occupy the acid site if the distance between the methanol oxygen and the framework oxygens surrounding the substitutional defect was shorter than 3.5 Å (Supporting Information, section S5). That methanol mainly occupied the acid site implies that hydrocarbons suitable for methylation will be co-adsorbed and interact with the framework and methanol, but not directly with the acid site. This can also be concluded by tracing the shortest hydrocarbon – acid site distance and the orientation of the co-adsorbed hydrocarbons in the AFI channel (Supporting Information, S5).

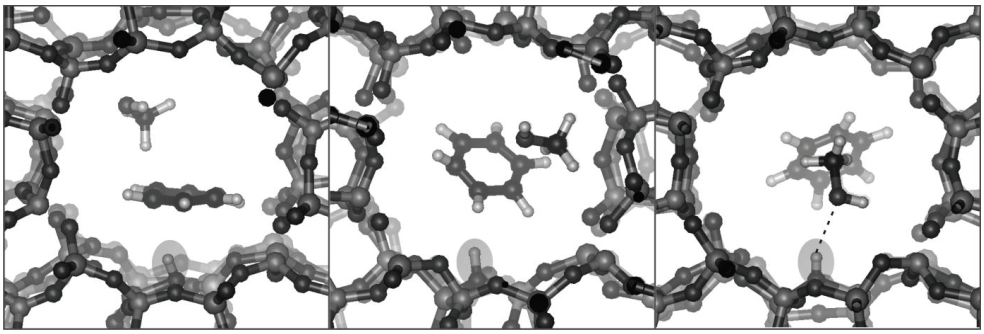

Figure 3.4: Left: Initial structure with benzene occupying the acid site and MeOH co-adsorbed in H-SAPO-5. Middle: during the first 1-2 ps of the MD simulation at 350 ºC methanol replaces benzene on the acid site. Right: methanol remains adsorbed on the acid site throughout the rest of the simulation. The acid site is highlighted.

Subsequently, geometry optimizations based on some relevant snapshots of the MD simulations were performed to get a detailed insight into the various stable co-adsorbed complexes that can be formed. Except for the co-adsorption of benzene in H-SSZ-24, two stable co-adsorption complexes of methanol and benzene or propene could be located on the potential energy surface at 0 K. One of these geometries strongly resembles a pre-reactive complex for the methylation reaction (Figure 3.5 (a) and (c)). A selection of the most important optimized co-adsorption complexes is displayed in Figure 3.5; a complete overview of all structures in both catalysts is given in Figure S6.1 and Figure S6.2. The corresponding adsorption energies for the selected snapshots are summarized in Table S6.1. The reported adsorption energies are purely electronic values and may give some insight into the interaction strength between guest molecules and the host material. A complete analysis of enthalpic and entropic contributions to fully understand the adsorption thermodynamics is beyond the scope of this article.

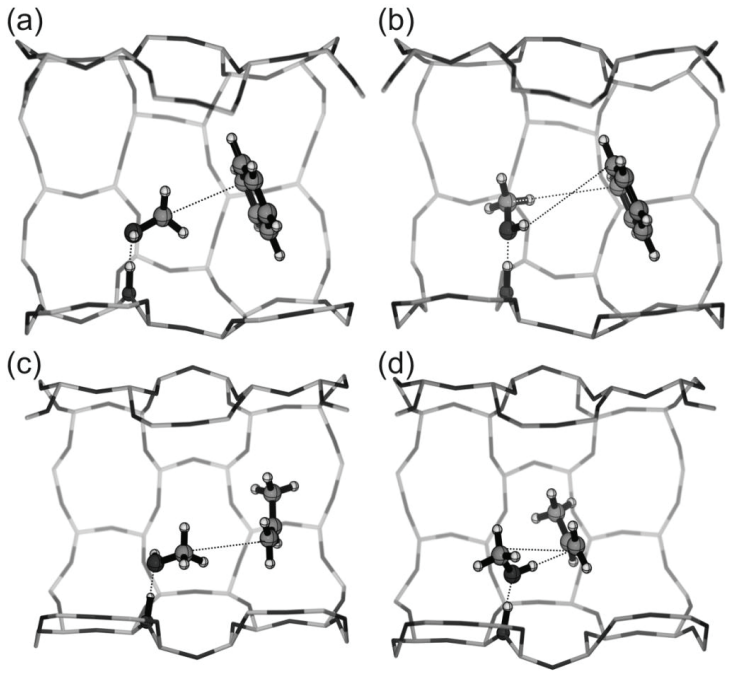

Figure 3.5. Optimized co-adsorbed complexes of methanol and benzene (a,b) and methanol and propene (c,d) in H-SSZ-24 and H-SAPO-5. Complexes a, c, and d apply for both H-SSZ-24 and H-SAPO-5.

As expected, methanol adsorption was stronger in the more acidic H-SSZ-24. Co-adsorption of benzene or propene was slightly more energetically favourable in H-SAPO-5 than in H-SSZ-24, which points to stronger interactions between guest molecules and the more polar silicoaluminophosphate. For H-SAPO-5, two energetically equivalent[1] adsorption complexes were found: with the methanol methyl group either pointing towards (Figure 3.5a) or away from (Figure 3.5b) benzene. For H-SSZ-24 the latter could not be located as a potential energy minimum. Two similar minima could be located on the potential energy surface in both structures (Figure 3.5c and d) for propene co-adsorption. In H-SSZ-24 the two stable states are energetically equivalent, whereas in H-SAPO-5 there is a slight preference

[1] For the DFT calculation performed here, energy differences up to 5 kJ/mol are considered insignificant.

for co-adsorption with a direct methanol proton – π-electron interaction (shown in Figure 3.5d). The multiple localized potential energy minima indicate the complexity of the potential energy surface (PES) of the co-adsorbed molecules in this large pore zeolite material, hence molecular dynamics are an indispensable tool to sample larger portions of the PES.

To clearly demonstrate the differences between the two materials, the probabilities of finding protonated methanol complexes and pre-reactive complexes for methylation during the MD runs were calculated, as both quantities are related to the reactivity of the co-adsorbed compounds towards methylation. The average shortest carbon-carbon interaction distances between methanol and benzene during the MD simulations at 350 ºC were 5.41 Å and 5.61 Å in H-SSZ-24 and H-SAPO-5 respectively. A shorter carbon-carbon atom interaction distance suggests a slightly higher methylation reactivity, as the distance the methyl group will have to bridge to form a transition state is smaller. To confirm the latter, we calculated transition states and the corresponding pre-reactive and product complexes for benzene methylation (Figure S7.1). The pre-reactive complex indeed resembles the states identified during the MD run with shorter C_{MeOH} - $C_{benzene}$ distance. A detailed kinetic analysis based on these optimized transition states is beyond the scope of this study but has been reported earlier for benzene methylation in H-ZSM-5 and H-beta [51]. To distinguish structures resembling the pre-reactive complex from other sampled states in the MD simulations at 350 ºC, the difference between the shortest methanol oxygen – benzene carbon distance and the shortest methanol carbon - benzene carbon distance was traced (Figure S4.2). A sampled state where this difference was higher than 0.5 Å was considered to resemble a pre-reactive complex, as the methyl group pointed towards the benzene ring. The probability to sample a pre-reactive complex was 35 % in H-SSZ-24 and 17 % in H-SAPO-5 (vertical axis in Figure 3.6). Furthermore, the distances between the methanol oxygen and the Brønsted acid proton during the MD runs of methanol and benzene indicated that methanol is protonated 19 % of the time

in H-SSZ-24, but only 2 % of the time in H-SAPO-5 (horizontal axis in Figure 3.6). From the relative population of the protonated and deprotonated state of methanol, free energy differences of 8 kJ/mol and 21 kJ/mol are obtained for protonation of methanol in the co-adsorbed complexes in H-SSZ-24 and H-SAPO-5 respectively, indicating a higher reactivity of the more acidic material (Eq. 1). This observation is straightforwardly correlated with the higher acid strength of H-SSZ-24 [52]. Note that both axes in Figure 3.6 indicate an increasing degree of reactivity. Additionally, it should be mentioned that the quantities on both axes are not expected to be 100% uncorrelated. Due to the charge transfer that occurs during methanol protonation, the interactions between methanol and benzene or propene will be slightly altered.

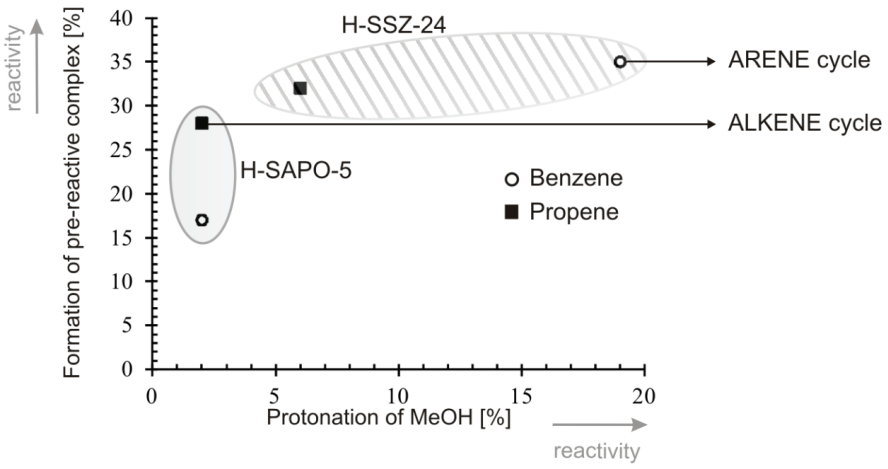

Figure 3.6: Degree of protonation of methanol versus the probability for the formation of a pre-reactive complex at 350 ºC for benzene and propene in H-SSZ-24 (shaded area) and H-SAPO-5 (filled area).

For co-adsorbed propene and methanol, the average shortest methanol carbon – propene carbon distances from the MD simulations were 5.83 Å in H-SSZ-24 and 5.54 Å in H-SAPO-5. In H-SSZ-24, this distance was significantly larger than for the corresponding co-adsorption complex for methanol and benzene (5.41 Å). In H-SAPO-5, the opposite was observed: the shortest methyl carbon – propene bond was slightly shorter than what was observed for benzene co-adsorption (5.61 Å). An overview of the time-averaged shortest distances is given in Figure S8.1. Furthermore, the optimized structure with the shortest methanol carbon – propene carbon distance (Figure 3.5c) looks like a pre-reactive complex for the methylation reaction, indicating that a geometrical analysis of the MD simulation can again reveal information on the reactivity of a co-adsorbed system. Note that kinetic studies on propene methylation in various zeolites were reported elsewhere [53, 54]. To compute the probability for sampling a pre-reactive complex during an MD run, the same procedure as described above for benzene co-adsorption was applied. The probabilities of sampling geometries in which the methanol methyl group points towards propene were 32 % and 28 % for H-SSZ-24 and H-SAPO-5 respectively (vertical axis in Figure 3.6). An analysis of the degree of methanol protonation in presence of propene further indicated that methanol was protonated during 6 % of the simulation time in H-SSZ-24, and 2 % of the simulation time in H-SAPO-5 (horizontal axis in Figure 3.6). The corresponding free energy differences were 15 and 20 kJ/mol for protonation of methanol with co-adsorbed propene in H-SSZ-24 and H-SAPO-5 respectively.

While the probability to form a pre-reactive complex with benzene was twice as high in H-SSZ-24 as in H-SAPO-5, the formation probabilities of a pre-reactive complex with propene in the two catalysts are very similar. Furthermore, the ease of protonation depends not only on the acid strength of the inorganic catalyst material, but also on the co-adsorbed

hydrocarbon compounds. In particular for H-SSZ-24, it can be concluded that protonation of methanol is enhanced by co-adsorption of benzene, compared to co-adsorption of propene.

In Figure 3.6, the reactivity increases from bottom-left to top-right, implying a higher general reactivity of H-SSZ-24 compared to H-SAPO-5. This is in line with the higher acid strength of H-SSZ-24 and was also observed experimentally, as all experimental reaction rates were significantly higher over H-SSZ-24 than over H-SAPO-5. From the experiments reported in Section 3.1 it could be concluded that reactions involving aromatics dominate over H-SSZ-24, whereas reactions involving aliphatics are strongly favoured over H-SAPO-5 (Figures 3.1 and 3.2). Furthermore, the methylation experiments of benzene and propene displayed in Figure 3.3 clearly show that while the rate of benzene methylation is significantly higher than that of propene methylation over H-SSZ-24, the two rates are similar over H-SAPO-5. The reactivity predicted by the probabilities for pre-reactive complex formation and the probability for methanol protonation during MD simulations correlate very well with these experimental findings. Figure 3.6 indicates a higher reactivity for benzene methylation than propene in H-SSZ-24, which was also observed experimentally (Figure 3.3). This, in turn, is in line with the arene cycle dominating the product formation in the MTH reaction over H-SSZ-24. Figure 3.6 also predicts a slightly higher methylation rate for propene than for benzene in H-SAPO-5, due to a higher probability of forming a pre-reactive complex. This is again in line with the experimental observation that the alkene cycle dominates the MTH reaction over H-SAPO-5. While Figure 3.3 displays a lower rate of propene than benzene methylation at 350 °C in H-SAPO-5, the lower selectivity to n-butenes during propene methylation than to toluene during benzene methylation may mask small differences in the methylation rates. When all products are considered, the total reactant conversion was slightly higher when propene was co-reacted with methanol than when benzene was co-reacted with methanol at 350 °C (see Figure S3.1).

Summarized, careful geometrical analysis of the MD trajectories at 350 ºC reveals that the probability to form a pre-reactive complex, combined with the degree of methanol protonation predicts the reactivity of co-adsorbed methanol and benzene or propene towards methylation reactions. Furthermore, the predicted and experimentally observed reactivity towards methylation of benzene and propene correlates well with the previously observed dominance of product formation fromthe arene cycle over H-SSZ-24 and the alkene cycle over H-SAPO-5 during the MTH reaction [23].

All simulations reported so far assume a one-step methylation mechanism. Methylation reactions can also occur in a stepwise fashion via a framework bound methoxy group [55]. MD simulations of both AFI materials loaded with a methoxy group and a co-adsorbed benzene or propene molecule at 350 ºC were performed. Analysis of the shortest distance between the methoxy group and the benzene or propene molecule indicates the same trend as observed for methanol as direct methylating agent. For the methoxy – benzene complex in H-SSZ-24 again a significantly shorter average interaction distance is observed (Supporting Information, S9). These results indicate that the prediction of reactivity of alkenes and aromatics towards methanol based on the dynamical behaviour of co-adsorbed complexes is irrespective of the exact methylation pathway.

4. Conclusions

In this study, a thorough assessment of the influence of zeolitic acid strength on zeolite-catalysed reactions was made by co-reaction experiments and molecular simulations of methanol and benzene and methanol and propene in the isostructural AFI materials H-SSZ-24 and H-SAPO-5. In line with what was earlier found for the MTH reaction in both catalysts, H-SAPO-5 clearly favours reactions involving alkenes, even at high benzene partial pressures and lower than 0.3 % benzene conversion at 250°C. A direct comparison of benzene and propene methylation at 350-400 °C further revealed that benzene methylation was significantly faster than propene methylation in H-SSZ-24, whereas the two reactions occur at similar rates in H-SAPO-5. A molecular level understanding of this observation was provided by performing DFT molecular dynamics simulations. As many energy minima may occur at real operating conditions, a molecular dynamics approach was applied. It could be concluded that benzene and methanol are likely to form a highly favourable co-adsorbed complex in H-SSZ-24. The trends in reactivity could be predicted from the geometries of the co-adsorbed methanol – hydrocarbon complexes in the two catalysts, combined with the degree of methanol protonation at 350 ºC. The latter was found to depend both on the zeolitic acidity and the characteristics of the co-adsorbed hydrocarbon. In particular, for co-adsorbed benzene in the more acidic H-SSZ-24, a highly favourable adsorption complex combined with a low free energy for methanol protonation predicts a significantly higher reactivity than for any of the other investigated situations. These theoretical findings confirm the observed experimental methylation rates and provide insight into why the MTO product formation is governed by different catalytic cycles in both AFI materials. Future work will focus on the comparison of experimentally obtained and theoretically calculated methylation rates under different process conditions in both materials.

Acknowledgements

This publication is part of the inGAP Centre of Research-based Innovation, which receives financial support from the Norwegian Research Council under Contract No. 174893.

K.D.W. is a PhD fellow funded by the Foundation of Scientific Research - Flanders (FWO). We are grateful to the Research Board of Ghent University and BELSPO in the frame of IAP P7/05. Funding was also received from the European Research Council under the European Community's Seventh Framework Program [FP7(2007-2013) ERC grant agreement number 240483]. Computational resources and services used in this work were provided by the Stevin Supercomputer Infrastructure of Ghent University and by the VSC (Flemish Supercomputer Center), funded by the Hercules Foundation and the Flemish Government – department EWI.

5. References

[1] T. Maesen, in: J. Čejka, H. van Bekkum, A. Corma, F. Schüth (Eds.) Introduction to zeolite science and practice, Elsevier, Amsterdam, 2007, pp. 1.

[2] J.F. Haw, Phys. Chem. Chem. Phys., 4 (2002) 5431.

[3] F. Bleken, M. Bjorgen, L. Palumbo, S. Bordiga, S. Svelle, K.P. Lillerud, U. Olsbye, Top. Catal., 52 (2009) 218.

[4] U. Olsbye, S. Svelle, M. Bjørgen, P. Beato, T.V.W. Janssens, F. Joensen, S. Bordiga, K.P. Lillerud, Angew. Chem. Int. Ed., 51 (2012) 5810.

[5] K. Hemelsoet, J. Van der Mynsbrugge, K. De Wispelaere, M. Waroquier, V. Van Speybroeck, ChemPhysChem, 14 (2013) 1526.

[6] M. Stöcker, Microporous Mesoporous Mater., 29 (1999) 3.

[7] S. Ilias, A. Bhan, ACS Catal., 3 (2013) 18.

[8] J.F. Haw, W.G. Song, D.M. Marcus, J.B. Nicholas, Acc. Chem. Res., 36 (2003) 317.

[9] I.M. Dahl, S. Kolboe, J. Catal., 161 (1996) 304.

[10] I.M. Dahl, S. Kolboe, J. Catal., 149 (1994) 458.

[11] I.M. Dahl, S. Kolboe, Catal. Lett., 20 (1993) 329.

[12] M. Bjørgen, S. Svelle, F. Joensen, J. Nerlov, S. Kolboe, F. Bonino, L. Palumbo, S. Bordiga, U. Olsbye, J. Catal., 249 (2007) 195.

[13] S. Svelle, F. Joensen, J. Nerlov, U. Olsbye, K.-P. Lillerud, S. Kolboe, M. Bjørgen, J. Am. Chem. Soc., 128 (2006) 14770.

[14] S. Teketel, U. Olsbye, K.P. Lillerud, P. Beato, S. Svelle, Microporous Mesoporous Mater., 136 (2010) 33.

[15] S. Teketel, S. Svelle, K.P. Lillerud, U. Olsbye, ChemCatChem, 1 (2009) 78.

[16] M. Bjørgen, S. Akyalcin, U. Olsbye, S. Benard, S. Kolboe, S. Svelle, J. Catal., 275 (2010) 170.

[17] S. Svelle, U. Olsbye, F. Joensen, M. Bjørgen, J. Phys. Chem. C, 111 (2007) 17981.

[18] M. Bjørgen, F. Joensen, K.-P. Lillerud, U. Olsbye, S. Svelle, Catal. Today, 142 (2009) 90.

[19] M. Bjørgen, U. Olsbye, D. Petersen, S. Kolboe, J. Catal., 221 (2004) 1.

[20] J.H. Ahn, B. Temel, E. Iglesia, Angew. Chem. Int. Ed., 48 (2009) 3814.

[21] D.A. Simonetti, J.H. Ahn, E. Iglesia, J. Catal., 277 (2011) 173.

[22] M. Westgård Erichsen, S. Svelle, U. Olsbye, J. Catal., 298 (2013) 94.

[23] M. Westgård Erichsen, S. Svelle, U. Olsbye, Catal. Today, 215 (2013) 216.

[24] J. Sauer, K.P. Schroder, V. Termath, Collect. Czech. Chem. Commun., 63 (1998) 1394.

[25] S. Bordiga, L. Regli, D. Cocina, C. Lamberti, M. Bjørgen, K.P. Lillerud, J. Phys. Chem. B, 109 (2005) 2779.

[26] R. Shah, J. D. Gale, M. C. Payne, Chem. Commun., (1997) 131.

[27] S. Svelle, P.O. Rønning, S. Kolboe, J. Catal., 224 (2004) 115.

[28] S. Svelle, P.O. Rønning, U. Olsbye, S. Kolboe, J. Catal., 234 (2005) 385.

[29] I.M. Hill, S.A. Hashimi, A. Bhan, J. Catal., 291 (2012) 155.

[30] S.L.C. Moors, K. De Wispelaere, J. Van der Mynsbrugge, M. Waroquier, V. Van Speybroeck, ACS Catal., 3 (2013) 2556.
[31] R.J. Gorte, Catal. Lett., 62 (1999) 1.
[32] O. Kresnawahjuesa, R.J. Gorte, D. de Oliveira, L.Y. Lau, Catal. Lett., 82 (2002) 155.
[33] R.J. Gorte, Catal. Today, 28 (1996) 405.
[34] J. VandeVondele, M. Krack, F. Mohamed, M. Parrinello, T. Chassaing, J. Hutter, Comput. Phys. Commun., 167 (2005) 103.
[35] G. Lippert, J. Hutter, M. Parrinello, Theor. Chem. Acc., 103 (1999) 124.
[36] G. Lippert, J. Hutter, M. Parrinello, Mol. Phys., 92 (1997) 477.
[37] K. Yang, J.J. Zheng, Y. Zhao, D.G. Truhlar, J. Chem. Phys., 132 (2010) 10.
[38] S. Goedecker, M. Teter, J. Hutter, Phys. Rev. B, 54 (1996) 1703.
[39] S. Grimme, J. Antony, S. Ehrlich, H. Krieg, J. Chem. Phys., 132 (2010) 19.
[40] A.N. Mlinar, P.M. Zimmerman, F.E. Celik, M. Head-Gordon, A.T. Bell, J. Catal., 288 (2012) 65.
[41] D. Frenkel, B. Smit, Understanding molecular simulations, second edition ed., Academic press, Elsevier, 2002.
[42] V. Van Speybroeck, K. De Wispelaere, J. Van der Mynsbrugge, M. Vandichel, K. Hemelsoet, M. Waroquier, Chem. Soc. Rev., (2014) DOI: 10.1039/C4CS00146J.
[43] S. Svelle, S. Kolboe, O. Swang, U. Olsbye, J. Phys. Chem. B, 109 (2005) 12874.
[44] R.Y. Brogaard, R. Henry, Y. Schuurman, A.J. Medford, P.G. Moses, P. Beato, S. Svelle, J.K. Nørskov, U. Olsbye, J. Catal., 314 (2014) 159.
[45] J. Van der Mynsbrugge, S.L.C. Moors, K. De Wispelaere, V. Van Speybroeck, ChemCatChem, 6 (2014) 1906.
[46] I. Hill, A. Malek, A. Bhan, ACS Catal., 3 (2013) 1992.
[47] B. Arstad, S. Kolboe, O. Swang, J. Phys. Chem. B, 106 (2002) 12722.
[48] J.H. Ahn, R. Kolvenbach, S.S. Al-Khattaf, A. Jentys, J.A. Lercher, ACS Catal., 3 (2013) 817.
[49] D. Lesthaeghe, B. De Sterck, V. Van Speybroeck, G.B. Marin, M. Waroquier, Angew. Chem. Int. Ed., 46 (2007) 1311.
[50] J. Macht, R.T. Carr, E. Iglesia, J. Am. Chem. Soc., 131 (2009) 6554.
[51] J. Van der Mynsbrugge, M. Visur, U. Olsbye, P. Beato, M. Bjørgen, V. Van Speybroeck, S. Svelle, J. Catal., 292 (2012) 201.
[52] G. Sastre, D.W. Lewis, A. Corma, Phys. Chem. Chem. Phys., 2 (2000) 177.
[53] V. Van Speybroeck, J. Van der Mynsbrugge, M. Vandichel, K. Hemelsoet, D. Lesthaeghe, A. Ghysels, G.B. Marin, M. Waroquier, J. Am. Chem. Soc., 133 (2010) 888.
[54] J. Van der Mynsbrugge, J. De Ridder, K. Hemelsoet, M. Waroquier, V. Van Speybroeck, Chem. Eur. J., 19 (2013) 11568.
[55] S. Svelle, M. Visur, U. Olsbye, S. Saepurahman, M. Bjørgen, Top. Catal., 54 (2011) 897.

Supplementary material for:

How zeolitic acid strength and composition alter the reactivity of alkenes and aromatics towards methanol

Marius Westgård Erichsen[†], *Kristof De Wispelaere*[‡], *Karen Hemelsoet*[‡], *Samuel L. C. Moors*[‡], *Thomas Deconinck*[‡], *Michel Waroquier*[‡], *Stian Svelle*[†], *Veronique Van Speybroeck*[‡*], *Unni Olsbye*[†*]

[†] inGAP Centre of Research Based Innovation, Department of Chemistry, University of Oslo, N-0315 Oslo, Norway

[‡] Center for Molecular Modeling (CMM), Ghent University, Technologiepark 903, B-9052 Zwijnaarde, Belgium

* *Corresponding authors*

S1. Catalyst characterisation

X-ray diffraction patterns of H-SAPO-5 and H-SSZ-24 are shown in Figure S1.1. Both diffractograms correspond to pure and highly crystalline AFI structures and no crystalline impurities were detected. SEM analysis (Figure S1.2) of the samples revealed the H-SAPO-5 samples to consist of hexagonal crystals roughly ~1 μm in diameter and 1-2 μm in length, while the H-SSZ-24 sample consisted of more irregular crystals smaller than 1 μm. The BET surface areas calculated from N_2 adsorption isotherms (Figure S1.3) of the samples were determined to be 332 m^2/g and 343 m^2/g for H-SAPO-5 and H-SSZ-24 respectively.

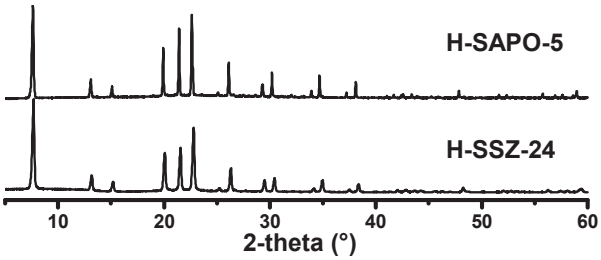

Figure S1.1: Powder XRD patterns of the catalysts employed in this work.

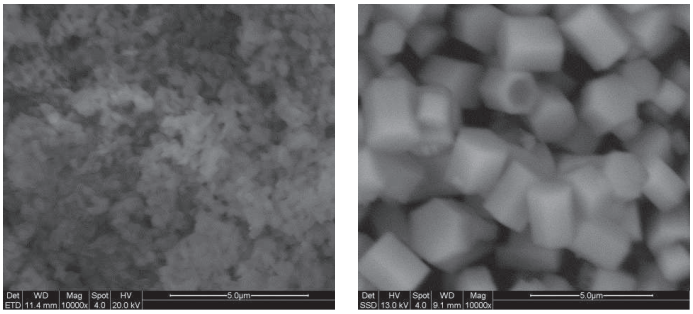

Figure S1.2: Representative SEM micrographs of the H-SSZ-24 sample (left) and H-SAPO-5 sample (right) employed in this work.

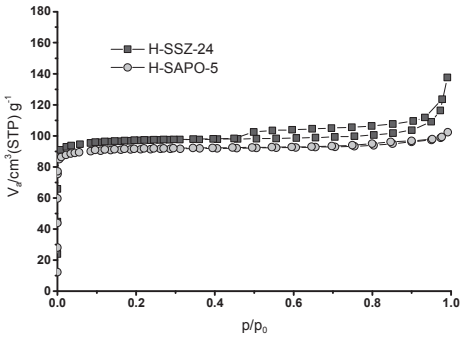

Figure S1.3: Adsorption isotherms from N_2 adsorption.

FT-IR spectra of the H-SAPO-5 sample subjected to increasing amounts of CO at -196 °C are presented in Figure S1.4. The spectral features of the sample have been previously described in detail [1]. The activated sample (black line) shows three previously assigned [2-5] absorption bands in the O-H stretching region: at 3678 (P-OH groups) and two bands at 3630 and 3530 cm^{-1} corresponding to bridging Si-OH-Al groups with the protons located in 12- and 6-rings of the AFI structure, respectively. As CO is adsorbed on the sample (grey lines in Figure S1.4), the Si-OH-Al band at 3630 cm^{-1} is eroded while two new bands grow at 3464 cm^{-1} and 3365 cm^{-1}. At high CO pressure, the P-OH band at 3678 cm^{-1} is also eroded, possibly accompanied by an increased intensity around 3500 cm^{-1}. While the reason for the appearance of two new bands when the Si-OH-Al band at 3630 cm^{-1} erodes is uncertain, it may be caused by a fermi-resonance effect similar to that proposed by Chakarova et al. [6] for H-ZSM-5. The corresponding spectra of the CO stretching region of the sample (Figure S1.4b) reveal a band for CO adsorbed on the acidic Si-OH-Al groups at 2174 cm^{-1}. The observation of only one band for CO adsorption at low coverage suggests that the observation of two bands in the OH region is spectral rather than representing two distinct sites.

FT-IR spectra of H-SSZ-24 are presented in Figure S1.5. A more detailed discussion can be found in [7]. The general spectroscopic features of H-SSZ-24 are very similar to those of H-SAPO-5, with three absorption bands observed in the O-H stretching region of the activated H-SSZ-24 sample (black line): 3747, 3612 and 3488 cm^{-1}. These bands are ascribed to Si-OH groups and to Si-OH-Al groups located in 12- and 6-rings respectively. The band positions correspond well with those reported by Martinez-Triguero et al [8]. As CO is adsorbed (grey lines), the Si-OH-Al band at 3612 cm^{-1} is eroded and a new band grows at 3295 cm^{-1}. At high CO coverage, the Si-OH band at 3747 cm^{-1} is also eroded, and a new band

appears at 3650 cm^{-1}. Again, the corresponding νCO region of the sample (Figure S1.5b) mirrors the observations from the νOH region. The frequency of CO adsorbed on the acidic Si-OH-Al groups is 2177 cm^{-1}. The interaction of the Si-OH groups in H-SSZ-24 with CO is also visible in the CO region, giving rise to a band at high CO coverage at around 2158 cm^{-1}.

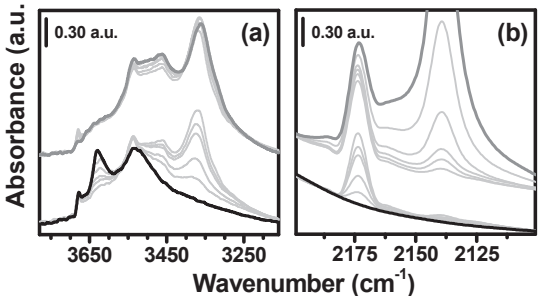

Figure S1.4: FT-IR spectra of increasing dosages of CO on H-SAPO-5 at -196 °C. In (a) the OH stretching region is shown, while (b) shows the CO stretching region. The black curves correspond to the activated sample, while the grey bold curves correspond to the spectrum of highest CO loading.

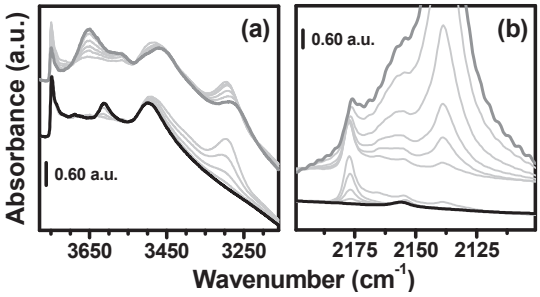

Figure S1.5: FT-IR spectra of increasing dosages of CO on H-SSZ-24 at -196 °C. In (a) the OH stretching region is shown, while (b) shows the CO stretching region. The black bold curves correspond to the activated sample, while the grey bold curves correspond to the spectrum of highest CO loading.

Overall, the key difference between the H-SAPO-5 and H-SSZ-24 is the significant difference in magnitude of the shift in OH stretching frequency for the Si-OH-Al groups when they interact with CO. The largest shift observed in H-SAPO-5 is $\Delta\nu_{OH}$ = -265 cm^{-1} while the shift in H-SSZ-24 is $\Delta\nu_{OH}$ = -317 cm^{-1} (corresponding $\Delta\nu_{CO}$ shifts are +34 cm^{-1} and +38 cm^{-1}), meaning that the acid sites of H-SSZ-24 are significantly stronger than those of H-SAPO-5.

S2. Supplementary data for section 3.1

S2.1. Conversion and Selectivity during methanol/benzene co-reactions at 250 °C and $P_{MeOH} = P_{Benzene} = 60$ mbar

Table S2.1: Conditions, conversion and detailed selectivity (in % carbon) during co-reaction of 60 mbar benzene with 60 mbar methanol at 250 °C over H-SSZ-24 and H-SAPO-5. Benzene conversion was calculated assuming one mole benzene is consumed per mole of (poly)MB formed and two per mole of diphenylmethane formed. Oxygenate conversion is calculated assuming all methyl groups and aliphatic products are produced from methanol, and formation of dimethyl ether (DME) is not included.

Catalyst	**H-SSZ-24**	**H-SAPO-5**
Benzene conversion (%)	0.20	0.22
Oxygenate conversion (%)	0.39	1.28
Selectivity (C%)		
C_2	0.5	0.5
C_3	1.1	1.1
C_4	0.9	16.1
C_{5+}	0.5	14.1
Toluene	41.3	28.6
Xylenes	9.4	3.3
TriMBs	7.4	8.1
TetraMBs	4.0	3.3
PentaMB	5.9	6.0
HexaMB	1.2	4.9
Diphenylmethane	22.4	4.9
Other Aromatics	5.5	9.2

S2.2. Isotopic labels of selected aromatic products from co-reaction of 60 mbar ^{12}C benzene with 60 mbar ^{13}C methanol at 250 °C over H-SSZ-24 and H-SAPO-5

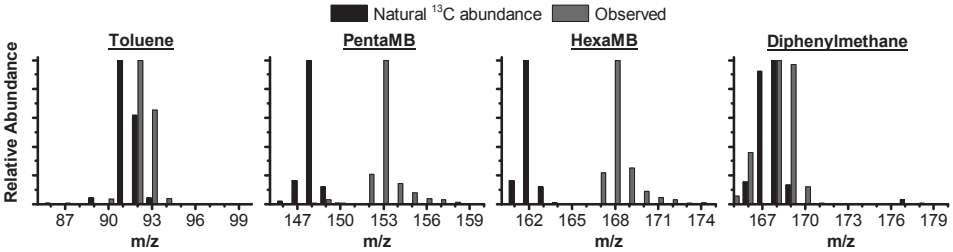

Figure S2.1: Observed mass spectra for effluent toluene, pentamethylbenzene, hexamethylbenzene and diphenylmethane during co reaction of 60 mbar ^{12}C benzene with 60 mbar ^{13}C-labelled methanol at 250 °C over H-SSZ-24. The black bars display the spectrum of the same compounds with natural abundance of ^{13}C.

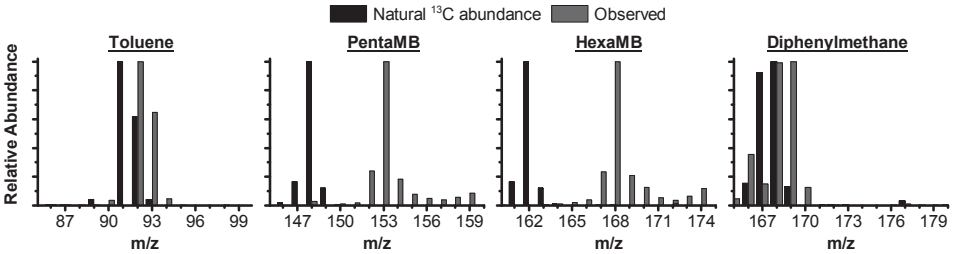

Figure S2.2: Observed mass spectra for effluent toluene, pentamethylbenzene, hexamethylbenzene and diphenylmethane during co reaction of 60 mbar ^{12}C benzene with 60 mbar ^{13}C-labelled methanol at 250 °C over H-SSZ-24. The black bars display the spectrum of the same compounds with natural abundance of ^{13}C.

S2.3. DME formation over H-SSZ-24 and H-SAPO-5 at 250 °C

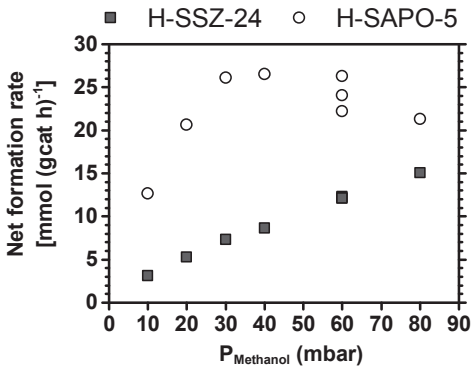

Figure S2.3: Net rates of formation of DME as a function of the methanol partial pressure during co-reactions of benzene and methanol at 250 °C over H-SSZ-24 and H-SAPO-5. PBenzene = 60 mbar. Total WHSV = 140-191 h^{-1} (H-SSZ-24) or 17.5-24 h^{-1} (H-SAPO-5). Note that the rates are given per gram catalyst, and that H-SAPO-5 contains fewer Brønsted acid sites than H-SSZ-24.

A prominent difference between the two catalysts is in the formation of dimethyl ether (DME) from methanol. Figure S2.3 displays the net rate of DME over the two catalysts. For H-SSZ-24, the rate of dimethyl ether formation displays a roughly first order dependence on methanol partial pressure and is far from thermodynamic equilibrium. At most 2 % of the methanol used was converted into DME at 250 °C over H-SSZ-24. Over H-SAPO-5 the situation differs significantly, and as much as 62% of the methanol is converted to DME at the lowest methanol partial pressures, while 16% is converted at the highest.

The reasons for this large difference in DME formation rates have not been investigated further, and are considered outside the scope of this work. However, the significantly higher rate of DME formation over H-SAPO-5 compared to H-SSZ-24 is surprising, since the rate of hydrocarbon formation is 2-3 times faster (per gram catalyst) over H-SSZ-24 than in H-SAPO-5 at the same conditions. A plausible explanation is that H-SAPO-5 contains additional sites capable of catalysing methanol dehydration to form DME. Indeed, previous works have shown activity for DME formation over pure aluminophosphate catalysts [9, 10]. A possibility is that P-OH groups present on the external surface or in defects possess enough acidity for this reaction, but not enough to catalyse hydrocarbon formation. Such P-OH groups are commonly observed in SAPO-5 materials [2-4].

S2.4. Benzene/methanol co-reactions at 350 °C

As it was difficult to study the rate of benzene methylation alone at 250 °C over H-SAPO-5, a similar series of experiments was performed at higher temperature as well. Figure S3.1 shows the results of co-reactions between 60 mbar benzene and a variable partial pressure of methanol. For both catalysts, the rate of reaction was significantly higher at 350°C than at 250°C.

Over H-SSZ-24 (Figure S3.1, left), the conversion of benzene was now around 2 % and increased slightly with an increase in methanol partial pressure. At these conditions, similar to what was observed at low temperature, the yield of other aromatics increased at the expense of toluene when methanol partial pressure increased. In contrast to what was observed at low temperature, the net formation rate of aliphatics was comparable to or larger than the rate of polymethylbenzene formation.

Looking at H-SAPO-5 (Figure S3.1, right), the difference from H-SSZ-24 was not as striking as at 250°C. The most noticeable difference was a higher selectivity to the first methylation product (toluene) at low methanol partial pressures. However, with an increase in methanol partial pressure, the net formation rate of aliphatics increases significantly faster than what was seen over H-SSZ-24, and at 80 mbar partial pressure of methanol is also significantly higher than the net rate of polymethylbenzene formation, and nearly as high as the net toluene formation rate.

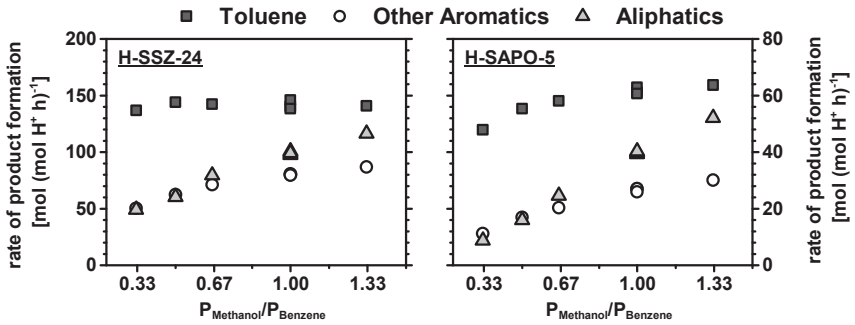

Figure S2.4: Net rates of formation of the main product groups during co-reactions of benzene and methanol as a function of the methanol partial pressure at 350 °C over H-SSZ-24 (left) and H-SAPO-5 (right). $P_{Benzene}$ = 60 mbar. Benzene feed rate = 13×10^3 mol (mol H^+)$^{-1}$ h^{-1} over H-SSZ-24 and 2.8×10^3 mol (mol H^+)$^{-1}$ h^{-1} over H-SAPO-5. Total WHSV = 140-191 h^{-1} (H-SSZ-24) or 17.5-24 h^{-1} (H-SAPO-5). The data have been corrected for deactivation.

While the product fractions thus look more similar in the two catalysts at 350ºC, a closer look at the aliphatics distribution again reveals significant differences. The net formation rates for different aliphatic products are shown in Figure 3.5 for both catalysts. Similar to what was observed at 250 °C, H-SSZ-24 produces mainly propene and ethene, with smaller amounts of larger aliphatics. Contrary to what was observed at 250 °C ethene and propene combined constitutes the largest fraction over H-SAPO-5 as well. However, the net formation rate of C_{4+} relative to C_2 and C_3 aliphatics is still significantly higher over H-SAPO-5 than over H-SSZ-24. As was observed at 250 °C, the average size of the aliphatic products increases with the partial pressure of methanol over H-SAPO-5, but this effect is not very pronounced over H-SSZ-24.

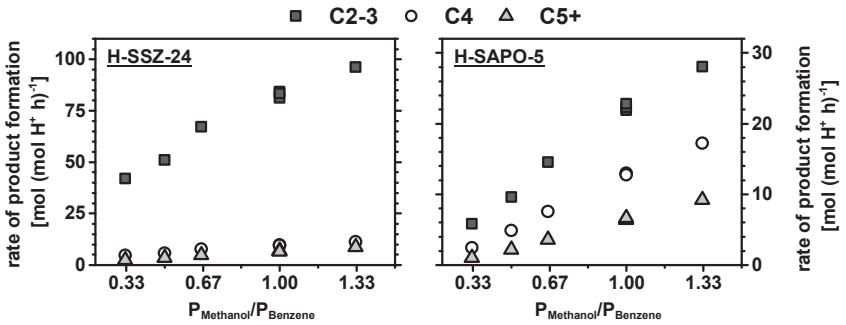

Figure S2.5: Net rates of formation for aliphatic products during co-reactions of benzene and methanol as a function of the methanol partial pressure at 350 °C over H-SSZ-24 (left) and H-SAPO-5 (right). $P_{Benzene}$ = 60 mbar. Benzene feed rate = 13×10^3 mol (mol H^+)$^{-1}$ h^{-1} over H-SSZ-24 and 2.8×10^3 mol (mol H^+)$^{-1}$ h^{-1} over H-SAPO-5. Total WHSV = 140-191 h^{-1} (H-SSZ-24) or 17.5-24 h^{-1} (H-SAPO-5). The data have been corrected for deactivation.

S3. Supplementary data for section 3.2.1

S3.1. Total feed conversion and selectivities during co-reaction of methanol with propene or benzene at 350-400°C.

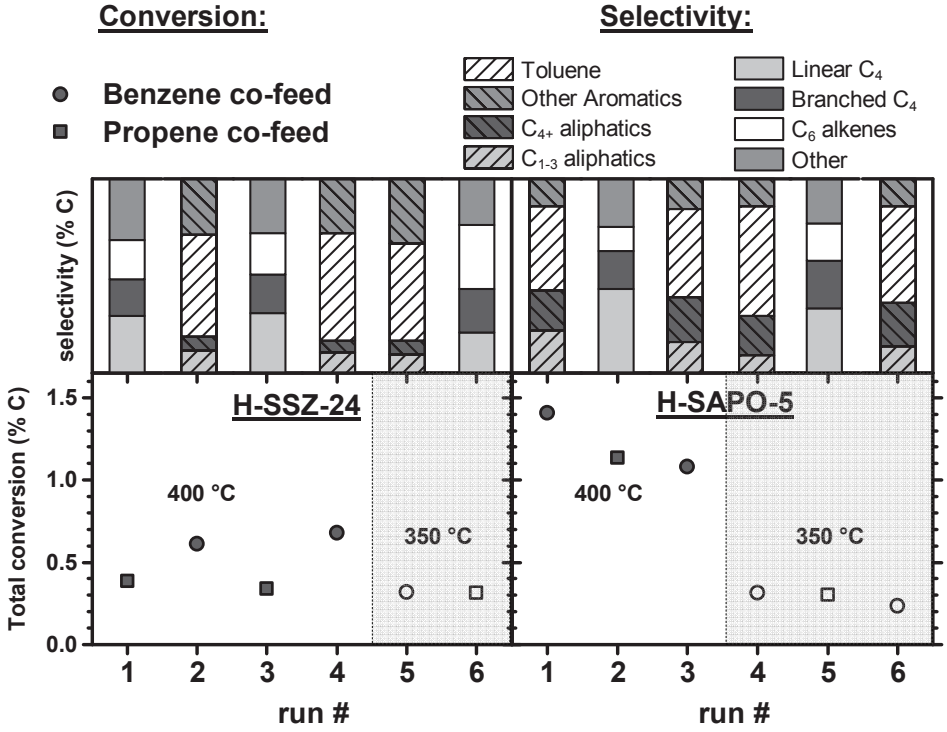

Figure S3.1: Conversion and selectivities during co-reactions of methanol with benzene or propene at 350 °C and 400 °C. The bottom plots show the total conversion of both reactants (methanol and either propene or benzene) as a function of the run number (the catalyst was regenerated between each run). Squares signify propene co-feed, while circles signify benzene co-feed. Filled symbols were experiments performed at 400 °C, while the experiments with unfilled symbols were performed at 350 °C. The bar graphs above display the grouped selectivity for each run. Note that the yield of C_6 alkenes (from dimerisation of propene) during propene co-feed over H-SSZ-24 increases with decreasing temperature. A similar trend has previously been observed over H-ZSM-5 for propene dimerisation [11]. This means that the total conversion during propene or benzene co-reaction over H-SSZ-24 at 350 °C is similar even though the net methylation rate of propene is significantly lower than the net methylation rate of benzene.

S3.2. Isotopic distributions of selected products during co-reaction of methanol with propene or benzene at 350-400°C .

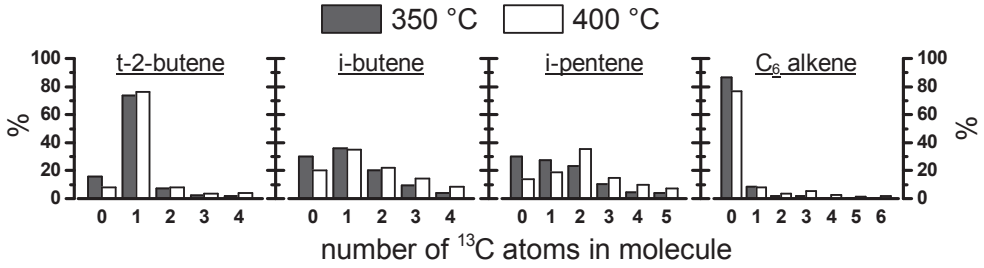

Figure S3.2: Number of ^{13}C-atoms (from ^{13}C-labelled methanol) in effluent t-2-butene, i-butene, 2-methyl-2-butene (i-pentene) and a representative C_6 alkene (unknown isomer) after 10 minutes of co-reaction of 60 mbar methanol and 60 mbar propene (WHSV = 512 h^{-1}) over H-SSZ-24 at 350 °C and 400 °C.

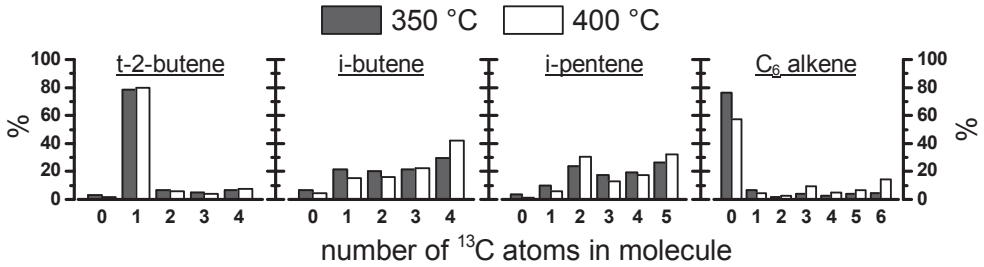

Figure S3.3: Number of ^{13}C-atoms (from ^{13}C-labelled methanol) in effluent t-2-butene, i-butene, 2-methyl-2-butene (i-pentene) and a representative C_6 alkene (unknown isomer) after 10 minutes of co-reaction of 60 mbar methanol and 60 mbar propene (WHSV = 68 h^{-1}) over H-SAPO-5 at 350 °C and 400 °C.

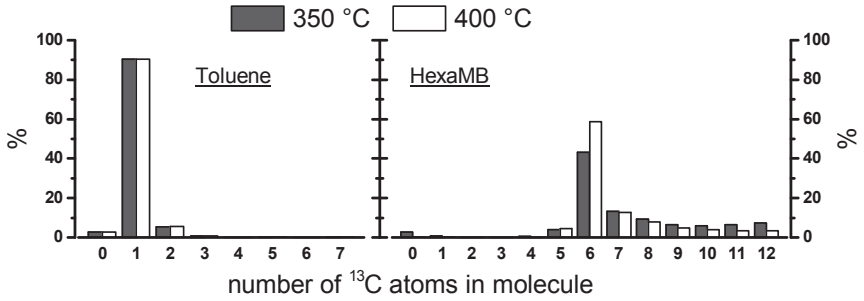

Figure S3.4: Number of ^{13}C-atoms (from ^{13}C-labelled methanol) in effluent toluene and hexamethylbenzene after 10 minutes of co-reaction of 60 mbar methanol and 60 mbar benzene (WHSV = 762 h^{-1}) over H-SSZ-24 at 350 °C and 400 °C.

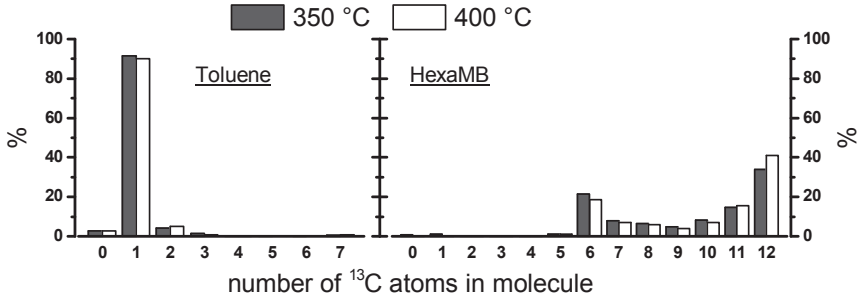

Figure S3.5: Number of ^{13}C-atoms (from ^{13}C-labelled methanol) in effluent toluene and hexamethylbenzene after 10 minutes of co-reaction of 60 mbar methanol and 60 mbar benzene (WHSV = 95 h^{-1}) over H-SAPO-5 at 350 °C and 400 °C.

S4. Supplementary computational details

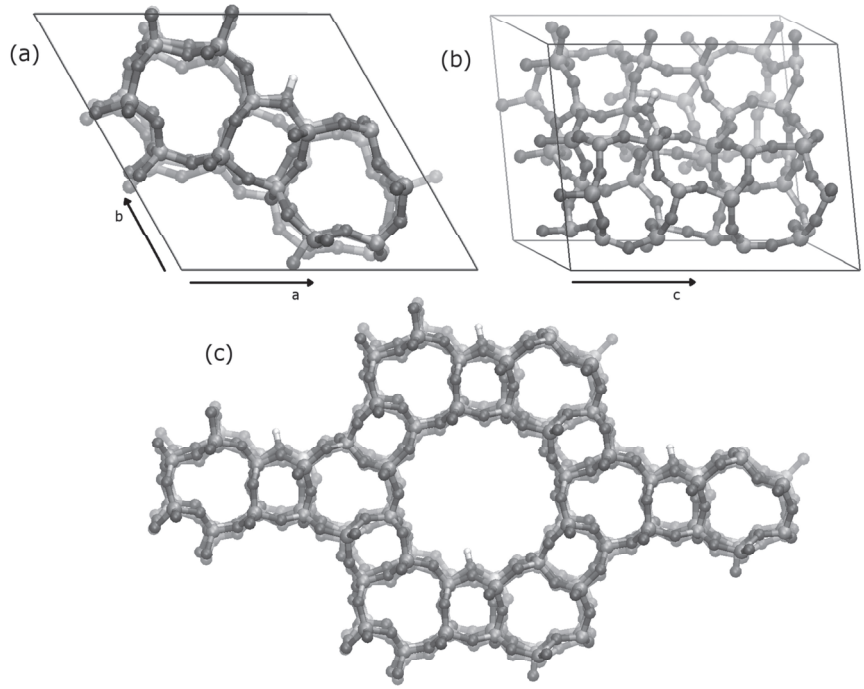

Figure S4.1: the 1x1x2 super cell of H-SAPO-5 used in all simulations.

NPT molecular dynamics (MD) simulations were performed at 350 ºC and 1 bar. After an equilibration run of 5 ps, a production run of 50 ps is performed. Hereby, the zeolitic framework is fully flexible. The temperature is controlled via a chain of 5 Nosé-Hoover thermostats. An integration time step of 0.5 fs was applied. The appropriate cell parameters were obtained from the NPT MD simulations with the appropriate guest molecules adsorbed in the framework.

Table S4.1: Average cell parameters obtained after NPT simulations at 350ºC with different loadings of the AFI simulation cells.

Framework	T (ºC)	Loading	V (Å^3)	a (Å)	b (Å)	c (Å)	α (º)	β (º)	γ (º)
H-SAPO-5	350	1MeOH	2895.38	14.0233	14.0348	16.9653	90	90	120
		1 BZ	2910.96	14.0319	14.0983	16.9912	90	90	120
		1 $C_3^=$	2895.84	14.0055	14.0645	16.9755	90	90	120
		1MeOH + 1BZ	2894.05	13.9979	14.0737	16.9631	90	90	120
		1MeOH + 1 $C_3^=$	2887.83	13.9817	14.0739	16.9459	90	90	120
H-SSZ-24	350	1MeOH	2806.84	13.8749	13.8793	16.8302	90	90	120
		1 BZ					90	90	120
		1 $C_3^=$	2805.38	13.8636	13.8954	16.8156	90	90	120
		1MeOH + 1BZ	2804.50	13.8775	13.8781	16.8144	90	90	120
		1MeOH + 1 $C_3^=$	2803.93	13.8699	13.8886	16.8075	90	90	120

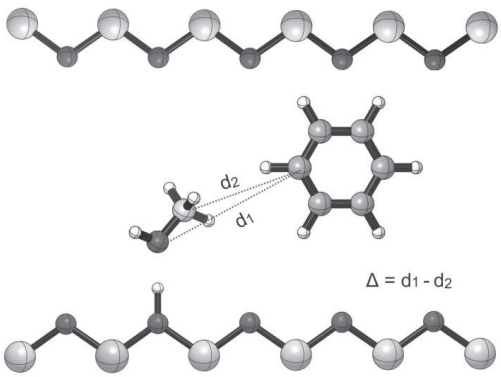

Figure S4.2: distances d_1 and d_2 are followed during the MD simulations of methanol and co-adsorbed benzene. A Δ-value higher than 0.5 Å is considered as a configuration wherein the methyl group is pointing towards the benzene molecule. An analogous procedure was followed for simulations of methanol and propene.

S5. Methanol coverage of acid sites at 350 ºC

Based on a distance criterion, the occupation of the acid site by methanol can be quantified for both materials when benzene and propene are co-adsorbed. If the shortest distance between the methanol oxygen and the framework oxygens in the tetrahedral surroundings of the substitutional defect is lower than 3.5Å, methanol is considered to occupy the acid site (Table S5.1).

Table S5.1. Probability for MeOH covering the acid site with co-adsorbed benzene or propene at 350 ºC

	H-SSZ-24	**H-SAPO-5**
MeOH + BZ	100%	98%
MeOH + $C_3^=$	94%	98%

The interaction of benzene with the acid site is monitored by the shortest distance of the center of mass (COM) of benzene with the three O atoms surrounding the substitutional defect. The probability density of this distance is plotted in Figure S5.1. To see the influence of the co-adsorption of benzene or propene with methanol, the results are compared with results from MD simulations for pure benzene and propene adsorbed in the AFI channels.

- In H-SSZ-24, the most probable benzene COM – Oz distance is lower upon co-adsorption with methanol than for the pure adsorption of benzene on the acid site (Figure S5.1a). This indicates that methanol and benzene strongly interact when methanol and benzene are co-adsorbed in H-SSZ-24. In H-SAPO-5, methanol just replaces benzene at the acid site (Figure S5.1b). From both Figures can be seen that benzene is replaced when co-adsorbed with methanol, to allow direct interaction between methanol and the acid site. Furthermore, from the curves corresponding with pure benzene adsorbed in H-SSZ-24 and H-SAPO-5 follows that in H-SAPO-5 the interaction between benzene and the acid site is stronger than in H-SSZ-24.
- For pure propene, the interactions with the acid site in H-SSZ-24 are stronger than in H-SAPO-5, as the most probable distance from the acid site to find propene is relatively short in H-SSZ-24 and shorter than in H-SAPO-5. Moreover, also propene is replaced by methanol upon co-adsorption in both materials.

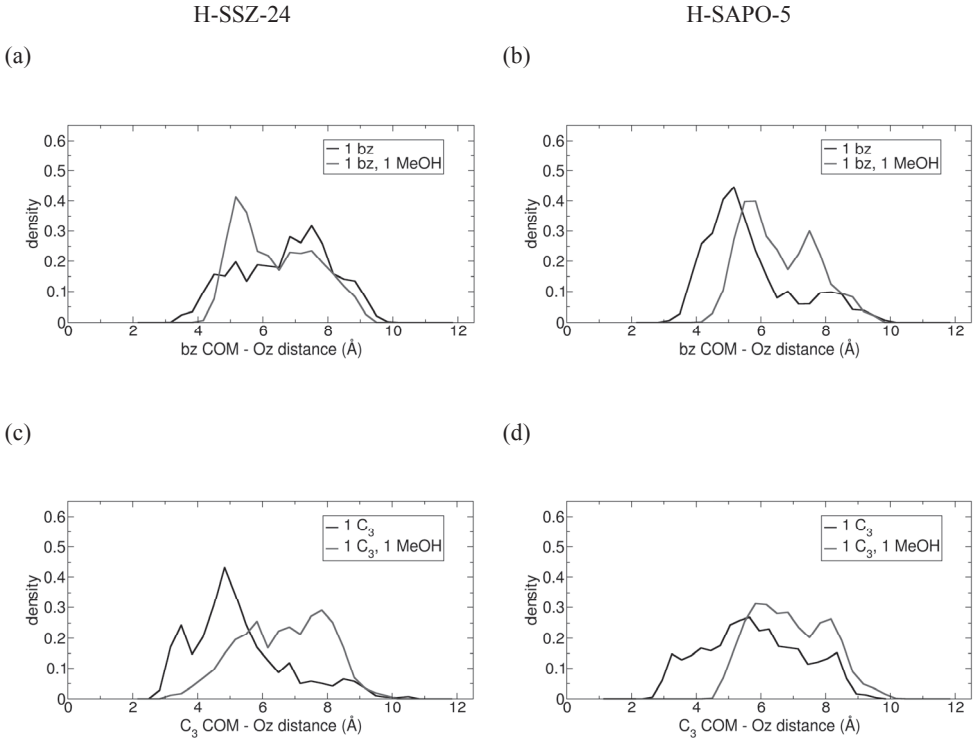

Figure S5.1. Probability densities of the benzene COM – acid site distances in H-SSZ-24 (a) and H-SAPO-5 (b) and the probability density of propene COM – acid site distances in H-SSZ-24 (c) and H-SAPO-5 (d), with and without a methanol molecule. Results were obtained after analysis of a MD simulation at 350 ºC.

Additionally, the orientation of benzene and propene in the AFI channels can be followed upon co-adsorption with methanol. Figure S5.2 displays the probability densities for the orientation of benzene and propene in the AFI channels throughout an MD simulation at 350 ºC. In the absence of methanol, benzene and propene preferentially orient the plane defined by the carbon atoms parallel to the channel axis to enable a good interaction between the π-electrons and the acid site. However, upon co-adsorption of methanol the preferential orientation of the hydrocarbons clearly shifts. As benzene and propene no longer have direct access to the acidic proton (*vide supra*), the hydrocarbon guest molecules reorient to maximize their interactions with the zeolitic channel wall.

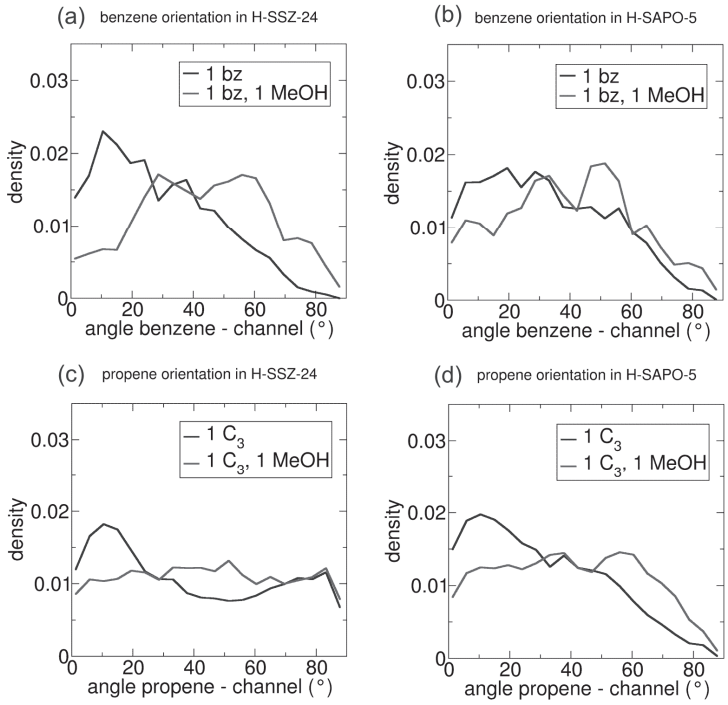

Figure S5.2: Probability densities for the orientation of benzene (a,b) and propene (c,d) in H-SSZ-24 (a,c) and H-SAPO-5 (b,d) in the absence (blue curve) and presence (red curve) of methanol during an MD simulation at 350ºC. The curves originate from histograms, normalized such that the area under each curve equals 1.

S6. Optimized co-adsorbed complexes and calculated adsorption and co-adsorption energies.

Table S6.1. Electronic adsorption energy (kJ/mol) for methanol (MeOH) on the acid site and benzene (BZ) or propene ($C_3^=$) co-adsorbed in H-SSZ-24 and H-SAPO-5 (Level of theory: revPBE-D3).

	H-SSZ-24	**H-SAPO-5**
	ΔE [kJ/mol]	ΔE [kJ/mol]
$MeOH_{,ads}$	-98.4	-83.2
$BZ_{,co\text{-}ads}$	-80.5[b]	-84.6[a]
		-88.9[b]
$C_3^={}_{,co\text{-}ads}$	-51.6[a]	-67.5[a]
	-53.9[b]	-59.5[b]

[a] Methyl group pointing away from the hydrocarbon (Figure 3.5 b,d)

[b] Methyl group pointing towards the hydrocarbon (Figure 3.5 a,c)

Figure S6.1 and Figure S6.2 depict the geometries of all the stable potential energy minima that could be located for the co-adsorption of methanol and benzene or propene respectively. For benzene co-adsorption in H-SAPO-5, two stable minima could be located. The two configurations differ in the orientation of methanol with respect to benzene. The methanol methyl group can either point towards or away from benzene (Figure S6.1 b and c respectively). In H-SSZ-24 only the configuration with methanol pointing towards benzene could be located as stable minimum (Figure S6.1 a).

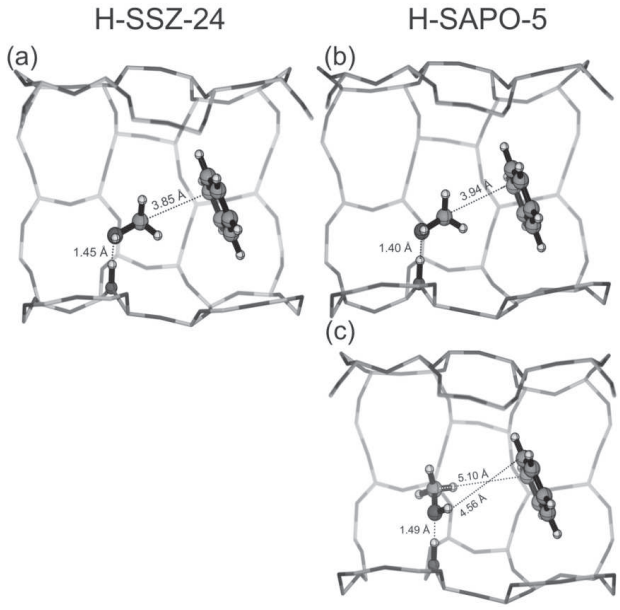

Figure S6.1: All geometries with indication of characteristic distances for co-adsorption of methanol and benzene in H-SSZ-24 (a) and H-SAPO-5 (b,c).

For propene co-adsorption two stable minima could be located on the potential energy surface in both materials. The two configurations again differ in the orientation of methanol with respect to propene. The methanol methyl group can either point towards or away from benzene (Figure S6.2 a,b and c,d respectively).

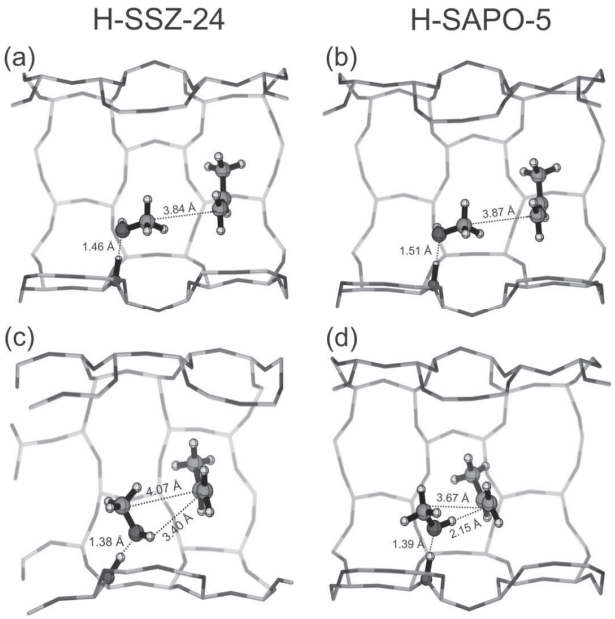

Figure S6.2: All geometries with indication of characteristic distances for co-adsorption of methanol and propene in H-SSZ-24 (a,c) and H-SAPO-5 (b,d).

S7. Optimized transition state, pre-reactive complex and product for the methylation of benzene in both AFI materials

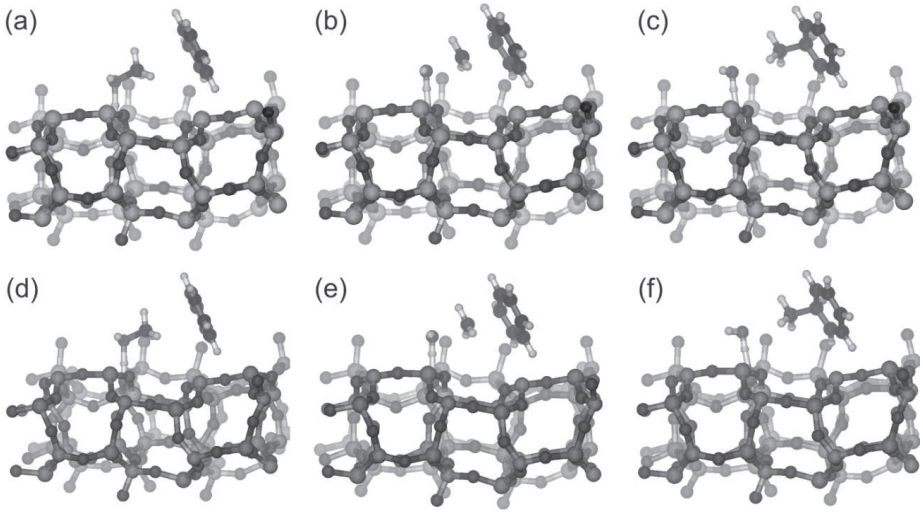

Figure S7.1: pre-reactive complex (a,d), transition state (b,e) and product (c,f) of the benzene methylation in H-SSZ-24 and H-SAPO-5 respectively.

S8. Overview of the time-averaged shortest methyl carbon – benzene/propene carbon distances

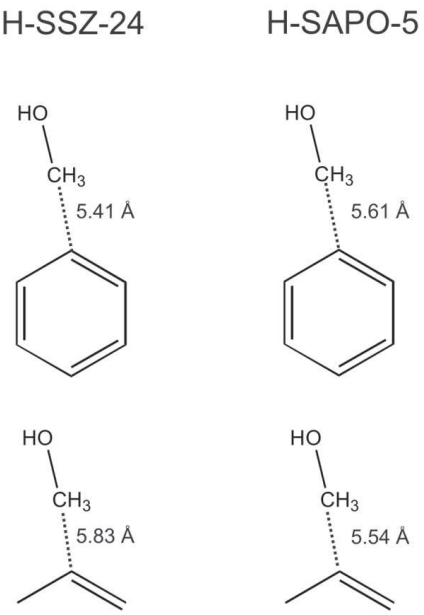

Figure S8.1: Time-averaged shortest distances between C_{MeOH} and $C_{benzene}$ or $C_{propene}$ in H-SSZ-24 and H-SAPO-5 after a 50 ps MD simulation**.**

S9. Dynamical behavior of benzene and propene adsorbed on a methoxy group in H-SSZ-24 and H-SAPO-5

- Methoxy as methylating agent for benzene methylation
    - Average MD C_m-C_{bz} distance in H-SSZ-24: 5.71 Å
    - Average MD C_m-C_{bz} distance in H-SAPO-5: 6.14 Å
- Methoxy as methylating agent for propene methylation
    - Average MD C_m-C_p distance in H-SSZ-24: 6.04 Å
    - Average MD C_m-C_p distance in H-SAPO-5: 6.27 Å

Supplementary References

[1] M. Westgård Erichsen, S. Svelle, U. Olsbye, J. Catal., 298 (2013) 94.
[2] J. Chen, P.A. Wright, S. Natarajan, J.M. Thomas, Stud. Surf. Sci. Catal., 84 (1994) 1731.
[3] B. Zibrowius, E. Loffler, M. Hunger, Zeolites, 12 (1992) 167.
[4] S.G. Hedge, P. Ratnasamy, L.M. Kustov, V.B. Kazansky, Zeolites, 8 (1988) 137.
[5] F. Schuth, D. Demuth, B. Zibrowius, J. Kornatowski, G. Finger, J. Am. Chem. Soc., 116 (1994) 1090.
[6] K. Chakarova, K. Hadjiivanov, J. Phys. Chem. C, 115 (2011) 4806.
[7] M. Westgård Erichsen, S. Svelle, U. Olsbye, Catal. Today, 215 (2013) 216.
[8] J. Martinez-Triguero, M.J. Diaz-Cabañas, M.A. Camblor, V. Fornés, T.L.M. Maesen, A. Corma, J. Catal., 182 (1999) 463.
[9] W. Dai, W. Kong, G. Wu, N. Li, L. Li, N. Guan, Catal. Commun., 12 (2011) 535.
[10] G. Lischke, B. Parlitz, U. Lohse, E. Schreier, R. Fricke, Appl. Catal. A, 166 (1998) 351.
[11] S. Svelle, P.O. Rønning, U. Olsbye, S. Kolboe, J. Catal., 234 (2005) 385.

“Reactivity of the heptamethylbenzenium cation – a combined mass spectrometric and catalytic investigation”

M. Westgård Erichsen*, M. Mortén, O. Sekiguchi, S. Svelle, E. Uggerud, U. Olsbye

Preliminary Manuscript

VI